

A GFRP BOND STRESS AND STRENGTH

**A GFRP BAR BOND STRESS AND STRENGTH:
COMPARISON OF BEAM-BOND AND PULLOUT TESTS
RESULTS**

By ELYAS MAKHMALBAF, B.ENG

**A Thesis Submitted to the School of Graduate Studies in
Partial Fulfilment of the Requirements for the Degree Masters
of Applied Science**

McMaster University

© Copyright by Elyas Makhmalbaf, April 2015

McMaster University MASTER OF APPLIED SCIENCE, (2015)

Hamilton, Ontario, Canada

TITLE: A GFRP Bar Bond Stress and Strength: Comparison of Beam-bond and Pullout Tests Results

AUTHOR: Elyas Makhmalbaf, B.Eng. (McMaster University)

SUPERVISOR: Professor A.G. Razaqpur

NUMBER OF PAGES: XXII, 227

Lay Abstract

The force that bonds a reinforcing rod to concrete is determined using three test methods. Each method is recommended by some design standards, but it is unclear how the results of these tests compare to each other. To shed light on the issue, a 15 *mm* fibre glass rod was tested using three well-known test methods. It was discovered that two of the methods give results that are reasonably close while the third gives variable results that generally do not agree with the results of the other two. It was also discovered that the required embedment length recommended for such a bar by design codes and standards are relatively excessive because they underestimate the actual bond strength of the rod. Since sometimes it may be difficult to provide such long length in practice, it is recommended that the code requirements be revisited.

Abstract

Four beam-bond test specimens, two in accordance with RILEM TC-RC5 recommendation, labelled as RILEM and two based on a modified form of the ACI 208 beam-bond test method, labelled as Notched, were tested in four-point bending to investigate the bond stress distribution and values along the bar embedment length of a 15 mm nominal diameter GFRP rebar. The beams experienced failure through the rupturing of the longitudinal GFRP tensile reinforcement. In addition, two Modified and ten Standard pullout specimens were tested using the same bar. The beam-bond and the Modified pullout specimens had embedment length of 600 mm while the Standard pullout specimens had, in accordance with CSA S806, 60 mm embedment, or four times the bar nominal diameter. The first Modified pullout specimen experienced concrete splitting failure and as a result, the second was lightly confined and failed by GFRP bar rupture. All ten Standard pullout specimens failed due to bar pullout.

It was determined that the actual bond stress distribution as a function of the embedment length is practically parabolic and can be described by the derivative of a modified form of the logistic growth function used to approximate the strain distribution along the embedment length. Furthermore, the maximum bond stress location progressively moves from the loaded-end towards the unloaded-end as the bond continues to deteriorate with increasing GFRP stress levels. The development length recommendations by ACI 440.1 and to a lesser degree, CSA S806 and CSA S6 are quite conservative compared to that which is required. It is observed that pullout tests alone cannot provide sufficient knowledge regarding the bond behaviour of FRP reinforcement; consequently, the results of beam-bond testing are more appropriate. Standard pullout tests may be incorporated into quality assurance programs with the understanding that they cannot provide valuable information regarding bond stress distribution and required development length in real structural elements with large embedment lengths. In terms of the beam-bond test method, the RILEM TC-RC5 design recommendation appears to be superior since it eschews severe stress perturbation caused by incidence of flexural cracks at beam midspan. As a result, it produces stability in the terms of the data gathered from the strain gauges placed on the GFRP bar. This benefit outweighs the ease of constructability of the Notched beams as well as their resemblance to real beams.

Acknowledgements

It has been a true honor and privilege to be able to conduct my studies under the supervision of Professor Dr. A.G. Razaqpur. His guidance and wealth of knowledge were instrumental in my progression at both the undergraduate and the graduate level. I truly appreciate his teachings and the time he invested in helping me and I am proud to be his student.

I would like to thank the staff at TEME Inc., especially the company President, Mr. Stephen Witts, the Vice President, Dr. Ahmed Mostafa and Mr. Jerzy Kwiatek for allowing me the usage of materials and equipment at their facility. Special thanks to Dr. Ahmed Mostafa who tested and provided me with the results of the ten Standard pullout specimens and on numerous occasions took time off from his busy schedule in order to provide guidance. To McMaster University's Civil Engineering department, Dr. Manuel Campedelli as well as the staff at ADL, thank you for all your assistance.

As for my family, first, I would like to thank my dear mother, Fatemeh, who made countless sacrifices to help me become successful and patiently stood by me throughout my academic career. I love you from the bottom of my heart mom. My dear aunt, Zahra, thank you for your prayers and for being patient with me through rain and shine. I love you and will always be there for you. To my uncle, Mahmood, thank you for teaching me to be disciplined academically and to continue gaining as much knowledge as possible. To my dear brother Karon, thank you for being there, for your encouragement and for making me smile in the face of challenges.

Table of Contents

Chapter 1 Introduction	1
1.1 General	1
1.2 Bond Behaviour and Strength in Conventional Steel Reinforced Concrete	2
1.2.1 Factors Affecting Bond Strength of Steel Reinforced Concrete Structures	3
1.2.2 The Phenomenon of Confinement and Splitting Failure	3
1.3 Fibre Reinforced Polymers (FRPs): An Alternative Solution to Conventional Steel Reinforcement	4
1.3.1 Characteristics of FRP	4
1.3.2 Polymers (Resins).....	5
1.3.3 Fibres	6
1.3.4 FRP Composite.....	6
1.4 Comparison of Physical and Mechanical Properties of Steel and FRP.....	7
1.4.1 Physical Properties.....	7
1.4.2 Mechanical Properties	8
1.5 Bond Behaviour of FRP	9
1.6 Purpose and Scope of Current Research Program	12
Chapter 2 Literature Review	13
2.1 General	13
2.2 Testing Methods for Bond Performance of Steel and FRP Rebars in Concrete	13
2.3 Bond Behaviour of Reinforcement in Concrete observed in Pullout Testing.....	15
2.4 Bond Behaviour of Reinforcement in Concrete observed in Beam-bond Testing...23	
2.5 Summary	31
Chapter 3 Experimental Program	34
3.1 General	34
3.2 Materials.....	35
3.2.1 GFRP Bar	35
3.2.2 Mild Steel.....	40
3.2.3 Concrete	41

3.2.3.1 Compressive Strength and Elastic Modulus	41
3.2.3.2 Tensile Strength	43
3.3 Test Equipment and Instrumentation	45
3.4 Test Specimens.....	46
3.4.1 Specimen Designation	46
3.4.2 Construction Detail of Test Beams.....	46
3.4.3 Construction Detail of Modified and Standard Pullout Specimens.....	54
3.4.4 Installation of Instrumentation.....	57
3.4.4.1 LVDTs	57
3.4.4.2 Strain Gauges	59
3.4.4.3 String Pot Potentiometers	62
3.5 Test Procedure.....	63
3.6 Loading Rate and Data Acquisition	71
Chapter 4 Experimental Results	72
4.1 General	72
4.2 Results and Observations for RILEM Beams BR1 and BR2.....	73
4.2.1 Key Observations.....	73
4.2.2 Load-deflection Behaviour	77
4.2.3 GFRP Bar Strain.....	80
4.2.4 GFRP Bar Slip.....	82
4.2.5 Post-test Inspection.....	82
4.3 Results and Observations for Notched Beams BN1 and BN2	87
4.3.1 Key Observations.....	87
4.3.2 Load-deflection Behaviour	94
4.3.3 GFRP Bar Strain.....	97
4.3.4 GFRP Bar Slip	99
4.3.5 Post-test Inspection.....	99
4.4 Summary of Beam-bond Specimens	102
4.5 Results and Observations for Modified Pullout Specimens MP1 and MP2	103
4.5.1 Key Observations.....	103
4.5.2 GFRP Bar Strain.....	109

4.5.3 GFRP Bar Slip	112
4.6 Results and Observations for Standard Pullout Specimens P1 to P10.....	113
Chapter 5 Analysis and Discussion	115
5.1 General	115
5.2 Beam Flexural Behaviour.....	116
5.3 Preliminary Analysis	118
5.3.1 Overview.....	118
5.3.2 RILEM Beams	119
5.3.3 Notched Beams	123
5.3.4 Modified Pullout Specimens	133
5.4 Concrete Splitting and Confinement	136
5.5 Bond Stress Distribution and Determination of Required Embedment Length	138
5.5.1 General.....	138
5.5.2 Current Practice	139
5.5.3 Bar Strain Distribution along Embedment Length	143
5.5.4 Alternative Method.....	148
5.6 Actual versus Uniform Bond Stress Distribution.....	166
5.7 Experimental versus Recommended Development Length	173
5.8 Effect of Test Method on Bond Behaviour and Bond Stress Distribution.....	181
5.9 Bond Stress Analysis of Standard Pullout Specimens	192
Chapter 6 Summary, Conclusions and Recommendations for Future Research	204
6.1 Summary	204
6.2 Conclusions	205
6.3 Recommendations for Future Research	207
List of References.....	208
Appendix A.....	215
A.1 General	215
A.2 Flexural Calculations.....	216
A.3 Shear Calculations	226

List of Figures

Figure 1:1: Splitting failure of concrete. Park and Paulay, (1975)	4
Figure 1:2: Composite material consisting of Fibres and Matrices. Intelligent sensing for innovative structures, (2006).....	5
Figure 1:3: Idealization of a unidirectional FRP. Intelligent sensing for innovative structures, (2006)	7
Figure 1:4: Methods of enhancing mechanical interlocking a) Ribbed; b) Sand-coated; c) Wrapped and Sand-coated FRP bars. ACI 440.1, (2006)	10
Figure 2:1: Pullout testing. ACI 408, (2003)	13
Figure 2:2: Beam-bond testing. ACI 408, (2003)	14
Figure 3:1: Tensile stress-strain relationship of specimens GFRP1 to GFRP10	36
Figure 3:2: Tensile stress-strain relationship of specimens GFRP11 to GFRP20	36
Figure 3:3: Tensile stress-strain relationship of specimens GFRP21 to GFRP30	37
Figure 3:4: Sudden rupture failure of GFRP bars	39
Figure 3:5: TEME Corp. GFRP bar with ribbed surface deformations	39
Figure 3:6: Tensile stress-strain behaviour of the steel specimens	40
Figure 3:7: Concrete cylinder compression testing. Specimen C2	42
Figure 3:8: Concrete split-cylinder testing.....	44
Figure 3:9: RILEM beam detail (All dimensions are in mm).....	49
Figure 3:10: RILEM beam detail: internal view	50
Figure 3:11: RILEM beam detail: midspan view	50
Figure 3:12: Notched beam detail (All dimensions are in mm).....	52
Figure 3:13: Notched beam detail: internal view	53
Figure 3:14: Notched beam detail: midspan view	53
Figure 3:15: Modified pullout specimen detail (All dimensions are in mm).....	55
Figure 3:16: Standard pullout specimen detail (All dimensions are in mm)	56
Figure 3:17: Detail of the midspan gripping mechanism for the RILEM and Notched beams. View 1. Notched beam shown.	57
Figure 3:18: Detail of the midspan gripping mechanism for the RILEM and Notched beams. View 2. Notched beam shown.	58
Figure 3:19: Detail of the midspan gripping mechanism for the RILEM and Notched beams. View 3. Notched beam shown.	58
Figure 3:20: GFRP bar reinforcement strain gauge detail for RILEM and Notched beams (Test End), as well as for the Modified pullout specimens (All dimensions are in mm) ..	59
Figure 3:21: PVC pipes used to protect the strain gauge wires in the beam specimens	60
Figure 3:22 GFRP bar reinforcement and PVC pipe protruding out of the beam formwork	61

Figure 3:23: PVC pipes used to protect the strain gauge wires in the Modified pullout specimens	61
Figure 3:24: String pot potentiometer detail for RILEM and Notched beams (All dimensions are in mm)	62
Figure 3:25: Test setup detail for the beam-bond specimens. View 1	64
Figure 3:26: Test setup detail for the beam-bond specimens. View 2	65
Figure 3:27: Test setup detail for the beam-bond specimens. View 3	66
Figure 3:28: Test setup detail for the Modified pullout specimens	68
Figure 3:29: Test setup detail for the Standard pullout specimens	69
Figure 3:30: 3D illustration of the test setup for the Modified pullout specimens	70
Figure 4:1: GFRP bar reinforcement strain gauge detail for RILEM and Notched beams (Test End), as well as for the Modified pullout specimens (All dimensions are in mm) ..	73
Figure 4:2 Moment arm determination of RILEM beams	74
Figure 4:3: BR1 before the test	75
Figure 4:4: BR1 at failure	75
Figure 4:5: BR2 before the test	76
Figure 4:6: BR2 at failure	77
Figure 4:7: Load-midspan deflection in BR1 and BR2	78
Figure 4:8: Deflection along BR1 and BR2 at different percentages of their respective maximum load, P	79
Figure 4:9: Load-GFRP bar strain in BR1 and BR2	81
Figure 4:10: Load-uncorrected L1 bar slip in BR1 and BR2	82
Figure 4:11: BR1 “Test End”	83
Figure 4:12: BR1, “Test End”. Marked lines on GFRP bar indicate observance of significant fibre disengagement	84
Figure 4:13: BR1 “Non-test End”	84
Figure 4:14: BR1 “Non-test End”. Showing the damage and rupture experienced by the GFRP bar	85
Figure 4:15: BR2 “Test End”	85
Figure 4:16: BR2, “Test End”. Marked lines on GFRP bar indicate observance of significant fibre disengagement	86
Figure 4:17: BR2 “Non-test End”	86
Figure 4:18: BR2 “Non-test End”. Showing the damage and rupture experienced by the GFRP bar	87
Figure 4:19: BN1 before the test	88
Figure 4:20: BN1 after the first flexural crack	89
Figure 4:21: BN1 after the second flexural crack	90
Figure 4:22: BN1 at failure	90
Figure 4:23: BN2 before the test	91
Figure 4:24: BN2 after the first flexural crack	92
Figure 4:25: BN2 after the second flexural crack	93

Figure 4:26: BN2 at failure	93
Figure 4:27: Load-midspan deflection in BN1 and BN2	94
Figure 4:28: Deflection along BN1 and BN2 at different percentages of their respective maximum load, P	96
Figure 4:29: Load-GFRP bar strain in BN1 and BN2	98
Figure 4:30: Load-uncorrected L1 bar slip in BN1 and BN2	99
Figure 4:31: BN1 “Test End”	100
Figure 4:32: BN1 “Test End”. Showing the damage and rupture experienced by the GFRP bar	101
Figure 4:33: BN2 “Test End”	101
Figure 4:34: BN2 “Test End”. Showing the damage and rupture experienced by the GFRP bar	102
Figure 4:35: MP1 before the test	104
Figure 4:36: MP1 at failure	105
Figure 4:37: HSS section used to provide light confinement for MP2	106
Figure 4:38: Lightly confined MP2	107
Figure 4:39: MP2 before the test	108
Figure 4:40: MP2 at failure	109
Figure 4:41: Load-GFRP bar axial strain in MP1 and MP2	111
Figure 4:42: Load-uncorrected L3 and L4 bar slip in MP1 and MP2	112
Figure 4:43: P1 before the test	113
Figure 5:1: GFRP bar reinforcement strain gauge detail for RILEM and Notched beams (Test End), as well as for the Modified pullout specimens (All dimensions are in mm)	118
Figure 5:2: Load - GFRP bar strain in BR1	120
Figure 5:3: Load - GFRP bar strain in BR2	120
Figure 5:4: Midspan GFRP bar stress - GFRP strain in BR1	121
Figure 5:5: Midspan GFRP bar stress - GFRP strain in BR2	122
Figure 5:6: Derived concrete stress-strain relationship for this experimental program	124
Figure 5:7: State of the concrete around the longitudinal GFRP tensile reinforcement	125
Figure 5:8: Load - GFRP bar strain in BN1	130
Figure 5:9: Load - GFRP bar strain in BN2	130
Figure 5:10: Midspan GFRP bar stress - GFRP strain in BN1	131
Figure 5:11: Midspan GFRP bar stress - GFRP strain in BN2	131
Figure 5:12: Load-uncorrected L1 in RILEM and Notched beam-bond tests	133
Figure 5:13: Load - GFRP bar axial strain in MP1	134
Figure 5:14: Load - GFRP bar axial strain in MP2	135
Figure 5:15: GFRP bar stress - GFRP axial strain in MP1	135
Figure 5:16: GFRP bar stress - GFRP axial strain in MP2	136
Figure 5:17: Internal bond forces. Tepfers and De Lorenzis, (2003)	137
Figure 5:18: Bond resistance of an embedded reinforcement	138

Figure 5:19: State of stress in an infinitesimal length of a reinforcing bar embedded in concrete	139
Figure 5:20: Equilibrium of an embedded stressed bar in concrete.....	141
Figure 5:21: Strain distribution along the bar embedment length of the RILEM beams at different percentages of their respective maximum load, P.....	145
Figure 5:22: Strain distribution along the bar embedment length of the Notched beams at different percentages of their respective maximum load, P.....	146
Figure 5:23: Strain distribution along the bar embedment length of the Modified pullout specimens at different percentages of their respective maximum load, P	147
Figure 5:24: Effect of the lack of information on the strain distribution between the positions of strain gauges.....	149
Figure 5:25: Proposed expression for defining strain as a function of bar embedment length.....	151
Figure 5:26: Experimental data points versus predicted strain distribution by Equation 5.33 for RILEM beams	153
Figure 5:27: Experimental data points versus predicted strain distribution by Equation 5.33 for Notched beams	154
Figure 5:28: Experimental data points versus predicted strain distribution by Equation 5.33 for Modified pullout specimen, MP2.....	155
Figure 5:29: Experimental data points versus predicted bond stress distribution by Equation 5.38 for RILEM beams.....	158
Figure 5:30: Experimental data points versus predicted bond stress distribution by Equation 5.38 for Notched beams.....	159
Figure 5:31: Experimental data points versus predicted bond stress distribution by Equation 5.38 for Modified pullouts specimen, MP2.....	160
Figure 5:32: GFRP bar slip along embedment length predicted by Equation 5.40 for RILEM beams	163
Figure 5:33: GFRP bar slip along embedment length predicted by Equation 5.40 for Notched beams.....	164
Figure 5:34: GFRP bar slip along embedment length predicted by Equation 5.40 for Modified pullout specimen, MP2	165
Figure 5:35: Method of calculating bond stress distribution	166
Figure 5:36: Actual versus uniform assumption of bond stress distribution in the RILEM beams at different percentages of their respective maximum load, P.....	168
Figure 5:37: Actual versus uniform assumption of bond stress distribution in the Notched beams at different percentages of their respective maximum load, P.....	169
Figure 5:38: Actual versus uniform assumption of bond stress distribution in the Modified pullout specimens at different percentages of their respective maximum load, P.....	170
Figure 5:39: Experimental versus theoretical bond stress for the RILEM beams assuming a uniform bond stress distribution.....	173

Figure 5:40: Guideline predictions of development lengths with increasing GFRP bar stress in the RILEM beams	179
Figure 5:41: Guideline predictions of development lengths with increasing GFRP bar stress in the Notched beams	180
Figure 5:42: Guideline predictions of development lengths with increasing GFRP bar stress in the Modified pullout specimens	180
Figure 5:43: Distance from the point of loaded-end LVDT attachment and the onset of the bar embedment for the beam-bond specimens.....	181
Figure 5:44: Distance from the point of loaded-end LVDT attachment and the onset of the bar embedment for the Modified pullout specimens	182
Figure 5:45: Corrected loaded-end bar slip versus integration of bar strains along its embedment length for the RILEM beams.....	185
Figure 5:46: Corrected loaded-end bar slip versus integration of bar strains along its embedment length for the Notched beams.....	185
Figure 5:47: Corrected loaded-end bar slip versus integration of bar strains along its embedment length for the Modified pullout specimen, MP2	186
Figure 5:48: Average bond stress versus the corrected loaded-end bar slip assuming uniform bond stress distribution	187
Figure 5:49: Bond stress distribution along the embedment length at a corrected loaded-end bar slip of 0.1 mm	188
Figure 5:50: Bond stress distribution along the embedment length at a corrected loaded-end bar slip of 0.5 mm	189
Figure 5:51: Bond stress distribution along the embedment length at a corrected loaded-end bar slip of 1 mm	189
Figure 5:52: Bond stress distribution along the embedment length at a corrected loaded-end bar slip of 1.5 mm	190
Figure 5:53: Bond stress distribution along the embedment length at a corrected loaded-end bar slip of 2 mm	190
Figure 5:54: Model proposed by Cosenza et al., (1995).....	194
Figure 5:55: Standard pullout specimen detail	195
Figure 5:56: Bond stress-GFRP bar slip in P1 and P2.....	197
Figure 5:57: Bond stress-GFRP bar slip in P3 and P4.....	198
Figure 5:58: Bond stress-GFRP bar slip in P5 and P6.....	199
Figure 5:59: Bond stress-GFRP bar slip in P7 and P8.....	200
Figure 5:60: Bond stress-GFRP bar slip in P9 and P10.....	201
Figure A:1: Notched beam detail	217
Figure A:2: Strain compatibility and equivalent stress block assumption.....	217
Figure A:3: Ultimate moment capacity calculation	221
Figure A:4: Midspan cracking moment calculation for the Notched beams (All dimensions are in mm).....	221

Figure A:5: Midspan cracked moment of inertia for the Notched beams (All dimensions are in mm)223
Figure A:6: RILEM beam detail224
Figure A:7: Average bending moment and shear diagrams for beam-bond specimens ..225

List of Tables

Table 1:1: General comparison between various Fibres. Intelligent sensing for innovative structures, (2006)	6
Table 1:2: Density and coefficient of thermal expansion for typical FRP and Steel reinforcing bars. ACI 440.1, (2006).....	8
Table 1:3: Mechanical properties for typical FRP and Steel reinforcing bars. ACI 440.1, (2006)	9
Table 2:1: Prior research on the bond behaviour of reinforcement in concrete structures using the pullout test method	15
Table 2:2: Prior research on the bond behaviour of reinforcement in concrete structures using the beam-bond test method	23
Table 3:1: GFRP tensile test results.....	38
Table 3:2: Steel tensile test results.....	40
Table 3:3: Concrete cylinder compressive strength results at 28-days.....	41
Table 3:4: Determination of the elastic modulus of concrete	43
Table 3:5: Concrete cylinder compressive strength results at time of testing	43
Table 3:6: Concrete tensile strength results at 28-days.....	44
Table 3:7: Concrete tensile strength results at time of testing	45
Table 4:1: Summary of beam-bond specimens.....	103
Table 4:2: Standard pullout specimen test results.....	114
Table 5:1 Comparison of ultimate and cracking moment results	117
Table 5:2: GFRP elastic moduli and ultimate stress obtained from RILEM beams.....	123
Table 5:3: Relevant material property values in this experimental program.....	124
Table 5:4: Summary of strain-load pairs at Points A, B and C.....	126
Table 5:5: Summary of strain-load pairs from Point C onwards	129
Table 5:6: GFRP ultimate stress obtained from Notched beams	132
Table 5:7: Maximum GFRP load used for normalization.....	143
Table 5:8: Values of the constant, b in Equation 5.33 used to produce fitted curves	156
Table 5:9: Peak experimental bond stress obtained using Equation 5.41	171
Table 5:10: Experimental versus theoretical average bond stress assuming a uniform distribution using Equation 5.42, at maximum load, P.....	172
Table 5:11: Determination of recommended development length for the GFRP bar in this experimental program	176
Table 5:12: Experimental ranges versus guideline predictions of development length for the RILEM beams	177
Table 5:13: Experimental ranges versus guideline predictions of development length for the Notched beams	178

Table 5:14: Experimental ranges versus guideline predictions of development length for the Modified pullout specimens	178
Table 5:15: Corrected loaded-end slip for the RILEM beams at different percentages of their respective maximum load, P	183
Table 5:16: Corrected loaded-end slip for the Notched beams at different percentages of their respective maximum load, P	183
Table 5:17: Corrected loaded-end slip for the Modified pullout specimen, MP2 at different percentages of its maximum load, P	184
Table 5:18: Average bond stress assuming a uniform bond stress distribution versus the corresponding corrected loaded-end bar slip, at the maximum load, P	187
Table 5:19: Peak bond stress obtained at specified corrected loaded-end bar slip values using the actual bond stress distribution	191
Table 5:20: α and p parameters for Standard pullout specimens obtained using unloaded-end bar slip data	196
Table 5:21: α and p parameters for Standard pullout specimens obtained using corrected loaded-end bar slip data	196
Table 5:22: Load value corresponding to onset of corrected loaded-end bar slip	202
Table 5:23: Maximum bond stress and corresponding corrected loaded-end bar slip.....	203
Table A:1: GFRP, steel and concrete properties	216
Table A:2: Overall beam detail	218

List of Abbreviations and Symbols

a	= Constant
A_b	= Cross sectional area of bar
A_c	= Cross sectional area of concrete in pullout specimen
Avg.	= Average
$A_{exp.}^{asc.}$	= Area under the ascending portion of the bond-slip curve obtained from experimental data
$A_{exp.}^{des.}$	= Area under the descending portion of the bond-slip curve obtained from experimental data
A_F	= Cross sectional area of FRP bar
A_s	= Cross sectional area of steel bar
b	= Constant
b_w	= Beam width
c	= Neutral axis depth from top of concrete section at beam midspan = Constant
c_b	= Balanced neutral axis depth
C	= Smaller of: Concrete cover to centre of the bar or 1/2 the distance between reinforcement in the same layer being developed
C_c	= Compression force in concrete
COV	= Coefficient of Variation
d	= Distance from top of beam cross section to centroid of the GFRP longitudinal tensile reinforcement
d'	= Distance from top of beam cross section to centroid of steel longitudinal compression reinforcement in Notched beams
d_b	= Bar diameter
d_{bF}	= Bar diameter of FRP bar
d_{bs}	= Bar diameter of steel bar
d_{clF}	= Clear cover to FRP reinforcement
d_{cls}	= Clear cover to steel stirrups
d_{cs}	= Smaller of: Concrete cover to centre of the bar or 2/3 the distance between reinforcement in the same layer that are to be developed
d_v	= Effective shear depth
E_b	= Modulus of elasticity of bar
E'_c	= Modulus of elasticity of concrete calculated once ϵ'_c is determined

E_c	= Modulus of elasticity of concrete based on CSA A23.3 at a time corresponding to testing of the beams and pullout specimens in this experimental program
E_c^{Pauw}	= Concrete tangent stiffness at a time corresponding to testing of the beams and pullout specimens in this experimental program
E_c^{28}	= Elastic modulus of concrete at 28-days
E_F	= Modulus of elasticity of FRP
E_s	= Modulus of elasticity of steel bar
f_b	= Stress in bar
f_c	= Stress in concrete corresponding to a given strain, ϵ_c
f'_c	= Compressive strength of concrete at a time corresponding to testing of the beams and pullout specimens in this experimental program
f'_c^{28}	= Compressive strength of concrete at 28-days
f_{cr}	= Cracking strength of concrete
f_F	= Stress in FRP bar
f_{Fu}	= Ultimate tensile strength of FRP bar
f_r	= Modulus of rupture of concrete at a time corresponding to testing of the beams and pullout specimens in this experimental program
f_r^{28}	= Modulus of rupture of concrete at 28-days
f_s	= Stress in steel bar
f_{su}	= Ultimate tensile strength of steel bar
f_t	= Tensile strength of concrete obtained from the split-cylinder test at a time corresponding to testing of the beams and pullout specimens in this experimental program
f_t^{28}	= Tensile strength of concrete obtained from split-cylinder test at 28-days
f_x	= Axial stress in bar
f_y	= Yield strength of steel bar
F_b	= Force in bar
F_c	= Force in concrete
h	= Beam height
I_{cr}	= Cracked moment of inertia at beam midspan
I_g	= Gross moment of inertia at beam midspan
jd	= Beam moment arm
jd_{BR1}	= Original moment arm in RILEM beam 1
jd_{BR2}	= Original moment arm in RILEM beam 2

k	= Decaying factor
kd	= Neutral axis depth from top of cracked concrete section at beam midspan used to calculate cracked moment of inertia
k_1	= Bar location factor
k_2	= Concrete density factor
k_3	= Bar size factor
k_4	= Bar fibre factor
	= Bar surface factor
k_5	= Bar surface profile factor
k_a	= Adjustment factor for the arch effect on shear strength
k_m	= Adjustment factor for impact of moment on shear strength
k_r	= Adjustment factor for impact of reinforcement rigidity on shear strength
	= Adjustment factor for impact of member size on shear strength
k_s	= Adjustment factor for impact of member size on shear strength
k_{tr}	= Transverse reinforcement index
l_d	= Development length
l_e	= Embedment length
L	= Beam length
$M_{cr}^{mid.}$	= Cracking moment at beam midspan
$M_{cr}^{non-mid.}$	= Cracking moment at regions other than beam midspan
M_{ext}	= External moment
M_{int}	= Internal moment
M_{max}	= Maximum moment sustained at beam midspan
$M_{post}^{mid.}$	= Moment at beam midspan immediately after $M_{cr}^{mid.}$
n	= Curve adjustment factor
	= Number of bars being developed along the potential plane of bond splitting
n_b	= Modular ratio of bar
n_F	= Modular ratio of FRP reinforcement
n_s	= Modular ratio of steel bar
p	= Constant parameter determined from experimental data
P	= Applied load
P_{max}	= Maximum applied load
s	= Bar slip
	= Transverse reinforcement spacing
s_c^l	= Corrected loaded-end bar slip
$s_{c\mu max}^l$	= Corrected loaded-end bar slip corresponding to μ_{max}

s_{uc}^l	= Uncorrected loaded-end bar slip
$s_{ult.}$	= Bar slip corresponding to $\mu_{ult.}$
s^{ul}	= Unloaded-end bar slip
$s_{\mu max}$	= Bar slip corresponding to μ_{max}
S.D.	= Standard deviation
T_F	= Tension force in FRP reinforcement
V_c	= Concrete contribution to shear resistance
V_f	= Shear demand
V_r	= Total shear resistance
V_{SS}	= Transverse steel reinforcement contribution to shear resistance
w_c	= Concrete density
x	= Distance from the onset of embedment length at the loaded-end towards the unloaded-end
y	= Neutral axis depth from top of uncracked concrete section at beam midspan used to calculate gross moment of inertia
α	= Bar location factor
	= Constant in bond stress-slip relationship
α_1 and β_1	= Equivalent concrete stress block parameters
Δ_b	= Deformation in the bar
Δ_c	= Deformation in the concrete
Δl	= Distance between successive strain gauges along reinforcement
$\Delta_{max}^{mid.}$	= Maximum beam midspan deflection
ϵ_b	= Strain of bar
ϵ_c	= Concrete strain
ϵ'_c	= Concrete strain at stress f'_c
ϵ_{cu}	= Ultimate strain of concrete
ϵ_s	= Strain of steel bar
ϵ_{su}	= Ultimate strain of steel rebar
ϵ_F	= Strain of FRP bar
ϵ_{FA}	= Strain of FRP bar corresponding to <i>Point A</i>
ϵ_{FB}	= Strain of FRP bar corresponding to <i>Point B</i>
ϵ_{FC}	= Strain of FRP bar corresponding to <i>Point C</i>
ϵ_{Fu}	= Ultimate strain of FRP
ϵ_l	= Longitudinal strain at mid-depth of beam cross section
$\epsilon_{SG1}^{\% pmax}$	= Strain output from SG1 at a given percentage of P_{max}
ϵ_{SG1}	= Strain of FRP bar at the location of SG1 which corresponds to the onset of the embedment length, referred to as the loaded-end

ε_{SGC}	= Strain of FRP bar at the location of SGC in the beam-bond specimens located at beam centre-line
ε_y	= Yield strain of steel rebar
λ	= Concrete density factor
μ	= Bond stress
$\mu_{\%pmax}$	= Average bond stress at a given percentage of P_{max} assuming uniform bond stress distribution
μ_{avg}^u	= Average bond stress assuming a uniform distribution and using the experimental embedment length
μ_{avg}^{ucode}	= Average bond stress assuming a uniform distribution and using code-based development lengths
μ_{max}	= Maximum bond stress
μ_{peak}	= Peak bond stress
$\mu_{ult.}$	= Bond stress at the end of the test
ρ	= Provided reinforcement ratio
ρ_b	= Balanced reinforcement ratio
ϕ_c	= Concrete resistance factor
ϕ_s	= Steel resistance factor

Declaration of Academic Achievement

I have designed, built and tested all the test specimens reported in this thesis, except the pullout specimens having short embedment length, which were tested by TEME Corp of Stoney Creek in Hamilton. I have analyzed all the test results, including the results of the specimens tested by TEME Corp. I have received assistance from technicians at Applied Dynamic Lab of McMaster University during testing and have received advice and assistance from my thesis supervisor at all stages and on all aspects of the research reported in this thesis, but I am solely responsible for the veracity and completeness of the thesis content.

Chapter 1 Introduction

1.1 General

The majority of current buildings and bridges make use of reinforced concrete; therefore, there is a consistent need to gain more knowledge concerning reinforced concrete behaviour and durability in a wide variety of circumstances. With the general understanding that concrete behaves well under compressive stresses while lacking adequate resistance to tensile stresses, the need arises for a composite material that is formed by introducing longitudinal reinforcement, most conventionally, steel bars, into the concrete to endow the composite with tensile strength and ductility.

The lack of durability of conventional reinforced concrete in aggressive environments, caused by the corrosion of steel reinforcement, has compelled infrastructure owners and designers to consider alternatives to steel reinforcement. Among these, Fibre Reinforced Polymer (FRP) rebars and prestressing tendons have attracted a great deal of attention practically and from the research perspective. The FRP bars are produced from fibres of glass (G), carbon (C) or aramid (A), embedded typically in a vinyl ester thermoset resin, resulting in GFRP, CFRP or AFRP reinforcing bars. Due to its lower cost, GFRP rebar has been applied more extensively than the other type of bars in the field, particularly as conventional reinforcement in bridge decks.

Although there exist standards and guidelines for the design of FRP reinforced concrete structures, including ACI 440.1, (2006), CSA S806, (2012) and CSA S6, (2006), there are still issues pertaining to FRP reinforced members that need to be investigated. One of the issues deals with the bond strength of FRP bars with concrete, a property that is key to the satisfactory performance of FRP reinforced concrete as a composite material. However, the current equations for bond and development length in FRP design standards are highly empirical and are essentially a modified version of similar equations for steel reinforcement. In reality, FRP and steel rebars have completely different surface treatments and properties, which are expected to influence the interaction between the FRP and concrete at their interface differently than at the steel rebar-concrete interface. Therefore, the bond behaviour and strength of a proprietary GFRP bar is the subject of this investigation. It is important to point out that practically all FRP bars are proprietary.

1.2 Bond Behaviour and Strength in Conventional Steel Reinforced Concrete

The introduction of steel reinforcement into concrete is associated with substantial bond or shear stresses between the concrete and the reinforcement. The steel reinforced concrete sections are designed to be under-reinforced in flexure, which implies that the reinforcement yields before ultimate strength is reached. For steel reinforcement to attain its yield stress and for the concrete member to reach its ultimate strength without loss of composite action, the reinforcement must be provided with adequate development length, which is the distance from the end of the reinforcement, which is stress free, to the critical section at which the steel begins to yield. The intent is to prevent bond failure in the form of bar pullout, concrete cover splitting or substantial slip, which may pose a serious concern as it may prevent the member from reaching its design strength and result in structural collapse without sufficient warning. Hence, design codes often conservatively specify development and splice lengths in order to prevent premature bond loss and ensure ductile failure. CSA A23.3, (2004).

For simplicity, when addressing flexural bond, the majority of design codes assume that the bond stress, which is the longitudinal shear stress at the concrete-bar interface, is uniformly distributed. Although such an assumption does not negatively influence the goal of ensuring ductile flexural failure, the actual interfacial stress distribution along the reinforcement is non-uniform. Park and Paulay, (1975)

It is important that the actual shape of the bond stress distribution be established because knowing the shape and some other key parameters including the maximum bond stress attainable would enable one to determine suitable equations for development length based on the assumptions of uniform bond stress. As stated earlier, development length formulas provided in design codes for steel reinforced concrete are empirical and they cannot be simply extended to FRP reinforced concrete members. On the other hand, it can be demonstrated theoretically that a number of key parameters influence the concrete-reinforcing bar bond strength and the required development length, irrespective of the type of reinforcement.

1.2.1 Factors Affecting Bond Strength of Steel Reinforced Concrete Structures

The primary factors that contribute to the bond strength and as a result influence the development length of rebars are the bar location in the structure, the presence of any coatings on the reinforcement, concrete strength and bar diameter. Reinforcement located with a relatively large depth of concrete cast below it have a weaker bond at the bar-concrete interface due to the wet concrete settlement below the bar, which reduces the confining effects of concrete and thus creates the need for a higher development length. Epoxy-coatings, which serve as corrosion protection, have a negative effect on bond development due to the smooth surface of such bars and codes address this by requiring a longer development length. The density and quality of concrete affect the required development length since an increase in aggregate quality and quantity allows for a higher bond stress tolerance and reduces the development length. Larger bar diameters are accompanied by an increase in localized stresses in the surrounding concrete and this justifies the use of a longer development length for larger bar sizes. CSA A23.3, (2004)

Secondary factors which contribute to bond strength are the presence of transverse reinforcement, location of neighboring bars and the yield strength of the reinforcement. Transverse reinforcement serves to increase the confining effects of concrete and hence reduce the development length required. The presence of closely positioned neighboring reinforcing bars allow for the superposition of stresses between the bars and this leads to higher development length. Lastly, reinforcement with higher yield strength require a longer development length. CSA A23.3, (2004)

It is important to point out that the surface profile of FRP bars vary and are neither similar to bare steel bars nor epoxy coated bars. FRP bars also have significantly higher tensile strength. Also, FRP is a linear elastic material, consequently it is nonductile and hence its development length would depend on its design ultimate stress. These differences will change the required development length for FRP bars.

1.2.2 The Phenomenon of Confinement and Splitting Failure

Providing a rebar with adequate development length can avoid bond or pullout failure but one must also avoid another undesirable type of failure known as splitting failure. In splitting failure as Figure 1:1 illustrates, the concrete surrounding the reinforcement simply splits away and in the absence of measures aimed at controlling the splitting cracks, the reinforced structure will experience an abrupt failure. Park and Paulay, (1975)

Providing sufficient transverse reinforcement in the form of stirrups can increase the confining effects of concrete that in turn can slow down or inhibit bond-splitting failures, CSA A23.3, (2004).

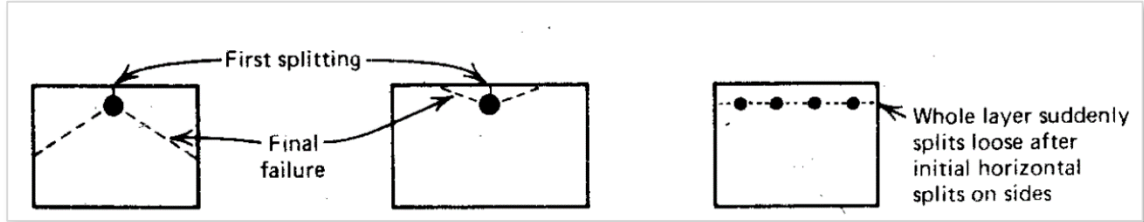


Figure 1:1: Splitting failure of concrete. Park and Paulay, (1975)

1.3 Fibre Reinforced Polymers (FRPs): An Alternative Solution to Conventional Steel Reinforcement

Wide scale use of fibre reinforced polymers began post World War 2 because of an increase in demand for lightweight, high-strength materials and the first applications of FRPs were in the aerospace and defence industries. During the 1990's, high maintenance costs of corroded steel reinforced concrete structures triggered a massive research into the application of FRPs in the structural industry. ACI 440.1, (2006)

The amount of knowledge and experience concerning steel reinforcement by far surpasses current understanding of relatively new technologies such as FRPs and therefore a continued investigation into this topic is crucial. The aim of the following section is to highlight the important characteristics of FRPs such as their constituents, properties and behaviour under various conditions.

1.3.1 Characteristics of FRP

It was stated earlier that concrete when combined with a reinforcement forms a composite material capable of behaving well under tension and compression. In a similar manner, FRPs contain polymer matrices and fibres as the two primary constituents and when combined, the resulting composite material can serve as an excellent reinforcement. However, FRP is not typically used as compression reinforcement due to its relatively low elastic modulus and lower compressive strength. Figure 1:2 illustrates the typical stress-

strain relationship of polymer matrices, fibres and the FRP composite material and note the higher strength of FRPs compared to mild steel reinforcement.

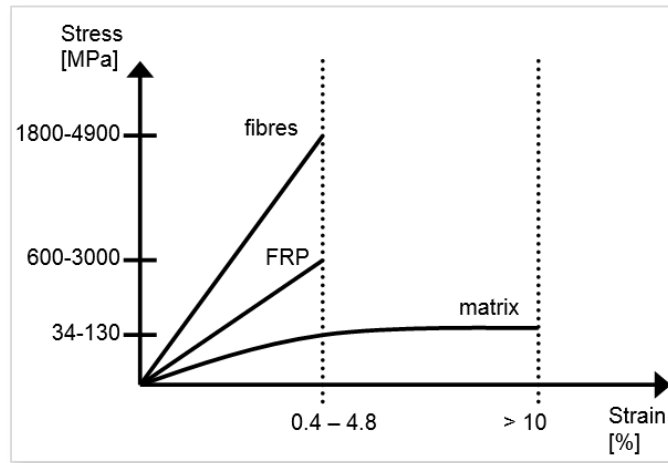


Figure 1:2: Composite material consisting of Fibres and Matrices. Intelligent sensing for innovative structures, (2006)

1.3.2 Polymers (Resins)

Polymers are organic compounds that consist of repeatedly attached monomers and they can be organized into two subcategories namely thermoplastic and thermosetting polymers. Thermoplastic polymers structurally hold monomers through the effect of Vander Waals forces while thermosetting polymers consist of chemical bonds between monomers. Due to their superior performance, thermosetting polymers are the choice when it comes to structural engineering applications and the well-known types of thermosetting polymers are epoxies, vinyl-esters and polyesters. Among the thermosetting polymers, vinyl-ester is the most efficient choice for FRP reinforcement applications due to its alkaline resistivity and a relatively lower shrinkage property. Overall, in the composite FRP material, the primary purpose of the polymer matrix, sometimes referred to as the resins, is to serve as a transfer medium of stress between fibres, bind fibres, provide dispersion of fibres and lastly, to protect the fibres against environmental factors. Intelligent sensing for innovative structures, (2006)

1.3.3 Fibres

As stated earlier, the three major conventional types of fibres include glass, carbon and aramid with each, as Table 1:1 demonstrates, possessing different properties.

Table 1:1: General comparison between various Fibres. Intelligent sensing for innovative structures, (2006)

Fibre Type	Relative cost	Tensile Strength	Modulus	Grades	General Comments
Glass	Inexpensive	High	Moderate	<ul style="list-style-type: none"> • E-Glass • R-Glass • AR-Glass 	<ul style="list-style-type: none"> • Non-weight/modulus critical applications
Carbon	Expensive	High	High	<ul style="list-style-type: none"> • Standard • Intermediate • High • Ultra-High 	<ul style="list-style-type: none"> • Weight/modulus critical applications • Excellent durability and fatigue resistance
Aramid	Moderate to High	High	Moderate	<ul style="list-style-type: none"> • 60 GPa modulus • 120 GPa modulus 	<ul style="list-style-type: none"> • Potential loss of durability due to UV degradation and moisture absorption • Low compressive and shear strength

Among the conventional fibres currently available in the industry, glass fibre is the prominent choice for FRPs, particularly when it comes to structural applications, ACI 440.1, (2006). This is mainly due to the low cost of glass fibres compared to carbon or aramid, which are several times more expensive.

1.3.4 FRP Composite

Once a fibre is embedded within a polymer matrix as shown in Figure 1:3, the resulting FRP has properties that are dependent on several factors such as the mechanical properties of the matrix and fibre, the fibre volume fraction and most importantly, the orientation of the fibres within the matrix. Fibre orientation is critical because FRPs are orthotropic materials hence their properties are directionally dependent. A unidirectional

FRP, typically used for structural purposes, have fibres aligned in one direction only and exhibit high tensile strengths along the fibres, with low to moderate strength perpendicular to the fibre direction. Intelligent sensing for innovative structures, (2006)

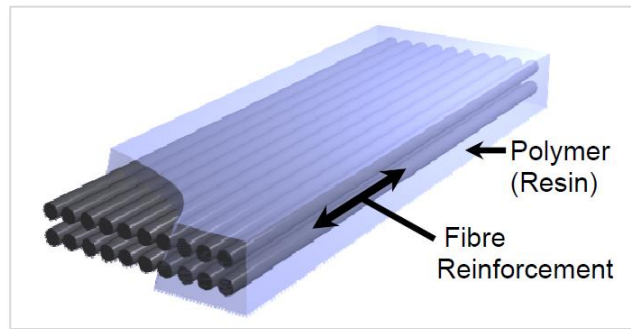


Figure 1:3: Idealization of a unidirectional FRP. Intelligent sensing for innovative structures, (2006)

There are a number of FRP manufacturing techniques, the most common being the pultrusion process, ACI 440, (2007), however, it is beyond the scope of this thesis to go into further details regarding the chemistry behind fibre reinforcement at the microscopic level or methods of manufacturing FRPs. As an excellent source of reference, the ACI Committee 440 has developed a report titled “Fibre Reinforced Polymer (FRP) Reinforcement for Concrete Structures” that provides a more in-depth discussion regarding FRPs at the micro level.

1.4 Comparison of Physical and Mechanical Properties of Steel and FRP

1.4.1 Physical Properties

In terms of the density of FRP materials, as Table 1:2 demonstrates for typical 0.5 to 0.7 volume fraction ratios, there is a substantial advantage since they are often a fraction of conventional steel, which leads to lower transportation costs and a more efficient handling by workers at the construction site. The coefficient of thermal expansion for steel and concrete are practically identical and isotropic in terms of the transverse and longitudinal directions whereas for FRP materials, thermal expansion coefficients are governed by fibres in the longitudinal direction and by resins in the transverse direction. High temperatures have a detrimental effect on FRP reinforcement and as temperatures

reach, a point called the glass transition temperature, the polymer component of the FRP material experiences changes in its molecular structure. As the polymer and subsequently the fibres begin to soften, there is a significant reduction in the ability of the polymer to transfer stresses from the concrete to the fibres and this results in a lower tensile and bond stress and a higher crack width and deflection level. ACI 440.1, (2006)

Table 1:2: Density and coefficient of thermal expansion for typical FRP and Steel reinforcing bars. ACI 440.1, (2006)

Bar type	Density (kg/m^3)	Coefficient of thermal expansion ($CTE \times 10^{-6}/^{\circ}C$)	
		Longitudinal, α_L	Transverse, α_T
GFRP	1,250 to 2,100	6.0 to 10.0	21.0 to 23.0
CFRP	1,500 to 1,600	-9.0 to 0.0	74.0 to 104.0
AFRP	1,250 to 1,400	-6.0 to -2.0	60.0 to 80.0
Steel	7,900	11.7	11.7

1.4.2 Mechanical Properties

Unlike steel, FRP does not yield but instead demonstrates elastic behaviour up to rupture. It is for this reason that the design of typical FRP reinforced concrete sections such as beams involve over-reinforcement to ensure failure by concrete crushing rather than failure by FRP rupture which would occur without sufficient warning.

Since the major component of the tensile carrying capacity of FRP materials is the fibre, the fibre to resin ratio plays a key role in the composite material's tensile strength. Steel bars do not exhibit significant change in tensile strength as a function of size changes, whereas experimental data show that FRP materials exhibit lower tensile strength as the size of the bars is proportionally increased. This phenomenon is referred to as shear lag. In terms of compression, due to a lack of substantial experimental data, as well as unpredictability in the results of previous experiments, there is often no recommendations regarding the implementation of FRPs as compression reinforcement. Note that tests by Mallick, (1988) and Wu (1990) have shown that the compressive strength of GFRP bars for example, can be as much as 55% of their tensile strength. In the event of moment reversals experienced during seismic loading, adequate confinement becomes necessary to mitigate potential buckling of FRP bars when in compression. The reason that the FRP reinforcement contribution to the compressive strength of concrete members is neglected is the limiting strain of concrete at ultimate and the relatively low elastic modulus of FRP, compared to steel reinforcement. Since shearing forces are in the transverse direction and orthogonal to the fibres, the resin is the main component of FRP that carry the shear resistance and logically, FRP materials are relatively weak in shear. Lastly, unlike steel, the bending of thermoset FRP must occur during the fabrication process since post fabrication

bending with small radii would result in the fracture of the bar. Table 1:3 highlights some of the key differences in terms of the mechanical properties of steel reinforcement versus glass, carbon and aramid FRPs and note that the values presented for the FRPs are for typical 0.5 to 0.7 volume fraction ratios. ACI 440.1, (2006)

Table 1:3: Mechanical properties for typical FRP and Steel reinforcing bars. ACI 440.1, (2006)

Property	GFRP	CFRP	AFRP	Steel
Nominal Yield Stress (MPa)	N/A	N/A	N/A	276 to 517
Tensile Strength (MPa)	483 to 1,600	600 to 3,690	1,720 to 2,540	483 to 690
Elastic Modulus (GPa)	35 to 51	120 to 580	41 to 125	200
Yield Strain (%)	N/A	N/A	N/A	0.14 to 0.25
Rupture Strain (%)	1.2 to 3.1	0.5 to 1.7	1.9 to 4.4	6.0 to 12.0

As mentioned previously, the application of GFRP in the construction industry by far surpasses CFRP and AFRP. GFRP bars are typically produced with vinyl-ester resin, which is a product of epoxy resin and acrylic or methacrylic acid and exhibit outstanding mechanical toughness, as well as corrosion resistance, making it ideal for structural engineering applications. There are a number of grades of glass fibres available such as alkali resistant AR glass and high strength S-2 glass, but the predominant grade is the electrical grade or the E-glass. The primary constituents of E-glass fibres are alumina-lime-borosilicate, which provide high tensile strength, moisture resistance and high electrical and thermal insulation characteristics. ACI 440, (2007)

1.5 Bond Behaviour of FRP

There are primarily three factors, which resist reinforcement pullout from concrete and they include the chemical bond between the polymer and the surrounding concrete, frictional resistance and mechanical interlocking due to ribs or weaving deformities on the bars. In terms of serviceability, there is a need for alterations in the design code for steel in order to take into account the fact that FRP reinforcement produce a system that is lower

in stiffness and possibly bond strength, but is corrosion resistant. The corrosion resistant component of a structure reinforced with FRPs allows for an increase in crack width limitations but the relatively lower stiffness results in a less tolerable deflection limit compared to steel reinforced structures. Figure 1:4 demonstrates three common industry methods of enhancing the bond performance of FRP bars namely producing deformed ribs, sand coating and helical wrapping or implementing a combination of the three. ACI 440.1, (2006)

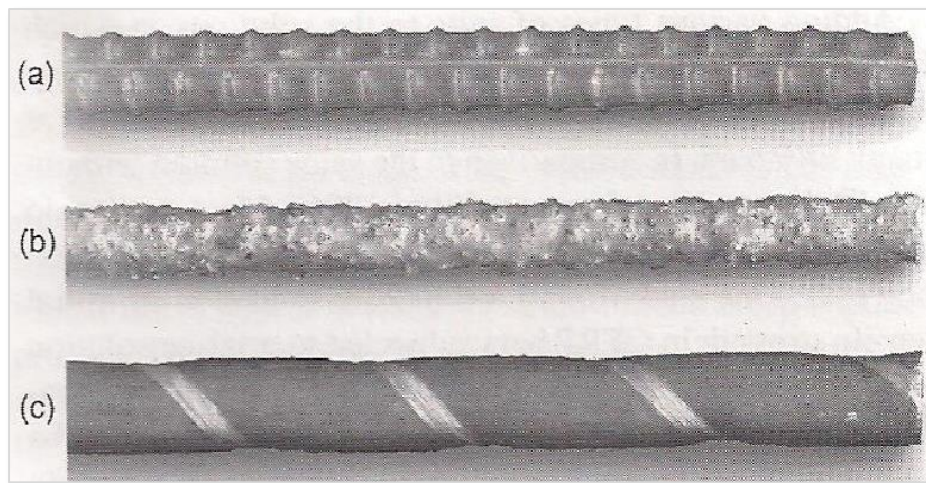


Figure 1:4: Methods of enhancing mechanical interlocking a) Ribbed; b) Sand-coated; c) Wrapped and Sand-coated FRP bars. ACI 440.1, (2006)

The ribs or surface deformities on a steel rebar allow the bar to transfer significant bond stresses through interlocking of the ribs with the surrounding concrete. In fact, as stated by Park and Paulay, (1975), the adhesion component of bond is negligible in the case of deformed steel rebars and bond stresses are mainly transferred by bearing stresses acting on the ribs and the shear stresses in the cylindrical shaped concrete between the ribs surrounding the bar. The complete loss of bond would signify the crushing of the concrete in front of the ribs and the shear failure of the concrete between the ribs.

In contrast, FRP ribs or surface deformations are made of resin, which do not have very high compressive strength and are susceptible to creep, meaning that one can expect bond failure due to the failure of ribs and higher slip compared to steel. Hence, FRP bars embedded in concrete of moderate to high strength are unlikely to experience bond failure due to failure of concrete. FRP bars with ribs but without sand coating will likely experience higher slip and lower bond strength than similar sized deformed steel rebar. Similarly, sand-coated FRP bars without ribs will achieve bond primarily by adhesion between the sand coating and the FRP bar surface on the one hand and between the sand coat and the surrounding concrete on the other. Failure of either mechanism will result in bond failure.

In an interesting study of the bond behaviour of plain steel reinforcing bars, Feldman and Bartlett, (2005) came up with equations for the maximum bond stress and bond-slip relationship of such bars. They concluded that the maximum bond stress is a nonlinear function of the bar surface roughness, a linear function of its development length and a nonlinear function of the concrete strength. However, only low strength concrete was used in this investigation.

Since FRP bars with sand coating are akin to plain steel rebars, these formulas may be modified and applied to FRP bars. For bars with surface deformations, the formulas may still apply after a surface slip of at least 1.0 *mm* because this level of slip would indicate substantial damage to the ribs in the FRP deformed bar. These issues require further investigation.

Another important issue is the manner in which bond tests are carried out. Pullout tests with short embedment length are most common and recommended by design standards CSA S806, (2012) and CSA S807, (2010), but these tests are more appropriate for determining the maximum bond stress and bond-slip relationship rather than providing accurate information about the bond stress distribution along the development length of a rebar in a beam. This is due to the fact that beams are characterized by vertical cracks along the development length and an uncracked region between the end of the bar and the point along the bar at which the moment in the beam equals its cracking moment. Hence, determination of the development length for this complex system is much more difficult than in a simple pullout test. Beam-bond tests are much more appropriate for determining the bond strength and development length of bars used as flexural reinforcement, but these tests are more difficult and time-consuming to perform compared to simple pullout tests. There is need for calibrating the results of pullout tests with beam-bond tests and if a systematic relationship could be established, then the results of pullout tests can be easily applied to bars used as flexural reinforcement. Few studies of this kind have been performed to date using FRP bars. Hence, in this thesis these issues will be investigated to gain better insight into the bond behaviour of FRP bars. Admittedly, due to time and resource constraints, only one bar size and type is investigated. Further research can expand the scope of the investigation if the current study provides some useful relationship between pullout test results and beam-bond test results.

1.6 Purpose and Scope of Current Research Program

In the past few decades there has been significant progress in understanding the behaviour of FRP reinforced concrete however, the focus of most of these studies has been on FRP material properties and on the flexural and shear strength of FRP reinforced and/or retrofitted concrete members. Although a number of investigators have addressed the problem of bond, some fundamental issues regarding the bond strength of FRP rebars in concrete need further examination. In particular, the effect of the relatively low elastic modulus and lack of yielding in FRP on the bond strength and bond stress distribution along its development length needs more investigation. In addition, the method of testing for bond, with particular focus on the beam-bond test, needs to be investigated in order to come up with a simple, yet effective, bond test for FRP reinforced flexural members.

In light of the above comments, the purpose of this experimental program is to investigate the bond stress distribution of a typical GFRP bar embedded in concrete, with particular focus on both the maximum bond stress and the shape of the bond stress distribution along the embedded bar. Another objective is to examine the variation in the GFRP bond stress as a function of the bond test method. The test methods to be examined include the traditional pullout tests and the less common but more realistic beam-bond tests. Note that unlike typical studies on bond performance, which often result in bar pullout, this experimental program is different in the sense that it will analyze the bond stress distribution up to the point of GFRP bar rupture which will give insight into the complete bond behaviour of GFRP bars. It should be pointed out that in design, bar pullout is avoided by providing the bar with adequate development length, hence, tests that focus on bar pullout behaviour do not reflect the expected behaviour of the bar in real applications. Lastly, there will be an evaluation of the accuracy of the development length specified by current standards, in particular the recommendations by the Canadian Standards Association and the American Concrete Institute. Note that all of the specimens in this experimental program will have the same GFRP bar type and diameter, strain gauge distribution, embedment length and concrete strength and casting method in order to ensure a direct comparison between the results of pullout and the beam-bond tests.

Chapter 2 Literature Review

2.1 General

Implementation of GFRP reinforcement in structural engineering is a relatively new topic and due to lack of sufficient data, design codes are often quite conservative. As more research and experimental results emerge, the understanding of FRP behaviour will become more comprehensive allowing this new technology to safely and economically replace conventional reinforcement where appropriate. The aim of the following section is to present some of the past research related to the behaviour and performance of FRP rebars. Note that although the emphasis of this experimental program is on GFRP bond performance, in order to gain more insight into the bond performance of rebars, some of the presented literature deals with steel reinforcement and its bond behaviour.

2.2 Testing Methods for Bond Performance of Steel and FRP Rebars in Concrete

In terms of the bond performance of steel reinforced concrete, for the past few decades, organizations such as the Canadian Standards Association, (CSA) and the American Concrete Institute, (ACI), have recommended the usage of pullout specimens as shown in Figure 2:1.

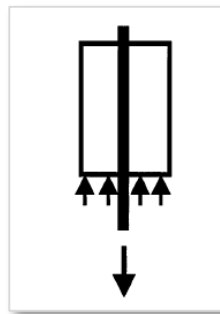


Figure 2:1: Pullout testing. ACI 408, (2003)

In the pullout test, the steel bar of interest is embedded within a concrete cylinder or prism and after the concrete has hardened, the bar is pulled out of the concrete from one end and the bar bond stress and relative slip to the concrete is determined. Generally, the stress is based on average bond stress within the embedded length, without actually determining the bond stress distribution. The pullout test cannot provide accurate data about the bond behaviour and strength of rebars in members subjected to bending, shear, etc. because the state of stress and strain around the bar are different in these cases. Although pullout testing has been the method of choice for a long period, prior to pullout testing, the primary means of evaluating the bond performance of steel rebars was through beam-bond tests as shown in Figure 2:2.

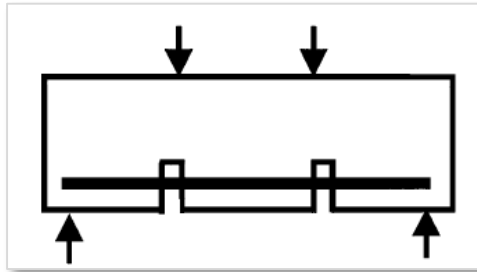


Figure 2:2: Beam-bond testing. ACI 408, (2003)

The evaluation of bond performance through beam-bond tests is more involved in terms of both constructing the specimens and performing the test, however, note the obvious fact that beam-bond tests bear a closer resemblance to typical structural elements used in construction. There are a number of well-established organizations which have proposed guidelines for constructing steel reinforced beams for the purpose of testing the bond behaviour and developing bond-slip relationships, namely ACI 208, (1958), RILEM TC-RC5, (1994) and BSI 12269-1, (2000).

The reason behind a shift in the industry's preference from beam-bond to pullout testing lies in the conclusions of comparative analysis between the experimental results from the two test methods obtained by researchers such as Soretz, (1972). In a detailed experimental program, he effectively showed that for steel bars, both test methods produce similar results and therefore it is understandable that the industry has moved towards the pullout test method due to its relative simplicity. However, given that the state of stress and strain in the concrete around the bar are not the same in beam-bond and pullout tests, the conclusion of Soretz, (1972) in the case of FRP rebars needs further examination.

Since pullout testing has become the primary method of determining the bond behaviour of steel reinforcement in concrete, organizations such as the CSA and ACI recommend the pullout test method for FRP materials as well; therefore, there are no well-

known guidelines for determining the bond performance of FRP bars through the beam-bond test. To the knowledge of the writer, the majority of previous researchers that have used beam-bond tests to evaluate the bond performance of FRP reinforcement have never analyzed the bond stress distribution of the FRP bar, particularly up to the point of its rupture and instead have assumed uniform bond stress distribution and subsequently analyzed numerous bond stress versus bar slip curves to reach certain conclusions.

2.3 Bond Behaviour of Reinforcement in Concrete observed in Pullout Testing

The following table summarizes typical experimental research performed to assess bond behaviour of reinforcement in concrete via pullout tests. The findings of these studies are summarized in this section.

Table 2.1: Prior research on the bond behaviour of reinforcement in concrete structures using the pullout test method

Research Title	Authors
Bond of FRP Reinforcement to Concrete – Experimental Results	Nanni et al., (1995)
Effect of High Temperature on Bond Strength of FRP Re-bars	Katz et al., (1999)
Bond Stresses Along Plain Steel Reinforcing Bars in Pullout Specimens	Feldman and Bartlett, (2007)
Interfacial Bond Strength of Glass Fibre Reinforced Polymer Bars in High-Strength Concrete	Lee et al., (2008)
Effect of FRP Bar Degradation on Interface Bond with High Strength Concrete	Davalos et al., (2008)
Bond Strength of Glass Fibre Reinforced Polymer Ribbed Bars in Normal Strength Concrete	Hao et al., (2009)
Bond Performance of FRP Re-bars with Various Surface Deformations in Reinforced Concrete	Esfandeh et al., (2009)
Fundamental Mechanisms of Bonding of Glass Fibre Reinforced Polymer Reinforcement to Concrete	Soong et al., (2011)
Effect of different Environments on Bond Strength of Glass Fibre-Reinforced Polymer and Steel Reinforcing Bars	Chen et al., (2012)

Nanni et al., (1995) performed an in-depth investigation into the bond performance of FRP reinforced concrete structures by conducting several tests using the direct pullout test

method. The study acknowledges the fact that in typical situations such as a beam, the concrete at both ends is in a state of tension whereas in direct pullout specimens the concrete at the loaded-end is in a state of compression. The control specimens had either smooth or machined FRP reinforcement of the type glass vinyl-ester, (GV), carbon vinyl-ester, (CV) or carbon epoxy, (CE) while the other specimens had conventional FRP or steel rebars as reinforcement. The experiment involved the testing of 150 mm cubic concrete blocks with a single FRP bar placed in an embedment length equivalent to either five or ten times the bar diameter and besides strain gauges and displacement transducers, the researchers also used strain probes via FRP coring in order to analyze the strain distribution in select specimens.

Overall, one of the conclusions of this experimental program was that the mechanical interlocking has a higher contribution to bond strength than the adhesion and frictional components. Second, the researchers found that surface geometries have the potential of enhancing the bond strength of FRP bars and in general, bars with smaller diameters exhibited superior performance compared to larger diameter bars. Third, contrary to the findings of other researchers, Nanni et al., (1995) noticed that despite variable concrete compressive strengths, specimen failure was consistently through FRP degradation rather than concrete crushing, indicating the insignificance of concrete strength as a variable in FRP bond behaviour. Finally, the authors concluded that the implementation of internal strain probes through the boring of the reinforcement for the purpose of strain distribution analysis is a reliable technique and particularly useful in the experimental programs involving deformed reinforcement.

Katz et al., (1999) conducted an experimental analysis on the effects of relatively high temperature on the bond behaviour of a variety of FRP bars and compared their results to the performance of conventional steel bars. Four FRP bar types, each possessing its own unique surface deformation characteristics as well as glass transition temperatures were tested and the authors decided to keep the bar diameter constant by using approximately the same nominal diameter for the FRP and steel bars. The test specimens were cylindrical with 150 mm diameter, 300 mm height and an embedment length equal to five times the bar diameter and all of the specimens used the same 35 MPa concrete. The tests involved either heating the cylinders to a predefined temperature before the pullout tests or subjecting the specimens to a certain loading first and then heating the cylinders until the onset of pullout. The authors assumed uniform stress distribution and used heating jackets to increase the temperature at a rate of approximately 5°C/min. to a maximum of 300°C.

Overall, from the development of numerous bond-slip curves, the authors noted that all of the reinforcement exhibited a general decrease in bond strength with increasing temperature but there was a fundamental difference between the failure mechanisms of steel compared to the FRP bars. The steel bars showed a relatively smaller decrease in bond strength with increasing temperature and the failure mechanism of the steel bars continued to be due to concrete crushing whereas FRP bars exhibited polymer degradations. In addition, with polymers being the weaker constituent of any FRP material, the FRP bars with polymeric lug deformations had a much weaker bond strength performance than FRPs with glass fibre helical wraps. Finally, experimental results showed that at room temperature, the bond strength of FRP bars are not only similar to steel but also at times larger. However, under high temperatures in the range of 180 to 250°C, the bond strength of both FRP and steel bars decreased with the reduction being more severe for the FRP bars.

Feldman and Bartlett, (2007) performed an investigation into the bond behaviour of plain steel bars in pullout specimens with the aim of highlighting the relationship between bond stress and bar force as well as the associated slip at the loaded-end and unloaded-end of the samples. The importance of this study arises from the fact that the majority of historical reinforced concrete buildings contain plain steel bars as reinforcement. These bars lack the mechanical interlock capability of deformed bars, thus they solely rely on chemical adhesion and frictional resistance in order to prevent pullout.

The experimental program involved the analysis of two pullout test specimens that were cylindrical and had 200 mm diameter and 800 mm length and in terms of the concrete compressive strength, one specimen had 16.5 and the other, 26.5 MPa strength, both of which are typical for historical buildings. In terms of the reinforcement, the study used a hot rolled tubular steel bar with 345 MPa tensile strength and a 32 × 32 mm square hollow cross section that effectively facilitated placement of strain gauges and wiring within the hollow cavity and allowed for complete contact between the exterior of the steel bar and the surrounding concrete. Concerning the instrumentation, from the loaded-end to the unloaded-end of the specimen, the researchers placed 24 strain gauges, 12 on each side within the hollow cavity of the steel bar at vertical spacing of approximately 77 mm and in addition, they placed a LVDT, at the unloaded-end in order to measure the corresponding slip.

From the subsequent testing and data analysis the authors were able to make several important conclusions with respect to the bond behaviour of plain steel bars embedded in concrete, the first being the observation that bond stresses are non-uniform between the

loaded-end and unloaded end. In addition, the peak load value coincided with the initiation of unloaded-end slippage, after which there was a dramatic increase in the slip rate causing a subsequent reduction in the load resistance and hence the bond strength of the tested samples. Lastly, by analyzing the average bond stress along the embedment length, they concluded that an increase in load causes a shift of the peak bond stress from the loaded-end towards the unloaded-end of the sample.

Lee et al., (2008) conducted a comparative analysis on the bond performance between conventional steel and GFRP reinforcement in concrete with different compressive strengths. Although previous literature had addressed the effects of increasing concrete compressive strength on FRP bond performance, the researchers in this study used some concrete with much higher strength. The compressive strengths of the concrete were 25.6, 35.3, 40.6, 56.3, 75.7 and 92.4 *MPa* and the maximum coarse aggregate size did not exceed 13 *mm* in order to ease handling and placement. For each concrete strength, nine test specimens were prepared in accordance with CSA S806, (2002), which specifies 150 *mm* cubic samples with a reinforcement embedment length of four times the bar diameter. Three different types of reinforcement were tested namely, a deformed steel bar, a sand-coated GFRP bar designated GFRP-SC and a helically wrapped sand-coated GFRP bar designated GFRP-HW. The deformed steel reinforcement had yield strength of 410 *MPa*, fracture strength of 560 *MPa* and elastic modulus of 200 *GPa* while the GFRP-SC had rupture strength of 690 *MPa* and elastic modulus of 42 *GPa*. The GFRP-HW had rupture strength of 617 *MPa* and elastic modulus of 40.8 *GPa* with both types of GFRPs having 70% by volume glass fibres. In order to eliminate one of the geometrical variables, all the bars had the same diameter of 12.4 *mm* and the study assumed the key parameters to be the type of bar and the compressive strength of concrete.

The results enabled the development of bond-slip curves and the researchers reached several conclusions regarding the bond performance of steel and FRPs in concretes having different compressive strengths. First, an increase in the compressive strength of concrete resulted in an increase in the bond performance of all three reinforcement types although the increase was greater in the steel reinforcement compared to the GFRP-SC and GFRP-HW bars. Second, as the compressive strength of concrete increased, the steel reinforcement continued to exhibit failure by concrete crushing at the concrete-bar interface. In normal strength concrete, just like steel, the GFRPs demonstrated the same concrete crushing behaviour at the concrete-bar interface, however, as the concrete compressive strength further increased, the main failure mode of the GFRPs switched to inter-laminar delamination at the resin-fibre level. In addition, a general observation of the data revealed that after the maximum load, the descending portion of the bond-slip curve

was much more gradual for GFRP-HW bars than they were for steel and GFRP-SC bars. Lastly, as the compressive strength of concrete increased, the slip prior to peak load decreased, and in general, these slip values were larger for GFRPs than for steel reinforcement.

Davalos et al., (2008) investigated the bond performance of different FRP bars in high-strength concrete subjected to a number of environmental conditionings, namely submergence in tap water at room temperature and at 60°C for a period of 90 days and exposure to repeated thermal cycles between -20 and 60°C for a period of 30 days. The experiment used three different glass FRPs and one carbon FRP and in order to eliminate the concrete type as a variable, 57 to 63 *MPa* concrete, classified as high-strength concrete, was used throughout the testing program. In terms of the diameter and surface conditions, GFRP type 1 and type 2, both had helical wrapping and sand coating and diameters of 9.5 and 12.7 *mm*, respectively, GFRP type 3 had only sand coating and 9.5 *mm* diameter and the CFRP bar had sand blasting and 9.0 *mm* diameter. The three types of GFRP bars had tensile strengths between 690 and 856 *MPa* and elastic moduli between 40.8 and 49.4 *GPa* while the CFRP bar had tensile strength of 2,587 *MPa* and elastic modulus of 124 *GPa*.

To investigate the bond performance of the different FRPs relative to each other, the researchers used cylindrical concrete specimens with 150 *mm* height and diameter to embed the bars. For studying the environmental conditioning parameters, the dimensions of the cylindrical test specimens were either 100 *mm* in diameter and 200 *mm* in height or 150 *mm* in diameter and 300 *mm* in height. The embedment length for all of the reinforcement was five times the bar diameter and at the end of the curing period, the researchers divided the specimens into four sets, with one set taken to pullout tests immediately and the other three sets being subjected to environmental conditionings prior to pullout testing.

One of the main conclusions reached was that in high-strength concrete, failure is due to the FRP reinforcement. Second, environmental conditioning, regardless of the type, resulted in a decrease in FRP bond strength and an increase in the slip of the degraded FRP bars during loading. Third, the environmental conditioning that involved tap water at a temperature of 60°C, exhibited a higher bond performance compared to the other environments and the researchers attribute this phenomenon to the swelling of the FRPs causing an increase in friction and mechanical interlocking. Lastly, thermal cycles, besides bar degradation, had an additional harmful component, which was concrete micro cracking and this caused an increase in unloaded-end slip, particularly in the GFRP reinforcement.

Hao et al., (2009) conducted an extensive research into the effects of the geometrical properties of GFRPs on the bond strength of reinforced concrete materials by conducting pullout testing on ninety standard specimens with a setup in accordance with CSA S806, (2002). All of the GFRP bars had the same approximate tensile strength of 710 *MPa* and elastic modulus of 41 *GPa* and the manufacturer responsible for the GFRPs provided consistent bars that varied only in nominal diameter, rib spacing and rib height. With the rib angles staying at a constant of 45°, the nominal diameters were either 8, 10, or 12 *mm*, the rib spacing varied from 0.5 to 3 times the bar diameter while the rib heights varied from 3 to 9% of the nominal GFRP diameter. The concrete used in all specimens had compressive strength of approximately 30 *MPa* and overall, the researchers ensured that the only variables in the pullout tests were the bar diameter, the rib spacing and the rib height.

These investigators used bond-slip relationship curves to propose three criteria for evaluating the bond integrity of GFRP bars with different geometrical properties. The first criterion was the value of the peak bond strength obtained while the second criterion was the slip associated with this peak value since a superior GFRP would reach its highest bond strength with relatively lower slip. Third, it was suggested that a gradual descent is preferable for the portion of the bond-slip curve after the peak bond stress because it represents incremental bearing failure as opposed to a sudden continuous failure, which would manifest itself as a sharp decline in the post-peak curve.

Overall, the study found that the GFRP with the most superior bond performance possessed a rib spacing equal to the rebar diameter and a rib height that was approximately 6% of the bar diameter. Furthermore, an important result of this experiment was the realization that further decrease in the rib spacing is not favourable as the concrete key in between the ribs become unable to provide adequate bearing action. Finally, they concluded that increasing the rib height increases the bearing area of the ribs and improves bond performance, however, as the rib height increases, the cross sectional area decreases and there is a certain height, above which the bond capacity will begin to decrease.

Esfandeh et al., (2009) conducted an experimental study investigating the effect of reinforcement surface conditions on the bond performance of FRP reinforced concrete structures. All of the FRP reinforcement had nominal diameter of 12.7 *mm* with the constituents being a 34% mixture of polyester and epoxy resin and 66% E-glass fibres. There were four reinforcement surface conditions in this study; namely, a smooth surface FRP designated (RO), a helically wrapped FRP, (RT), a sand-coated FRP, (RS) and a helically wrapped and sand-coated bar, (RTS). All reinforcement had the same concrete

mix design with compressive strength of 30 *MPa*. In addition, all of the RT and RTS reinforcement had 17 *mm* pitch and 3 *mm* lug height. Furthermore, the pullout test specimens were cylindrical and had height of 300 *mm* and diameter of 150 *mm*. To counter concrete cracking during the pullout tests, the test specimens were confined by steel ring wrapping and overall, the variable parameters were the embedment length, which was set at either 120 or 180 *mm* and the four different reinforcement surface conditions.

It was concluded that the presence of surface deformities vastly increases the bond performance of FRPs and furthermore from the four different bar types, the RTS bars had the most superior bond behaviour. It is noteworthy to mention that in the specimens with 180 *mm* embedment, the RS bars had bond strength values that were comparable to the RTS bars indicating that sand coating has a greater contribution to improved bond performance than helical wrapping.

Soong et al., (2011) investigated interfacial bond strength by separating the three components contributing to bond performance, which are chemical bonding, bearing resistance through mechanical interlocking and frictional effects. All of the bars in this experimental program had the same approximate diameter of 12 to 14 *mm*, however, in terms of the surface condition, the experimenters used six different GFRP types with the first three being smooth, (S), sand-coated, (SC) and machined, (M). The last three surface conditions varied in terms of the pitch, with bars designated as RL, SL and TL having pitch of 4.4, 11.95 and 26.9 *mm*, respectively. The GFRP bars had tensile strength ranging from 683 to 770 *MPa* and elastic modulus between 40 and 42 *GPa*. The cylindrical test specimens had diameter of 152.4 *mm* and height of 304.8 *mm* and in all the specimens, the concrete strength was nearly 50 *MPa*.

Several conclusions were drawn to breakdown the maximum pullout load, designated F_p , into its constituents F_d , (de-bond load), F_b , (bearing load) and F_f , (frictional load). First, in terms of the contribution from chemical bonding, the researchers measured the de-bond load F_d which was the point at which the unloaded-end began to slip indicating the progression of de-bonding over the span of the embedment length and the transition from static to dynamic frictional resistance. Keeping the embedment length constant, the expectation was that the F_d would have the same value across all specimens, however, the results showed a significant difference. Intuitively, the researchers attributed the difference in F_d values to the underestimation of contact surface area, the bearing component in lugged bars and the concept of static friction varying for one bar to another. Second, in terms of the bearing resistance component, surprisingly, when examining the loading between F_d and F_p , the researchers obtained similar values for SC bars and lugged bars. In addition, for

SC bars, the bearing resistance was dependent upon the roughness of the surface and adherence of the sand particles to the main longitudinal bar. Third, concerning the dynamic frictional component, the S bar had the least dynamic frictional stress while the SC bar had the most and the RL, TL, SL and M bars demonstrated values that were comparable to each other. The researchers also noticed that the frictional force during loading up to F_p was different from the frictional force measured after F_p . Lastly, an interesting observation by the researchers showed that the loading rate has the potential of having a significant effect on the pullout load though this topic was not the focus of the experiment.

Chen et al., (2012) conducted a comparative experiment on the bond performance of steel and GFRP bars subjected to a variety of environmental conditions. The researchers prepared 90 specimens reinforced with either steel or GFRP of diameter 17 and 16 mm and ultimate strength of 455 and 400 MPa, respectively. Furthermore, the steel had yield strength of 335 MPa and elastic modulus of 205 GPa while the GFRP bar had elastic modulus of 33 GPa. In terms of the environmental conditionings, five different environments were applied namely; tap water, sodium hydroxide, sodium chloride, hydrogen chloride and controlled indoor conditions and the specimens in each environment had exposure time of either 30, 60 or 90 days. In order to simulate practical situations, prior to environmental conditionings, the ends of the cylindrical specimens were coated so that solution diffusion could only occur through the sides of the cylinders. The test specimens had 100 mm height and 75 mm diameter and the concrete compressive strength remained constant in this experimental program since all of the specimens had the same approximate concrete strength of 33.96 MPa.

The investigators observed that the bond strength of environmentally conditioned specimens was actually somewhat higher than the strength of controlled specimens, a phenomenon attributed to the curing effects of water increasing the concrete compressive strength. In addition, GFRP and steel reinforced specimens demonstrated similar bond performances under simulated high humidity, alkaline, and oceanic environments, however, there was a detrimental effect noticeable on all specimens subjected to acidic environments particularly the GFRP reinforced samples.

2.4 Bond Behaviour of Reinforcement in Concrete observed in Beam-bond Testing

Table 2:2 summarizes typical studies performed by some researchers on the bond behaviour of reinforcement in concrete based on beam-bond tests. These are described in this section.

Table 2:2: Prior research on the bond behaviour of reinforcement in concrete structures using the beam-bond test method

Research Title	Authors
Bond Stress Distribution on Reinforcing Steel in Beams and Pullout Specimens	Perry and Thompson, (1966)
Development Length for Fibre Reinforced Plastic Bars	Daniali, (1992)
Bond Strength and Load Distribution of Composite GFRP Reinforcing Bars in Concrete	Benmokrane et al., (1996)
Experimental and Numerical Evaluation of Bond Properties between Reinforcement and Concrete	Moreno and Bastos, (2006)
Bond-slip behaviour of Self-compacting Concrete and Vibrated Concrete using Pullout and Beam Tests	Menezes et al., (2008)
Bond Behaviour of Reinforcing Bars in Self-compacting Concrete: Experimental Determination by using Beam Tests	Desnerck et al., (2010)
An Experimental Study on the Flexural Bending Characteristics of a Concrete Beam Reinforced with a GFRP Rebar	Oh et al., (2010)
Beam Test Research on Bond Behaviour between Steel Bar and Concrete in Salt-frost Environment	Xu et al., (2011)
Experimental Study on Bond Performance of GFRP Bars in Self-compacting Steel Fibre Reinforced Concrete	Mazaheripour et al., (2013)

Perry and Thompson, (1966) investigated the variation in bond stress distribution of steel bars embedded in beam specimens versus bars embedded in eccentric pullout specimens. The study used strain gauges placed within the interior of the steel bars by first creating a groove within each half-bar and then welding the two half-bars together effectively ensuring full bond between the exterior of the steel bar and the concrete. There are two types of beam specimens in this experimental program, namely beams with a crack in the constant moment region and beams possessing a bar cut-off point and this study focused on the differences between the bond stress distribution in eccentric pullout specimens versus the region of crack and bar cut-off point of the beam specimens. For each of the three test methods, one sample was cast using 17.2, 27.6 and 34.5 MPa concrete in

order to investigate the effect of concrete strength on the bar tension and bond stress distribution.

Concerning the eccentric pullout specimens, the researchers found that the position of the maximum bond stress value shifts away from the loaded-end of the specimens towards the unloaded-end with increasing load and with decreasing concrete compressive strength. For the beams with a single crack, the experimental results indicated that although the maximum bond stress, which occurred at a location of approximately 38 mm from the crack, increased with increasing load, there was no shift in the location of the maximum bond stress values from the loaded-end towards the unloaded-end. Unfortunately, the inconsistencies in the crack formation around the original crack prevented an analysis on the effect of concrete strength on the bond stress distribution of the cracked beams. Furthermore, performance of cracked beams versus bar cut-off beams were not comparable and the authors attribute this to the fact that the two beams had different moment distribution patterns in the regions of interest. Overall, the authors did not find any similarity in terms of the bond stress distribution between the eccentric pullout samples, the cracked beams and the bar cut-off beams although all three test methods produced comparable maximum bond stress values.

Daniali, (1992) performed an experimental analysis on the bond behaviour of flexural FRP reinforced concrete structures through the construction and testing of 30 notched beam specimens. The study used four different sizes of GFRP longitudinal reinforcement with diameters of 9.5, 12.7, 19.1 and 25.4 mm, each with different tensile strength and elastic moduli and furthermore all of the specimens used 27.6 MPa concrete. The values of the tensile strength depended on the bar size and varied from 276 to 760 MPa while the elastic modulus varied from 20.7 to 49.7 GPa. The construction of the beams followed the majority of the recommendations of ACI 208, (1958). The test beams had length 3,048 mm, free length 2,845 mm and cross section 203 by 457 mm. The test setup comprised four-point bending and the placement of strain gages on the bar at the location of the two notches at the ends of the constant moment region facilitated monitoring of the bar strain throughout the testing process.

The first 27 beams, labelled Phase 1, used a single number 12.7, 19.1 or 25.4 mm diameter GFRP bar as longitudinal reinforcement with 9.5 mm diameter GFRP bars as transverse stirrups in the shear span of the beams. The last three beams, designated as Phase 2, used a single 19.1 mm diameter GFRP bar as longitudinal reinforcement but contained the 9.5 mm diameter GFRP bars as stirrups over the entire span of the beams. Furthermore,

Phase 1 beams had embedment lengths varying from 203 to 762 *mm* depending on the bar size while all Phase 2 beams had an embedment length of 457 *mm*.

The results of the tests can be described by one of the four modes of failure; namely, tension failure of the longitudinal reinforcement, pullout failure due to shearing of the ribs of the GFRP bars, splitting failure in the constant moment region due to lack of transverse reinforcement and lastly, failure due to creep deformations under sustained loading. It was evident that for the 12.7 *mm* diameter GFRP bars, a development length of 203 *mm* was sufficient for the bar to achieve its ultimate strength while the 19.1 *mm* diameter bars developed their ultimate strength and failed in tension only if shear reinforcement existed over the entire length of the beam. Lastly, all 25.4 *mm* diameter bars experienced bond failure, having tensile strain at failure equal to 70 to 90% of the bar ultimate strain capacity while under sustained loadings, the beams experienced premature bond failure at 70% of the ultimate strength of the bar.

In order to highlight the fundamental difference between the bond performances of GFRP versus steel bars, Benmokrane et al., (1996) tested five pullout as well as twenty beam specimens using GFRP and steel reinforcement. The study used either a GFRP bar with an average tensile strength of 683 *MPa* and elastic modulus of 42 *GPa* or a standard deformed steel bar as reinforcement. The concrete in this experimental program for both the pullout and the beam-bond tests had a normal density with an approximate 31 *MPa* compressive strength.

For three of the five pullout specimens, the study used a GFRP bar with diameter of 19.1 *mm* and in the remaining two pullout specimens, standard deformed steel bars were used, which were also 19.1 *mm* in diameter. The pullout specimens were cylindrical with diameter of 254 *mm* and length of 400 *mm* and the reinforcing bar for each specimen had an embedment length of twenty times the bar diameter. In addition, in order to analyze the bond stress distribution as well as stress variation along the embedment length, each bar used in the pullout specimens had six strain gauges placed along their surface at different locations.

For the beams, the study investigated four different bar diameters as longitudinal reinforcement and the embedment length was ten times the respective bar diameter. The bar diameters were either 12.7, 15.6, 19.1 or 25.4 *mm* and the testing procedure for the beams followed recommendations of RILEM TC-RC5, (1994). Three strain gauges were placed on the beams with one being at the centre of the reinforcement and the other two being at the centre of the embedment length in the right and left of the sample, respectively.

In terms of the test results for the pullout specimens, the study was able to conclude that for both GFRP and steel reinforcing bars, the tensile stress as well as the bond stress along the bar produced an overall non-linear pattern. In addition, data from the pullout tests also revealed that tensile stresses decreased drastically as one moved from the loaded-end towards the unloaded-end. Furthermore, as the bond between the concrete and the bar began to fail at the loaded-end, the maximum bond stress shifted towards the unloaded-end.

Regarding the beam-bond tests, a comparative analysis of GFRP and steel bars of the same diameter revealed that GFRP bars possess considerably lower bond strength values compared to steel reinforcement. Lastly, a comparison between the beam-bond tests and the pullout tests indicated that pullout tests produce higher bond strength values than beam-bond tests and these investigators attributed this to the fact that the concrete around a pullout specimen is in a state of compression while in a beam-bond specimen the surrounding concrete is in a state of tension. The findings of this study are particularly important because it revealed that pullout test results should not be directly used to estimate the bond strength of GFRP bars in beams subjected to bending.

Moreno and Bastos, (2006) performed an experimental evaluation and a numerical analysis on the bond behaviour of steel reinforced beams with four different types of concrete; namely, normal strength, (NSC), steel fibre reinforced, (SFRC) and two different structural light weight aggregate concretes, (SLWAC). The concrete compressive strengths were 61.6 MPa for NSC, 52.3 MPa for SFRC, 30.8 MPa for SLWAC1 and 23.7 MPa for SLWAC2 and the longitudinal steel bars had diameter of 16 mm , with a 580 MPa yield strength and 200 GPa elastic modulus. The researchers constructed five beam specimens in accordance with RILEM TC-RC5, (1994) recommendations and the study used embedment lengths of either five or ten times the bar diameter. More specifically, from the five specimens, one was with NSC and steel embedment length of ten times the bar diameter while the other four were with embedment length of five times the bar diameter with either NSC, SFRC, LWAC1 or LWAC2. The study defined bond failure as the occurrence of a 3 mm slip at the unloaded-end of either half-beam, at which point the testing was halted, the longitudinal steel protruding from the failed half-beam was gripped and the testing was continued until the other half-beam failed, effectively producing two sets of results per specimen.

Based on the test results, the one specimen with the embedment length of ten times the bar diameter failed through steel yielding at an average bond stress of 15 MPa , while the rest of the specimens with embedment lengths of five times the bar diameter, experienced bond failure and achieved average bond strength between 13 and 30 MPa . The bond

strength values between the two half-beams were inconsistent and at times significantly different, a phenomenon the investigators attributed to the deformation caused when the reinforcement at one end of the specimen is gripped to achieve failure at the other end and to the fact that the lever arm is continuously changing as the specimen deforms. Unfortunately, overall the results of this study were inconclusive due to the large differences observed in replicate specimens.

Menezes et al., (2008) performed pullout and beam-bond tests in order to evaluate the bond strength of steel reinforcement in self-compacting concrete, (SCC) as opposed to vibrated concrete, (VC). The researchers examined the effect of concrete compressive strength, 30 or 60 *MPa*, steel reinforcement diameter, 10 or 16 *mm* and concrete type, either SCC or VC. Both steel reinforcement bar sizes had yield strength of 500 *MPa*. In terms of the pullout test setup, the investigators followed the recommendations of RILEM TC-RC6, (1994) and accordingly, used an embedment length of five times the bar diameter and for the beam-bond tests, RILEM TC-RC5, (1994) recommendations were followed and as a result, an embedment length of ten times the bar diameter was used.

The test results showed that the pullout and beam-bond specimens consisting of normal-strength concrete and reinforced with 10 *mm* diameter bars produced similar results in terms of bond-slip behaviour and both experienced slippage failure regardless of the SCC or VC type concrete used. In addition, the normal-strength concrete using 16 *mm* diameter bars experienced concrete splitting failure in the pullout tests but not in the beam-bond tests due to the confining effects of the transverse reinforcement in the beam-bond specimens. An analysis of the pullout specimens of normal-strength concrete revealed that SCC mixes are superior to VC type concrete in terms of bond behaviour and the investigators attributed this to the use of fillers in SCC mixes, which act to improve the bond between the interfaces of concrete and steel. The high-strength concrete pullout specimens experienced splitting of the concrete cover while the high-strength concrete beam-bond specimens, benefiting from the presence of transverse reinforcement, did not experience concrete splitting but rather demonstrated steel yielding signifying the achievement of ultimate bond strength.

Overall, the pullout and beam-bond specimens produced similar results in terms of ultimate bond strength and ultimate slip values with the exception of the high-strength concrete specimens, which produced higher slip values in pullout tests compared to beam-bond tests. In addition, the researchers recommended that since the pullout and beam-bond tests of the steel bars generally produced similar bond-slip relationships, with differences being negligible, it is more logical and practical to continue implementing pullout tests for the determination of the bond behaviour of steel reinforced structures.

Desnerck et al., (2010) performed a comprehensive evaluation of the bond strength between longitudinal steel reinforcement and concrete by testing 36 beam-bond specimens, designed in accordance with RILEM TC-RC5, (1994) recommendations. Steel bars with a wide range of diameters; namely, 12, 20, 25, 32 and 40 *mm* were tested. The research aimed to evaluate the differences between conventional vibrated concrete, (CVC) as well as two powder types of self-compacting concrete, (SCC). The CVC had compressive strength of 58.4 *MPa* while the SCC1 and SCC2 had compressive strength of 71.7 and 62.1 *MPa*, respectively and the steel bars had yield strength between 542 and 641 *MPa* and ultimate strength between 681 and 750 *MPa* depending on the bar diameter. Despite RILEM TC-RC5, (1994) recommendations of a reinforcement bond length of ten times the bar diameter, the researchers implemented a bond length equivalent to five times the bar diameter in order to ensure bar pullout and prevent steel yielding or rupture.

From the analysis of bond stress versus slip curves, the study reached several conclusions regarding the influence of the concrete type and reinforcement diameter on the bond behaviour of steel reinforced beams. First, with smaller diameter steel reinforcement, the two self-compacting concretes, SCC1 and SCC2, demonstrated superiority in terms of bond strength when compared to CVC; however, as the diameter of the steel reinforcement increased, the SCCs and CVC exhibited comparable bond behaviours. In addition, when comparing CVC and SCC1, which had the same water to cement ratio, the researchers found that SCC1, which had limestone fillers, demonstrated a much higher compressive strength, which in turn enhanced the bond performance of the steel reinforcement. Lastly, the bond stress versus slip curves also revealed that as the bar diameter increases, the slip corresponding to the ultimate bond strength also increases. In essence, larger diameter bars produce higher slip values before realizing their full capacity.

Oh et al., (2010) conducted an experimental analysis on the bond characteristics of GFRP and steel longitudinal reinforcement in concrete beams with the aim of simulating the behaviour of flexural members. In terms of the reinforcement properties, both the steel and the GFRP bars had nominal diameter of 9.53 *mm*, with the GFRP bars having 616 *MPa* ultimate tensile strength and 42.9 *GPa* elastic modulus and the steel bars having 600 *MPa* ultimate tensile strength and 200 *GPa* elastic modulus. The surface of both types of reinforcement in this experiment had deformed ribs and the main parameter, besides the reinforcement type, was the embedment length, which was either 5, 10 or 15 times the nominal bar diameter. For each of the three embedment lengths, the researchers constructed four beams, two steel reinforced and two GFRP reinforced and the same 27 *MPa* concrete compressive strength was used to make all the beams. The beam construction was in accordance with British Standards BSI 12269-1, (2000) which recommends beams with a

curved notch at the centre with the purpose of mitigating stress concentrations. The tests were performed under four-point bending and for each beam, a strain gauge was placed on the reinforcement at the centre of the beam to measure its strain.

Overall, the predominant mode of failure for the majority of specimens with an embedment length of five or ten times the bar diameter was pullout, however, for the embedment length of 15 times the bar diameter, concrete splitting failure occurred. From the analysis of the load versus displacement curves, the researchers concluded that despite their lower elastic modulus, the GFRP bars achieved maximum loadings that were comparable, even at times even greater than the steel reinforcement, however, the post peak behaviour of GFRP bars experienced a sharper decline compared to steel.

The researchers noted that using a constant moment arm at the mid-section of the beam for ultimate strength calculations might not be appropriate since the moment arm is constantly changing as the beam deflects. Therefore, data from the strain gauge placed on the reinforcement at the centre of the beam was used to calculate the tensile force in the bar. Comparative analysis of the bond stress versus slip curves using a constant moment arm and curves produced by using the strain gauge method revealed that when using the strain gauge data, the bond strength results for specimens with short embedment length was somewhat lower.

Concerning the steel reinforced specimens, when the embedment length was five times the bar diameter, the strain corresponding to the peak load was lower than the yielding strain of the steel, however, at embedment lengths of 10 and 15 times the bar diameter, the same strain was significantly higher than the yield strain. Lastly, the slip generated by some of the GFRPs at the maximum bond stress was somewhat lower than the equivalent slip in steel reinforced beams, which led the researchers to suggest that certain GFRP surface deformations can in fact, result in a bond stress versus slip behaviour that is superior to steel.

Xu et al., (2011) investigated the effects of freeze and thaw cycles on the bond performance of steel reinforced concrete structures and in terms of the beam-bond specimen construction, followed the recommendations of RILEM TC-RC5, (1994). The steel longitudinal reinforcement investigated in this study had 20 mm diameter, 412.5 MPa yield strength and 557.5 MPa ultimate strength with an embedment length of ten times the bar diameter and the concrete had 44 MPa compressive strength. First, the beam specimens were immersed in 3% NaCl solution for a period of four days and then subjected to 0, 50, 100 and 200 freeze and thaw cycles. Following the environmental conditioning, the beams were tested in four-point bending.

Overall, in terms of the effects of the freeze and thaw cycles, the researchers noticed a substantial decrease in the ultimate bond strength with increased cycles, highlighting microscopic concrete damage and internal crack formation due to repeated cycles as the primary cause. In addition, the investigators concluded that as specimen size increased and more transverse reinforcement was added in the form of stirrups, freeze and thaw cycles became less of an issue and their effects on the bond between concrete and the reinforcement diminished. The researchers attributed this phenomenon to the fact that large specimens, with a relatively increased number of transverse reinforcement, have an enhanced ability to provide confining effects and prevent volume expansions caused by internal cracks.

Mazaheripour et al., (2013) performed an experimental program using 36 beam-bond tests in order to analyze the bond behaviour of GFRPs embedded in a new type of steel fibre reinforced self-compacting concrete, (SFRSCC). In terms of the design of the beam specimens, the researchers closely followed RILEM TC-RC5, (1994) recommendations and the parameters investigated in this experiment are the GFRP bar diameter and surface characteristics, the bonded length and the concrete cover thickness. The first type of GFRP in this experimental program, labelled Type A, had a ribbed treatment and diameter of either 8 or 12 *mm* with tensile strength of 1,500 and 1,350 *MPa* and elastic modulus of 65 and 56 *GPa*, respectively. The second type of GFRP investigated, labelled Type B, had a sand-coated surface treatment, diameter of 12 *mm*, tensile strength of 1,000 *MPa* and elastic modulus of 49 *GPa*.

As a means of enhancing the properties of the self-compacting concrete, the researchers used hooked-end steel fibres and for the 36 specimens, a total of five batches of the SFRSCC was produced. The concrete compressive strength for these batches ranged from 58.8 to 67.6 *MPa*. Contrary to recommendations of RILEM TC-RC5, (1994), the researchers fixed the embedment length on one of the half-blocks of the beams at 335 *mm* while varying the embedment length of the other half-block. In addition, shear reinforcement was not used in the beams in order to analyze the effectiveness of the SFRSCC, which was a high performance mix, designed to provide sufficient shear resistance in the absence of any transverse reinforcement. For each type of GFRP bar, A or B, the experimenters implemented an embedment length of either 5, 10 or 20 times the respective bar diameter with either 15 or 30 *mm* concrete cover.

The study used two LVDTs to measure the change in the moment arm between the centre of the steel hinge and the centre of the GFRP reinforcement and subsequently calculated the change in the GFRP bar force via equilibrium analysis. For comparison

purposes, the experimenters also placed a strain gauge on the GFRP reinforcement at midspan in order to calculate the bar force variation directly. Analysis of the data gathered revealed that the difference between the bar force calculated using the equilibrium analysis method versus the strain gauge method was negligible and the authors decided to use the strain gauge data for their conclusions.

Overall, regarding the two GFRP types, the results indicated that irrespective of the embedment length and the concrete cover, Type A bars consistently produced higher bond strength than Type B bars. The bearing resistance provided by the particular ribs of the Type A bars produced a higher pullout force than the sand-coated surface treatment of the Type B bars. As for the bar diameter effect, the researchers found that with a cover thickness of 15 mm, the bar diameter had negligible influence on the maximum bond stress, however, at a cover of 30 mm, the bond strength of the 12 mm diameter bars were at times higher than the 8 mm bars. Concerning the embedment length parameter, the study concluded that as the embedment length increased, the bond strength decreased, which is thought to be a result of the non-linear bond stress distribution along the reinforcement embedment length. In addition, embedment lengths as high as 20 times the bar diameter were insufficient in developing the ultimate tensile capacity of the GFRP bars. Lastly, beams with 30 mm concrete cover, due to the corresponding enhancement of confining effects, showed superior bond behaviour in terms of the maximum and the residual bond strength.

2.5 Summary

Pullout tests were performed by a number of investigators to study the bond behaviour of GFRP and/or steel rebars embedded in concrete. Nanni et al., (1995) concluded that the mechanical interlock contribution to bond strength by far exceeds the contribution from the adhesion and frictional components and furthermore, the choice of bar surface geometry can enhance bond performance. Katz et al., (1999) performed an investigation into the effects of high temperature on FRP bond performance and noted a significant decrease in bond strength with an increase in temperature and this was attributed to polymer degradation. Feldman and Bartlett, (2007) analyzed the bond stress distribution of hot rolled tubular steel bars and concluded that with an increase in load, there is a progressive shift in the peak bond stress from the loaded-end towards the unloaded-end of pullout specimens. Lee et al., (2008) noticed that initially, an increase in concrete compressive

strength will result in an enhancement of FRP bond performance, however, as concrete strength continues to increase, the mode of failure changes from concrete crushing to inter-laminar shear failure at the resin-fibre level. Davalos et al., (2008) highlighted the importance of preventing degradation of the resin component of FRPs and concluded that exposure to thermal cycles not only damages the resins but also further decreases bond performance by causing concrete micro-cracking. Hao et al., (2009) performed an in-depth investigation into the effects of surface geometry on the bond performance of GFRPs and noticed that bars with rib spacing equivalent to the bar diameter and rib height 6% of the bar diameter exhibited superior bond performance. Esfandeh et al., (2009) found that in terms of surface deformities, a combination of helical wrapping and sand coating, as well as a relatively large embedment length vastly enhances the bond performance of GFRP bars. Soong et al., (2011) investigated the constituents of bond force; namely, de-bond, bearing and frictional force and concluded that in terms of GFRP bars, the majority of the pullout resistance comes from the frictional and the bearing components of the bond force. Lastly, from the investigation of several different environmental conditions, Chen et al., (2012) noticed that acidic environments have the most negative impact on the bond performance of GFRP and steel reinforced structures.

Other investigators used the beam-bond test to study the bond behaviour and strength of GFRP and steel bars under variable conditions. Perry and Thompson, (1966) studied the bond stress distribution of steel bars embedded in pullout specimens, beams with a crack as well as beams with bar cut-off points and noted a discrepancy between the three test methods when it comes to the resulting bond stress distribution. In an extensive study of 30 FRP reinforced concrete beams, Daniali, (1992) concluded that in order to develop the ultimate strength of the FRP bar prior to bond failure, it is beneficial to consider adding stirrups over the entire span of the beam and furthermore, sustained loadings below the ultimate strength of the FRP could lead to premature bond failure. Benmokrane et al., (1996) conducted an in-depth investigation into the bond performance of GFRP bars using pullout and beam-bond tests and one of the major conclusions was that pullout tests produce higher bond strength values compared to beam-bond tests. Moreno and Bastos, (2006) conducted steel reinforced beam-bond testing using the RILEM TC-RC5, (1994) recommendations and noted that the pullout failure of the longitudinal reinforcement in one half-block can significantly alter the data gathered from the other half-block. In a comparative analysis of steel bond behaviour under different test methods, Menezes et al., (2008) found that for constant concrete strength, concrete type and steel bar diameter, both the beam-bond test and the more practical pullout test produce similar bond strength results. Desnerck et al., (2010) conducted an investigation into the bond performance of steel reinforced beam-bond specimens and concluded that self-compacting concrete is slightly superior to conventional concrete and in addition, an increase in bar diameter results in a

corresponding increase in slip at ultimate bond strength. Oh et al., (2010) performed a comparative analysis between the bond behaviour of steel versus GFRP reinforced concrete beam-bond specimens and noted that a GFRP bar with adequate surface characteristics can develop bond strength values that are similar to if not at times greater than the corresponding steel reinforced beams. Concerning the bond performance of longitudinal tensile reinforcement in flexural structures, Xu et al., (2011) found that an increase in freeze and thaw cycles is detrimental to the ultimate bond strength of steel reinforced concrete beam-bond specimens; however, this problem was mitigated with an increase in the specimen size as it resulted in an increase in the provided transverse reinforcement and corresponding confinement. From the beam-bond testing of 36 GFRP reinforced specimens, Mazaheripour et al., (2013) concluded that increased concrete cover is beneficial to bond performance while an increase in embedment length or bar diameter can lead to concrete splitting and large slippage, both of which are detrimental to bond performance.

Overall, to the knowledge of the writer and from numerous literature reviews, some of which have been presented in this paper, there is no definite conclusion among experimenters on whether the pullout and the beam-bond test method yield the same results in terms of the bond performance of FRP reinforcement. Thus, one questions the heavy reliance of most current standards, including the ACI and the CSA, as well as quality assurance programs, on using the bond strength obtained from simple pullout specimens as a true indicator of the bond behaviour of FRP bars in members having a different state of stress than the pullout specimens. As stated earlier, since in practice, bar pullout is avoided with the inclusion of an adequate embedment length, intuitively, the conventional pullout test method is not able to provide an accurate representation of the reinforcement bond behaviour in real applications. Lastly, from a review of past experimental programs, it is evident that there has not been a focus on the distribution as well as the shape and variation of the bond stress along an embedded FRP bar in concrete, particularly as a function of the bond test method. Consequently, there is need for further investigation with respect to this issue.

Chapter 3 Experimental Program

3.1 General

The main purpose of this experimental program is to study the bond behaviour of a typical GFRP bar, focusing particularly on the bond stress distribution along the reinforcement. The first phase of this study, however, starts with extensive tensile testing of GFRP bars conducted in collaboration with the bar manufacturer. In order to eliminate the influence of material constituents or bar size on bond behaviour, all of the GFRP bars in this experimental program are from the same batch and Section 3.2.1 will highlight the important properties of the particular bar investigated for bond.

In terms of the testing method, as previously mentioned, the typical pullout test for studying bond behaviour appears unrealistic in the sense that it puts the surrounding concrete in a state of compression when in practical situations the concrete around the longitudinal tensile reinforcement in beams is actually in a state of tension. To get a sense of the importance of this phenomenon, the current study investigates the bond performance of GFRP bars using pullout testing as well as two different types of beam-bond tests.

The first type of beam-bond test, named RILEM, after the European testing organization RILEM, follow the recommendations by RILEM TC-RC5, (1994), which involve two half-beams joined together with a steel hinge at the top, or near the compression face, at beam midspan and a usual longitudinal reinforcement passing through the blocks at the bottom. The second type of test, named Notched, represents a proposed modified method for beam-bond testing, which bears resemblance to the recommendations by ACI 208, (1958) and involves the construction of a full beam with a notch at the bottom of the beam, at midspan, large enough to expose the longitudinal reinforcement. Note that the Notched beams, because of the fact that they do not possess a steel hinge and a complete separation of the surface of the blocks at midsection, bear closer resemblance to the condition developed in typical reinforced concrete beams where full bond development is expected to occur. Overall, unlike tests that follow current guidelines, often resulting in complete bar pullout during the testing process, the Modified pullout and the beam-bond specimens in this experimental program, due to a sufficient embedment length, allow for the complete analysis of the GFRP's bond stress distribution up to bar rupture. This enables one to study the change in bond stress distribution along the embedment length up to the

bar rupture and to determine the development length of the bar. Lastly, the bond behaviour of Standard pullout specimens with short embedment length will be analyzed.

3.2 Materials

The materials in this study include the GFRP bar under analysis for bond performance, mild steel rebars used to provide transverse reinforcement in the beam-bond specimens and establish their stability during casting and lastly, normal strength concrete.

3.2.1 GFRP Bar

Since FRPs behave linear-elastically, their primary mechanical properties of interest are their elastic modulus and ultimate tensile strength which can be determined through tensile testing using current standard methods. As mentioned previously, this experimental program began with extensive tensile testing of the GFRP bar after each alteration of fibre content, resin type and manufacturing process in order to obtain the ideal GFRP bar that would satisfy the CSA S807, (2010) specifications. Since the purpose of this study is to analyze the bond stress distribution of GFRP bars, there is no need here to enter into significant detail regarding the manufacturing process and it suffices to mention that all of the GFRP bars in this experimental program are of the same approximate diameter, having a fibre content of around 80% and are made of the same fibre type and resin.

In addition, the bars are from the same batch of production and Figure 3:1 to Figure 3:3 show the tensile stress-strain behaviour of the 30 specimens tested at room temperature while Table 3:1 presents the bar size, ultimate tensile strength and elastic modulus. From the observation of these figures, it is evident that a certain degree of non-linearity exists in the tensile stress-strain relationship of the bars and this is attributed to the natural variability in manufacturing as well as surface fibre delamination. For tensile testing, ASTM D7205/D7205M, (2011) calls for the anchorage of an FRP bar at both ends using steel tubing filled with a material strong enough to prevent and/or minimize slippage of the bar before it has reached its ultimate strength. The tensile testing was performed using a Universal Testing Machine with capacity of 2,000 *kN* along with an electronic extensometer and a data acquisition system to obtain the stress-strain relationship.

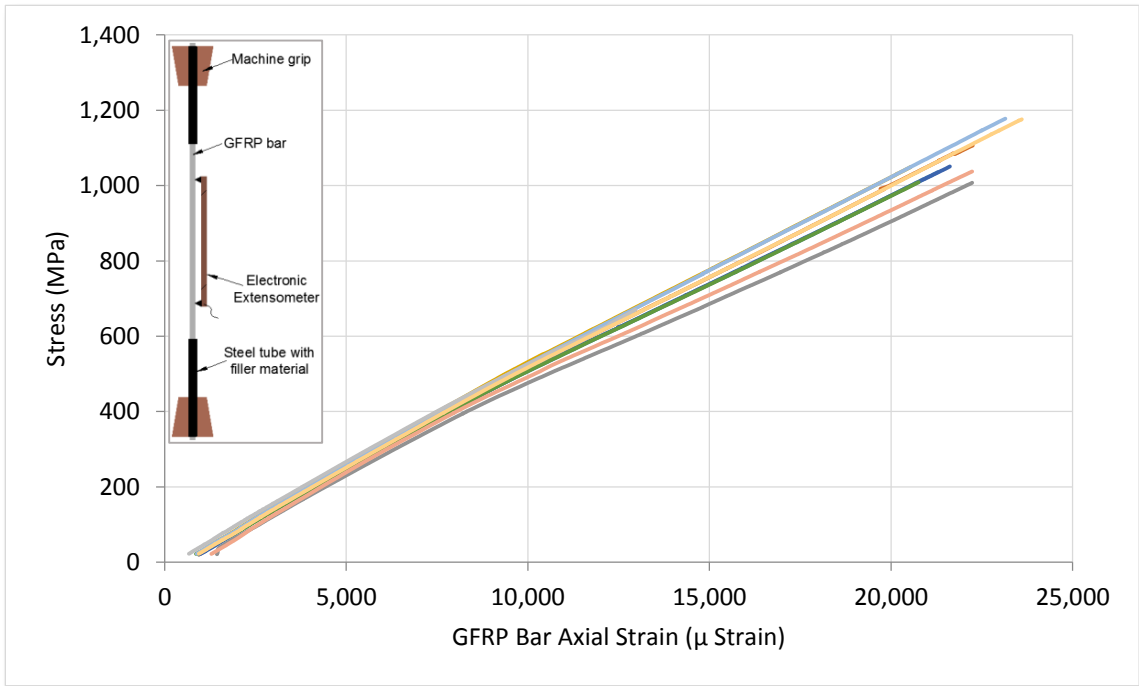


Figure 3:1: Tensile stress-strain relationship of specimens GFRP1 to GFRP10

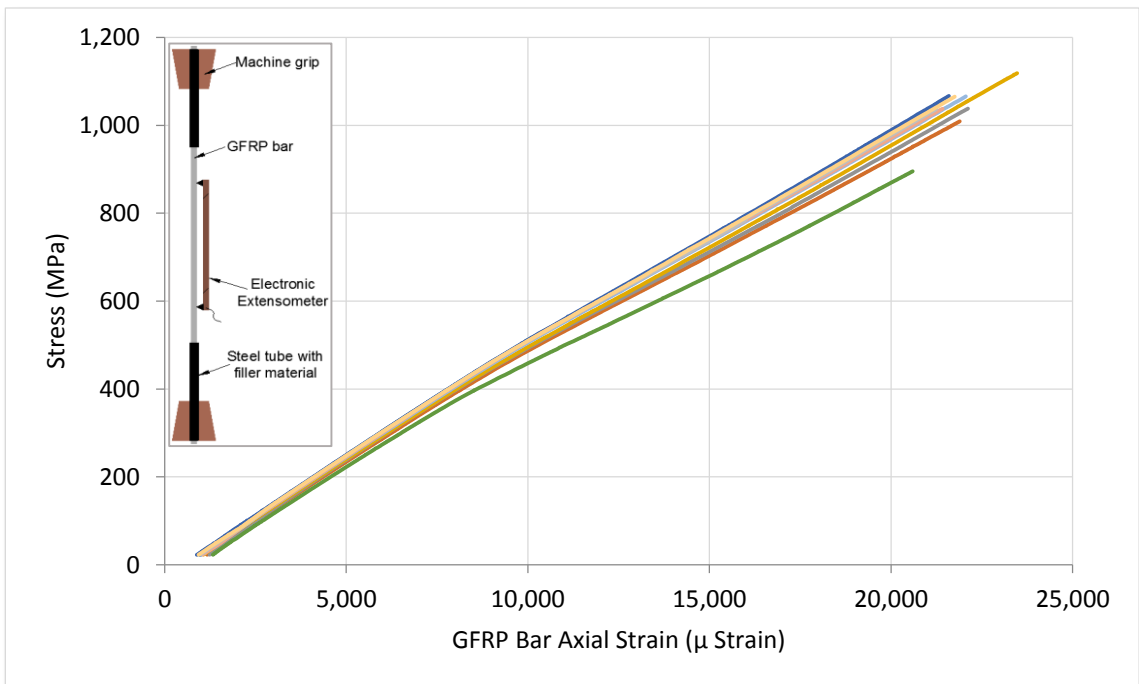


Figure 3:2: Tensile stress-strain relationship of specimens GFRP11 to GFRP20

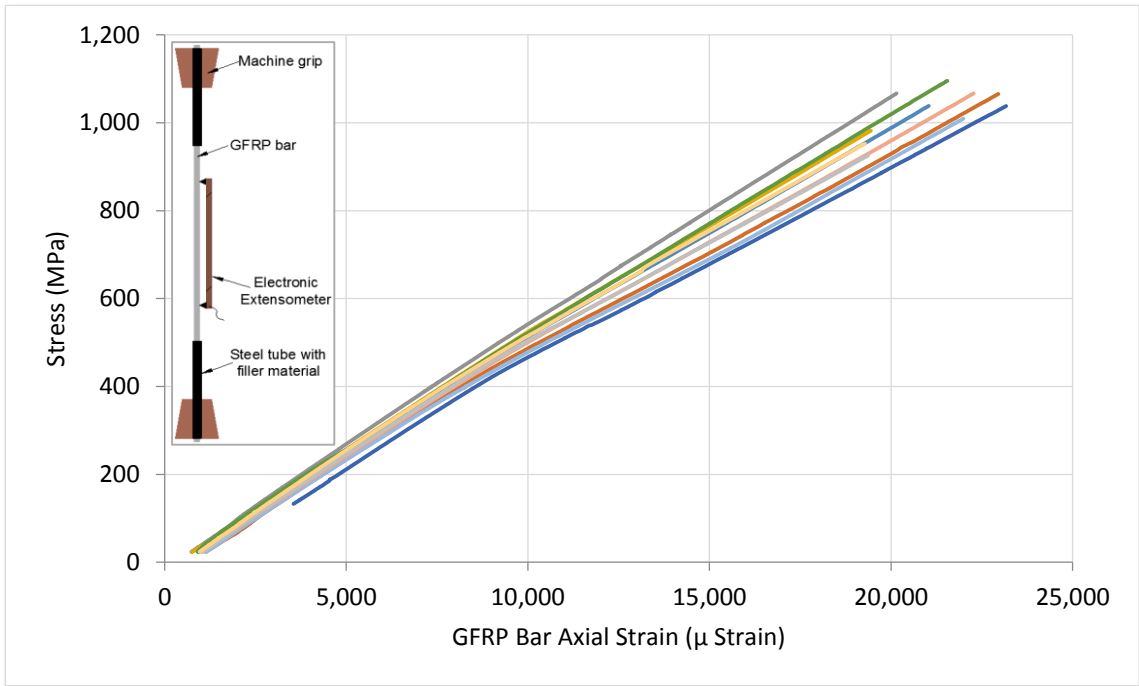


Figure 3:3: Tensile stress-strain relationship of specimens GFRP21 to GFRP30

Table 3:1: GFRP tensile test results

Bar Designation	d_{bF} (mm)	f_{Fu} (MPa)	E_F (GPa)
G1	14.7	1,141	51.9
G2	14.8	1,064	51.6
G3	14.8	1,020	48.1
G4	14.7	1,063	54.4
G5	14.7	1,090	51.9
G6	14.8	1,060	51.8
G7	14.8	1,192	52.9
G8	14.8	1,059	49.4
G9	14.8	1,080	51.7
G10	14.8	1,196	51.7
G11	14.8	1,032	52.3
G12	14.8	1,020	50.0
G13	14.8	1,053	50.0
G14	14.8	1,128	49.5
G15	14.8	1,097	51.8
G16	14.8	914	47.5
G17	14.8	1,073	51.7
G18	14.8	1,043	52.5
G19	14.8	1,049	52.0
G20	14.8	1,067	51.9
G21	14.8	1,050	52.3
G22	14.8	1,088	48.6
G23	14.8	1,150	54.2
G24	14.8	998	53.7
G25	14.8	1,058	48.5
G26	14.8	1,124	52.9
G27	14.8	1,025	48.0
G28	14.8	1,099	50.8
G29	14.8	968	52.5
G30	14.8	986	52.5
Avg.	--	1,066	51.3
S.D.	--	61	1.8
COV (%)	--	6	3.6

With reference to Table 3:1, based on calculations using the actual bar diameter, the average tensile strength and elastic modulus of the GFRP bar was 1,066 MPa and 51.3 GPa, respectively and Figure 3:4 shows the typical sudden rupture of the GFRP during the tensile testing which is characteristic of linearly elastic materials.



Figure 3:4: Sudden rupture failure of GFRP bars

Concerning the surface conditions, by wrapping a glass roving tightly around the core of the bar prior to curing and then taking the wrap off after the curing, the surface of the GFRP bars had a ribbed deformation pattern as shown in Figure 3:5, which enhances the bar's bond performance in concrete. The height and pitch of the ribs for this bar were roughly 0.35 and 10 mm, $\pm 10\%$, respectively.



Figure 3:5: TEME Corp. GFRP bar with ribbed surface deformations

3.2.2 Mild Steel

For the transverse reinforcement in both beam types as well as the longitudinal rebars necessary to provide them with stability during concrete casting, No. 10, Grade 400 deformed steel bars were used. Three steel specimens from the same batch as those used in the beams were tested in tension in accordance with ASTM A370, (2014) in order to ensure that the specified steel yield strength values used in the preliminary calculations were reasonably reached. The testing was performed using a Tinius Olsen Universal Testing Machine with 600 kN capacity for load determination and a standard electronic extensometer for strain measurements. Figure 3:6 shows the tensile stress-strain curves of the three specimens and Table 3:2 presents the results of the tests.

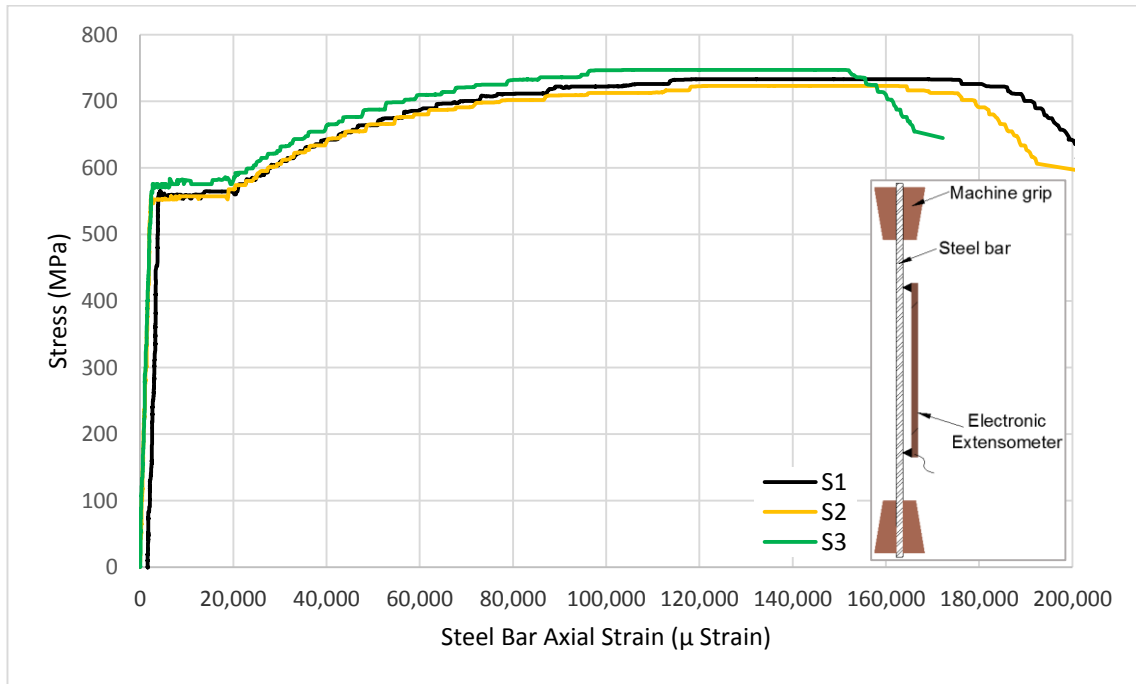


Figure 3:6: Tensile stress-strain behaviour of the steel specimens

Table 3:2: Steel tensile test results

Bar Designation	d_{bs} (mm)	f_y (MPa)	ϵ_y	E_s (GPa)	f_{su} (MPa)	ϵ_{su} (%)
S1	10.5	565	0.0026	219.1	733	16
S2	10.6	552	0.0024	228.3	723	15
S3	10.4	576	0.0029	199.5	747	15
Avg.	10.5	564	0.0026	215.6	735	15

With reference to Table 3:2, based on calculations using the actual bar diameter, the average yield strength of the deformed steel rebars was 564 MPa, the ultimate strength was 735 MPa and the elastic modulus was 215.6 GPa indicating that the specified values by the manufacturer were conservative. The results from the three specimens are comparable and therefore using the average tensile strength and elastic modulus values is reasonable and in addition, note that the elastic modulus is approximately 8% higher than the 200 GPa commonly assumed in design.

3.2.3 Concrete

Concrete was ordered from a local ready mix plant with specified compressive strength of 30 MPa, maximum aggregate size of 20 mm and slump of 100 mm. All of the test specimens in this experimental program, as well as thirteen 150 mm diameter, 300 mm long concrete cylinders, were cast using a single concrete batch. The casting method such as the rodding and vibration procedures as well as the laboratory temperature, adhered to the recommendations of ASTM C192/C192M, (2014). After casting, in order to minimize rapid evaporation of water from the concrete, plastic covers were used around all of the specimens for a period of two weeks. The fresh concrete had a density of 2,370 kg/m³, classified as normal density concrete.

3.2.3.1 Compressive Strength and Elastic Modulus

Five cylinders were tested in compression in accordance with ASTM C39/C39M, (2014) to determine their 28-day compressive strength and note that in order to avoid stress concentrations during the testing process, the cylinders were first capped with sulfur following the procedure outlined in ASTM C617/C617M, (2012). The results of the tests are summarized in Table 3:3 and it can be seen that the concrete had an average 28-day strength of 35.2 MPa with standard deviation of 1.9 MPa.

Table 3:3: Concrete cylinder compressive strength results at 28-days

Specimen Designation	f'_c^{28} (MPa)
C1	34.9
C2	33.3
C3	33.6
C4	35.9
C5	38.5
Avg.	35.2
S.D.	1.9

Knowledge of the elastic modulus with an accuracy beyond that which CSA A23.3, (2004) provides is unnecessary for the purposes of this experimental program, however, as a check, the use of a Demec gauge on specimen C2 allowed for the development of the concrete stress-strain relationship. As Figure 3:7 illustrates, the placement of Demec disks on the opposite sides of the cylinder allowed for manual strain readings at different load increments, however, the full concrete stress-strain curve could not be captured using this method due to safety concerns. Nonetheless, gauge readings were sufficient to satisfy the requirements of ASTM C469/C469M, (2014) for elastic modulus determination and hence one can compare the elastic modulus obtained from the stress-strain curve with its predicted value by CSA A23.3, (2004).

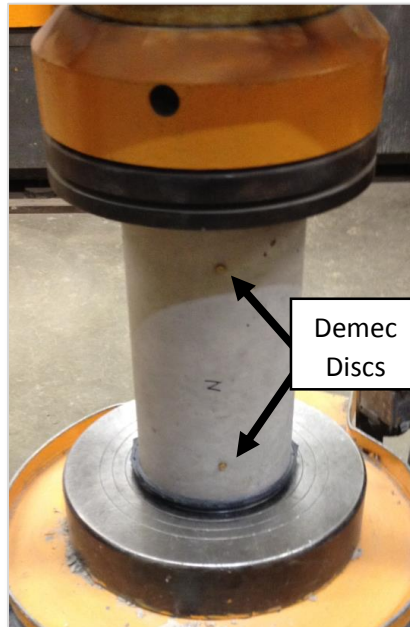


Figure 3:7: Concrete cylinder compression testing. Specimen C2

Table 3:4: Determination of the elastic modulus of concrete

Elastic Modulus of Concrete	
Specimen C2	$f'_c{}^{28} = 33.3 \text{ MPa}$
ASTM C469/C469M, (2014) <i>Eq. 3</i>	$S_2 = 0.4 * 33.3 \approx 13.3$ – (Stress at 40% of max load) $S_1 \approx 1.3$ - (Stress corresponding to 50μ Strain) $\epsilon_2 \approx 0.00055$ - (Strain at 40% of max load) $E_c^{28} = (S_2 - S_1) / (\epsilon_2 - 0.00005) \approx 24,200 \text{ MPa}$
CSA A23.3, (2004) <i>Cl. 8.6.2.3</i>	$E_c^{28} = 4500 \sqrt{f'_c{}^{28}} \approx 26,000 \text{ MPa}$

With reference to Table 3:4, CSA A23.3, (2004), provides an elastic modulus that is relatively close (within 7%) of the measured value and as mentioned previously, within the scope of this study, a more accurate knowledge of the elastic modulus is not warranted. Three additional concrete cylinders were tested in compression during the span of time between the 15th and 16th week post-casting, which coincided with the testing of the beams and the pullout specimens and Table 3:5 shows the results.

Table 3:5: Concrete cylinder compressive strength results at time of testing

Specimen Designation	f'_c (MPa)
C1	35.5
C2	36.8
C3	37.1
Avg.	36.5

Thus, the average compressive strength at 28-days was approximately 35.2 MPa while at the time of the specimen testing it was 36.5 MPa, which indicates a slight increase as expected.

3.2.3.2 Tensile Strength

At the age of 28-days, three concrete cylinders were tested in split-cylinder test, Figure 3:8, in order determine the concrete tensile strength. Table 3:6 shows the results as well as a comparison with the mean value obtained by numerous split-cylinder tests conducted by MacGregor and Wight, (2005) and the modulus of rupture value computed based on the CSA A23.3, (2004) recommendation.



Figure 3:8: Concrete split-cylinder testing

Table 3:6: Concrete tensile strength results at 28-days

Specimen Designation	f_t^{28} (MPa)
1	2.38
2	2.08
3	2.65
Avg.	2.37
MacGregor and Wight, (2005)	$f_t^{28} = 0.5314 \sqrt{f_c'^{28}} = 3.15$
CSA S806, (2012) Cl. 8.3.2.8	$f_r^{28} = 0.6\lambda \sqrt{f_c'^{28}} = 0.6 \times 1.0 \times \sqrt{35.2} = 3.56$

It can be seen that the average of the three test values is reasonably close to the prediction by MacGregor and Wight, (2005) and CSA A23.3, (2004) with the test value being somewhat smaller. Furthermore, as MacGregor and Wight, (2005) noted, there can be significant variability in the results of split-cylinder tests. At the time of the testing of the beams and the pullout specimens, an additional two split-cylinder tests were performed and the results are shown in Table 3:7 and again, the measured and the predicted values seem reasonably close.

Table 3:7: Concrete tensile strength results at time of testing

Specimen Designation	f_t (MPa)
1	2.63
2	2.62
Avg.	2.63
MacGregor and Wight, (2005)	$f_t^{28} = 0.5314 \sqrt{f'_c} = \mathbf{3.21}$
CSA S806, (2012) Cl. 8.3.2.8	$f_r = 0.6\lambda \sqrt{f'_c} = 0.6 \times 1.0 \times \sqrt{36.5} = \mathbf{3.62}$

3.3 Test Equipment and Instrumentation

The primary equipment and instrumentation that this experimental program employed consists of load cells, Linear Variable Displacement Transducers (LVDTs), string pot potentiometers, electrical resistant strain gauges and a data acquisition system. The strain gauges were used to assess the bond stress distribution along the GFRP bar, however, since each strain gauge placement debonds the GFRP from the concrete at that location, there was a limit on the number of strain gauges that could be placed. At locations requiring strain gauges, the application of a thin layer of epoxy on the GFRP bar, followed by surface smoothing with two grades of sand disks, ensured that the strain gauges had uniform contact surface. The thin layer of epoxy was necessary since it was determined that using sand disks to smoothen the GFRP bar surface, especially considering that the nominal diameter of these bars was 15 mm, had the potential of causing damage to the bar core and surrounding glass fibres. The LVDTs were used to measure the loaded-end as well as the unloaded-end slip of the GFRP bar in both the beam and the pullout specimens while the string pot potentiometers were used to measure the beam deflection along its length. Throughout this paper, L, SG and SP will be abbreviations referring to LVDTs, strain gauges and string pot potentiometers, respectively.

3.4 Test Specimens

3.4.1 Specimen Designation

The designation of the test specimens in this experimental program are as follows:

- a) Two identical RILEM beams (BR1 and BR2): The RILEM beams possess the characteristic steel hinge at the top of the midspan, along with a single longitudinal reinforcement at the bottom.
- b) Two identical Notched beams (BN1 and BN2): The Notched beams are a modified form of the beam-bond test specimens recommended by ACI 208, (1958) and contain a notch at the bottom of the beam at midspan, which exposes the longitudinal reinforcement in the notch region.
- c) Two identical Modified pullout specimens (MP1 and MP2): These specimens differ from typical pullout samples in that their reinforcement embedment length is identical to the beam specimens and is therefore forty times the nominal bar diameter which by far exceeds typical guidelines which recommend embedment lengths of four to five times the bar diameter.
- d) Ten identical Standard pullout specimens (P1 to P10): The construction of these specimens follow the recommendations of CSA S806, (2012), *Annex G* and accordingly, have a reinforcement embedment length that is 60 mm, equivalent to four times the nominal bar diameter.

3.4.2 Construction Detail of Test Beams

Since FRP reinforcement have a linearly elastic behaviour and their failure is abrupt, most current standards such as the CSA S806, (2012) generally ensure that the stress in the FRP longitudinal tensile reinforcement does not reach its ultimate strength at failure of FRP reinforced members. However, the purpose of this study is to capture the bond-stress distribution at all stress levels up to rupture, hence it is necessary to design the beams in such a way that failure would occur by rupture of the longitudinal GFRP tensile reinforcement. The overall beam design followed recommendations by CSA S806, (2012) guaranteeing failure by rupture of a 15 mm nominal diameter GFRP bar with an estimated tensile strength of 1,066 MPa which resulted in a beam with a substantial cross section despite using only a single GFRP bar as tensile reinforcement. It was critical for this study to avoid shear failure of the RILEM and the Notched beams and therefore the design was such that the beam shear strength was substantially greater than the maximum shear force that they were expected to sustain.

Both the RILEM and Notched beams had 2,000 *mm* length, 400 *mm* width and 500 *mm* height, with 15 *mm* clear cover for the reinforcement cage and 35 *mm* clear cover for the GFRP longitudinal reinforcement. The length and cross section were substantially larger than the beams used in other experimental programs investigating bond behaviour through the beam-bond test and this is due to the fact that unlike previous investigations, this study avoids pullout failure and ensures bar rupture.

The testing of the beams were under four-point bending, involving two point loads with the distance between the point loads being 200 *mm* and the beam ends had 150 *mm* overhang from the support leading to an effective shear span of 750 *mm*. The design calculations for the beams are presented in Appendix A. Along its 2000 *mm* length, each beam had one half designated as the “Test End” and the other half as the “Non-test End” and the GFRP longitudinal tensile reinforcement had an embedment length of 40 times the GFRP nominal bar diameter, or equivalently 600 *mm*, in the “Test End” and 900 *mm* embedment in the “Non-test End”. Concerning the GFRP embedment in the “Test End” of the beams, from the beam centreline, the first 200 *mm* was debonded, followed by 600 *mm* of embedment, and again, 200 *mm* of debonded region up to the end of the beam. In the “Non-test End”, from the beam centreline, up to the first 100 *mm*, which also corresponded to the end of the constant moment region, the GFRP was unbonded with the remaining 900 *mm* beyond this point bonded to the concrete. The debonding was accomplished with the application of a layer of electrical tape, followed by duct tape and oil.

Typically, beam-bond tests, in accordance with well-known recommendations such as RILEM TC-RC5, (1994), have an identical embedment profile of the longitudinal tensile reinforcement in both halves of the beam in contrast to this study which has 600 *mm* embedment along one-half of the beam length and 900 *mm* along the other. The reason behind this difference stems from the knowledge gathered from Moreno and Bastos, (2006), who in their experiment, followed RILEM TC-RC5, (1994) guidelines and accordingly, when the inevitable reinforcement pullout failure occurred on one side of the beam, used an external grip to secure the rebar and continued the test until the rebar pullout failure occurred at the other side of the beam. As previously mentioned, Moreno and Bastos, (2006) found that the two bond strength values obtained from each beam were highly inconsistent and they attributed this to the deformation caused when the rebar on one side of the beam pulls out sooner than the other and as a result has to be gripped. Thus, to avoid such inconsistency, this experimental program has a different embedment length on either side of the beam, meaning that if the bar were to pullout, it would most likely occur first at the “Test End” of the beam with the smaller, 600 *mm* embedment length. Mazaheripour et al., (2013) also chose to have a tensile reinforcement with different

embedment lengths on either side of their beams, however, note that this method also means that from each beam, only one set of bond related data can be gathered, which in the case of this experimental program, comes from the “Test End” of the beams. Despite recognizing and avoiding this problem associated with strictly following typical beam-bond test guidelines such as the RILEM TC-RC5, (1994), the writer was highly confident that the 600 *mm* embedment length would be sufficient to cause GFRP bar rupture without slip occurring at the unloaded-end of the beams.

Figure 3:9 shows an overall view of the RILEM beams which consist of two half-beams joined by a longitudinal GFRP reinforcement at the bottom and a steel hinge at the top, which serves as the point through which the resultant compression force at the centre of the beam acts. The creation of a ledge at the top of the RILEM beams with height of 80 *mm* and width of 20 *mm* allowed for the placement of the steel hinge and any remaining gaps were filled with hydro-stone in order to create uniform contact area between the steel hinge and the concrete. With reference to Figure 3:9, note that the longitudinal steel rebars at the top and the bottom of the beams, providing stability to the transverse reinforcement, terminate near the beam midspan with clear cover of 15 *mm* and therefore, as mentioned earlier, the two half-beams are joined only by the steel hinge at the top and the GFRP longitudinal reinforcement at the bottom. In addition, with the application of a layer of electrical tape, followed by duct tape and oil, the steel reinforcement at the bottom of the beams were debonded from the concrete to ensure that they do not interfere with the bond performance of the GFRP bar and are not able to contribute to the flexural resistance of the beams. Figure 3:10 and Figure 3:11 show 3D illustrations of the RILEM beams from different angles in order to present a better understanding of the beam detail.

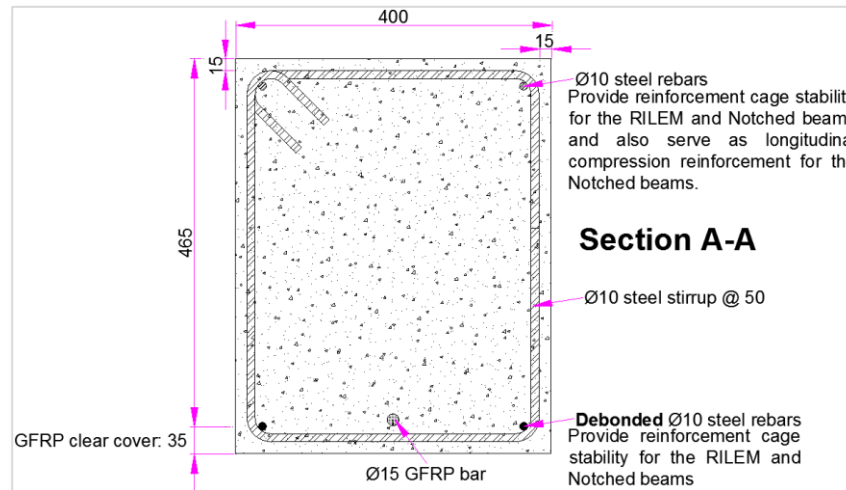
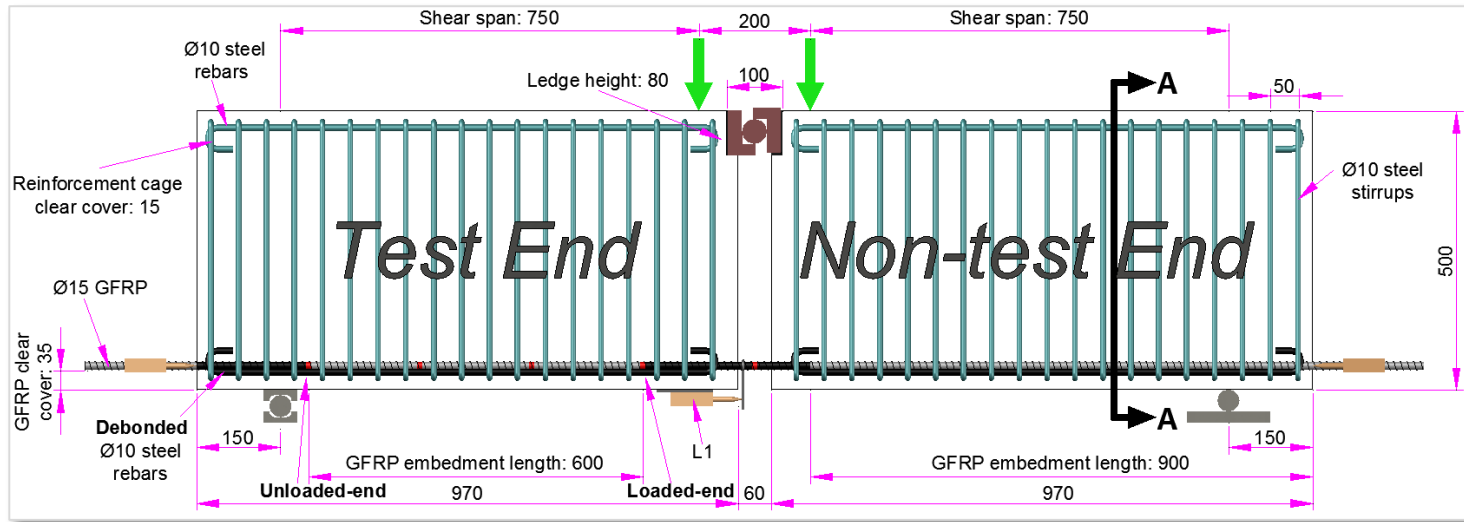


Figure 3:9: RILEM beam detail (All dimensions are in mm)

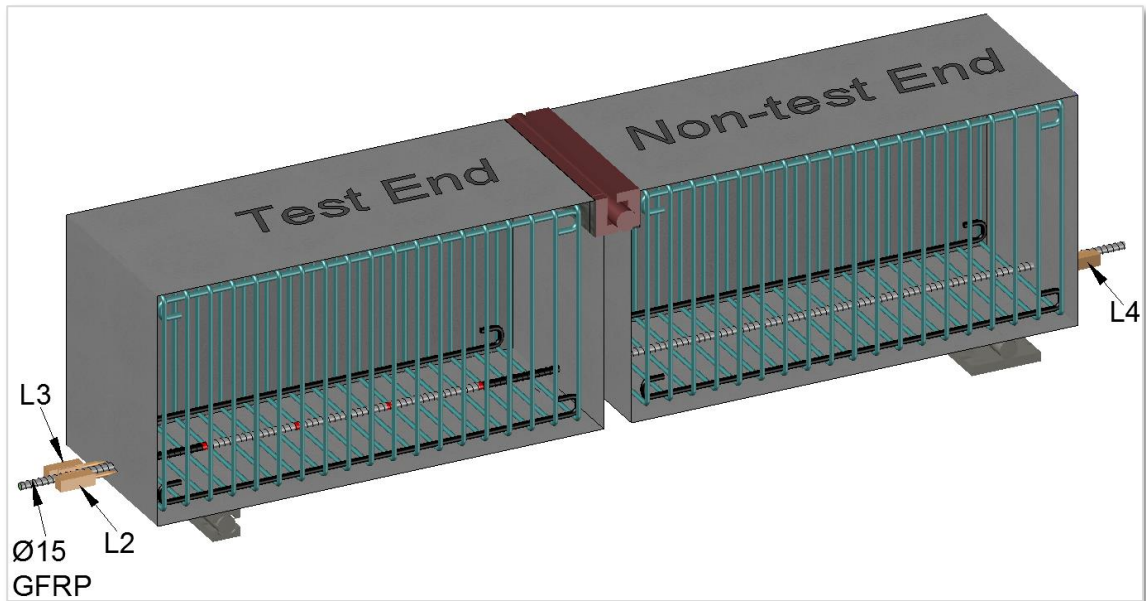


Figure 3:10: RILEM beam detail: internal view

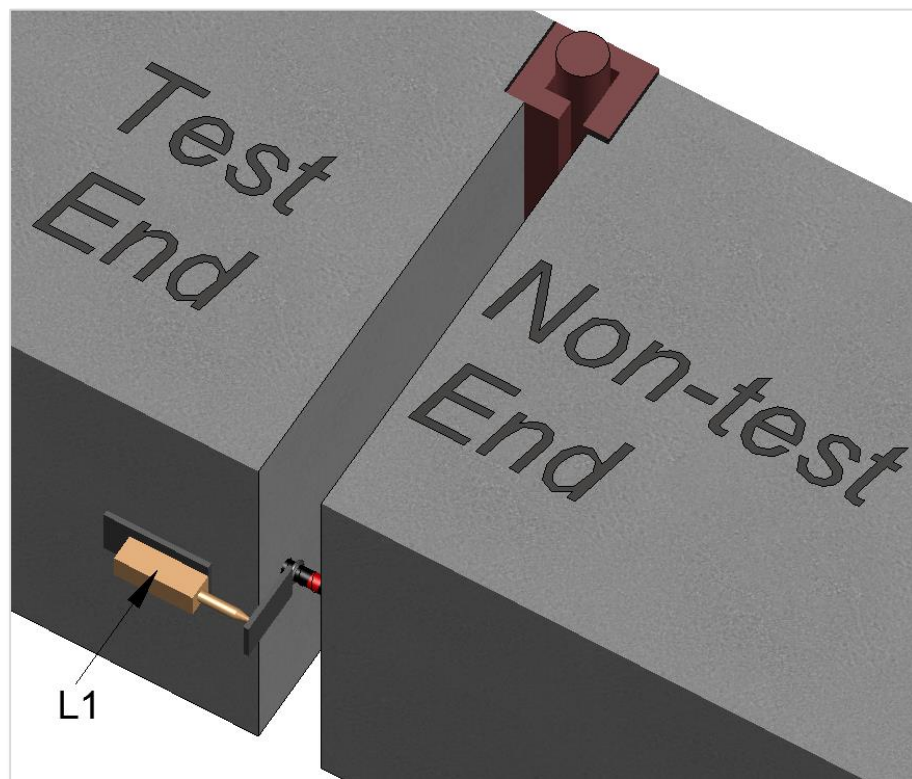


Figure 3:11: RILEM beam detail: midspan view

The Notched beams had a square notch at the bottom of midspan with length of 60 *mm*, which was equivalent to the spacing of the midspan gap in the RILEM beams. Figure 3:12 shows an overall view of the Notched beams and note that the longitudinal steel reinforcement at the top of the beam provides stability to the reinforcement cage but also serves as compression reinforcement. Once again, from this figure, note that the longitudinal steel reinforcement at the bottom, using the same method as in the RILEM beams, is debonded from the concrete and terminate, with clear cover of 15 *mm*, prior to reaching the notch at midspan. Thus, just as in the RILEM beams, for the Notched beams, there is a guarantee that the bottom steel reinforcement does not affect the bond performance of the GFRP bar and is not able to contribute to the flexural resistance of the beams. For more clarity, Figure 3:13 and Figure 3:14 show 3D illustrations of these beams.

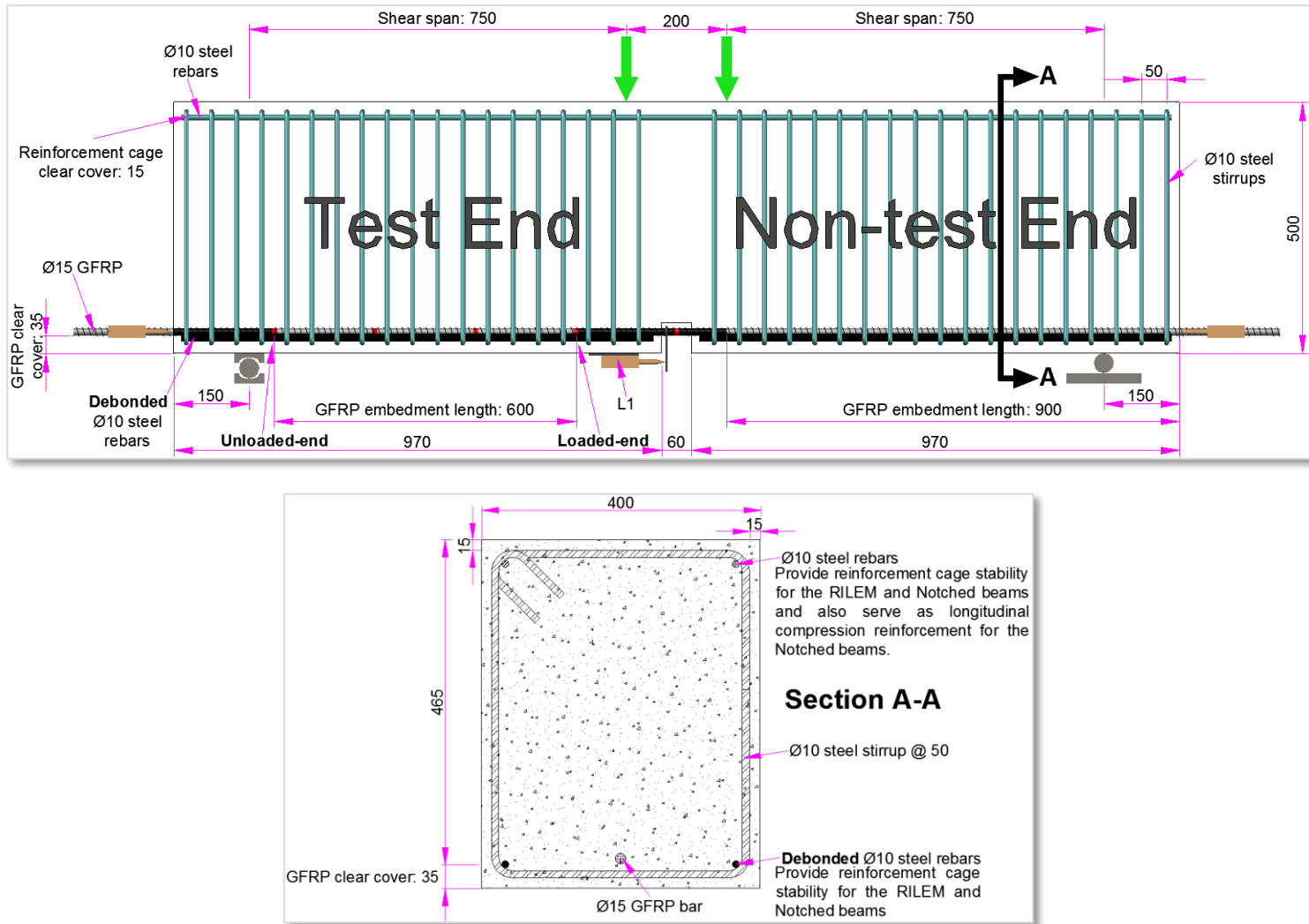


Figure 3:12: Notched beam detail (All dimensions are in mm)

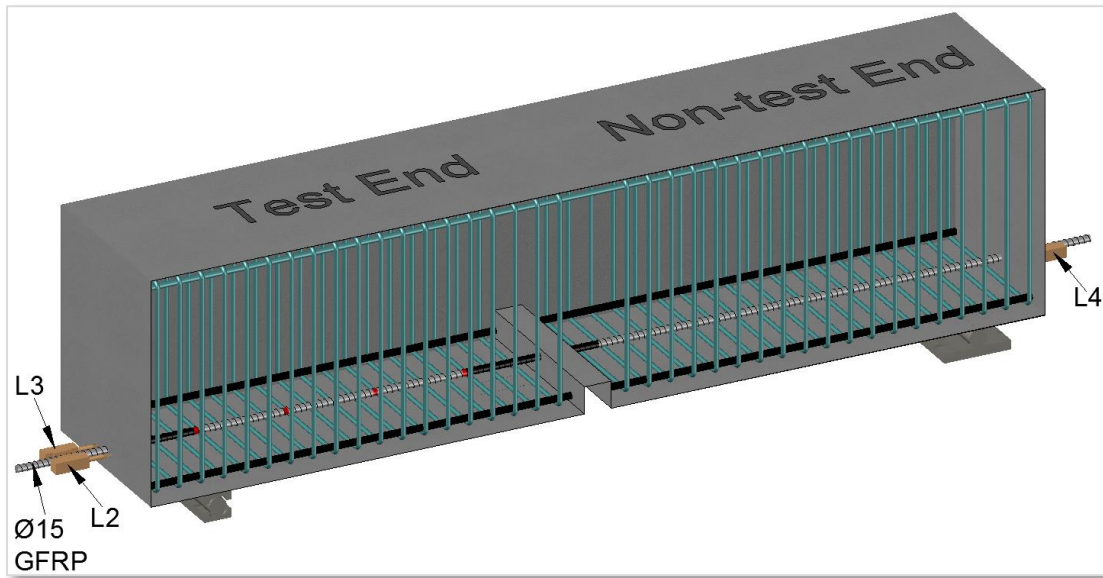


Figure 3:13: Notched beam detail: internal view

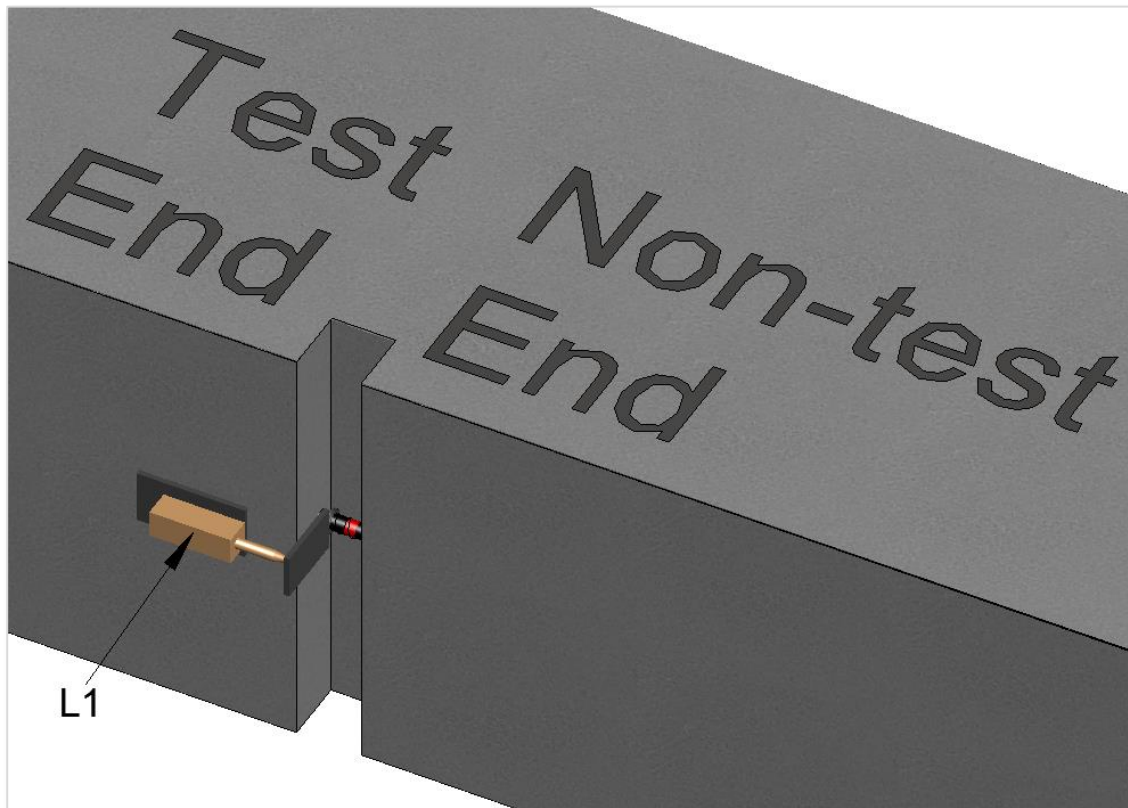
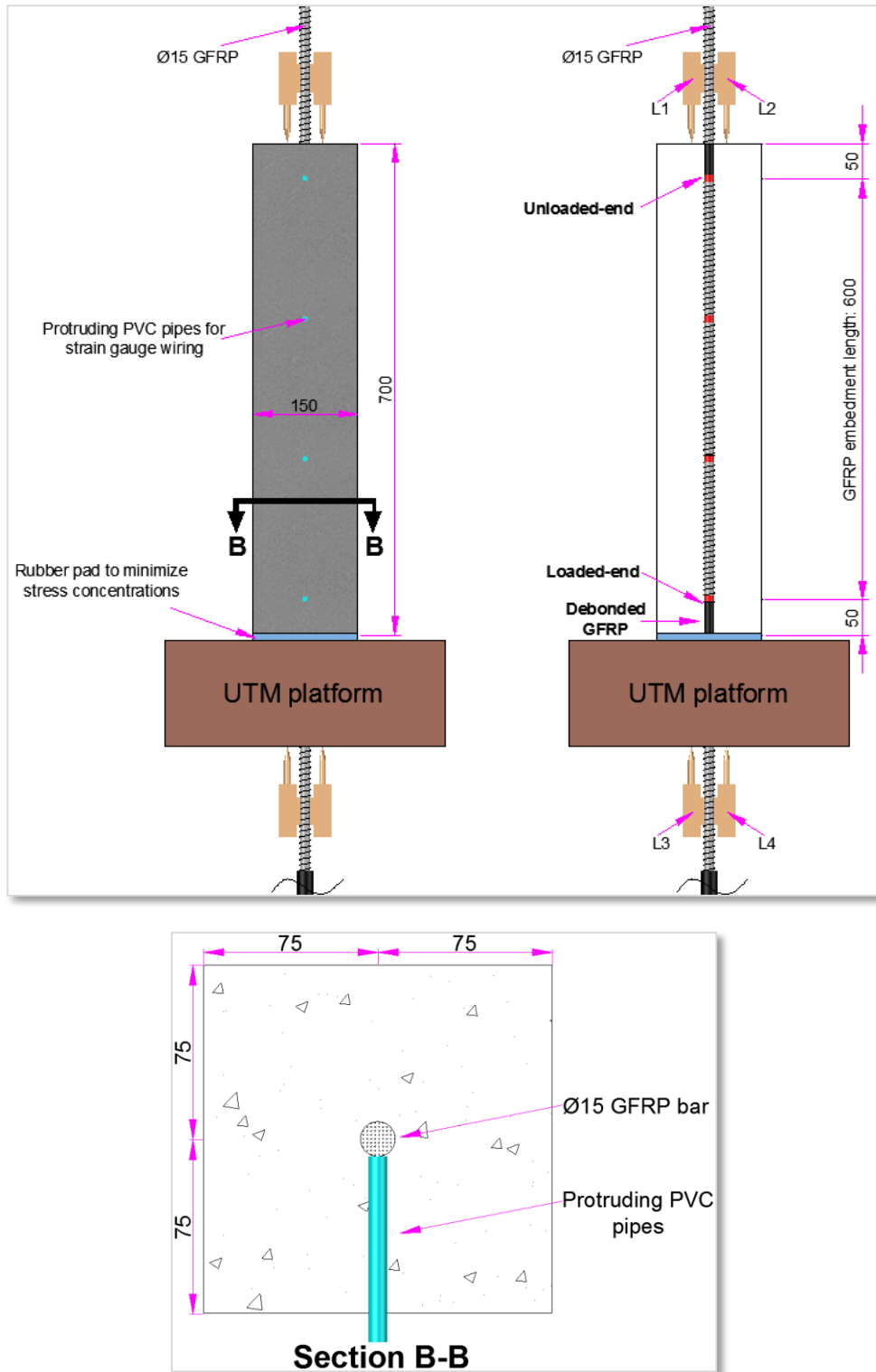


Figure 3:14: Notched beam detail: midspan view

3.4.3 Construction Detail of Modified and Standard Pullout Specimens

The Modified pullout specimens in this experimental program had GFRP bar embedment length of 600 mm and thus were identical to the “Test End” of the beam specimens and this allows for a direct comparison between the beam-bond and the pullout testing method. The total height of the Modified pullout specimens, however, was 700 mm and therefore, in order to achieve 600 mm embedment length, the top and bottom 50 mm of the GFRP bar in these specimens was debonded from the concrete using the same method as in the beam-bond specimens. The choice of the length of the GFRP bar protruding from the loaded-end of the specimens had to be substantial in order to facilitate the placement of a two-inch steel pipe around the GFRP bar with a length greater than the 600 mm GFRP embedment. The pouring of a filler material into the steel pipe provided an adequate gripping mechanism for the Universal Testing Machine to pull down on and the choice of an embedment length in the pipe that is larger than the pullout specimen ensured that the bar would either pullout or rupture during testing. Figure 3:15 presents an overall view of the Modified pullout specimens and note that the protruding PVC pipes were necessary to protect and accommodate the strain gauge wiring and the rubber pad at the bottom of the specimens minimized the formation of stress concentrations during loading. Due to laboratory limitations, the loading of the Modified pullout specimens involved physically lifting these samples several meters onto the Universal Testing Machine platform and therefore, given the large length of the sample, the 150 × 150 mm cross section was the practical option.



3.4.4 Installation of Instrumentation

3.4.4.1 LVDTs

With reference to Figure 3:9 and Figure 3:11 for the RILEM beams and Figure 3:12 and Figure 3:14 for the Notched beams, there was a LVDT, designated as L1, attached near the midspan in order to measure the loaded-end slip of the GFRP reinforcement. Figure 3:17 to Figure 3:19 show the gripping mechanism used to attach L1 to the GFRP reinforcement and note that the position of this LVDT is towards the “Test End” face of the beam specimens, with distance of 10 mm from the midspan. To address the unlikely event that the GFRP bar would experience a slip at the unloaded-end, with reference to Figure 3:9 and Figure 3:10 for the RILEM beams and Figure 3:12 and Figure 3:13 for the Notched beams, L2 and L3 measured the unloaded-end bar slip at the “Test End” while L4 measured the unloaded-end bar slip at the “Non-test End” of the beams.

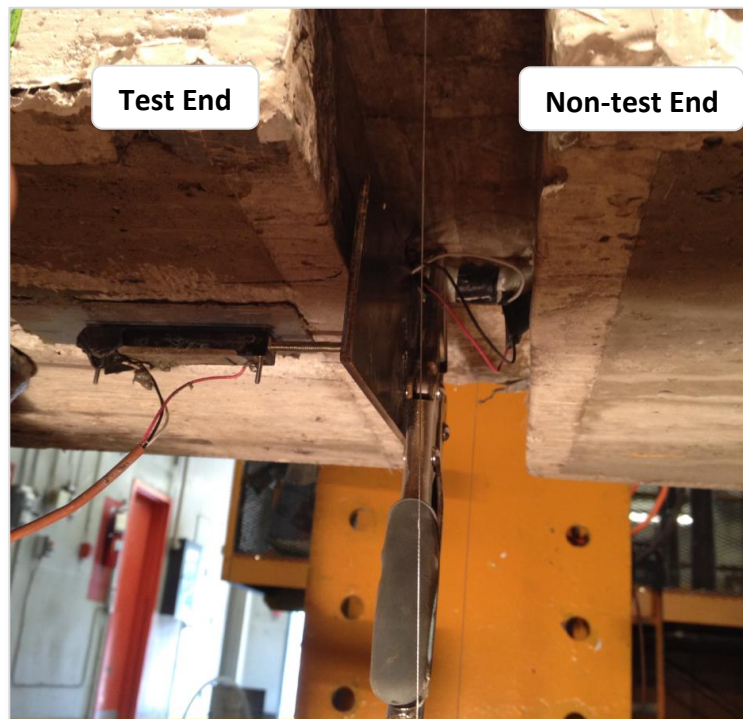


Figure 3:17: Detail of the midspan gripping mechanism for the RILEM and Notched beams. View 1. Notched beam shown.

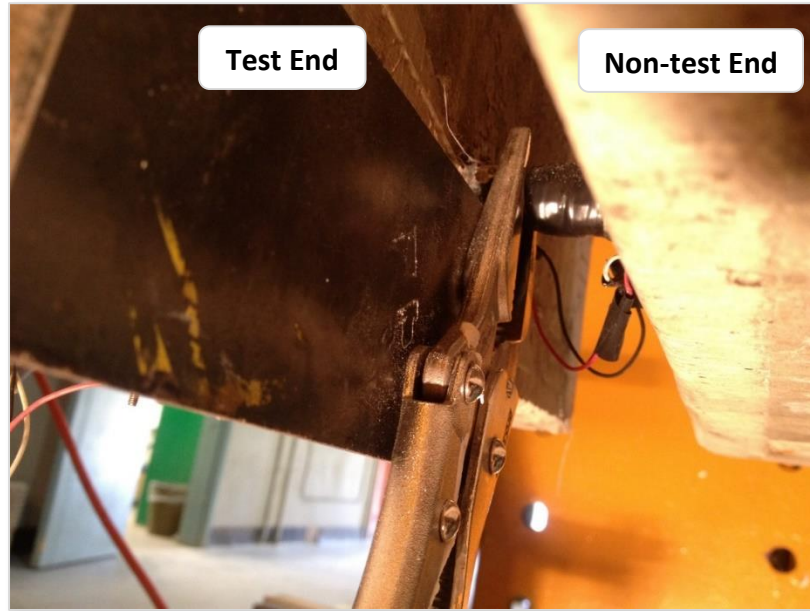


Figure 3:18: Detail of the midspan gripping mechanism for the RILEM and Notched beams. View 2. Notched beam shown.

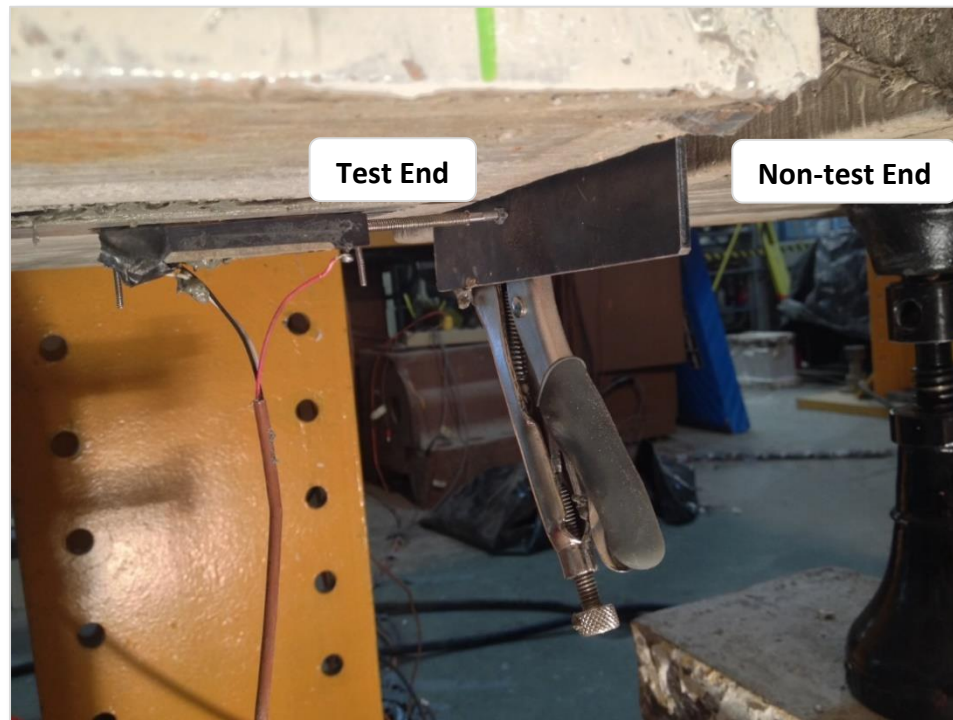


Figure 3:19: Detail of the midspan gripping mechanism for the RILEM and Notched beams. View 3. Notched beam shown.

Concerning the Modified pullout specimens, with reference to Figure 3:15, L1 and L2 measured the unloaded-end slip while L3 and L4 measured the loaded-end slip of the GFRP reinforcement. For the Standard pullout specimens, with reference to Figure 3:16, L1 to L3 measured the unloaded-end bar slip while L4 to L6 measured the loaded-end bar slip.

3.4.4.2 Strain Gauges

Strain gauges were installed on the GFRP bar reinforcement to capture its deformations along a portion of its length and to use these deformations in order to establish the bond stress distribution along its critical bond length. The number of strain gauges along the GFRP bar reinforcement was limited since each strain gauge partially de-bonds the bar from the concrete at that location. With reference to Figure 3:9, Figure 3:12 and Figure 3:15, note that the number and spacing of strain gauges, shown in red, along the 600 mm embedment length, were identical for both beam types as well as for the Modified pullout specimens and this allows for a direct comparison of strain data between different testing methods. The beam specimens had, in addition, a strain gauge, labelled SGC, on the GFRP bar reinforcement at midspan. Figure 3:20 illustrates the number and spacing of all strain gauges for both beam types and for the Modified pullout specimens.

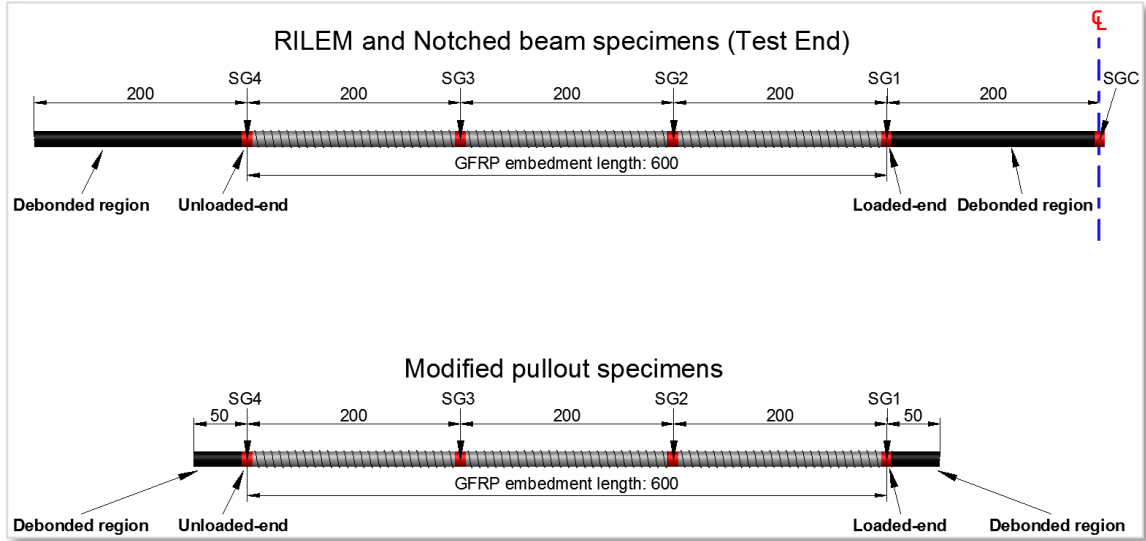


Figure 3:20: GFRP bar reinforcement strain gauge detail for RILEM and Notched beams (Test End), as well as for the Modified pullout specimens (All dimensions are in mm)

Since the beams had height of 500 mm, there was the probability that the concrete casting would damage some of the strain gauge wires, hence to avoid this, the wires were passed along the bottom of the stirrups and as Figure 3:21 and Figure 3:22

illustrate, through a PVC pipe which ran along the edges of the stirrups. Note that for the RILEM and Notched beams, in the 60 mm region along the GFRP bar at midspan, the bar was completely exposed without any contact with concrete and therefore it was debonded and there was no need for any electrical or duct tape except at the location of the SGC placement. Concerning the Modified pullout specimens, as Figure 3:23 shows, the wire for each strain gauge along the embedment length immediately passed through a PVC pipe and this was necessary to protect the strain gauge wiring during the concrete casting.

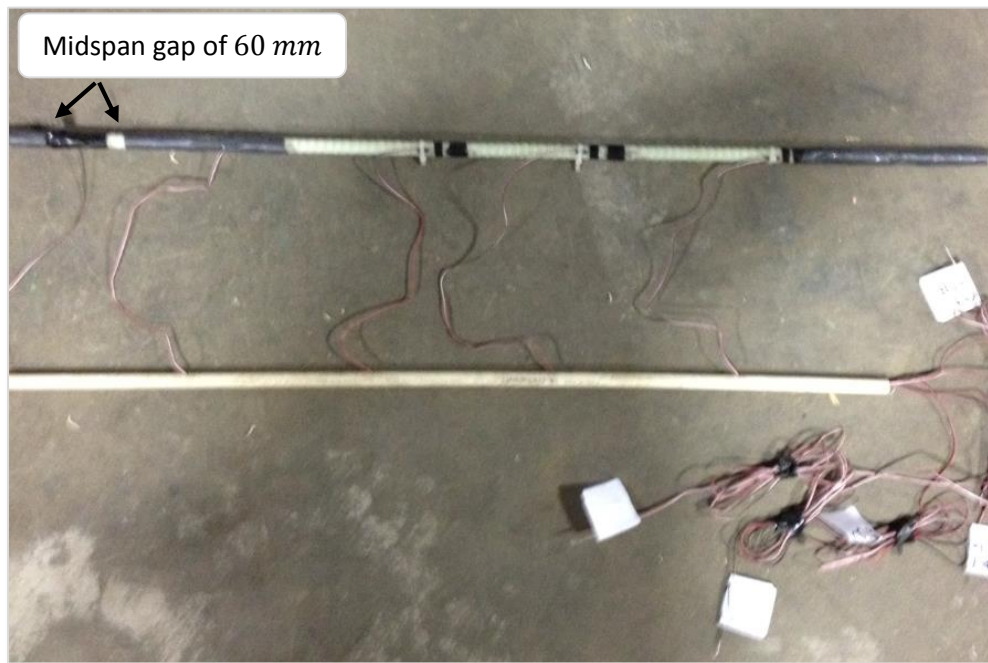


Figure 3:21: PVC pipes used to protect the strain gauge wires in the beam specimens

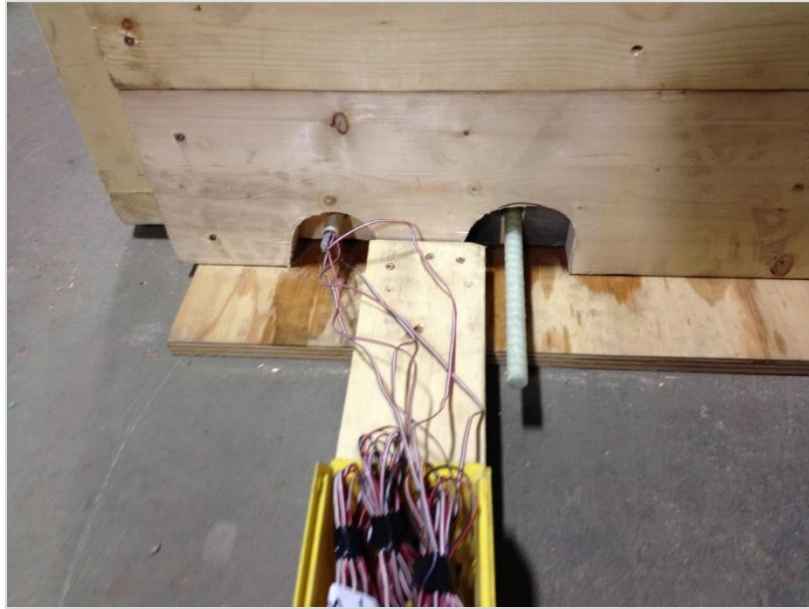


Figure 3:22 GFRP bar reinforcement and PVC pipe protruding out of the beam formwork



Figure 3:23: PVC pipes used to protect the strain gauge wires in the Modified pullout specimens

3.4.4.3 String Pot Potentiometers

All of the beam specimens in this experimental program had string pot potentiometers attached at the midspan as well as 500 mm to the right and to the left of the midspan in order to facilitate an analysis of the variation in beam deflection during different loading stages. Figure 3:24 provides an illustration as well as the designation of the string pot potentiometers in the beam specimens.

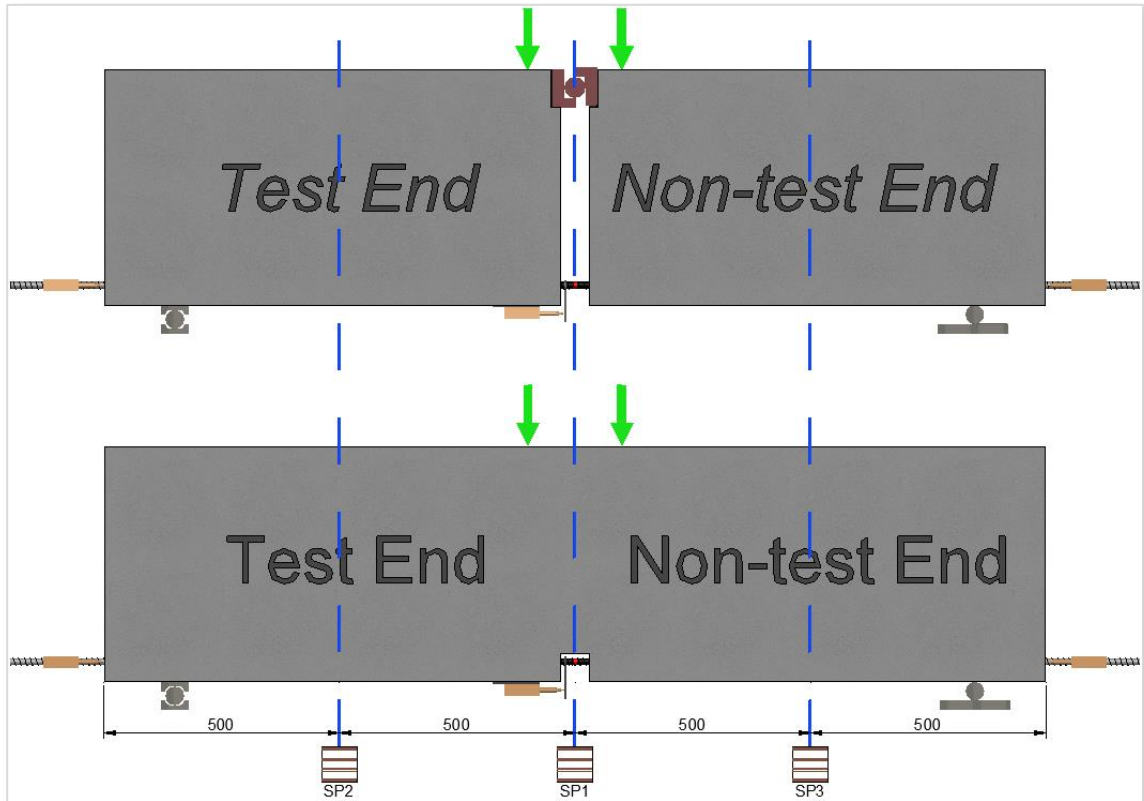


Figure 3:24: String pot potentiometer detail for RILEM and Notched beams (All dimensions are in mm)

3.5 Test Procedure

The beam-bond tests made use of a steel frame, with a hydraulic jack at the centre and the attachment of a load cell to the jack as well as a string pot potentiometer, allowed the choice of either displacement or load-control testing. Since the beams had to be tested under two-point loading, a steel spreader beam combined with a steel hinge and roller as well as steel plates were used to convert the single point load from the hydraulic jack into two equal point loads. The supports at the bottom of the beam, in an identical manner, made use of a steel hinge, a roller and steel plates and note that in order to prevent stress concentrations, the space between the beam surface and the loading plates at the top and the reaction plates at the bottom was filled with a layer of hydro-stone. In addition, because the length of the loading and reaction plates were either equal to or greater than the 400 mm beam width, the load distribution on the beam was uniform. Finally, the thickness and orientation of these plates were such that the beams were level in all directions. Figure 3:25 to Figure 3:27 provide further detail of the test setup for the RILEM and Notched beams.

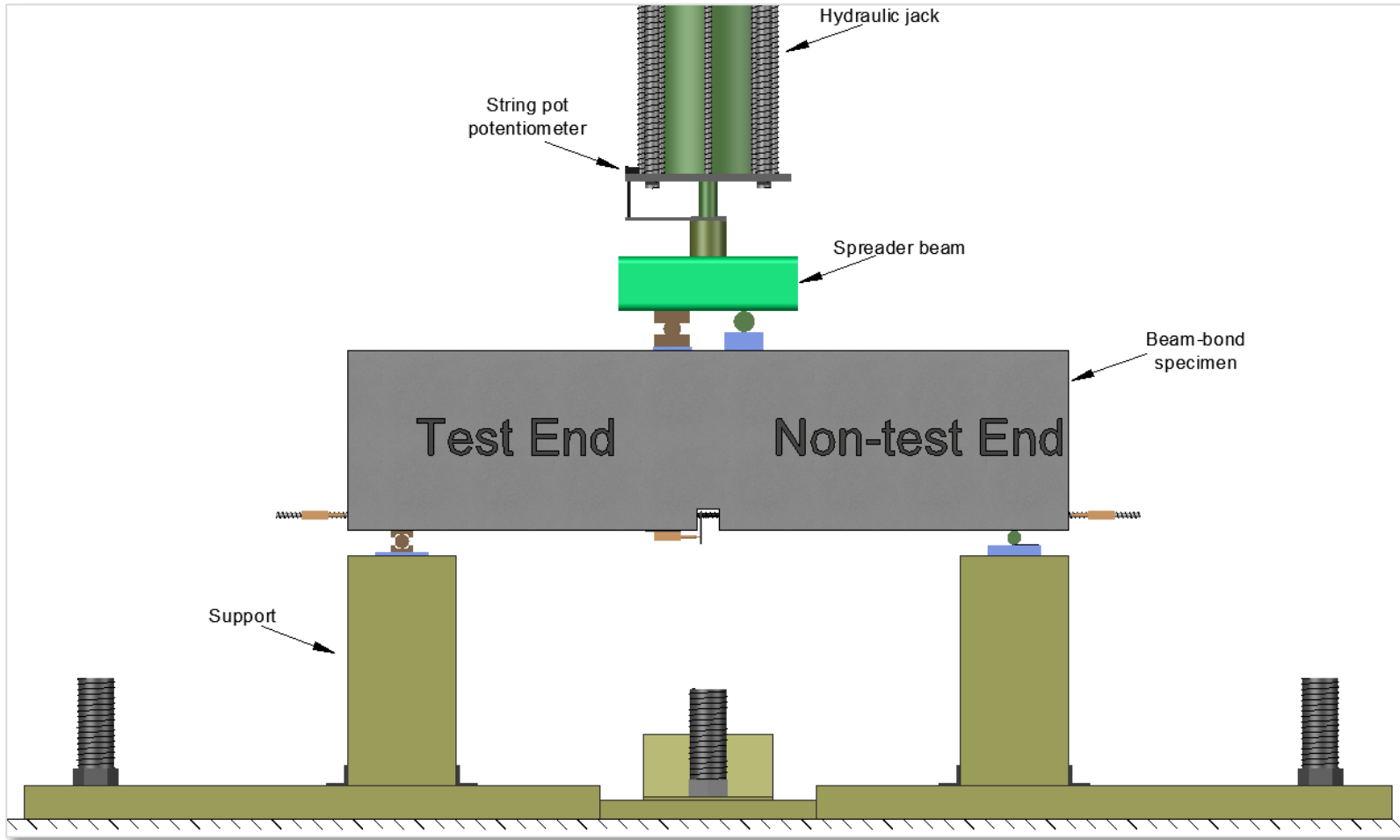


Figure 3:25: Test setup detail for the beam-bond specimens. View 1

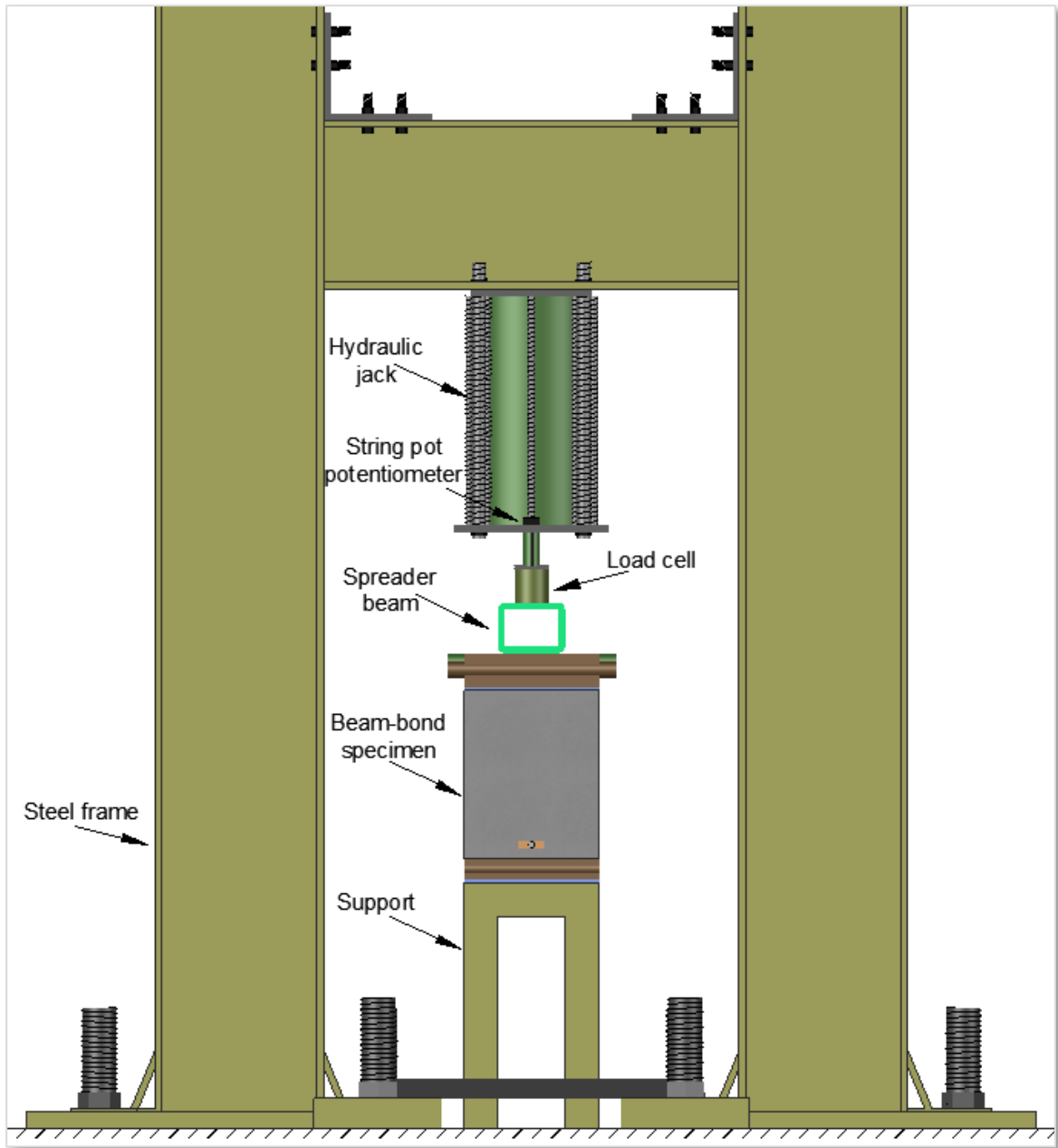


Figure 3:26: Test setup detail for the beam-bond specimens. View 2

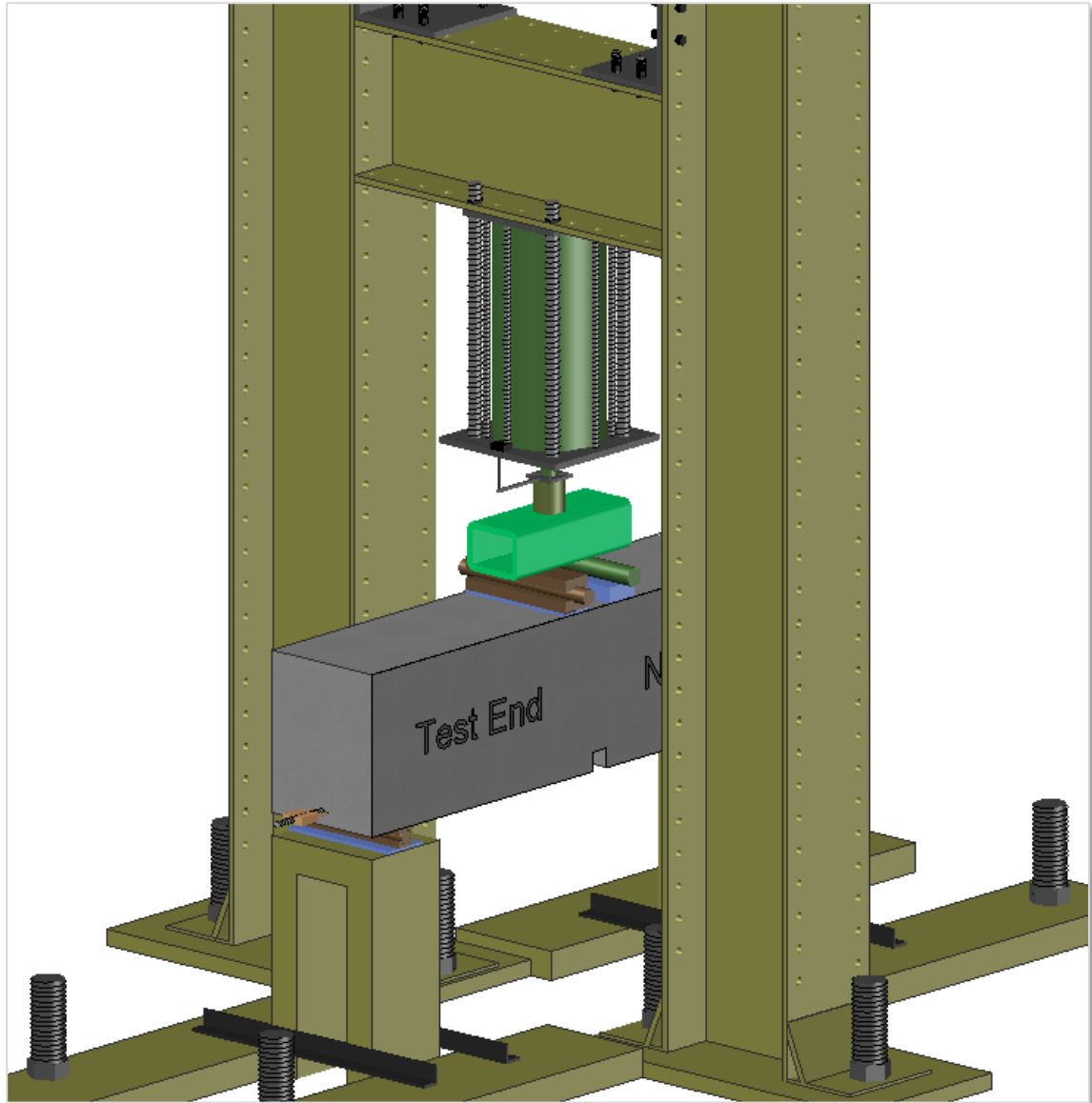


Figure 3:27: Test setup detail for the beam-bond specimens. View 3

The test setup for the Modified and Standard pullout specimens made use of a Universal Testing Machine and with reference to Figure 3:28 and Figure 3:29 involved first, positioning the specimen on the top stationary head of the machine and then gripping the steel pipe of the specimen via the bottom head and moving the bottom head downwards to load the specimen. Lastly, for further clarification, Figure 3:30 provides a 3D illustration of the test setup for the Modified pullout specimens and note that the setup for the Standard pullout specimens is identical.

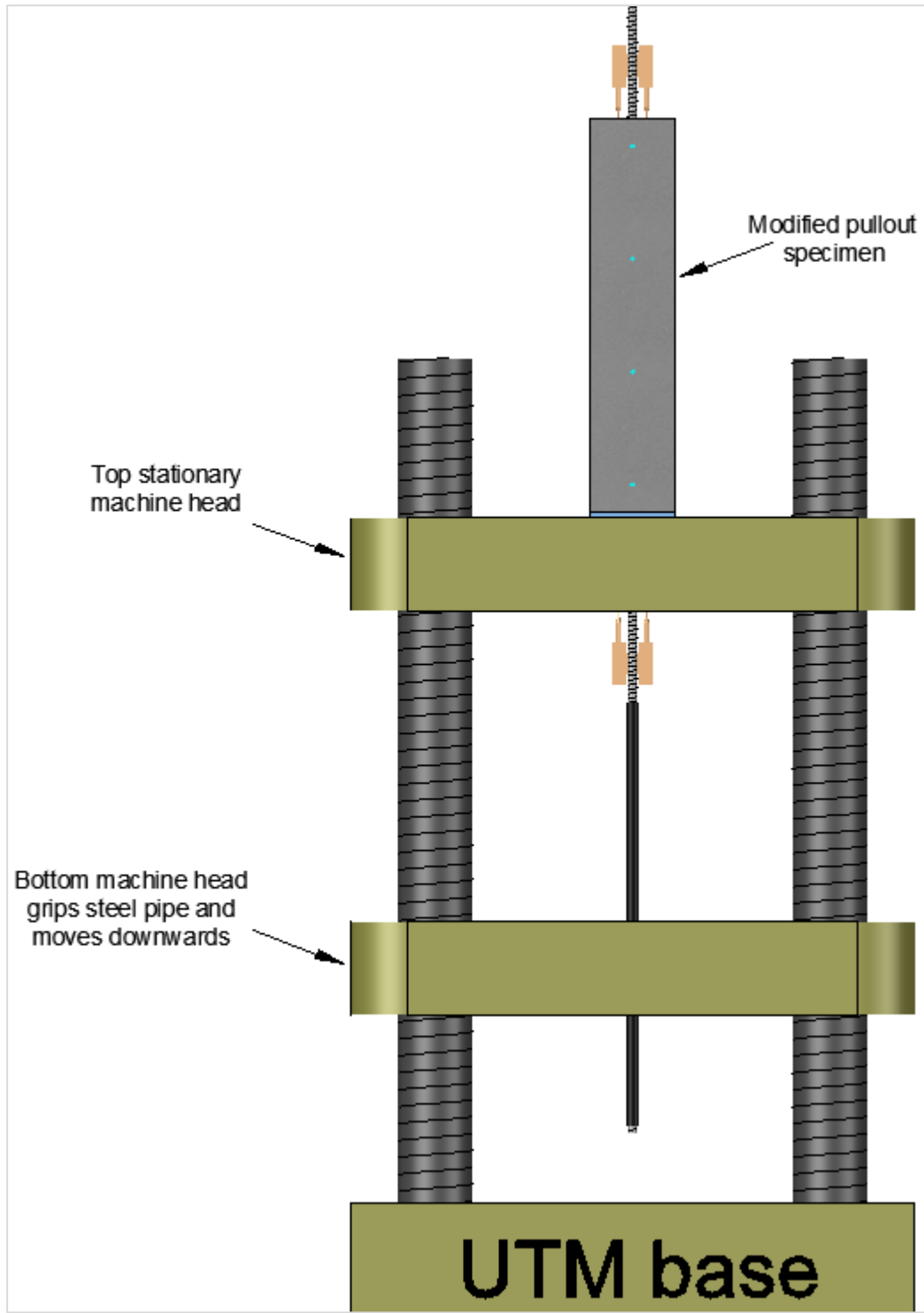


Figure 3:28: Test setup detail for the Modified pullout specimens

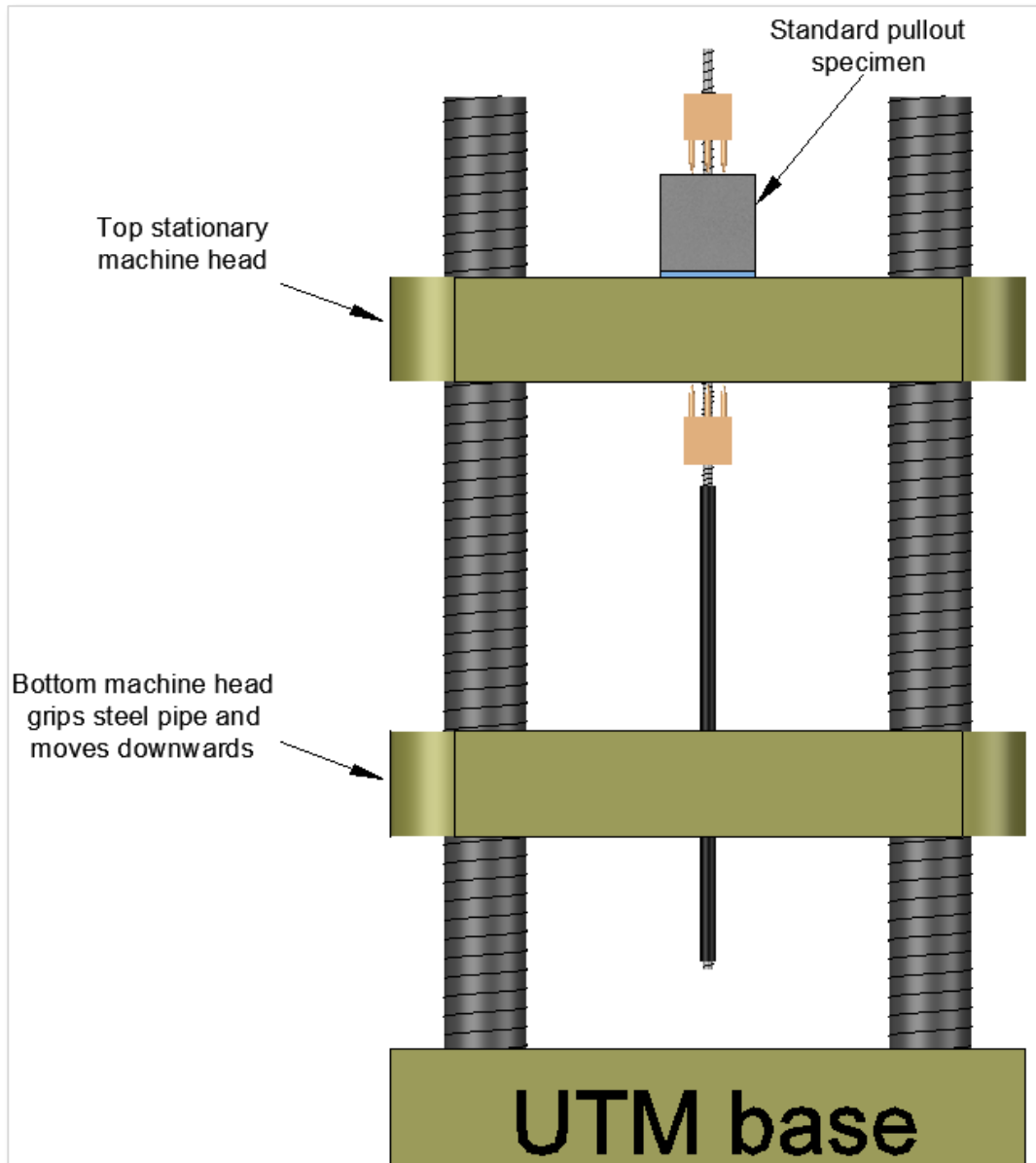


Figure 3:29: Test setup detail for the Standard pullout specimens

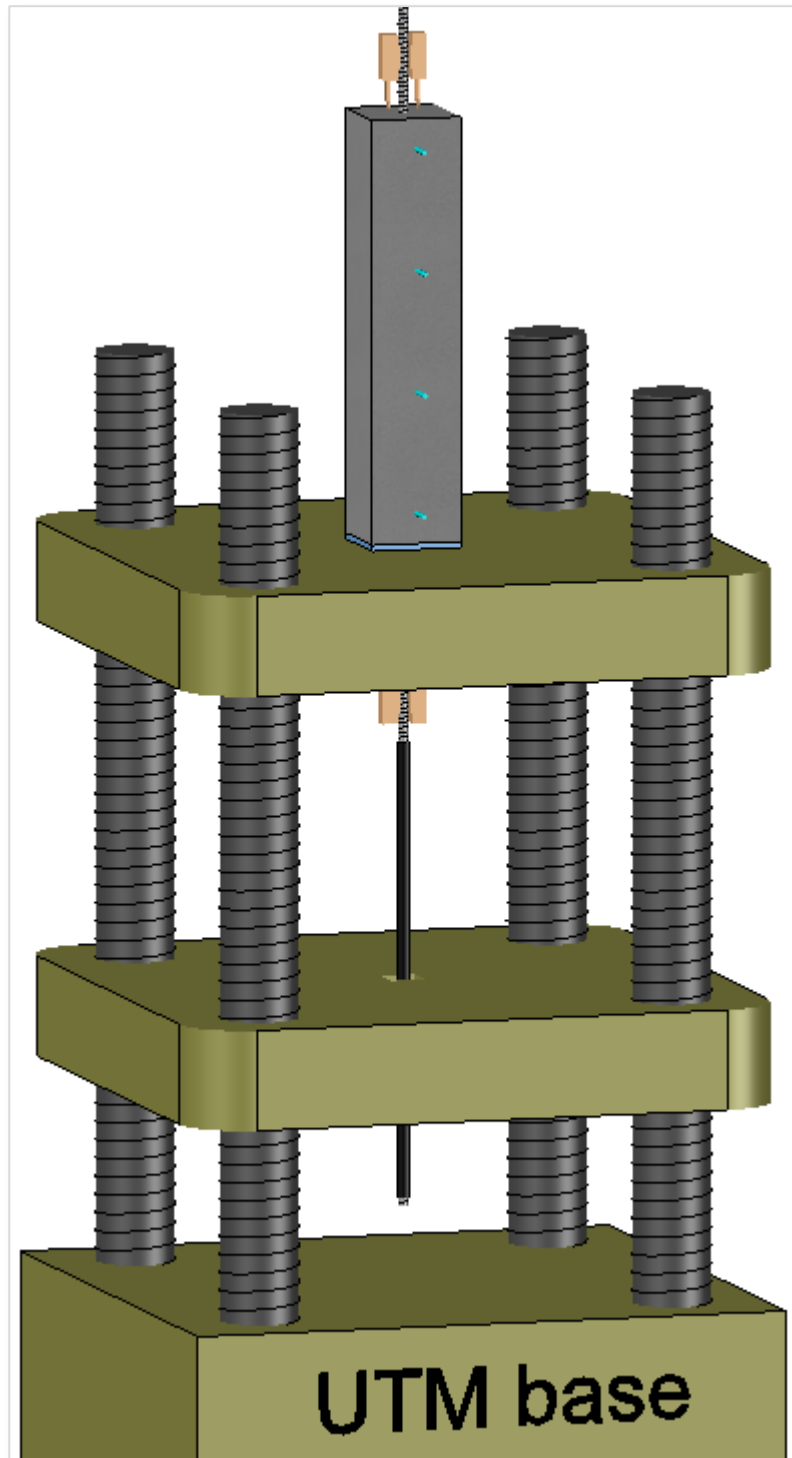


Figure 3:30: 3D illustration of the test setup for the Modified pullout specimens

3.6 Loading Rate and Data Acquisition

In terms of the beam-bond specimens, since the RILEM beams had the steel hinge at midspan, they were precracked at midspan and due to this fact, their testing involved displacement-control mode at a constant rate of 0.5 mm/min. up to beam failure. The testing of the Notched beams however, first, consisted of load-control mode at 5 kN/min. up to roughly the theoretical cracking load, followed by a switch to displacement-control mode at an initial rate of 1 mm/min. and subsequently decreasing to 0.5 mm/min. , at which point the loading rate remained constant up to beam failure. For the Modified and Standard pullout specimens, the loading rate, which, with reference to Figure 3:28 and Figure 3:29, corresponded to the rate at which the bottom machine head moved downwards, was 1.27 mm/min. and note that this value is equivalent to the maximum loading rate allowed by CSA S806, (2012), *Annex G*. Lastly, all of the specimens in this experimental program made use of a data acquisition system that gathered the output from the load cell, strain gauges, LVDTs as well as string pot potentiometers at a rate of once every 0.5 second.

Chapter 4 Experimental Results

4.1 General

The purpose of this section is to present the data gathered during the testing of the beams and the pullout specimens as well as to highlight important observations made during the tests. While the nominal diameter of the GFRP bar in this experimental program was 15 mm, for all of the specimens the actual diameter was approximately 14.8 mm and all subsequent calculations will use the actual GFRP bar diameter. The placement of strain gauges along the GFRP reinforcement bar allowed for the collection of information regarding the variation of bar strain from the loaded-end towards the unloaded-end. Concerning the beam-bond specimens, prior to the initiation of the testing, one face of each beam was painted white and a 100 × 100 mm grid was drawn on it to allow for monitoring of the location and propagation of any cracks formed during the test.

For ease of referencing Figure 3:20, which shows the placement of strain gauges along the GFRP reinforcement bar for both the beam-bond and the Modified pullout specimens, is reproduced and presented as Figure 4:1. Concerning the LVDT placements, as mentioned earlier, for the beam-bond specimens, L1 measured the loaded-end slip, L2 and L3 measured the unloaded-end slip at the “Test End” and L4 measured the unloaded-end slip at the “Non-test End” of the beams. For the Modified pullout specimens, L1 and L2 measured the unloaded-end slip while L3 and L4 measured the loaded-end bar slip. For the Standard pullout specimens, L1 to L3 measured the unloaded-end slip while L4 to L6 measured the loaded-end bar slip. For the beam-bond specimens, in terms of string pot potentiometers, as illustrated previously, SP1 measured the midspan deflection while SP2 and SP3, respectively, measured the deflection at 500 mm from the midspan towards the “Test End” and the “Non-test End” of the beams.

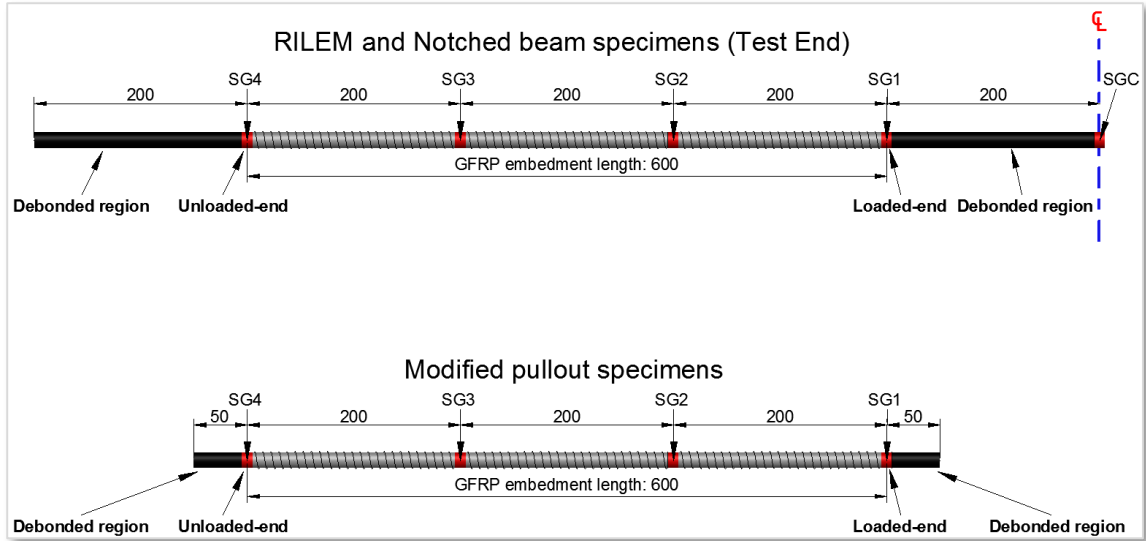


Figure 4:1: GFRP bar reinforcement strain gauge detail for RILEM and Notched beams (Test End), as well as for the Modified pullout specimens (All dimensions are in mm)

4.2 Results and Observations for RILEM Beams BR1 and BR2

4.2.1 Key Observations

For the RILEM beams, the moment arm is the distance between the centre of the steel hinge and the centre of the longitudinal GFRP reinforcement and as the beam deflects and the steel hinge rotates, the value of the original moment arm changes accordingly. However, since the changes in the moment arm are very subtle, the majority of past experimenters as well as the RILEM TC-RC5, (1994) recommendation simply assume a constant moment arm during the testing. For BR1, prior to the initiation of the test, the moment arm was 432.6 mm while for BR2, it was 428.6 mm and the reason for the difference, as Figure 4:2 illustrates, is the difference in the hydro-stone thickness on which the steel hinge was seated.

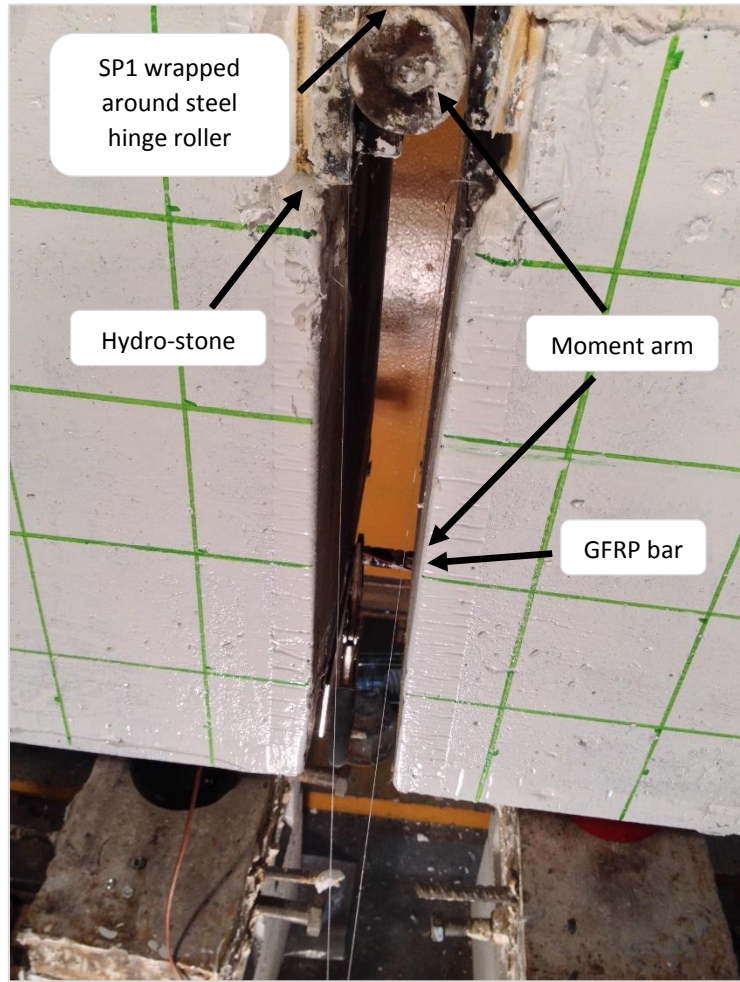


Figure 4:2 Moment arm determination of RILEM beams

Prior to the commencement of loading and data recording and during the process of placing the steel hinge and the appropriate instrumentation, the two half-beams were supported by hydraulic jacks since in the absence of a secured steel hinge at midspan, the two halves would collapse. As the loading was commenced, the jacks were removed once it was noticed that the two halves were fully engaged through the steel hinge. However, the recording by the data acquisition system began prior to the removal of the two jacks.

BR1 in Figure 4:3, experienced a primarily flexural crack at an observed load of 153.5 kN , corresponding to a maximum moment of $57.6 \text{ kN} \cdot \text{m}$. The crack, which initiated at the beam bottom, spanned 250 to 330 mm horizontally from the centre of the beam towards the “Non-test End” and was 250 mm high as Figure 4:4 illustrates.

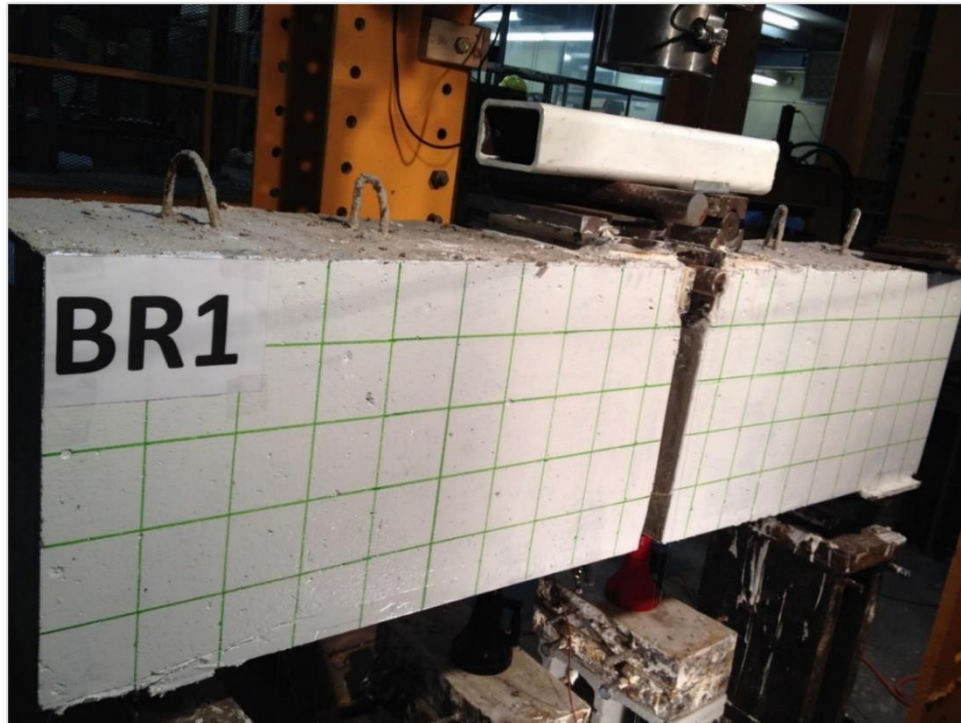


Figure 4:3: BR1 before the test



Figure 4:4: BR1 at failure

The propagation and widening of the crack after its initial occurrence was minimal and not noticeable to the naked eye. No other crack formed for the remainder of the test,

which lasted until a maximum load of approximately 206.0 kN , or equivalently, a maximum moment of $77.2\text{ kN} \cdot \text{m}$ and a corresponding midspan deflection of 15.1 mm . The maximum moment corresponded to the sudden rupture of the majority of the fibres in the GFRP longitudinal reinforcement, after which, the load began to precipitously decline.

BR2 did not experience any cracking during the entire loading process up to failure by GFRP bar rupture and Figure 4:5 and Figure 4:6 show the state of the beam before and after the testing. The maximum load reached in this beam was 194.0 kN , which corresponds to a maximum moment of $72.8\text{ kN} \cdot \text{m}$ and a midspan deflection of 13.9 mm , after which, the GFRP bar ruptured and there was a drastic decline in the load.

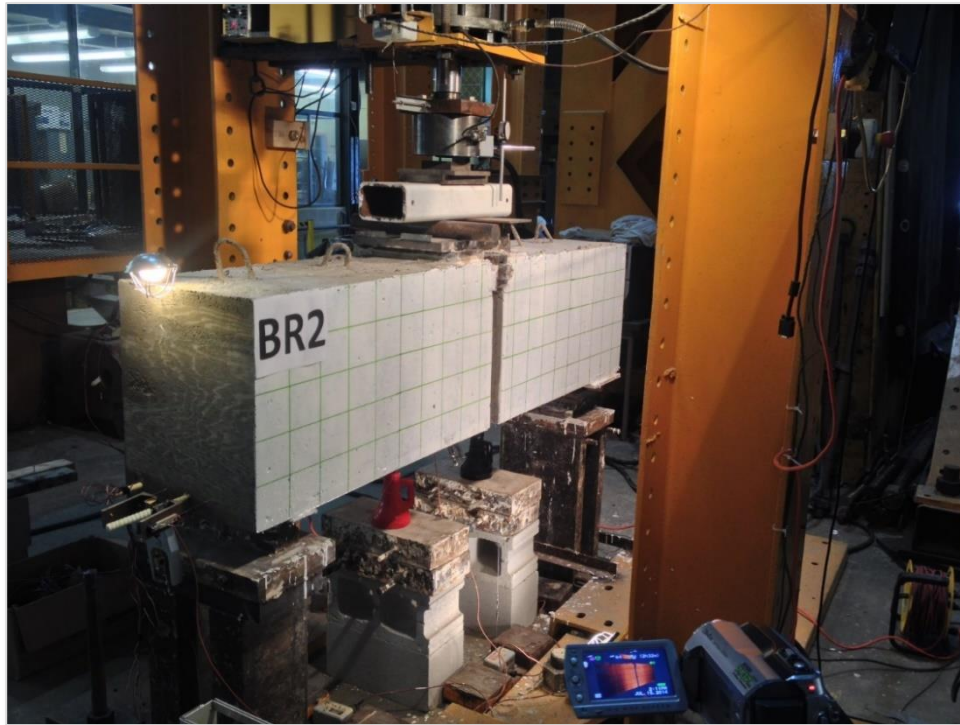


Figure 4:5: BR2 before the test

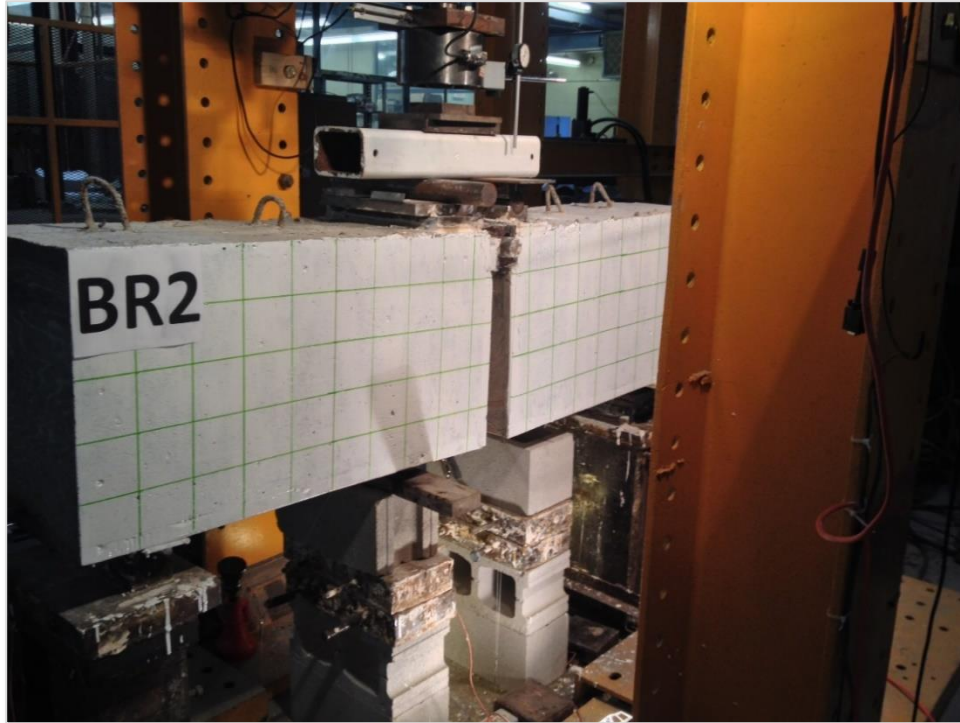


Figure 4:6: BR2 at failure

4.2.2 Load-deflection Behaviour

Figure 4:7 presents the load versus midspan deflection curve for BR1 and BR2, and note that for both beams, there is a steady non-linearity from the very beginning of the test. As neither concrete nor FRP behaves nonlinearly at low load or stress levels, the observed nonlinearity could only be ascribed to the change in the moment arm at midspan, caused by the relative vertical movement of the hinge centre and the centroid of the GFRP bar cross-section. In addition, the formation of the flexural crack in BR1, leads to a small drop in load, but subsequently the load-deflection curve for this beam returns to its original path and continues on that path until failure.

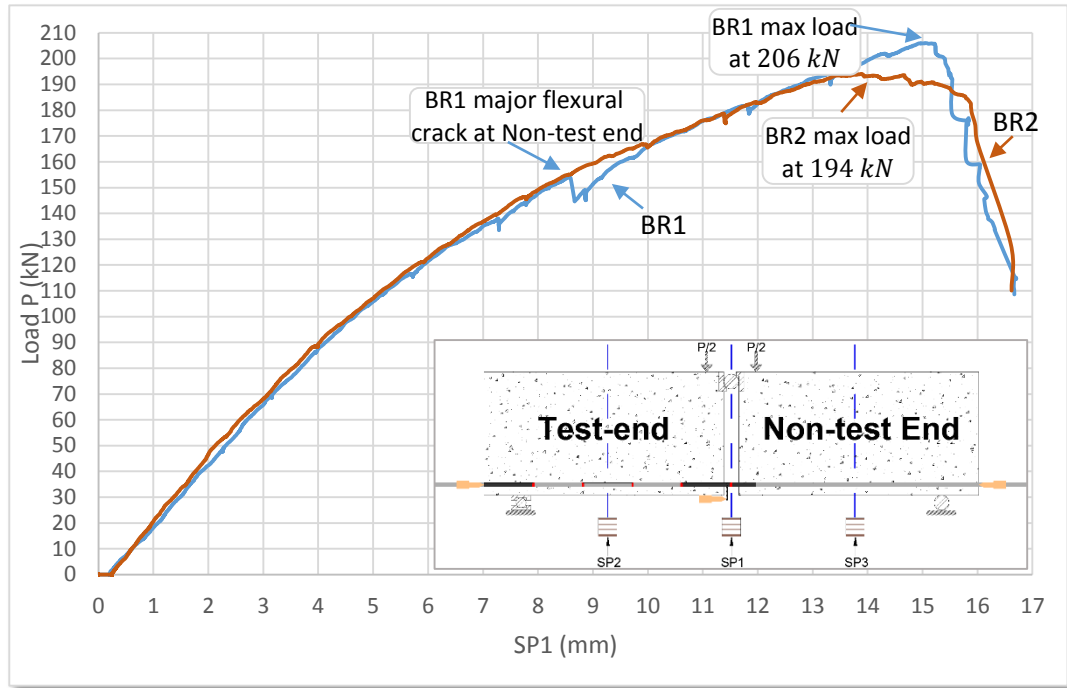


Figure 4:7: Load-midspan deflection in BR1 and BR2

Figure 4:8 presents a plot of the deflection for the RILEM beams along their length at different stages of their respective failure load and from this figure one can observe that overall, the behaviour of the beams, particularly with increasing loads, were symmetric with respect to the midspan centreline.

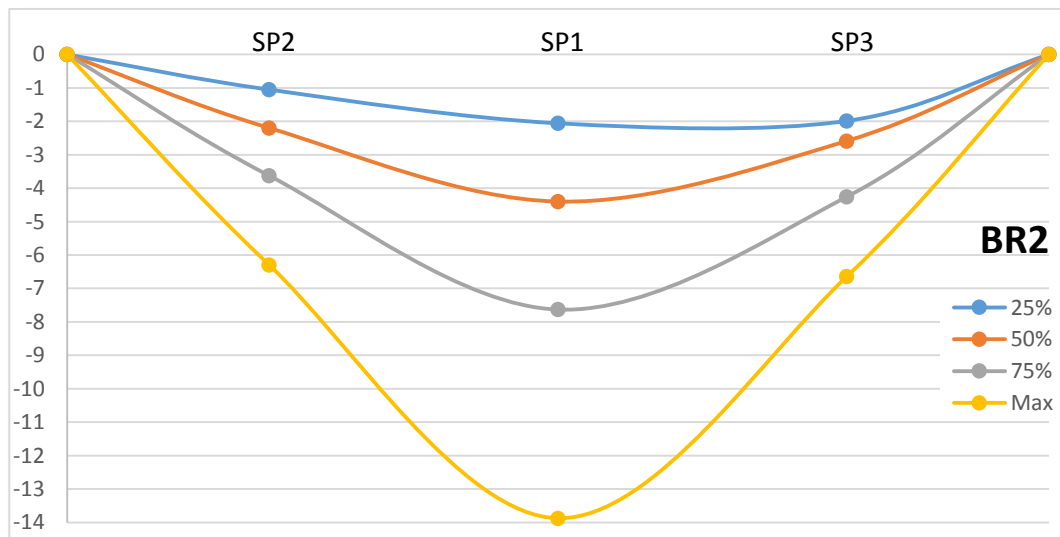
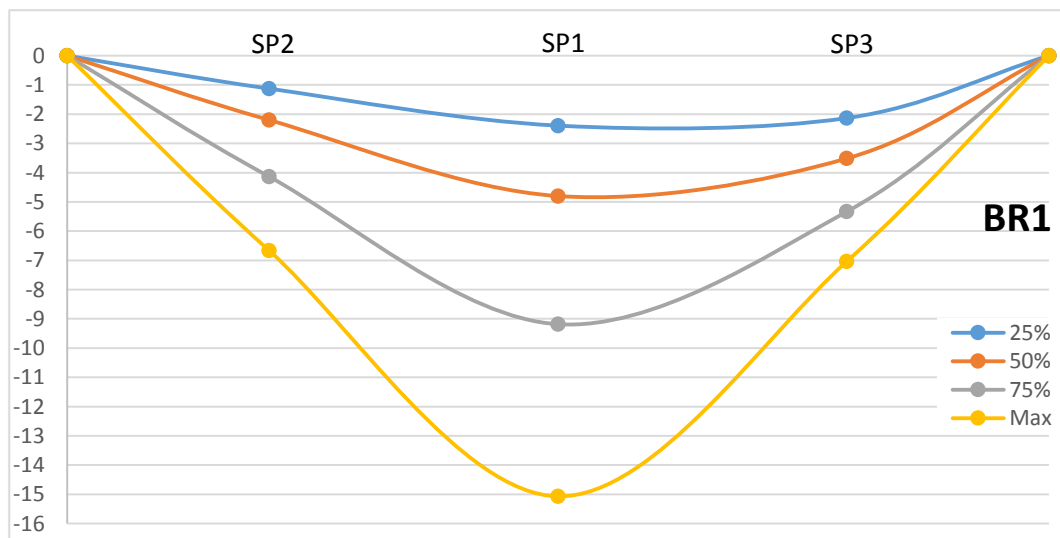
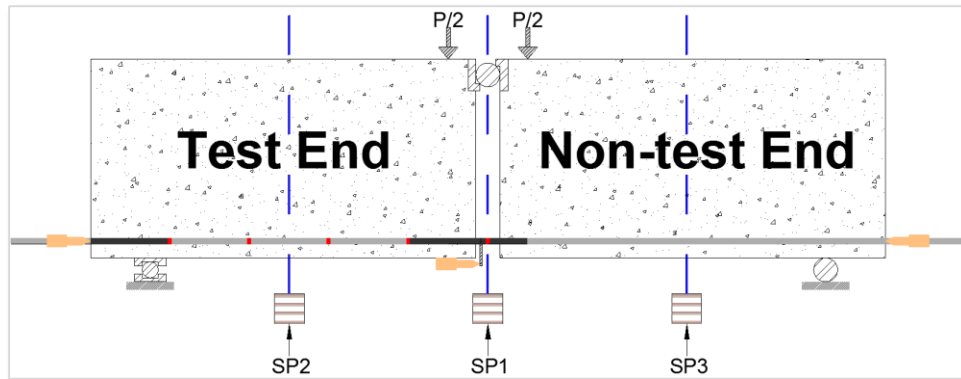


Figure 4:8: Deflection along BR1 and BR2 at different percentages of their respective maximum load, P

4.2.3 GFRP Bar Strain

Figure 4:9 shows the variation of load versus the strain in the GFRP bar for BR1 and BR2 up to their respective beam failure load. Since the portion of the GFRP bar between SGC and SG1 is unbonded, as expected, for both beams, their respective strain readings by SGC and SG1 are practically identical up to the point where both gauges were functioning. Furthermore, SGC and SG1 readings show that the load-strain relationship is almost linear. Concerning BR1, note that at a load of 128 kN , which corresponds to approximately 62% of the beam failure load, BR1-SGC readings jumped from 9,442 to $71,542,050\ \mu\text{ strain}$ indicating gauge failure and thus, the figure does not show BR1-SGC readings beyond 128 kN . The perturbation in BR1-SG1 readings occurred at practically the same time as BR1-SGC stopped functioning, but BR1-SG1 subsequently continued to record strain until failure. For BR2, at a load of approximately 145 kN , corresponding to 75% of the beam failure load, SGC began exhibiting a high degree of non-linearity while SG1 strain readings experienced a sudden decrease followed by constant readings despite increases in load, which indicates gauge failure. For both beams, note that the SG4 values are practically zero throughout the loading process and this means that the provided bond length was adequate to allow the GFRP bar to reach its rupture.

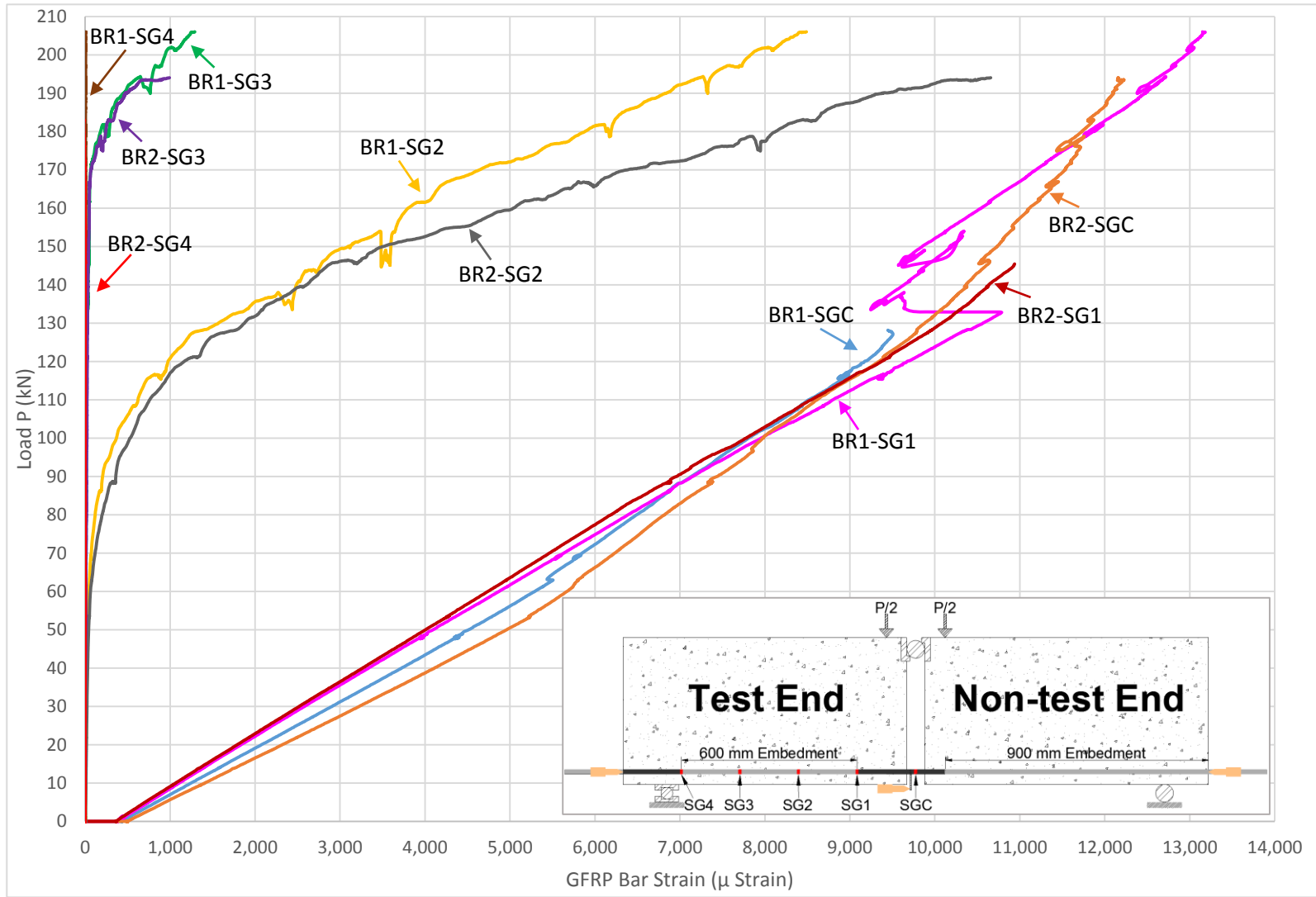


Figure 4:9: Load-GFRP bar strain in BR1 and BR2

4.2.4 GFRP Bar Slip

Figure 4:10 shows a plot of the load versus the loaded-end bar slip for both beams up to their respective beam failure load. Note that this plot does not account for the elastic elongation that occurs between the point of L1 attachment and the position of SG1. The correction for this elastic elongation is discussed in Section 5.8, however Figure 4:10 does serve the purpose of showing the slip pattern and an uncorrected loaded-end slip value of 9.6 mm for BR1 and 8.7 mm for BR2 at their respective beam failure load. For both beams, L2, L3 and L4 did not show any slip for the duration of the test and this indicates that the provided GFRP bar embedment length was in fact sufficient to prevent pullout failure.

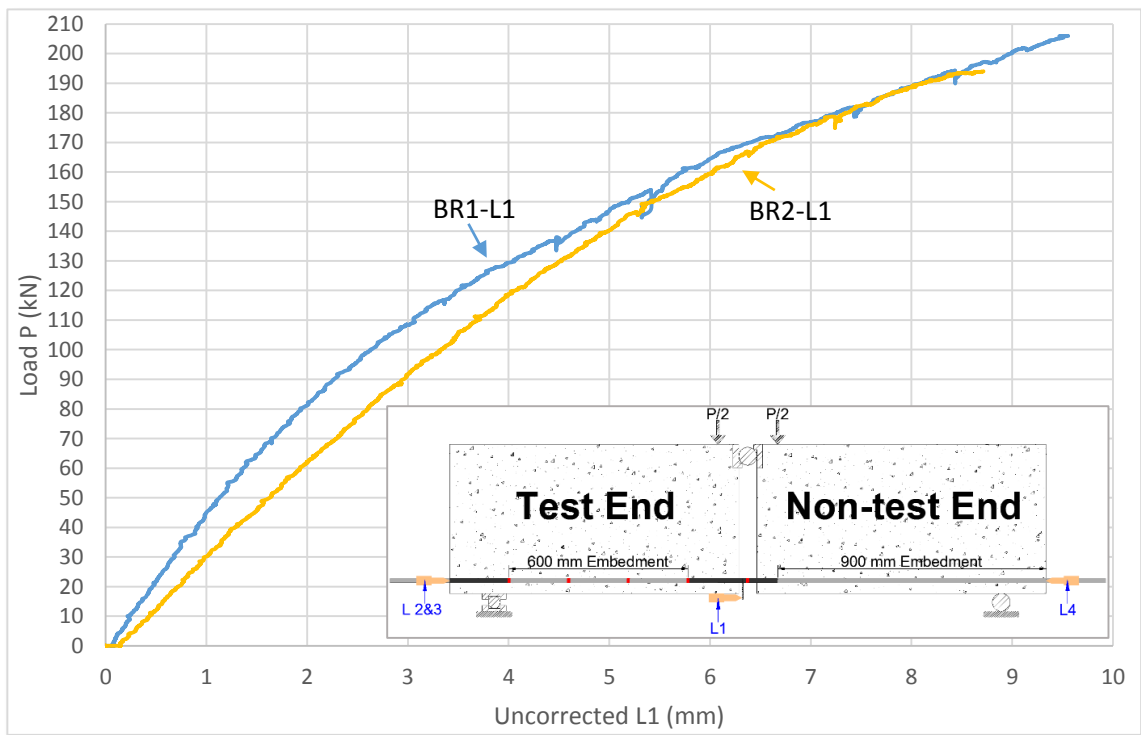


Figure 4:10: Load-uncorrected L1 bar slip in BR1 and BR2

4.2.5 Post-test Inspection

For both RILEM beams, after the completion of the test, the GFRP bar in the maximum moment region and a portion beyond was exposed and the stirrups were cut in order to allow full inspection of the bar. Figure 4:11 shows the “Test End” of BR1 where the taped region along the GFRP bar is the unbonded section and Figure 4:12 is the GFRP bar with the tapes removed and the portions where it was evident that a significant amount of GFRP fibres had disengaged from the core, highlighted with a black marker. In a similar manner, Figure 4:13 and Figure 4:14 show the “Non-test End” of BR1 and note from Figure

4:14 that upon the removal of the tapes, a large portion of the exterior GFRP fibres completely detached from the bar core. Concerning BR2, Figure 4:15 shows the “Test End” with the tapes over the unbonded portion and Figure 4:16 is the GFRP bar with the tapes removed, showing GFRP fibre disengagements as highlighted. Figure 4:17 and Figure 4:18 present the “Non-test End” of BR2 and one can observe that the GFRP bar within the constant moment region had severe damage to its exterior fibres and core. From these figures, it is evident that the rupture of the GFRP bar occurred primarily within the constant moment region; furthermore, the damage on the GFRP bar was more heavily concentrated in the “Non-test End” of the beams.



Figure 4:11: BR1 “Test End”



Figure 4:12: BRI, "Test End". Marked lines on GFRP bar indicate observance of significant fibre disengagement



Figure 4:13: BRI "Non-test End"



Figure 4:14: BR1 “Non-test End”. Showing the damage and rupture experienced by the GFRP bar

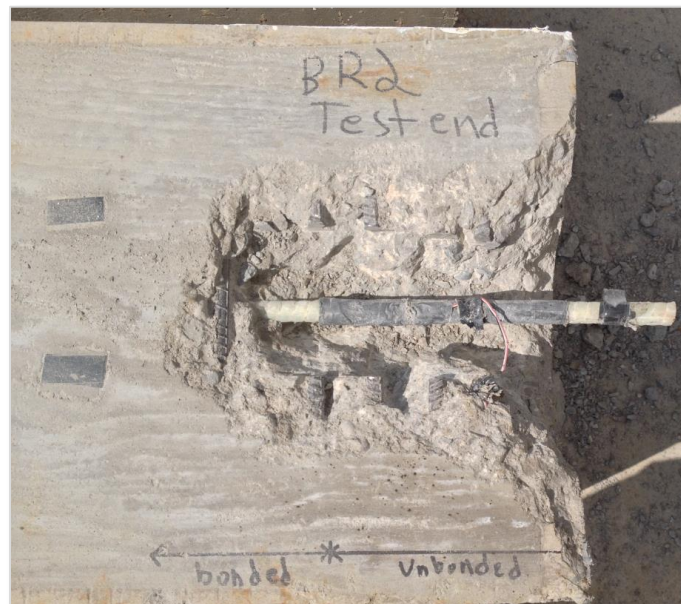


Figure 4:15: BR2 “Test End”

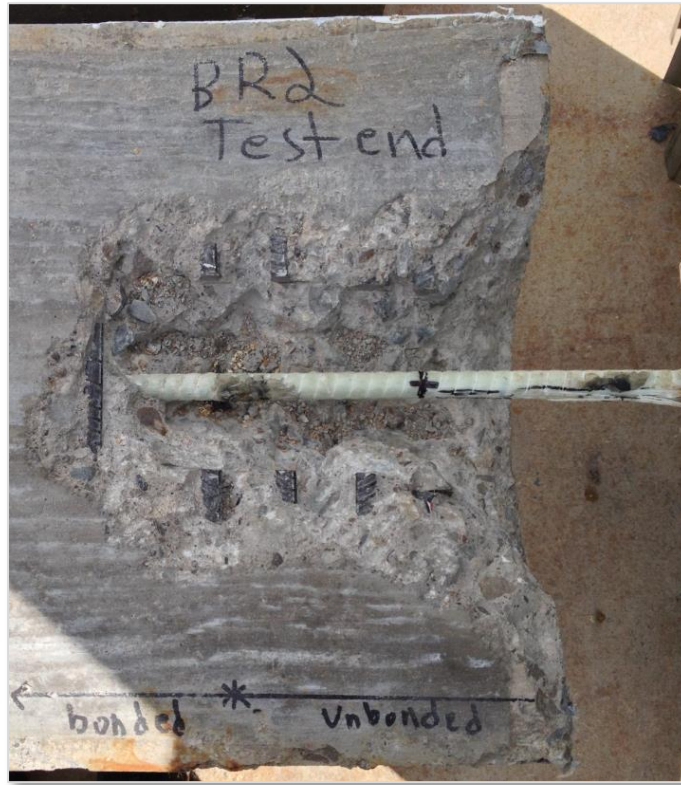


Figure 4:16: BR2, “Test End”. Marked lines on GFRP bar indicate observance of significant fibre disengagement



Figure 4:17: BR2 “Non-test End”



Figure 4:18: BR2 “Non-test End”. Showing the damage and rupture experienced by the GFRP bar

4.3 Results and Observations for Notched Beams BN1 and BN2

4.3.1 Key Observations

Although strictly not necessary in the case of the Notched beams, they were, similar to the RILEM beams, supported by jacks prior to the application of load but the data recording was commenced before removing the jacks. BN1 in Figure 4:19 was loaded up to a value of approximately 107.0 kN or equivalently, a moment value of $40.1 \text{ kN} \cdot \text{m}$, at which point, as Figure 4:20 illustrates, a major flexural crack appeared at the edge of the notch towards the “Test End” side of the beam. The crack initiated at the beam bottom and this is likely due to stress concentrations caused by the notch. The immediate vertical extension of the flexural crack was profound such that roughly 50 mm of uncracked concrete remained between the end of the crack and the top of the beam, however, the

propagation and widening of this crack for the remainder of the test was minimal and unnoticeable by the naked eye.

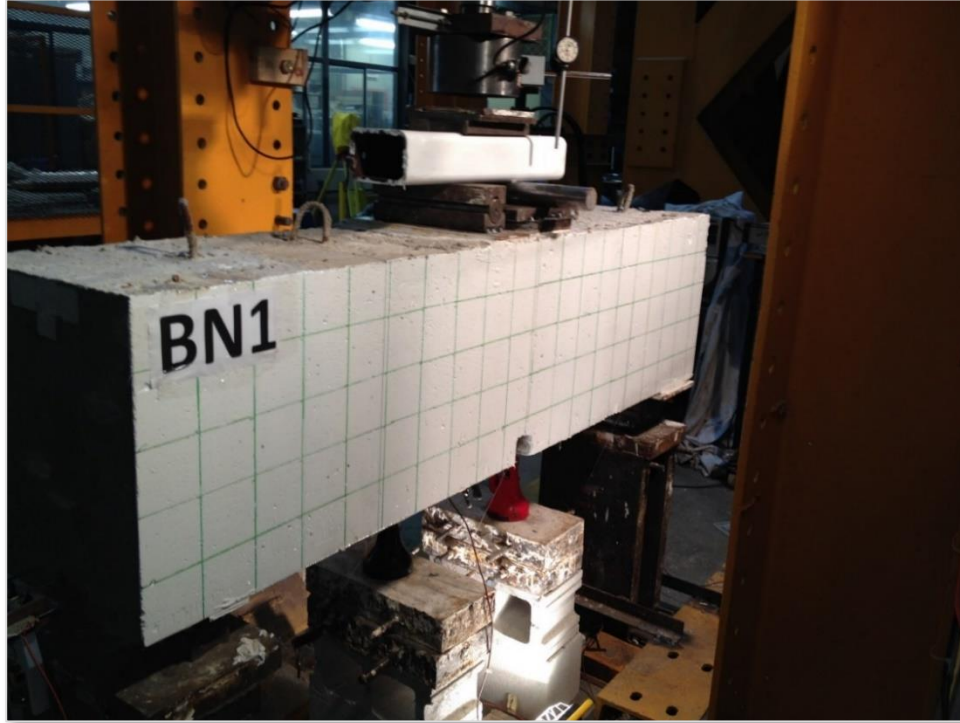


Figure 4:19: BN1 before the test



Figure 4:20: BN1 after the first flexural crack

No other cracks were visible until a load of approximately 178.0 kN , corresponding to a moment of $66.8\text{ kN} \cdot \text{m}$, when a second flexural crack appeared with a relatively small inclination from the vertical. The location of this crack, as Figure 4:21 illustrates, extended 200 to 340 mm horizontally from the midspan of the beam towards the “Non-test End” and was approximately 420 mm high. With reference to Figure 4:21, note that at the time of the occurrence of the second crack, there was a noticeable widening of the first crack, particularly near its top portion. The loading was continued, without the occurrence of any other crack, until a maximum value of 213.9 kN , or equivalently maximum moment of $80.2\text{ kN} \cdot \text{m}$ and a corresponding midspan deflection of 13.7 mm was reached, at which point the GFRP bar experienced sudden rupture with a characteristic audible noise. After the rupture of the GFRP bar, the load value began decreasing drastically and Figure 4:22 shows the state of the beam at failure.



Figure 4:21: BN1 after the second flexural crack

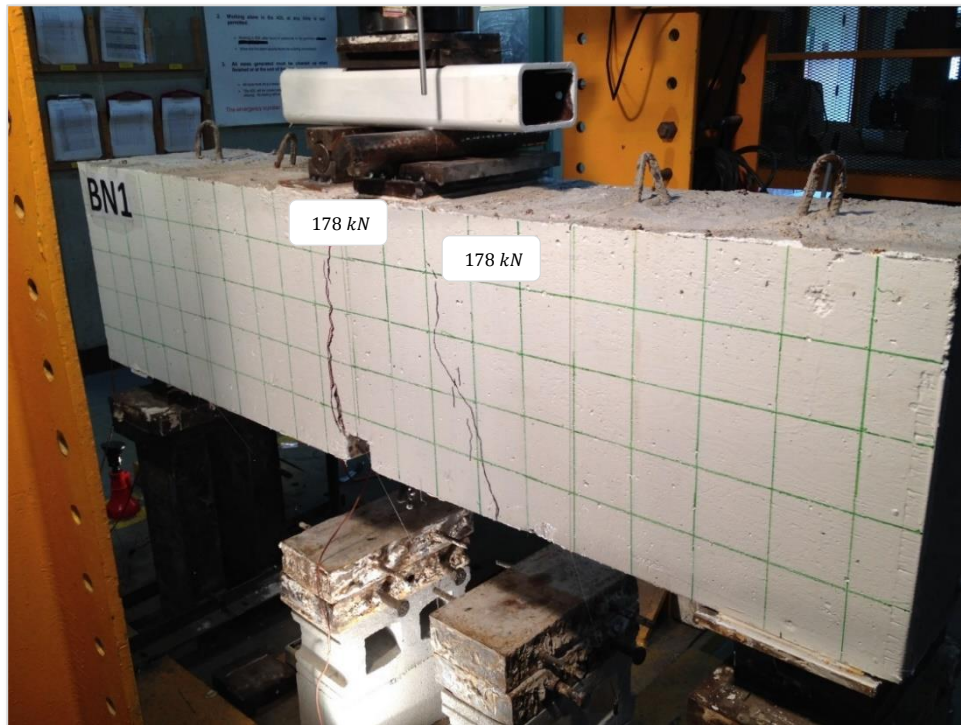


Figure 4:22: BN1 at failure

Concerning BN2 in Figure 4:23, the loading continued up to an observed value of 104.0 kN , or equivalently $39.0\text{ kN} \cdot \text{m}$, at which point a flexural crack occurred at the edge of the notch towards the “Non-test End” side of the beam as Figure 4:24 illustrates. The vertical extension of this crack was substantial since approximately 40 mm of uncracked concrete remained between the end of the crack and the top of the beam and in addition, this crack did not have a noticeable propagation nor widening for the remainder of the test.

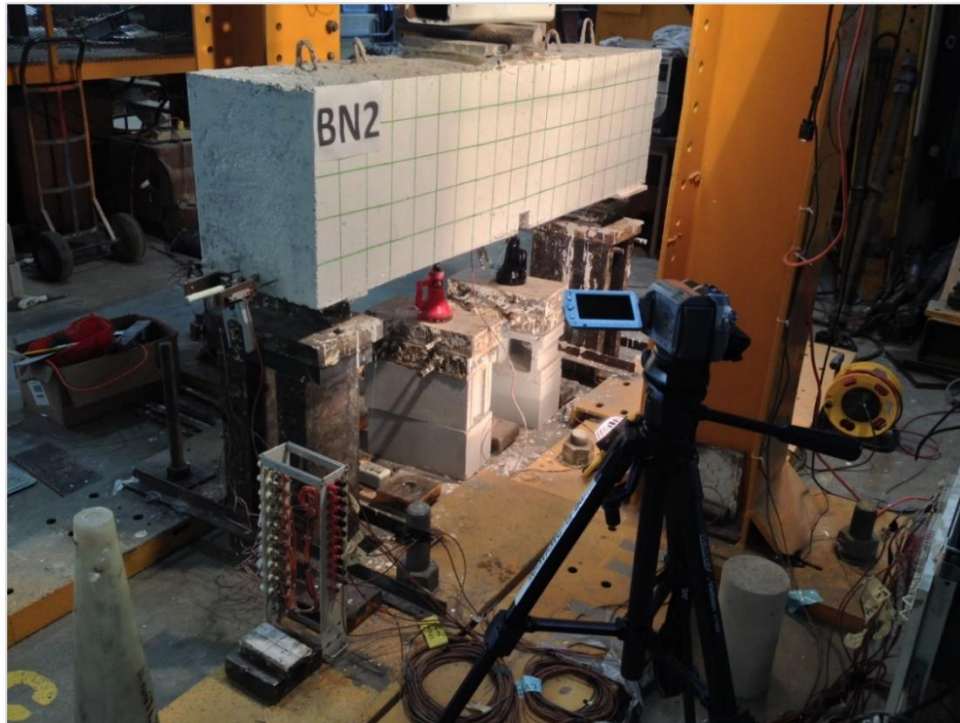


Figure 4:23: BN2 before the test



Figure 4:24: BN2 after the first flexural crack

After the occurrence of this flexural crack, no additional cracking occurred until a load of approximately 163.0 kN or a corresponding moment of $61.1\text{ kN} \cdot \text{m}$, when a second flexural crack occurred. Figure 4:25 shows this crack, which spanned a horizontal distance between 210 to 340 mm from the beam midspan towards the “Non-test End” and had an approximate vertical extension of 430 mm . Figure 4:26 shows the failure state of the beam, which was by GFRP bar rupture at a maximum load of 221.3 kN , or equivalently, a maximum moment of $83.0\text{ kN} \cdot \text{m}$ and a corresponding midspan deflection of 15.4 mm .

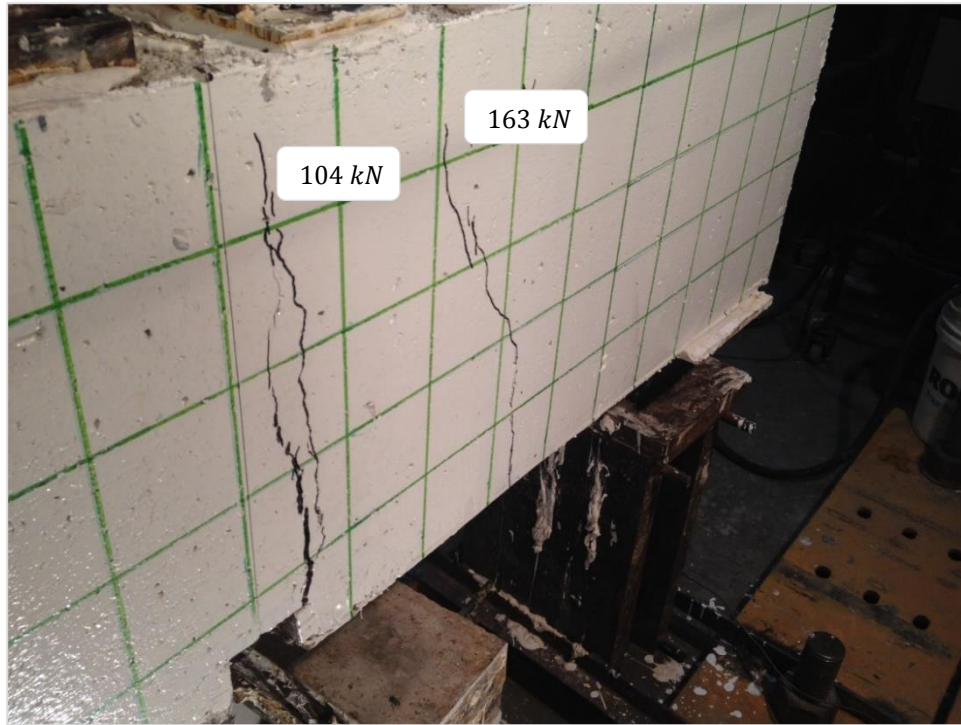


Figure 4:25: BN2 after the second flexural crack

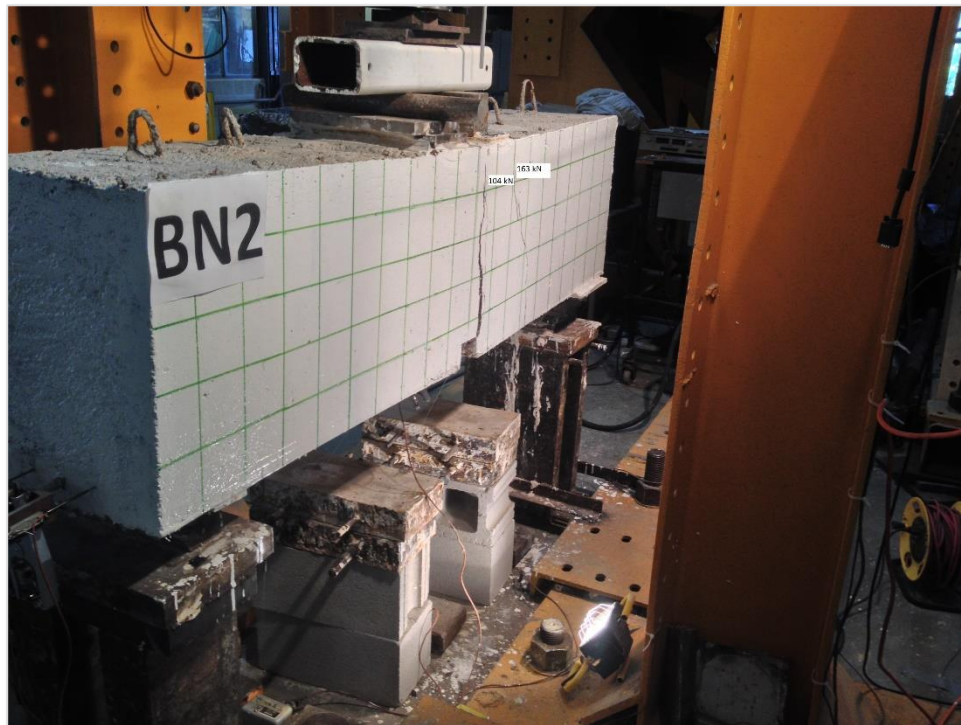


Figure 4:26: BN2 at failure

4.3.2 Load-deflection Behaviour

Figure 4:27 shows the load-midspan deflection curve for BN1 and BN2 that is typical of FRP reinforced concrete members. With the advent of each crack, the beam loses some stiffness while between cracking events its stiffness remains basically constant. Clearly, the major event is the formation of the first major flexural crack which leads to a severe reduction in stiffness and a drastic increase in displacement. It has to be emphasized that due to the relatively small elastic modulus of GFRP and the presence of only one 15 mm nominal diameter bar, the cracked beam moment of inertia is a tiny fraction of its uncracked moment of inertia, thus cracking, engenders drastic increase in beam displacement. In addition, it is interesting to observe that the degree of nonlinearity between the first and second major flexural cracks in BN1 and BN2 is smaller compared to the overall nonlinearity of the load-midspan deflection curve for the RILEM beams.

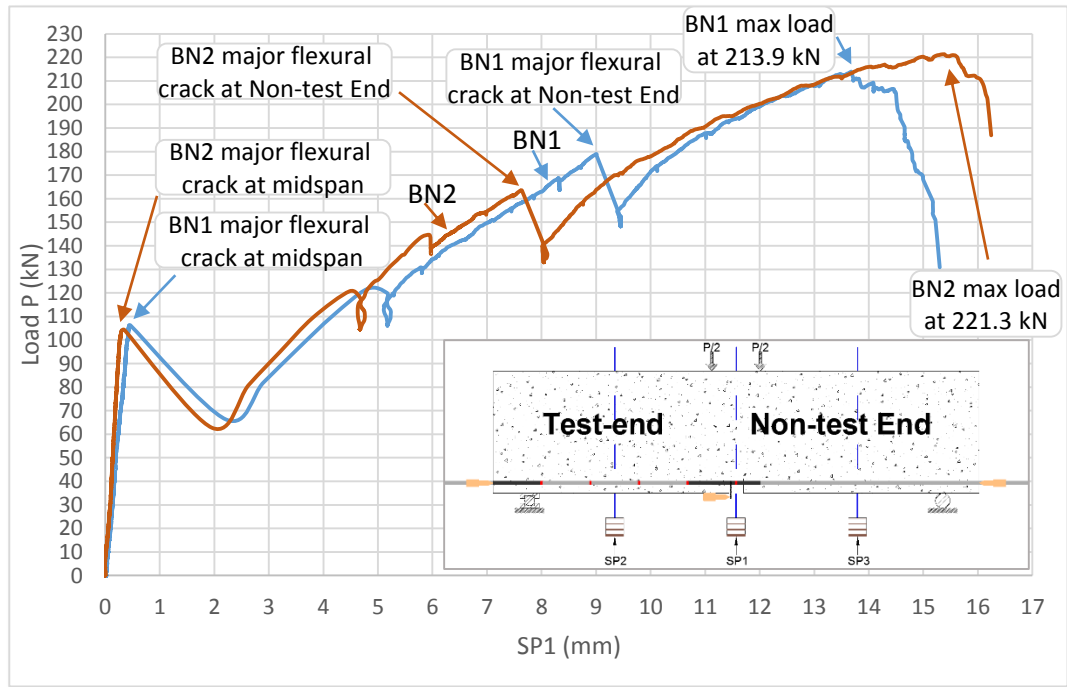


Figure 4:27: Load-midspan deflection in BN1 and BN2

With reference to Figure 4:28, which is a plot of the deflection along the Notched beams at various stages of their respective failure load, it is evident that throughout the testing, the deflected shape of these beams with respect to the midspan centreline was symmetric. Note from this figure that at 25% of their respective P_{max} , both Notched beams were uncracked and thus their deflections along the beam are negligible and this is in contrast to the behaviour of the RILEM beams, which did not benefit from the presence of concrete continuity at midspan. In Figure 4:28, for BN1 at 25% of P_{max} , there is no value

for SP3 since this string pot potentiometer behaved somewhat erratically at low loads but stabilized as the loading increased.

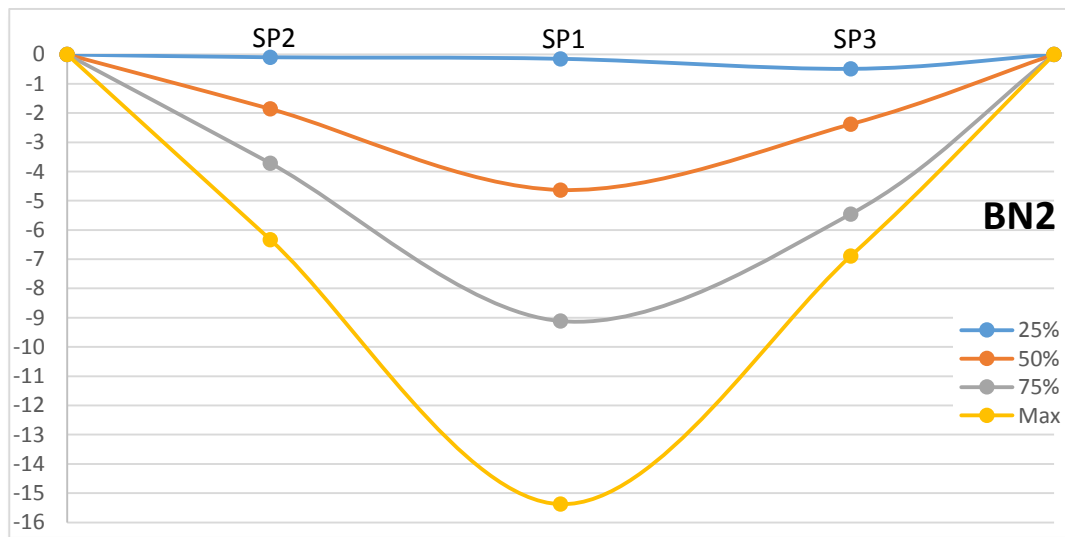
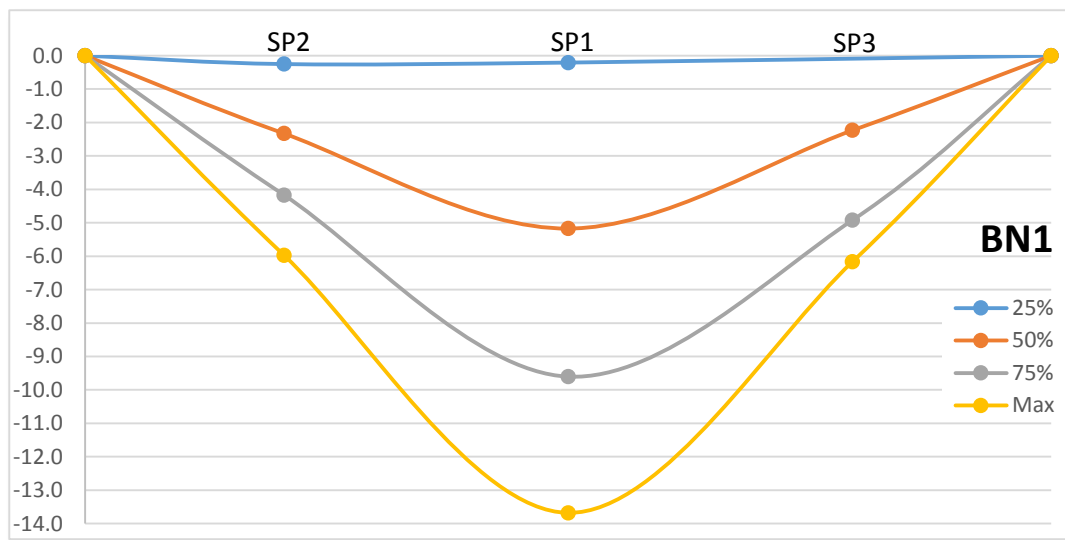
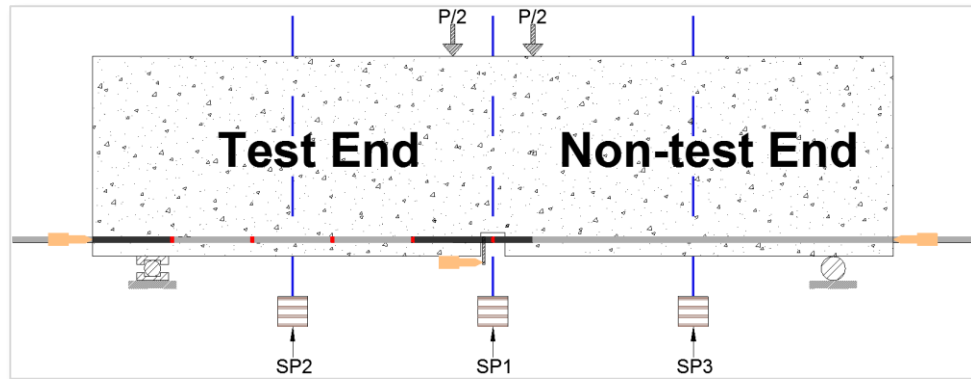


Figure 4:28: Deflection along BN1 and BN2 at different percentages of their respective maximum load, P

4.3.3 GFRP Bar Strain

Figure 4:29 is a plot of load versus the variation in bar strain for both Notched beams up to their respective beam failure load and note the difference between the behaviour of SGC and SG1 in these beams as opposed to the RILEM beams presented earlier in Figure 4:9. In the RILEM beams, the load-strain diagram revealed that with increasing load, SGC and SG1 values increased in a relatively linear fashion from the beginning to the end of the test without a significant change in slope. The reason for this behaviour is that, by design, the entire compressive force was concentrated on the steel hinge at the top of the beam while the tensile force had to go through the longitudinal GFRP reinforcement at the bottom. In the case of the Notched beams, in the uncracked beam, concrete resists nearly all the tension and the contribution of the GFRP bar, as Figure 4:29 illustrates, is practically negligible. Hence, for the Notched beams, there is an expectation of a change in the slopes of load versus SGC and SG1 before and after the occurrence of the major flexural crack near midspan. As mentioned earlier, the extent of this crack was severe such that BN1 had roughly 50 mm while BN2 had 40 mm of uncracked concrete remaining in the top portion of the beam. Thus, one can conclude that after the major flexural crack near midspan, the behaviour of the Notched beams will resemble the RILEM beams since the entire compressive force will act within a relatively small uncracked concrete section at the top, while the tensile force will be resisted, solely, by the longitudinal GFRP reinforcement at the bottom of the beam.

In general, at the location of a crack, there can be a significant jump in strain values since the effect of tension-stiffening brought on by the concrete practically disappears and the longitudinal reinforcement must solely resist the tensile force. For the Notched beams, unfortunately, as Figure 4:29 illustrates, almost immediately after the major flexural crack near midspan, SGC and SG1 experienced failure. The reason for this failure is most likely the inability of the delicate surface strain gauges to withstand the sudden shock and energy release caused by the crack formation. For BN2-SGC, note that strain values beyond the load of 140 kN, or equivalently, 63% of the beam failure load, quickly increased to 66,481,210 $\mu strain$. Similarly, for BN2-SG2, only strain readings up to a load of approximately 205.8 kN, which corresponds to 93% of the beam failure load are shown since beyond this point, the strain gauge failed as its readings suddenly increased from 10,585 to 79,725,550 $\mu strain$.

For BN1, SG2, SG3 and SG4 and for BN2, SG3 and SG4 remained functional until the end of the test. Lastly, it can be seen that the bar strain at the location of SG4 is practically zero throughout the loading process of both beams and this means that the provided bond length is adequate to allow the GFRP bar to rupture, without experiencing pullout.

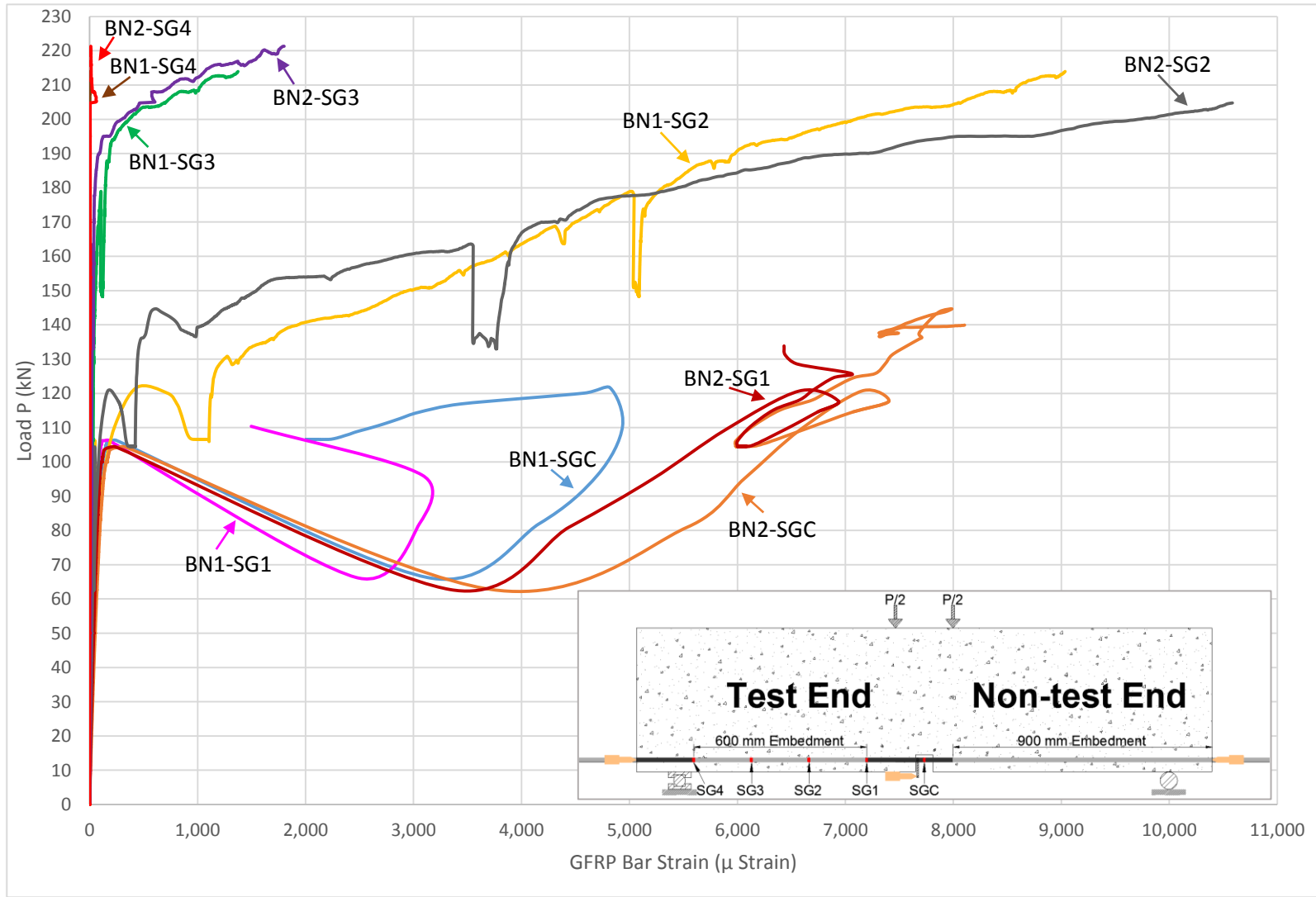


Figure 4:29: Load-GFRP bar strain in BN1 and BN2

4.3.4 GFRP Bar Slip

Figure 4:30 is a plot of load versus the uncorrected loaded-end bar slip for BN1 and BN2 up to their respective beam failure load and note that for BN1-L1, the midspan flexural crack caused a partial detachment of the gripping mechanism for this LVDT. BN2 however, did not experience a failure of its L1 and produced an uncorrected loaded-end bar slip value of 10.5 mm at the beam failure load. Lastly, for both Notched beams, L2, L3 and L4 did not show any slip readings for the duration of the test and this reinforces the conclusion from the SG4 data that the 600 mm embedment length was sufficient to allow GFRP bar failure by rupture rather than pullout.

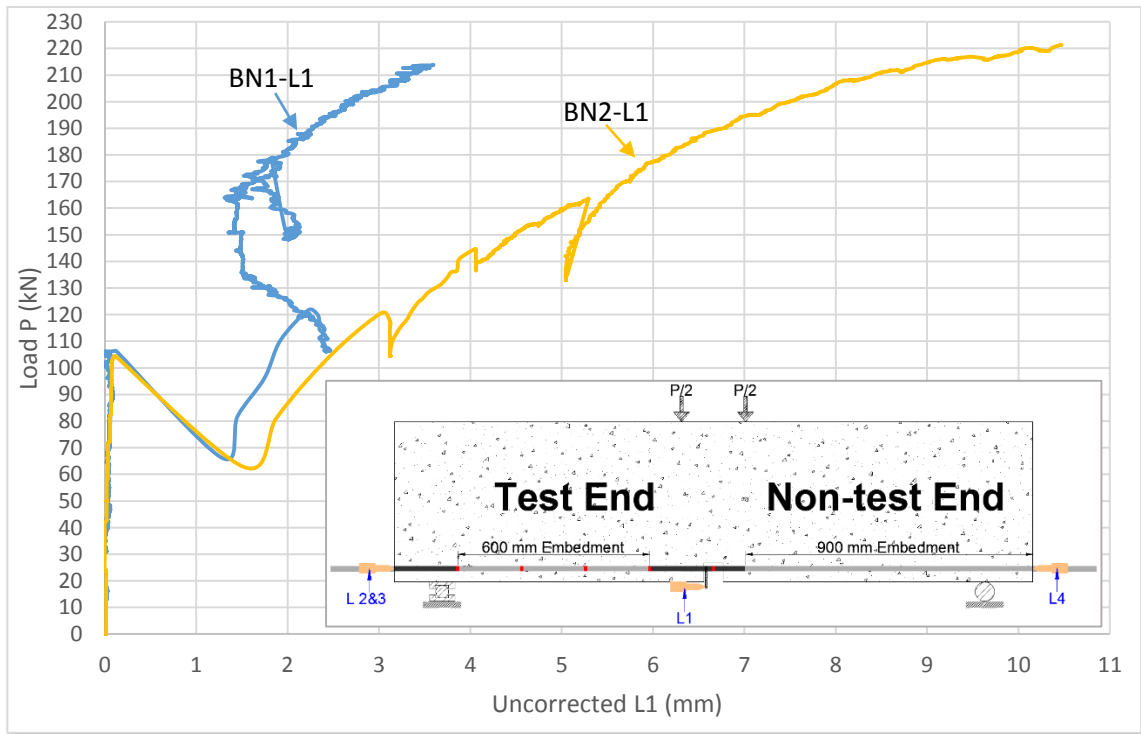


Figure 4:30: Load-uncorrected L1 bar slip in BN1 and BN2

4.3.5 Post-test Inspection

After the completion of the testing, for both Notched beams, in the midspan region, the concrete to the GFRP longitudinal reinforcement was removed and the stirrups were cut for further inspection. Figure 4:31 shows BN1 with the tapes on the GFRP bar over the debonded region to the left and right of the midspan while Figure 4:32 is the GFRP bar with the tapes removed. Similarly, for BN2, Figure 4:33 and Figure 4:34 show the GFRP bar and its rupture over the midspan region and as evident from Figure 4:34, upon removal of the tapes, a portion of the GFRP fibres completely disengaged from the bar core. Overall,

from Figure 4:31 to Figure 4:34, one can conclude that the most significant damage to the GFRP bar occurred over the constant moment region where the bar experienced its highest state of stress and in addition, similar to the RILEM beams, the GFRP damage was more heavily concentrated on the “Non-test End” of the beams.



Figure 4:31: BN1 “Test End”



Figure 4:32: BN1 "Test End". Showing the damage and rupture experienced by the GFRP bar



Figure 4:33: BN2 "Test End"



Figure 4:34: BN2 "Test End". Showing the damage and rupture experienced by the GFRP bar

4.4 Summary of Beam-bond Specimens

Both the RILEM and Notched beams experienced flexural tension failure through the rupture of the GFRP longitudinal reinforcement and this allows for an analysis of the bond stress distribution at different load levels up to the maximum load. A method of ensuring the reliability and consistency of the gathered information is to compare quantities such as the maximum moment and deflection, cracking load and loaded-end slip values as presented in Table 4:1.

As mentioned earlier, there is no flexural cracking at midspan for the RILEM beams since they have a steel hinge system and furthermore as the data in the table indicate, the maximum moment, midspan deflection and uncorrected loaded-end slip values for BR1 and BR2 were quite comparable. For the two Notched beams as well, the midspan and non-midspan flexural cracking moment, maximum moment and midspan deflection exhibit a

high degree of similarity. A comparison of the average results for the RILEM versus the Notched beams show similarity in terms of the maximum moment and maximum midspan deflection, however, as far as the average maximum moment is concerned, it is evident that the Notched beams had a slightly higher strength. One of the explanations for the relatively lower maximum moment for the RILEM beams is the fact that the original moment arm for these beams and their subsequent variation during the test process is a function of the vertical location of the steel hinge. Overall, the performance and the mentioned results from the beams are reasonably close to each other; therefore, the data gathered is reliable and its usage is justified for the purposes of this study.

Table 4.1: Summary of beam-bond specimens

Beam Designation	$M_{cr}^{mid.}$ ($kN \cdot m$)	$M_{cr}^{non-mid.}$ ($kN \cdot m$)	M_{max} ($kN \cdot m$)	$\Delta_{max}^{mid.}$ (mm)	s_{uc}^l at M_{max} (mm)
BR1	N/A	57.6	77.2	15.1	9.6
BR2	N/A	None	72.8	13.9	8.7
Avg.	--	--	75.0	14.5	9.2
BN1	40.1	66.8	80.2	13.7	Malfunction
BN2	39.0	61.1	83.0	15.4	10.5
Avg.	39.6	64.0	81.6	14.6	--

4.5 Results and Observations for Modified Pullout Specimens MP1 and MP2

4.5.1 Key Observations

As mentioned earlier, the $150 \times 150 \text{ mm}$ cross section for the Modified pullout specimens was the most practical option and despite this choice, the loading proved to be difficult due to the heavy weight and the large overall length of these samples. In order to prevent a concrete splitting failure, ACI 440.3, (2004) recommends 200 mm cubic specimens and in the event of splitting failure a shift to 300 mm cubic specimens. CSA S806, (2012) recommends concrete side covers that are at least five to six times the bar diameter and note that the Modified pullout specimens in this experimental program have a concrete side cover that is approximately 4.5 times the nominal GFRP bar diameter. This was determined to be sufficiently close to the recommended value, so the possibility of a splitting failure was assumed to be minimal. With reference to Table 3:1, the average tensile strength of the GFRP bar in this experimental program was $1,066 \text{ MPa}$ and with an actual

diameter of 14.8 mm, the anticipated failure load by GFRP rupture was approximately 183.4 kN.

MP1 in Figure 4:35, was loaded until a maximum value of roughly 140.0 kN, corresponding to 76% of the anticipated GFRP rupture load, at which point the concrete specimen suddenly split along its vertical centreline as shown in Figure 4:36. This splitting failure was most likely due to inadequate concrete cover, which given the laboratory limitations stated previously, could not be avoided, however, to reiterate, the provided concrete cover was very close to the recommended CSA S806, (2012) value.

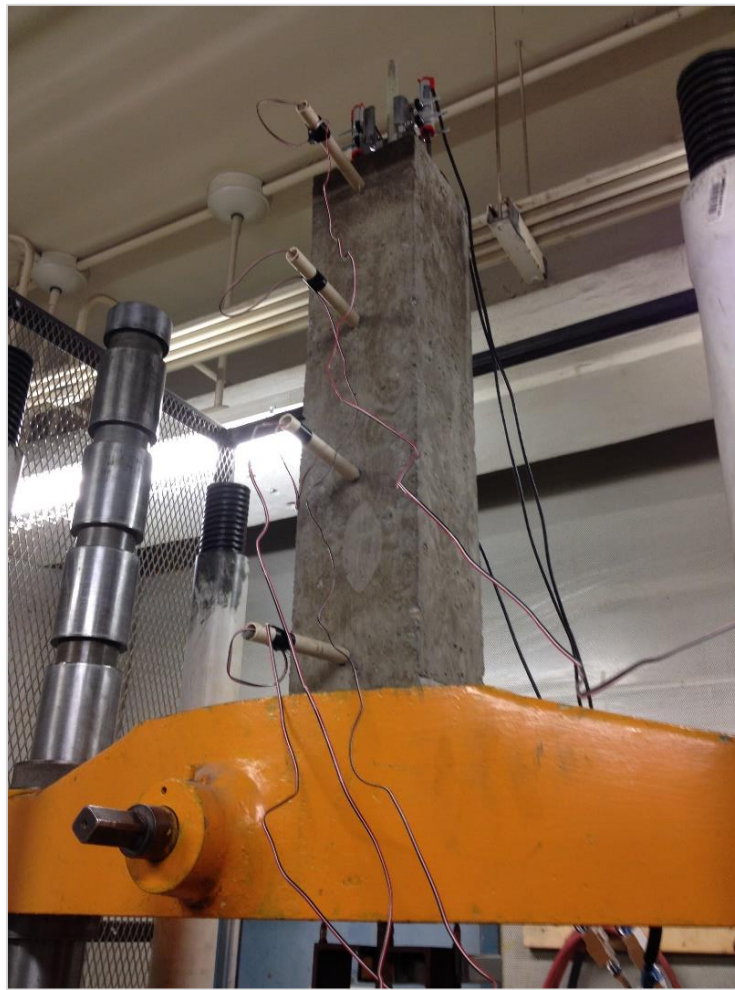


Figure 4:35: MP1 before the test



Figure 4:36: MP1 at failure

For MP2, to avoid concrete splitting as in MP1, it was decided to lightly confine the specimen. This confinement was achieved using hollow structural steel section with an internal dimension slightly larger than the specimen and an overall length of 700 mm, which was equivalent to the length of the specimen. The first step was to cut the HSS section into two pieces and then as Figure 4:37 illustrates, weld small steel angles to the HSS in order to allow for the attachment of high strength bolts used to apply confinement. The HSS section was cut in such a way as to leave a strip of open space to allow for the protrusion of the PVC pipes from the specimen and to provide a means of increasing the confinement by tightening of the bolts. During the placement of the HSS section around the specimen, the strip of open space was sealed shut using a duct tape in order to facilitate the pouring of hydro-stone into the gap between the specimen and the HSS. The purpose of the hydro-stone was to minimize stress concentrations that would arise if the steel were

in uneven contact with the specimen. After the hardening of the hydro-stone, a slow tightening of the high strength bolts allowed for an increase in the overall confinement around the specimen. Figure 4:38 provides a 3D representation of the confined specimen.



Figure 4:37: HSS section used to provide light confinement for MP2

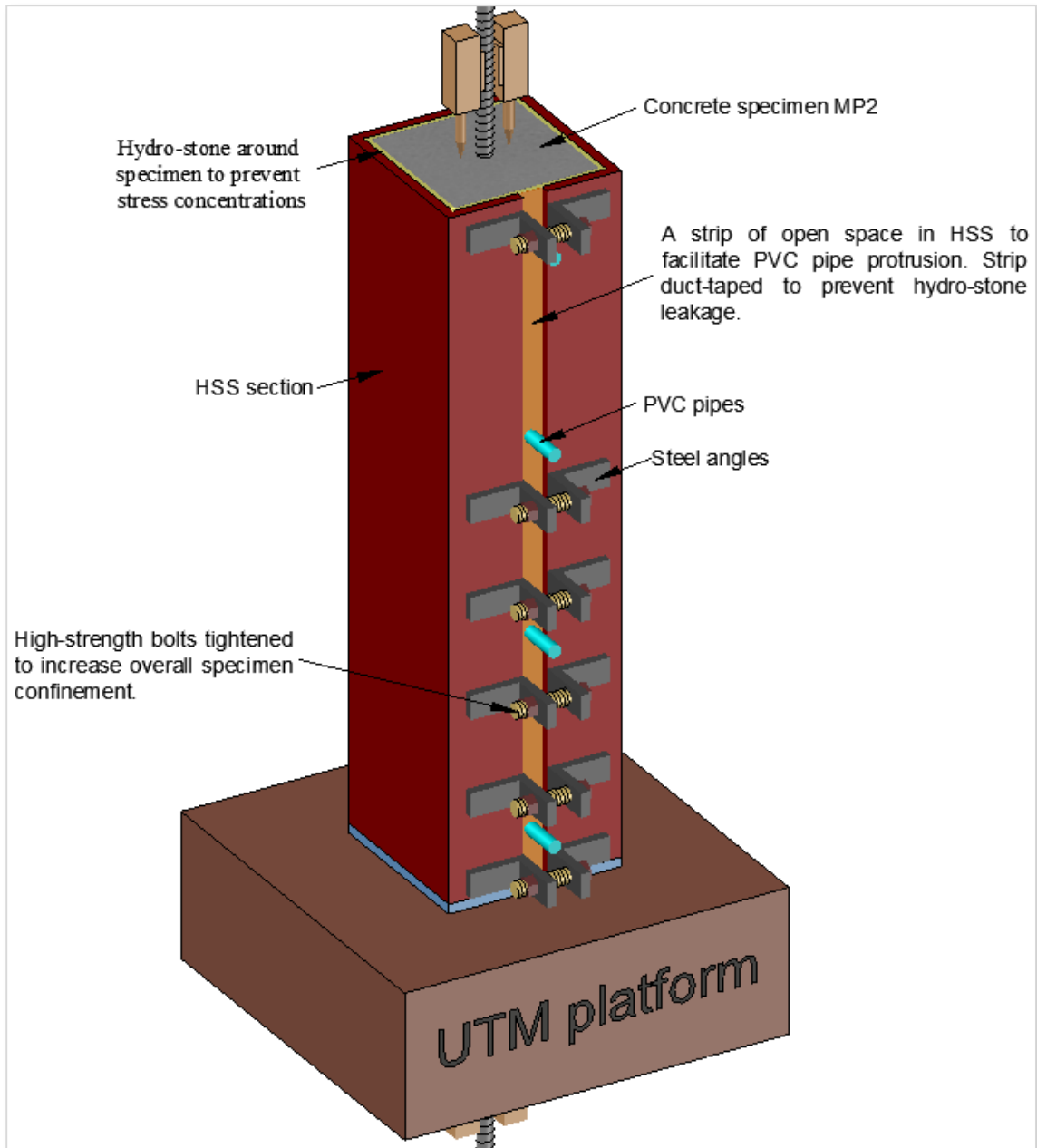


Figure 4:38: Lightly confined MP2

MP2 in Figure 4:39 was loaded until a maximum value of 178.8 kN , which is relatively close to the anticipated failure load of 183.4 kN mentioned earlier, at which point the GFRP bar suddenly ruptured and the load value decreased. Figure 4:40 shows a zoomed view of the GFRP bar, below the top machine platen, after specimen failure.



Figure 4:39: MP2 before the test



Figure 4:40: MP2 at failure

4.5.2 GFRP Bar Strain

Figure 4:41 is a plot of load versus the strain in the GFRP bar in MP1 and MP2 up to their failure by concrete splitting and GFRP rupture, respectively. For MP1, SG3 outputs were lost due to its designated data acquisition channel malfunctioning during the test. Observation of this figure as well as analysis of the data show that MP1-SG1 experiences failure at approximately 109.0 kN , which corresponds to 59% of the anticipated GFRP rupture load while MP2-SG1 fails at roughly 80.0 kN or equivalently, 45% of the GFRP rupture load in MP2. The failure of SG1 in both MP1 and MP2 at the stated load levels is evident through either constant strain or continued drastic decreases in strain despite increases in load levels beyond roughly 109.0 kN for MP1 and 80.0 kN for MP2. Note that the load versus SG1 data for the beam-bond specimens, prior to their failure, had a high degree of linearity, however, for the Modified pullout samples, the readings begin to show a non-linear behaviour at early stages of loading. For both Modified pullout specimens, throughout the loading process, in a similar manner to the beam-bond specimens, the strain recorded by SG4 was negligible. This means that the development length until the recorded load level corresponding to concrete splitting for MP1 and until the GFRP rupture failure load for MP2, was less than the provided 600 mm embedment

length. One can also notice that MP2-SG3 recorded very small strain values throughout the loading process, hence the required development length for this confined specimen, was much less than 600 *mm*.

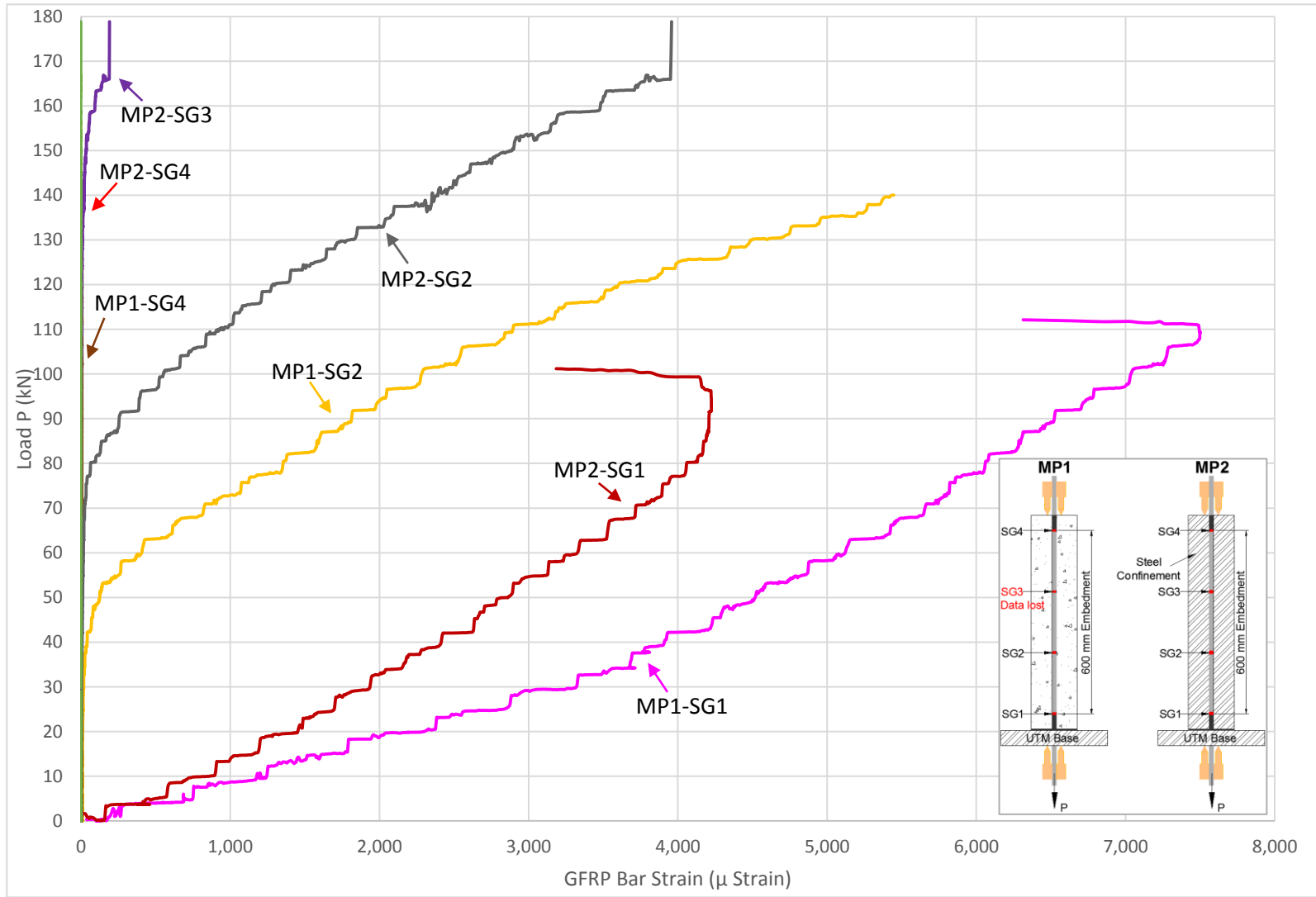


Figure 4:41: Load-GFRP bar axial strain in MP1 and MP2

4.5.3 GFRP Bar Slip

Figure 4:42 is a plot of load versus the uncorrected loaded-end bar slip for MP1 and MP2 up to their failure by concrete splitting and GFRP rupture, respectively. With reference to this figure, the uncorrected loaded-end slip for MP1, at its concrete splitting load, was 12.2 and 12.1 mm for L3 and L4, respectively. For MP2 at the GFRP rupture load, L3 and L4 had an uncorrected slip of 11.2 and 12.2 mm, respectively. Lastly, concerning the unloaded-end slip, for both MP1 and MP2, L1 and L2 did not show any slip values throughout the loading process indicating the sufficiency of the 600 mm embedment length.

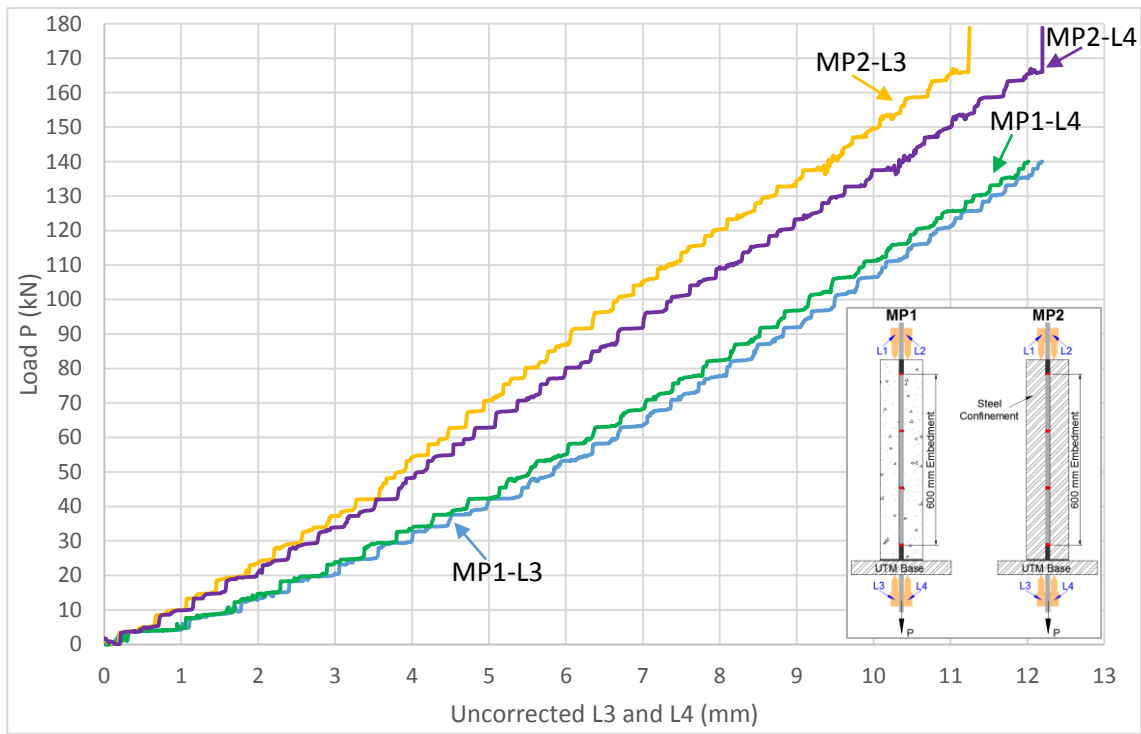


Figure 4:42: Load-uncorrected L3 and L4 bar slip in MP1 and MP2

4.6 Results and Observations for Standard Pullout Specimens P1 to P10

For the Standard pullout tests, as expected, due to a relatively short embedment length of four times the nominal GFRP bar diameter, or 60 mm , all ten specimens failed through GFRP bar pullout at axial load values ranging between 29.0 to 48.0 kN . Figure 4:43 shows the testing of one of these specimens while Table 4:2 provides the test results and note, with reference to Figure 3:16, that the average unloaded-end slip, s^{ul} was obtained using L1 to L3 readings while the average uncorrected loaded-end slip, s_{uc}^l was obtained using data from L4 to L6. Experimental bond stress versus slip curves as well as evaluation of the theoretical local bond stress-slip model adopted by CEB-FIP Model Code, (2010) will be presented and discussed in detail in Section 5.9 .



Figure 4:43: P1 before the test

Table 4:2: Standard pullout specimen test results

Specimen Designation	P_{max} (kN)	s^{ul} at P_{max} (mm)	s_{uc}^l at P_{max} (mm)
P1	48.0	2.9	5.4
P2	39.0	2.2	5.1
P3	34.8	2.4	5.2
P4	29.0	1.8	4.3
P5	46.5	2.2	5.3
P6	42.6	2.6	6.3
P7	41.7	2.9	5.9
P8	37.8	2.3	5.0
P9	39.9	2.3	5.3
P10	42.2	2.1	5.8
Avg.	40.1	2.4	5.4
S.D.	5.5	0.4	0.6
COV (%)	13.8	15.3	10.4

This completes the raw data gathered in these tests. In the following chapter, the analysis of the results will be performed in order establish the bond stress distribution along the bar and its variation with the applied load as well as the maximum bond stress observed in each test.

Chapter 5 Analysis and Discussion

5.1 General

Through the analysis and discussion of the obtained experimental results, with particular focus on the bond behaviour of the GFRP reinforcement investigated and the bond stress distribution along the bar embedment length, this section aims to accomplish the following:

1. Concerning the beam-bond tests, comparison between the ultimate moment capacities observed from experimental results versus the theoretical predictions by CSA S806, (2012).
2. A preliminary analysis in order to approximate the behaviour of certain strain gauges along the GFRP bar as well as BN1-L1, past their respective failure point during testing.
3. The possible cause of the splitting failure observed in MP1 as well as the effect of the light confinement provided in MP2, particularly on the pattern of the bond stress distribution.
4. In conformity with the main goal of this investigation, derivation of an expression that will estimate the bond stress distribution along a given embedment length at different stages of loading up to and including the bar rupture stage.
5. Comparison of the actual bond stress distribution along the bar embedment length to the uniform distribution approximation assumed by current guidelines.
6. Comparison of the required development length approximated experimentally versus the development length recommended by ACI 440.1, (2006), CSA S806, (2012) and CSA S6, (2006).
7. Using the bond stress distribution and bond-slip relationship for the RILEM and Notched beam-bond test and the Modified pullout test to evaluate the heavy reliance of current guidelines on using the pullout test method as the sole means of judging the bond performance of reinforcement. In addition, comparing the performance of RILEM versus the Notched beam-bond specimens and recommending the preferred beam-bond test method for capturing the bond behaviour of embedded reinforcement in flexural members.

8. Analysis of bond stress versus slip curves of the Standard pullout specimens and assessment of the accuracy of the local bond stress-slip model adopted by CEB-FIP Model Code, (2010).

5.2 Beam Flexural Behaviour

The test beams were designed to ensure, with a high degree of probability, tension failure in the form of GFRP bar rupture. Concerning the RILEM beams, since the steel hinge near the top of the beam was unlikely to yield before the GFRP bar tensile reinforcement rupture, it was presumed that failure would be initiated by GFRP bar rupture. Beam failure in any mode other than the rupturing of the tensile reinforcement would not allow a complete analysis of the bond stress distribution of the GFRP bar up to its ultimate tensile strength, which is one of the main objectives of this study. Appendix A presents the theoretical calculations for the moment and shear capacity of the Notched and RILEM beams based on conventional code-based analysis and note that these calculations reveal that due to the choice of a large cross section and only one tensile reinforcing bar, the reinforcement ratio provided is well below the balanced reinforcement ratio, effectively ensuring tension failure. Furthermore, the presence of steel stirrups at a close spacing of 50 mm avoid the shear mode of failure and the 35 mm clear cover for the GFRP reinforcement is designed to prevent any splitting failure.

The calculations of Appendix A make use of GFRP, concrete and steel material properties obtained from the test data presented in Section 3.2 and furthermore, the flexural calculations do not include resistance factors since all of the specimens were constructed and tested in a controlled laboratory environment. The recommendations by CSA S806, (2012) are followed, which similar to other standards, uses strain compatibility analysis for the calculation of the ultimate moment capacity of beams. The main assumptions in this standard are that plane sections remain plane before and after bending, there exists perfect bond between the reinforcement and the concrete and the contribution of concrete to tensile resistance is zero. Since the design of the beams in this experimental program had to avoid concrete crushing at ultimate capacity, the stress block parameters provided by CSA S806, (2012) are not applicable and therefore, Appendix A computations make use of the well-established concrete stress-strain relationship by Popovics, (1970) and Hognestad et al., (1955). Lastly, for the Notched beams, the calculation of the midspan gross and cracked moment of inertia takes into account the loss of the cross sectional area brought on by the notch, which had 60 mm height.

Table 5:1 provides a comparison between the midspan ultimate moment capacity, M_{max} as well as the first cracking moment, M_{cr} obtained from the experimental results and the theoretical code-based calculations.

Table 5:1 Comparison of ultimate and cracking moment results

Beam	Experimental		Theoretical		
	M_{max} (kN · m)	M_{cr} (kN · m)	M_{max} (kN · m)	M_{cr} (kN · m) CSA S806, (2012) Cl. 8.3.2.6 and 8.3.2.8	M_{cr} (kN · m) CSA S6, (2006) Cl. 8.8.4.4 and 8.4.1.8.1
BR1	77.2	N/A	79.3	N/A	N/A
BR2	72.8	N/A	78.6	N/A	N/A
BN1	80.2	40.1	82.0	48.2	32.1
BN2	83.0	39.0	82.0	48.2	32.1

The ultimate moment capacity obtained from the theoretical code-based calculations agree well with the experimental results, however, concerning the cracking moment, CSA S806, (2012) and CSA S6, (2006) provide an over and underestimation, respectively. The discrepancy between the two standards in predicting the cracking moment is the result of the fact that for normal density concrete, CSA S806, (2012) specifies a modulus of rupture equal to $0.6\sqrt{f'_c}$ in its cracking moment equation while the CSA S6, (2006) recommends using $0.4\sqrt{f'_c}$. Furthermore, the presence of the notch would cause stress concentrations and is likely to cause early cracking than anticipated by the CSA method, which does not involve the notch effect. This may explain the difference between the theoretical and observed cracking moment values. Lastly, as stated earlier, in terms of the experimental results, the RILEM beams had a lower ultimate moment capacity compared to the Notched beams and this is due to the steel hinge pre-defining the location of the resultant compressive force at the beginning of the test. Overall, both the RILEM and the Notched beams experienced flexural failure through GFRP bar rupture and therefore the initial design was correct in preventing other modes of failure, which included concrete crushing, shear and bond failure.

5.3 Preliminary Analysis

5.3.1 Overview

In order to compare the full spectrum of the experimental bond stress distribution along the GFRP reinforcement, it is first necessary to discuss the failure of certain strain gauges in both the beam and the Modified pullout specimens and to examine the L1 failure in BN1. Figure 5:1, which is a reproduction of Figure 3:20, shows the strain gauge locations on the GFRP bars for both test methods and note that the strain gauges that failed were located in regions where the GFRP was under the highest level of stress, which corresponded to SGC and SG1 for the beam specimens and SG1 for the Modified pullout samples.

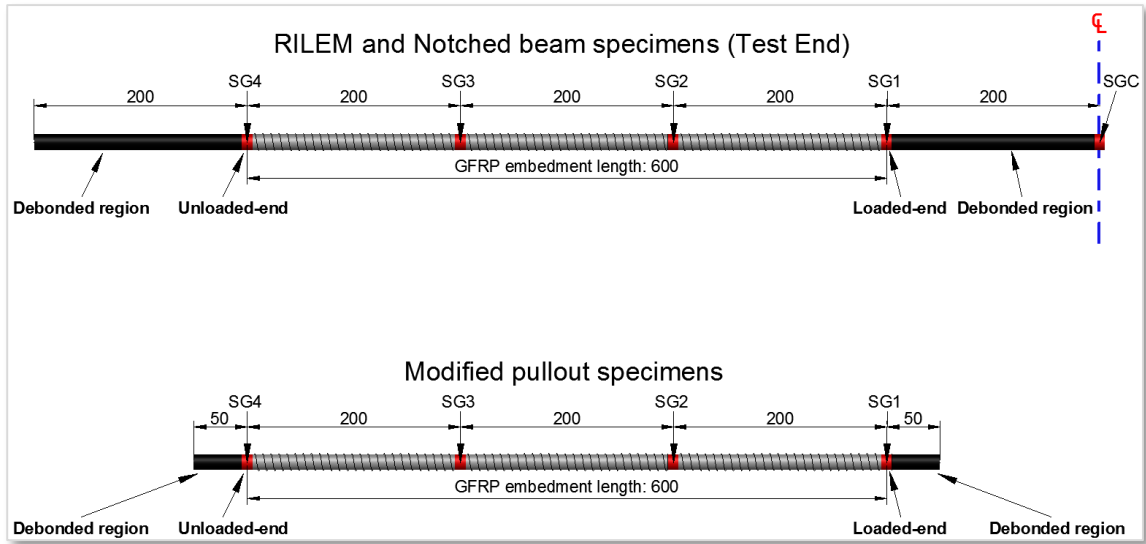


Figure 5:1: GFRP bar reinforcement strain gauge detail for RILEM and Notched beams (Test End), as well as for the Modified pullout specimens (All dimensions are in mm)

There are three main explanations for the sudden strain gauge failures which occurred approximately between 45 to 93% of the bar tensile strength, the first being possible de-bonding of the strain gauge from the GFRP surface at these stress values. The second is the gradual detachment of some of the external fibres of the GFRP bar at stress values that fall within the mentioned range, a phenomenon first observed during tensile testing. These fibre detachments can occur at any location along the outer perimeter of the bar that experience a stress level beyond a critical value, however, their nature is less severe than the abrupt rupturing of the fibres at the GFRP’s ultimate tensile strength. The third possibility, which is applicable to the Notched beams, is the inability of the SGC and SG1

in these beams to function properly shortly after the shock and energy release associated with the occurrence of the first flexural crack at midspan. When the Notched beams experienced this flexural crack, there was an instantaneous drop in load as the hydraulic jack attempted to adjust to the sudden loss of beam stiffness and furthermore there was a rapid increase in demand on the longitudinal reinforcement, particularly at the location of the crack. This demand, which manifests itself through a large increase in the longitudinal tensile reinforcement strain, is more profound for GFRP reinforced beams due to the relatively lower elastic modulus of these bars compared to steel and the fact that in the current tests, only one GFRP bar was used as tensile reinforcement. Although SGC and SG1 in the Notched beams were able to function after this large increase in strain, during the phase where the hydraulic jack begins to reapply the load, these strain gauges failed due to their inability to adjust to the large unloading and reloading that occurred within a short period of time.

5.3.2 RILEM Beams

For BR1, SGC and SG1 failed at approximately 62% of the ultimate beam failure load and because these bars behave in a linear elastic fashion up to rupture, evident by the tensile test results presented in Figure 3:1 to Figure 3:3, the use of a linear regression to provide an approximation of the remaining strain values for SGC and SG1 is justified. The same argument is applicable for BR2, which experienced a failure of its SGC and SG1 at approximately 75% of the beam capacity and Figure 5:2 and Figure 5:3 provide a plot of the load versus strain gauge data for BR1 and BR2, respectively, showing the incorporation of the linear regressions.

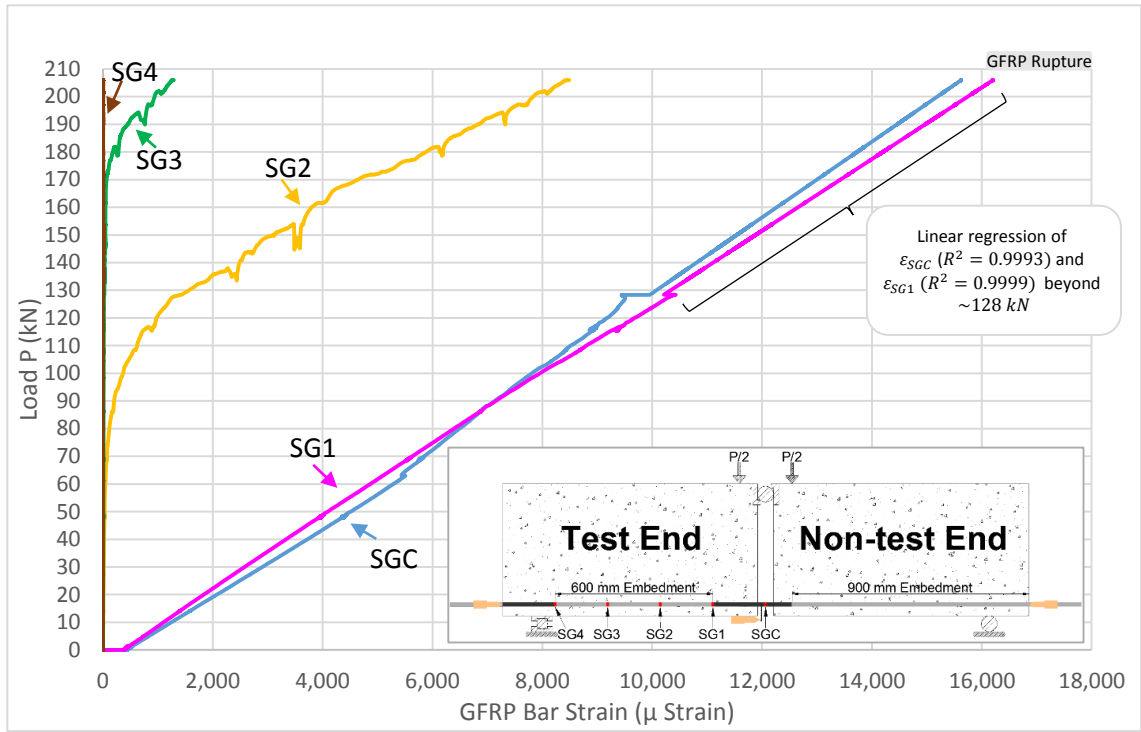


Figure 5.2: Load - GFRP bar strain in BR1

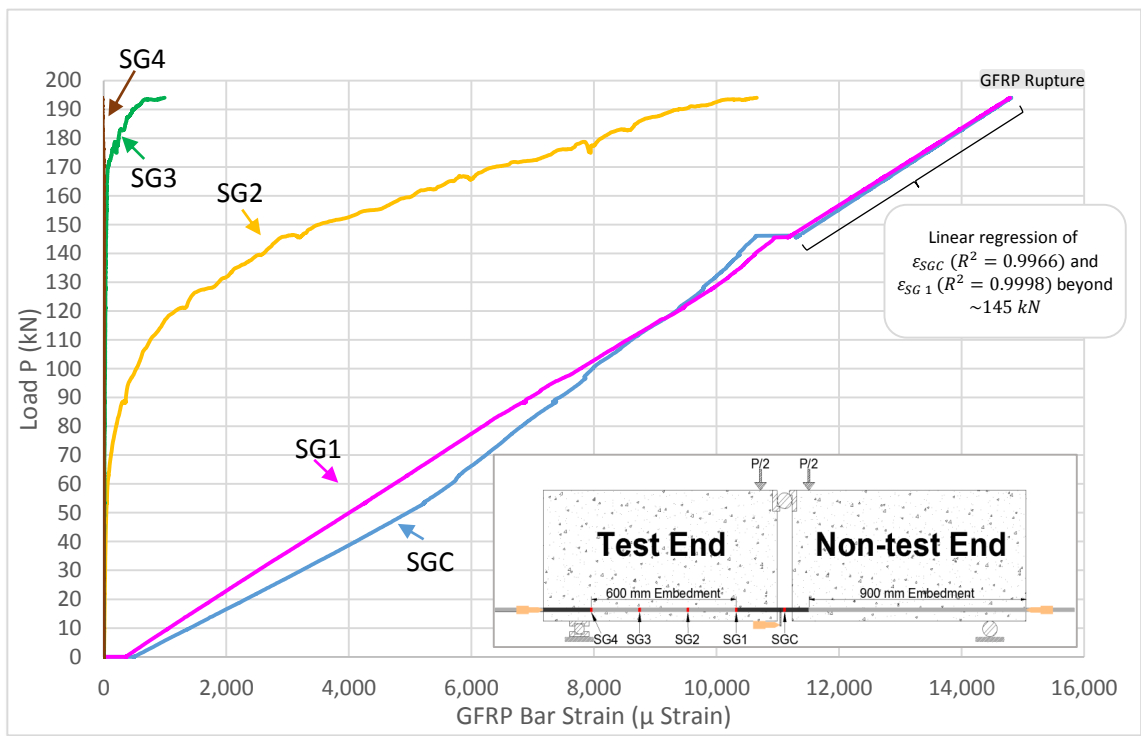


Figure 5.3: Load - GFRP bar strain in BR2

Another method of presenting the strain gauge data, which was also used by Benmokrane et al. (1996), is to plot the midspan GFRP bar stress against the values from the strain gauges placed on the GFRP. This method involves determining the moment at midspan corresponding to the applied load, followed by the calculation of the force and the stress in the GFRP reinforcement at midspan by setting the internal moment resistance equal to the corresponding applied moment and assuming a constant moment arm. As indicated by Benmokrane et al. (1996), there two advantages to these plots, the first being the fact that the slope of the data from SGC provides the value of the GFRP elastic modulus. The second advantage is that there can be an estimation of the extent of the bond failure between the concrete and the GFRP by observing the slopes of the strain gauge data along the GFRP bar in sections other than the midspan.

In their study, in terms of the beam design and testing, Benmokrane et al. (1996) followed the recommendations of RILEM TC-RC5, (1994), as have done the majority of researchers who have conducted beam-bond testing. Accordingly, they assumed a constant moment arm, jd , for all levels of loading. Overall, by utilizing the data presented in Figure 5:2 and Figure 5:3 and by applying the procedure described earlier, it is possible to plot the midspan bar stress against the strain gauge data and Figure 5:4 and Figure 5:5 show these plots for BR1 and BR2, respectively.

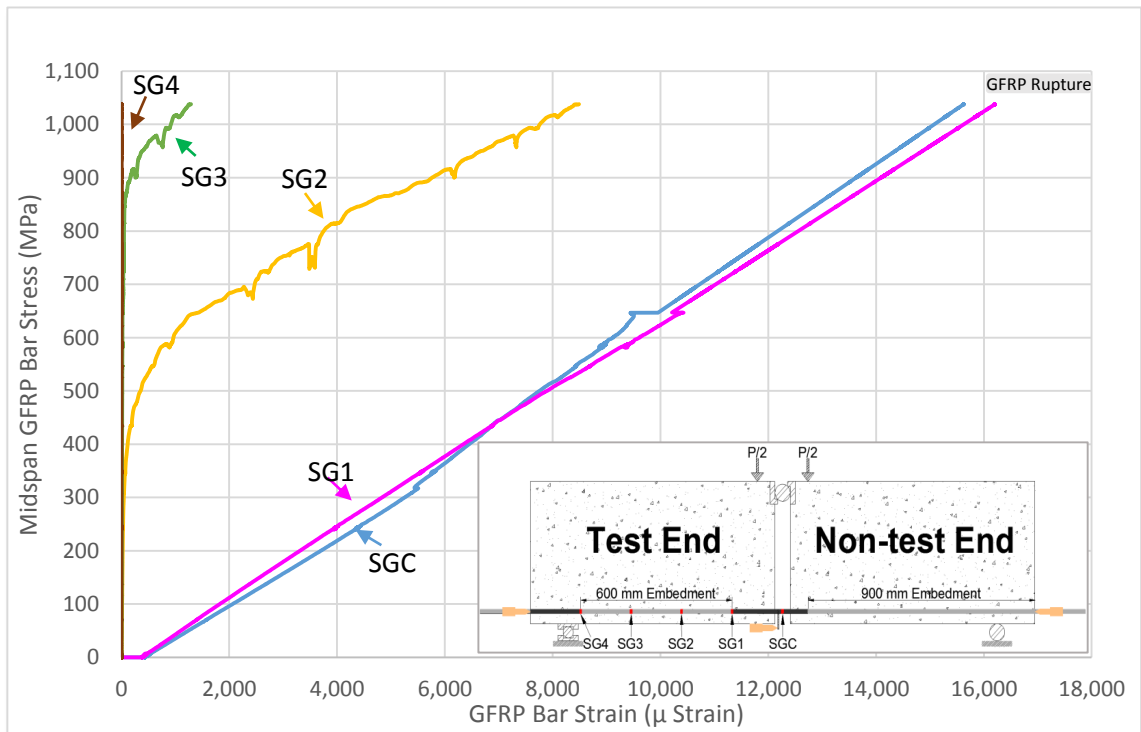


Figure 5:4: Midspan GFRP bar stress - GFRP strain in BR1

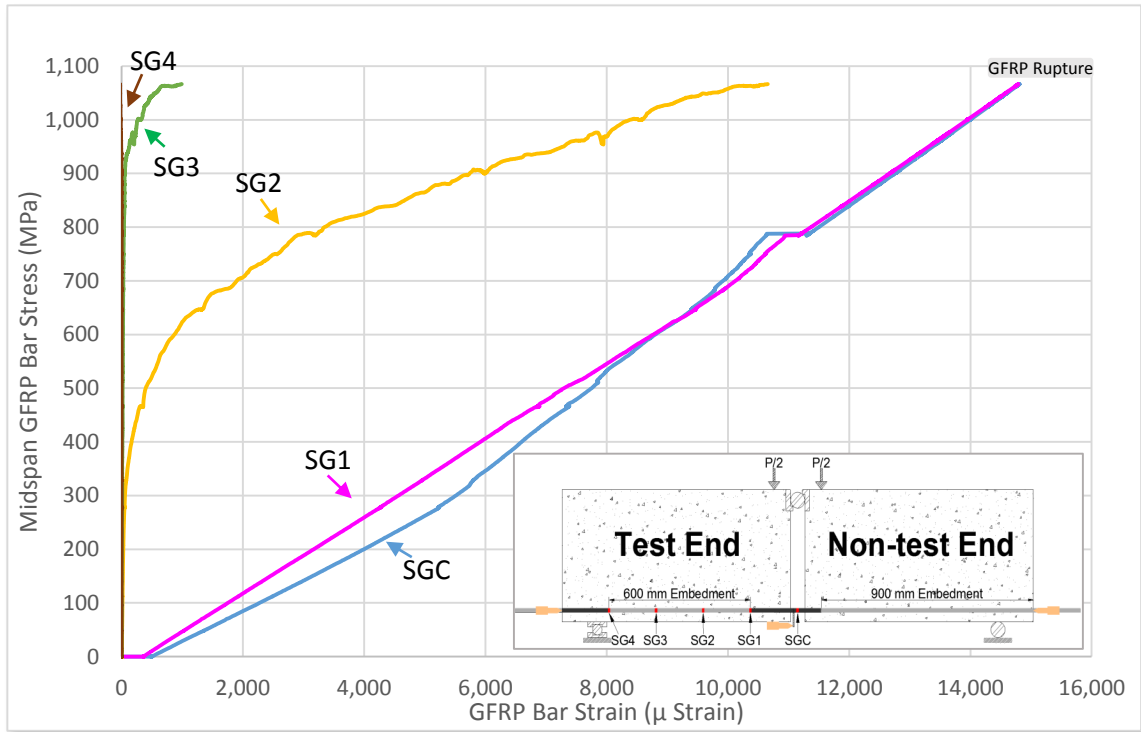


Figure 5:5: Midspan GFRP bar stress - GFRP strain in BR2

Table 5:2 shows the values for the slopes of SGC and SG1 for both beams and with reference to Table 3:1, there was an expectation that these slopes would be approximately equal to 51.3 *GPa*, the average elastic modulus of the GFRP bar obtained from tensile testing. However, this is not the case and one explanation for the beams demonstrating a higher GFRP elastic modulus is the poor quality of the gripping system used for attaching the electronic extensometer onto the GFRP bar during the tensile testing. Other possibilities for this discrepancy warrant further investigation, however, since the obtained GFRP elastic moduli show consistency, analysis of all specimens in this experimental program, including the RILEM beams themselves, will utilize the average elastic modulus value shown in Table 5:2. Note that for the RILEM beams, in regions close to the point of GFRP rupture, multiplying the average elastic modulus by the obtained SGC values will result in a slightly different GFRP stress level in comparison to the stress obtained using the constant *jd* and requirement of equilibrium. This is due to the possible change in the moment arm as well as the application of an average elastic modulus from Table 5:2, therefore, the strain distribution analysis of the RILEM beams will use the maximum GFRP stresses obtained by multiplying the average elastic modulus by the respective SGC values. This is the reason why f_{Fu} in Table 5:2 differs slightly from Figure 5:4 and Figure 5:5. However, from this table, note that the average f_{Fu} is comparable to the average of 1,066 *MPa* obtained from the GFRP tensile tests, therefore, given the fact that the GFRP bar rupture mode of failure

was also confirmed by inspection, one can state that the strain approximations beyond the point of their respective strain gauge failure are reasonable.

Table 5.2: GFRP elastic moduli and ultimate stress obtained from RILEM beams

RILEM Beam Strain Gauge	E_F (GPa)	f_{Fu} (Mpa)
BR1-SGC	69.0	1,065
BR1-SG1	65.2	1,105
BR2-SGC	70.3	1,010
BR2-SG1	68.1	1,008
Avg.	68.2	1,047

5.3.3 Notched Beams

Concerning the Notched beams, in order to address the failure of SGC and SG1 shortly after midspan flexural cracking and determine subsequent strain values, this study uses a full nonlinear analysis, involving the requirements of equilibrium, compatibility and the constitutive laws of concrete and GFRP. First, it is necessary to obtain the stress-strain relationship of concrete in this experimental program. This is achieved by using Equation 5.1 based on Thorenfeldt et al., (1987) recommendation, originally proposed by Popovics, (1970).

$$\frac{f_c}{f'_c} = \frac{n(\epsilon_c/\epsilon'_c)}{n - 1 + (\epsilon_c/\epsilon'_c)^{nk}} \quad \text{Equation 5.1}$$

For normal density concrete, the parameters in Equation 5.1 are defined as follows:

$$n = 0.8 + \frac{f'_c}{17} \text{ Curve adjustment factor [Popovics, (1970)]}$$

$$E_c^{Pauw} = w_c^{1.5} 0.043 \sqrt{f'_c} \text{ Concrete tangent stiffness [Pauw, (1960)]}$$

$$k = 0.67 + \frac{f'_c}{62} \geq 1.0 \text{ Decaying factor [Popovics, (1970)]}$$

$$\epsilon'_c = \frac{f'_c}{E_c^{Pauw}} \frac{n}{n-1}$$

Note that the value of ϵ'_c above is not simply f'_c divided by the concrete elastic modulus presented in Table 3:4 since the modulus will vary with increasing stress, particularly beyond the linear elastic range of the stress-strain curve. With ϵ'_c and f'_c known, E'_c can be calculated as follows:

$$E'_c = \frac{f'_c}{\epsilon'_c} \quad \text{Equation 5.2}$$

Using the provided equations, Table 5:3 shows all the relevant material property values in this experimental program and Figure 5:6 illustrates the resulting concrete stress-strain relationship.

Table 5:3: Relevant material property values in this experimental program

Variable	Value
A_F	172 mm ²
E'_c	19.8 GPa
E_c^{Pauw}	29.9 GPa
E_F	68.2 GPa
f'_c	36.5 MPa
k	1.3
n	2.9
w_c	2,370 kg/m ³
ϵ'_c	1,843 μ strain

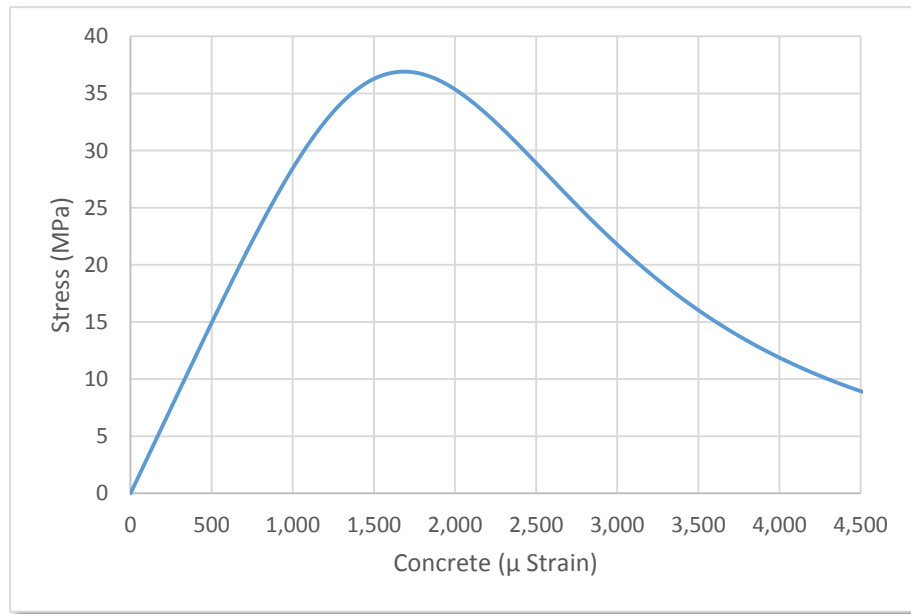


Figure 5:6: Derived concrete stress-strain relationship for this experimental program

With reference to Figure 5:7, from the onset of the four-point bending test to the failure of the Notched beams, one can use three stages to describe the behaviour of the concrete around the GFRP longitudinal tensile reinforcement. Prior to the midspan flexural crack, *Stage 1*, up to *Point A*, the uncracked concrete offers a substantial contribution to the tensile resistance of the section and this is evident through the negligible ϵ_{SGC} and ϵ_{SG1} values observed in Figure 4:29 for this stage. *Stage 2* represents a transition between uncracked and fully cracked concrete and also corresponds to the portion of the test

immediately after the midspan flexural crack where the load value, P drops, *Point B* and subsequently increases.

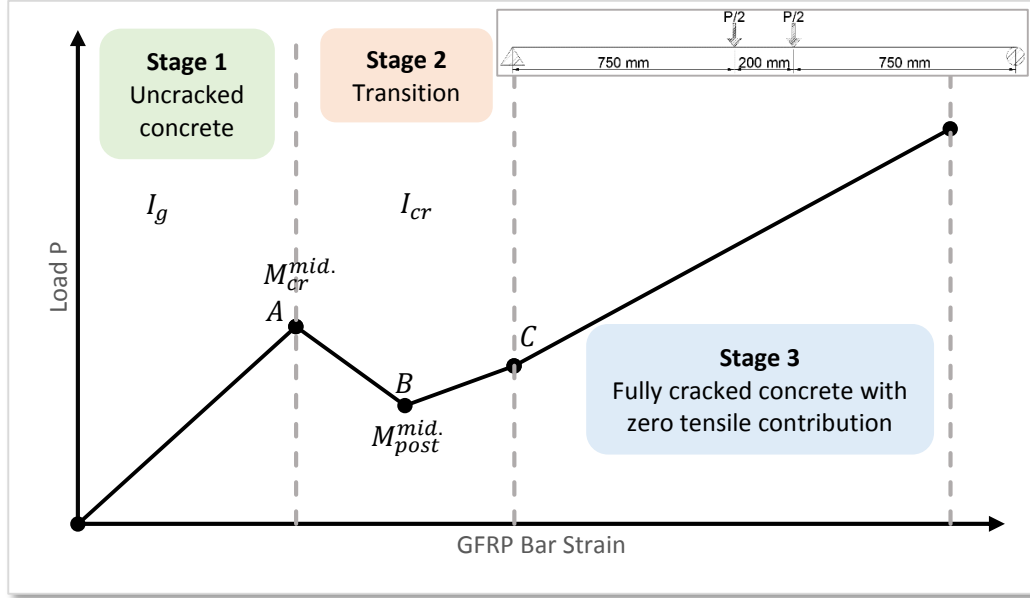


Figure 5:7: State of the concrete around the longitudinal GFRP tensile reinforcement

Thus, at *Point A*, the theoretical value of ϵ_{SGC} and ϵ_{SG1} is,

$$\epsilon_{FA} = \frac{M_{cr}^{mid.} \cdot (d - y)}{I_g E_F} \quad \text{Equation 5.3}$$

while at *Point B*, using the cracked moment of inertia,

$$\epsilon_{FB} = \frac{M_{post}^{mid.} \cdot (d - kd)}{I_{cr} E_F} \quad \text{Equation 5.4}$$

The calculation steps and values of y , kd , I_g and I_{cr} can be found in Appendix A and note in Equation 5.3 and Equation 5.4, $M_{cr}^{mid.}$ and $M_{post}^{mid.}$, are obtained from the experimental data and correspondingly, refer to the moment occurring at and immediately after the occurrence of the midspan flexural crack. For the Notched beams, the average approximate value of $M_{cr}^{mid.}$ and $M_{post}^{mid.}$ were 39.5 and $24.2 \text{ kN} \cdot \text{m}$, respectively. With a shear span of 750 mm , the associated total load, P for $M_{cr}^{mid.}$ is 105.5 kN and for $M_{post}^{mid.}$ is 64.5 kN . As stated earlier, for both beams, ϵ_{SGC} and ϵ_{SG1} failed immediately after the midspan flexural crack. More specifically, for BN1, the failure of these strain gauges

occurred at P of approximately 66.3 kN while for BN2, the failure was encountered at roughly, 62.8 kN .

Stage 3, beginning from *Point C*, involves fully cracked concrete that does not contribute to the tensile resistance of the section and solely relies on the longitudinal GFRP tensile reinforcement. The load value for *Point C* is obtained from the experimental data for each beam and corresponds to the next increment in load following the initial decrease at *Point B*. For BN1, this load is 81.9 kN while for BN2 it is 81.0 kN . For clarification, Table 5:4 presents a summary of the preceding information and note that all moments and forces are in units of $\text{kN} \cdot \text{m}$ and kN , respectively.

Table 5:4: Summary of strain-load pairs at Points A, B and C

$(\epsilon_F, P), (\mu \text{ Strain}, \text{kN}) \text{ pair}$			
Point	Theoretical	BN1-Experimental	BN2-Experimental
A	$\epsilon_{FA} = \frac{M_{cr}^{mid.}(d - y)}{I_g E_F}$ $M_{cr}^{mid.} = 39.5$ $P = 105.5$ $(\epsilon_{FA}, P) = (47.1, 105.5)$	$P = 106.9$ $\epsilon_{SGC} = 248.5$ $\epsilon_{SG1} = 175.5$ $(\epsilon_{FA}, P)_{SGC} = (248.5, 106.9)$ $(\epsilon_{FA}, P)_{SG1} = (175.5, 106.9)$	$P = 104.0$ $\epsilon_{SGC} = 327.6$ $\epsilon_{SG1} = 242.4$ $(\epsilon_{FA}, P)_{SGC} = (327.6, 104.0)$ $(\epsilon_{FA}, P)_{SG1} = (242.4, 104.0)$
B	$\epsilon_{FB} = \frac{M_{post}^{mid.}(d - kd)}{I_{cr} E_F}$ $M_{post}^{mid.} = 24.2$ $P = 64.5$ $(\epsilon_{FB}, P) = (1,837.6, 64.5)$	$P = 66.3$ $\epsilon_{SGC} = 3,129.5$ $\epsilon_{SG1} = 2,470.4$ $(\epsilon_{FB}, P)_{SGC} = (3,129.5, 66.3)$ $(\epsilon_{FB}, P)_{SG1} = (2,470.4, 66.3)$	$P = 62.8$ $\epsilon_{SGC} = 3,720.4$ $\epsilon_{SG1} = 3,335.6$ $(\epsilon_{FB}, P)_{SGC} = (3,720.4, 62.8)$ $(\epsilon_{FB}, P)_{SG1} = (3,335.6, 62.8)$
C		$P = 81.9 \text{ (BN1)}$ $P = 81.0 \text{ (BN2)}$	

For each beam, this study intends to connect the (ϵ_{FB}, P) points to the corresponding (ϵ_{FC}, P) coordinate and therefore the next step is to determine the value of ϵ_{FC} for BN1 and BN2 and note that this procedure assumes that beyond *Point C*, the concrete no longer contributes to tensile resistance. Equation 5.5 and Equation 5.6 present the expressions for the sum of compressive and tensile forces in flexural reinforced concrete members, assuming that the concrete in the tensile zone is incapable of any contribution and that the longitudinal reinforcement resists all tensile forces, CSA S806, (2012). Observe that Equation 5.5 ignores any compression steel and its contribution to force, C_c . As stated earlier, the extent of the flexural crack at midspan was profound such that only

50 and 40 mm of concrete remained intact for BN1 and BN2, respectively, after which point for both beams, the crack remained stable and for the remainder of the test, showed minimal progression upwards, clearly not noticeable to the naked eye. Since for both beams, the flexural crack at midspan did not propagate, the assumption that the concrete is unable to contribute to any tensile resistance beyond this point is valid and the derivation of ε_{SGC} and ε_{SG1} strain values are expected to be accurate.

$$C_c = \alpha_1 f'_c b_w \beta_1 c \quad \text{Equation 5.5}$$

$$T_F = \varepsilon_F E_F A_F \quad \text{Equation 5.6}$$

For a cross section with constant width, which is the case in this experimental program, Collins and Mitchell, (1991) present Equation 5.7 and Equation 5.8, also referred to as the Hognestad et al., (1955) parabola, for calculating the stress block parameters corresponding the concrete stress-strain relationship given by Figure 5:6.

$$\alpha_1 \beta_1 = \frac{\varepsilon_c}{\varepsilon'_c} - \frac{1}{3} \left(\frac{\varepsilon_c}{\varepsilon'_c} \right)^2 \quad \text{Equation 5.7}$$

$$\beta_1 = \frac{4 - (\varepsilon_c / \varepsilon'_c)}{6 - 2 (\varepsilon_c / \varepsilon'_c)} \quad \text{Equation 5.8}$$

With the preceding information and considering the fact that there are no axial loads applied to the beams in this experimental program, the sum of the compressive forces must be equal to the sum of the tensile forces.

$$C_c = T_F \quad \text{Equation 5.9}$$

or

$$\alpha_1 f'_c b_w \beta_1 c = \varepsilon_F E_F A_F \quad \text{Equation 5.10}$$

Substituting for $\alpha_1 \beta_1$ from Equation 5.7

$$\left[\frac{\varepsilon_c}{\varepsilon'_c} - \frac{1}{3} \left(\frac{\varepsilon_c}{\varepsilon'_c} \right)^2 \right] f'_c b_w c = \varepsilon_F E_F A_F \quad \text{Equation 5.11}$$

With a linear strain distribution along the height of the cross section, it is possible to use similar triangles and express ε_c in terms of ε_F and c and arrive at Equation 5.12, which can be inserted into Equation 5.8 and Equation 5.11.

$$\varepsilon_c = \frac{c(\varepsilon_F)}{d - c} \quad \text{Equation 5.12}$$

Now using the usual equations of statics and the requirements of equilibrium, one can write,

$$M_{int} = T \left(d - \frac{\beta_1 c}{2} \right) \quad \text{Equation 5.13}$$

Additionally, since the external moments must equal the internal moments,

$$M_{ext} = M_{int} \quad \text{Equation 5.14}$$

$$\left(\frac{P}{2} \right) (\text{Beam shear span}) = M_{int} \quad \text{Equation 5.15}$$

In order to calculate the load for a given GFRP strain value, first, a strain value for the GFRP is assumed at section of maximum moment and Equation 5.11 is used to calculate the neutral axis depth, c . Then Equation 5.13 and Equation 5.15 are used to calculate the internal moment and the load, P . This process is continued up to the maximum value of P for BN1 and BN2 determined experimentally, however, it results in the two beams having identical ε_{SGC} and ε_{SG1} values except at regions close to the strain gauge failures and at the ultimate state since BN1 reached a maximum P value of 213.9 kN while BN2 failed at 221.3 kN. This procedure is reliable, since as illustrated and mentioned previously, BN1 and BN2 exhibited a high degree of similarity in terms of their ultimate flexural capacity, crack formation, as well as strain gauge outputs and failures. Furthermore, in all of the beam specimens, ε_{SGC} and ε_{SG1} prior to failure demonstrated close to identical strain values, highlighting the effectiveness of the 200 mm un-bonded distance between them.

Table 5:5 presents typical results using the outlined procedure and notice the very small variation in the moment arm as the load increases. This affirms the observation made during the test regarding the crack height in the constant moment arm zone, which, for both beams, did not change noticeably with increasing load. In addition, it also corroborates the reliability of this study as well as the RILEM TC-RC5, (1994) guidelines in assuming a constant moment arm for typical beam-bond tests. At the ultimate capacity of the beams, the corresponding concrete strain remain below the ϵ'_c value of $1,843 \mu strain$ signifying that throughout the duration of the test process, the concrete strain were well within the ascending portion of the stress-strain relationship shown in Figure 5:6.

Table 5:5: Summary of strain-load pairs from Point C onwards

ϵ_F ($\mu strain$)	ϵ_c ($\mu strain$)	T_F (kN)	Moment arm (mm)	M_{int} ($kN \cdot m$)	P from M_{int} (kN)
5,775	349	67.700	448.751	30.381	81.015 (BN2 at Point C)
5,840	354	68.462	448.745	30.722	81.926 (BN1 at Point C)
10,000	622	117.230	448.383	52.564	140.170
15,280	990	179.128	447.817	80.216	213.910 (BN1 Failure)
15,810	1,028	185.341	447.751	82.987	221.297 (BN2 Failure)

Figure 5:8 and Figure 5:9 show the computed and experimental load versus strain plots for BN1 and BN2, respectively. Concerning the failure of ϵ_{SG2} in BN2 at 93% of the maximum load, or equivalently, $205.8 kN$, a linear regression of its final slope prior to failure is sufficient since no cracking or sudden events occurred beyond approximately 74% of the maximum load. With the failure of the mentioned strain gauges accounted for and necessary computations made, Figure 5:10 and Figure 5:11 show the bar stress versus the strain for BN1 and BN2, respectively and note that the bar stress in the case of Notched beams is determined by multiplying ϵ_{SGC} strain values by the bar average elastic modulus presented in Table 5:2.

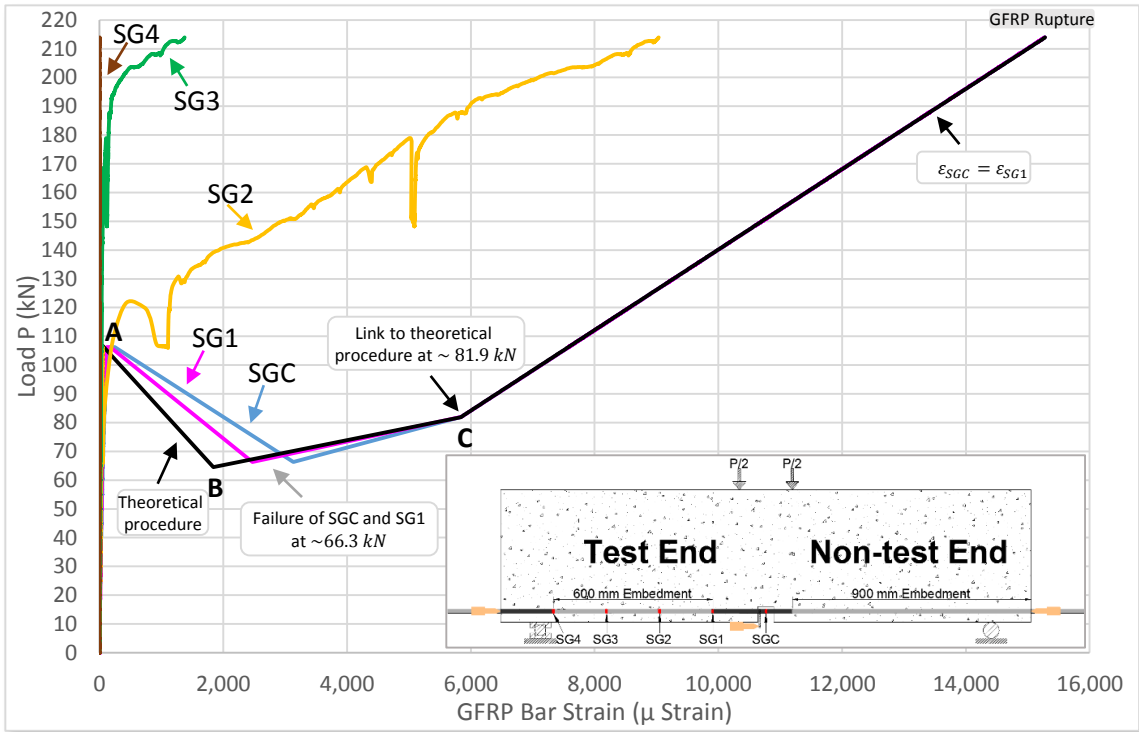


Figure 5:8: Load - GFRP bar strain in BN1

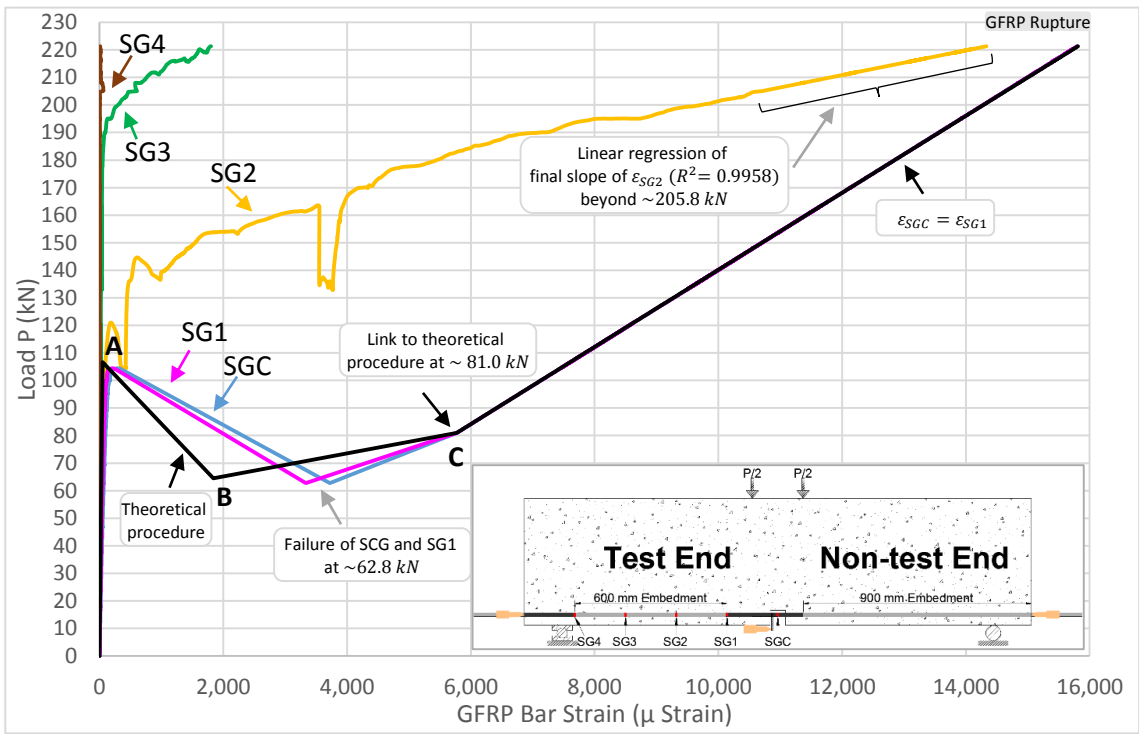


Figure 5:9: Load - GFRP bar strain in BN2

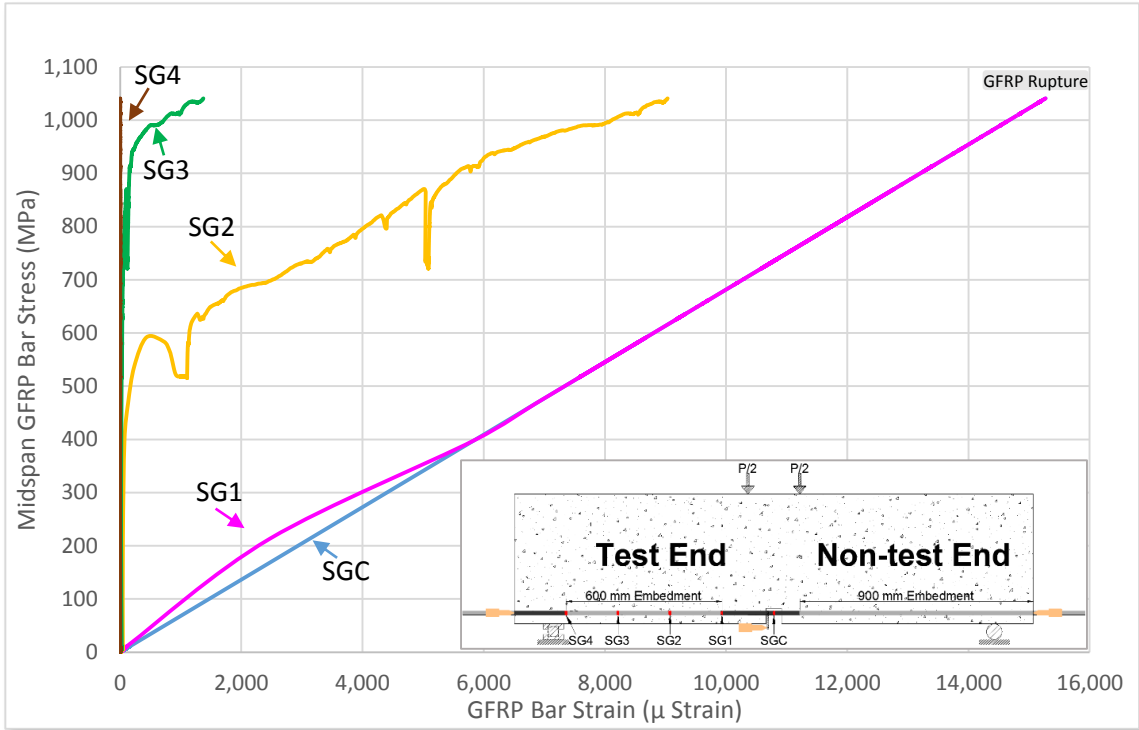


Figure 5:10: Midspan GFRP bar stress - GFRP strain in BN1

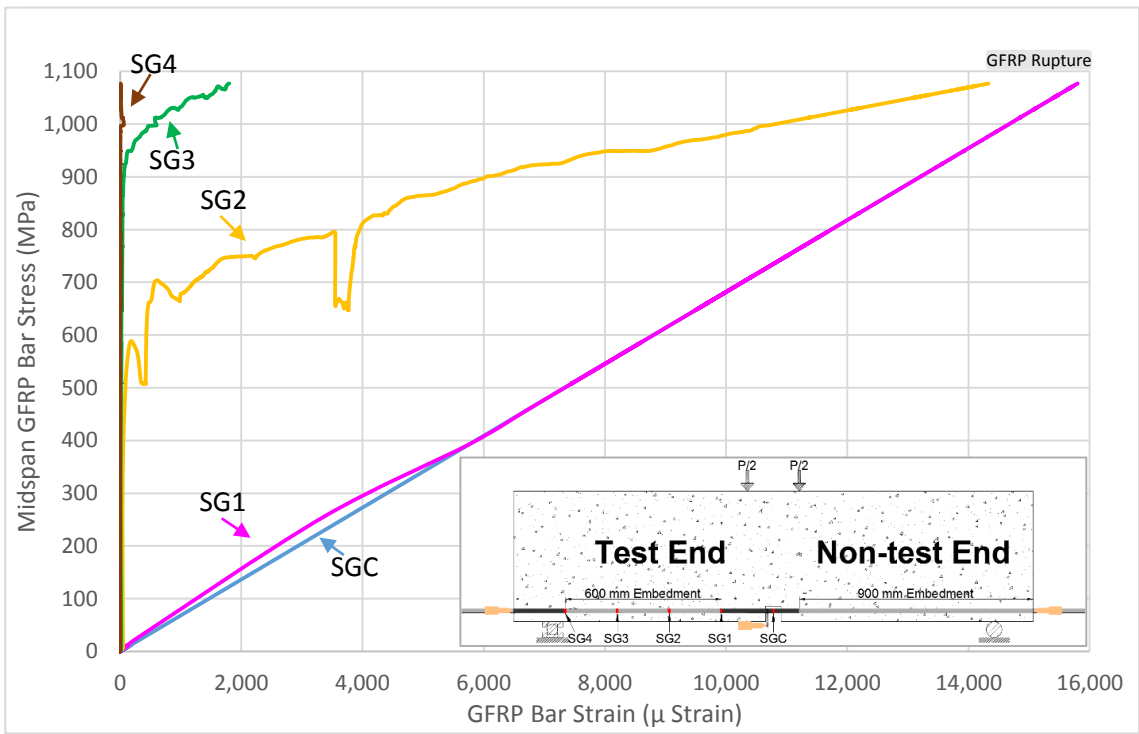


Figure 5:11: Midspan GFRP bar stress - GFRP strain in BN2

Overall, for the Notched beams, the strain approximations for SGC and SG1 beyond the point of their respective strain gauge failure results in the ultimate GFRP bar stresses presented in Table 5:6 and similar to the RILEM beams, note that these values are fairly consistent with the average of GFRP tensile test results presented in Table 3:1. This confirms the appropriateness of the method used to approximate the behavior of these strain gauges beyond their failure point.

Table 5:6: GFRP ultimate stress obtained from Notched beams

Notched Beam Strain Gauge	f_{Fu} (Mpa)
BN1-SGC and SG1	1,041
BN2-SGC and SG1	1,077
Avg.	1,059

The loaded-end bar slip measured by L1 is important for the purposes of this experimental program and it is therefore necessary to address the failure of L1 in BN1. As stated earlier, by inspection, it was discovered that this failure occurred due to the partial detachment of the gripping system shortly after the midspan flexural crack, at an approximate load of 66 kN. Figure 5:12 plots the load versus the L1 values for all of the beams for comparison purposes. With reference to this figure, up to the point shortly after the occurrence of the midspan flexural crack, BN1-L1 and BN2-L1 values are practically identical. However, during the subsequent reloading phase, BN2-L1 as expected, begins to show readings comparable to BR1-L1 and BR2-L1 whereas BN1-L1 readings, as Figure 4:30 illustrated, become highly unstable.

Besides L1 values for BN1 and BN2 being almost identical prior to the failure of BN1-L1, as mentioned previously, the overall flexural capacity, midspan and secondary crack formation as well as strain gauge readings for BN1 and BN2 are also highly comparable. This information justifies the approximation of BN1-L1 beyond its failure by assuming that it will follow the same pattern as BN2-L1. Therefore, the usage of a 3rd degree polynomial regression obtained from BN2-L1 with ($R^2 = 0.9489$) allows for the approximation of BN1-L1 beyond its failure at 66 kN, which corresponds to *Point B* in Figure 5:12. This results in an uncorrected loaded-end bar slip value of 8.9 mm at the failure load of BN1.

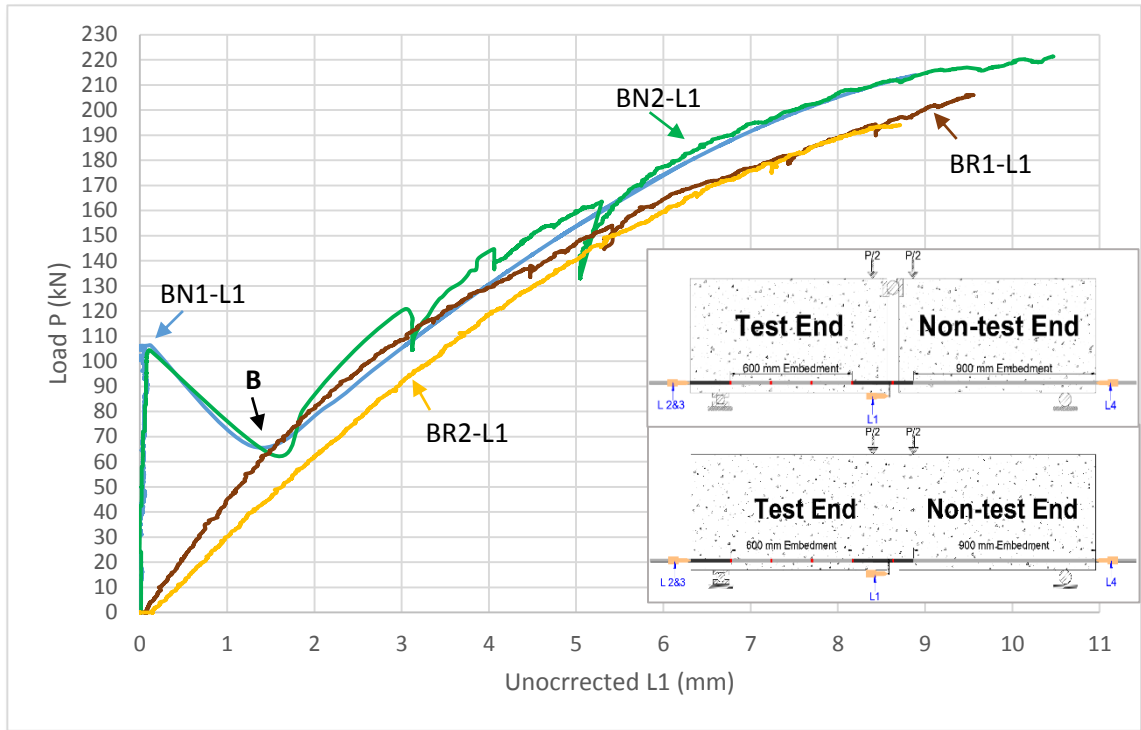


Figure 5:12: Load-uncorrected L1 in RILEM and Notched beam-bond tests

5.3.4 Modified Pullout Specimens

In the Modified pullout specimens, SG1 for both MP1 and MP2 failed during testing, evident by the fact that they began exhibiting a non-linear behaviour in the early stages of loading and furthermore, showed decreasing strain values despite continued increases in the loading. However, unlike the beam-bond tests, the pullout specimens are concentrically loaded and the direction of loading is along the longitudinal axis of the GFRP bar. This, combined with the fact that the 50 mm distance between the bottom of the specimen and the position of SG1 is un-bonded, allows for the direct determination of the ϵ_{SG1} values through the usage of the external applied load, P , as shown in Equation 5.16.

$$\epsilon_{SG1} = \frac{P}{A_F E_F} \tag{Equation 5.16}$$

Figure 5:13 and Figure 5:14 plot the load versus the GFRP axial strain for MP1 and MP2, respectively. For MP1, which was unconfined, unfortunately, the concrete splitting failure prevents the ability to compare, at all load levels, the bond stress distribution of MP1

to the beam-bond test results. In order to remain consistent with the presentation of the beam-bond test data, Figure 5:15 for MP1 and Figure 5:16 for MP2, plot the GFRP stress obtained by dividing P by A_F against the axial strain values along the GFRP bar. Note that as stated earlier, data from MP1-SG3 was lost during the test due to the malfunctioning of the designated data acquisition channel.

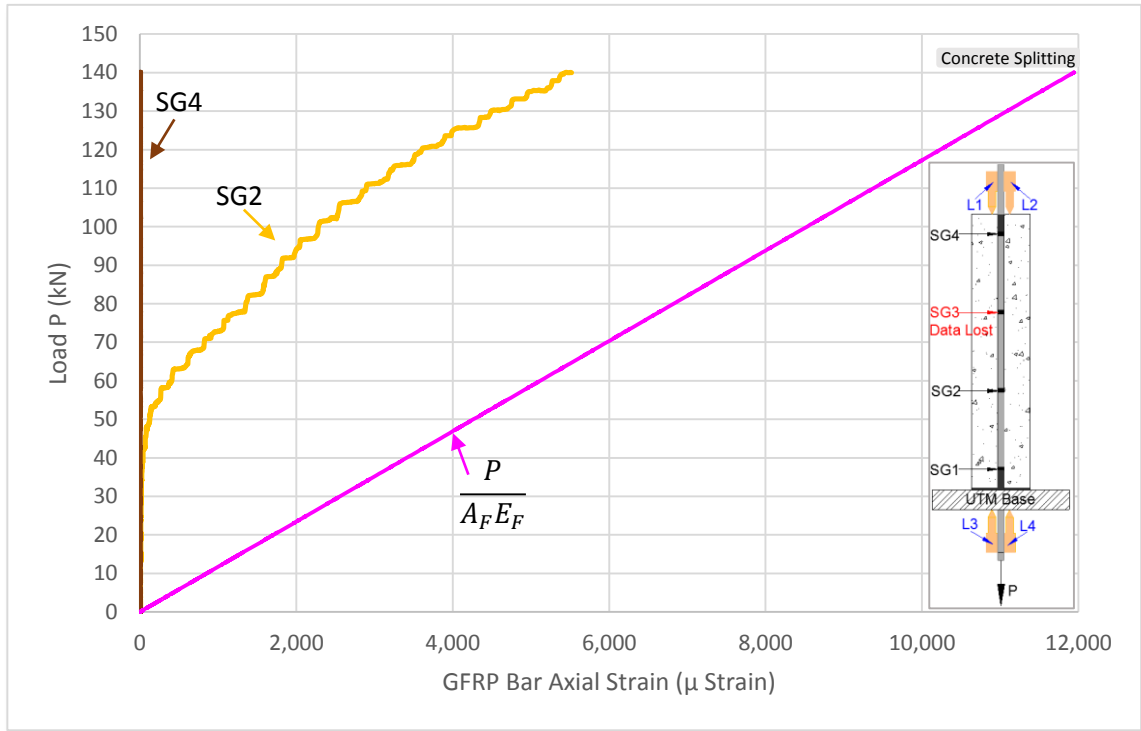


Figure 5:13: Load - GFRP bar axial strain in MP1

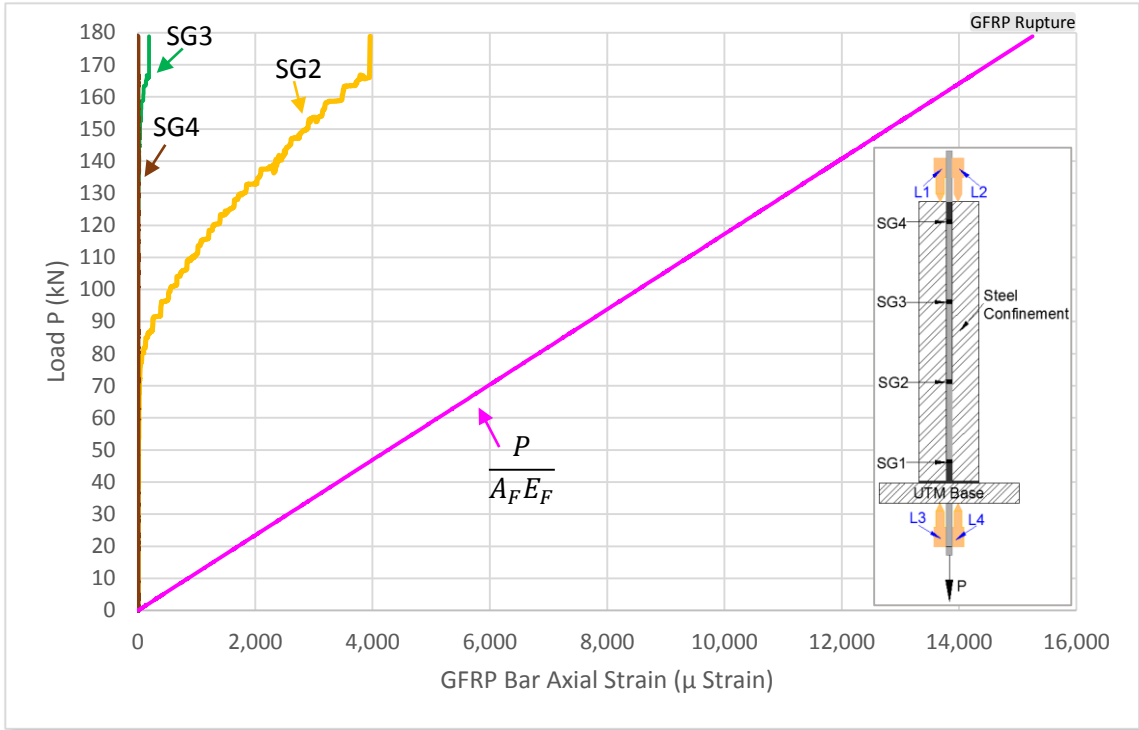


Figure 5:14: Load - GFRP bar axial strain in MP2

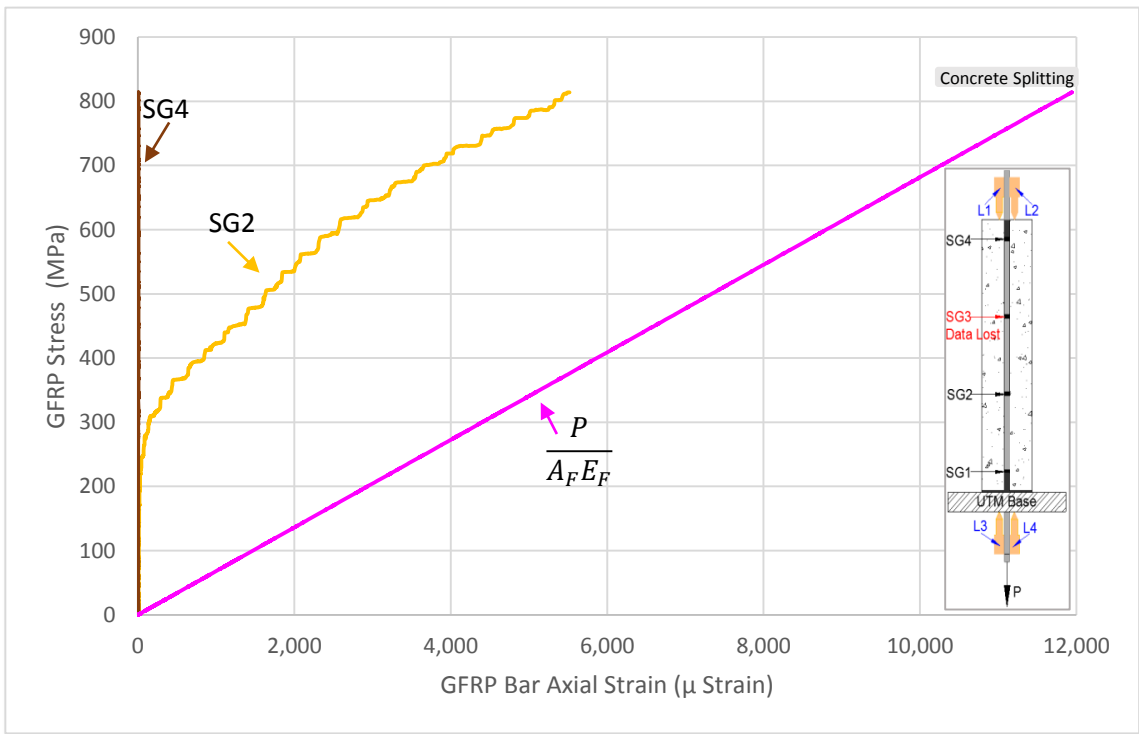


Figure 5:15: GFRP bar stress - GFRP axial strain in MP1

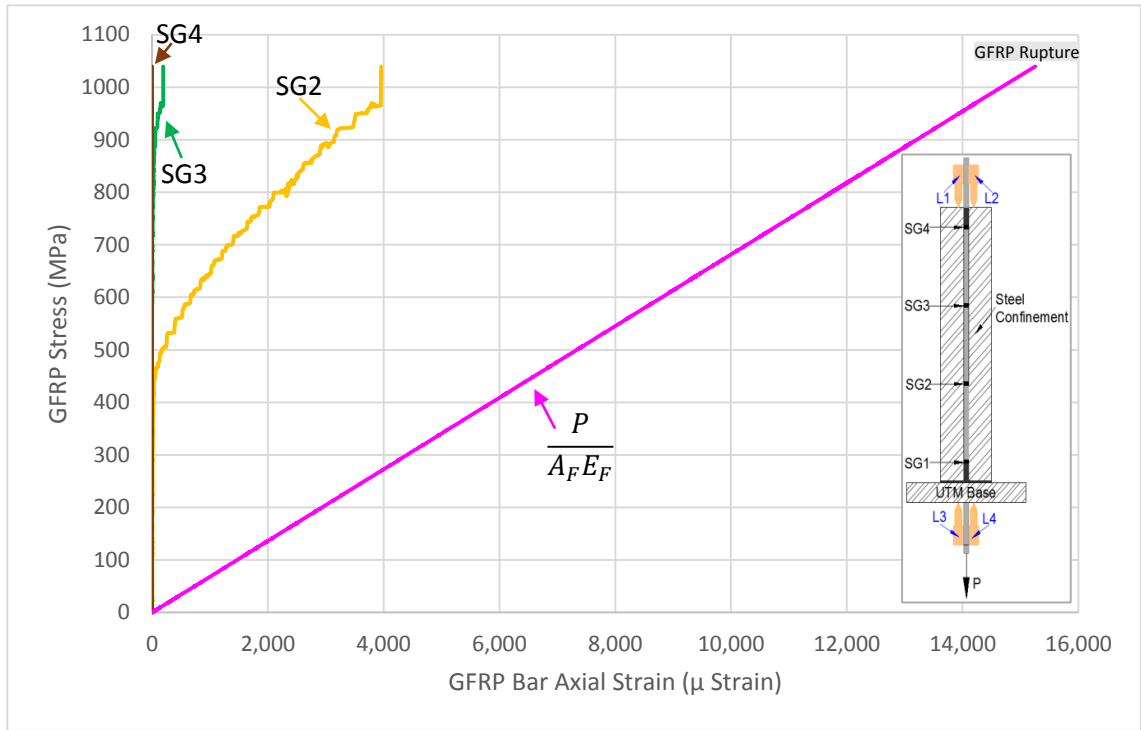


Figure 5:16: GFRP bar stress - GFRP axial strain in MP2

5.4 Concrete Splitting and Confinement

Concerning the concrete splitting failure of MP1, the CEB-FIP, (2000) provides a detailed explanation for this phenomenon, harking back to the observations first made by Abrams, (1913), who realized that bar deformations induce bearing stresses in the surrounding concrete in an inclined manner. In order to gain a better understanding of these inclined, radial forces, the majority of researchers who address bond splitting behaviour often use an enhanced visual representation suggested by Tepfers, (1973) and shown in Figure 5:17. According to Tepfers, (1973), the radial component of these forces are balanced by concrete tensile stresses forming in a hoop-like fashion in the immediate vicinity around the bar and when these stresses exceed the tensile strength of the concrete, splitting cracks develop. Thus, in MP1, a substantial number of these micro-splitting cracks were able to propagate through the entire clear cover of the specimen and since there was no other form of confinement besides the concrete, the sample eventually failed due to concrete splitting. Although bond-splitting failure is not a focus of this experimental

program, the preceding explanation was given to provide a reason for the observed behaviour of MP1.

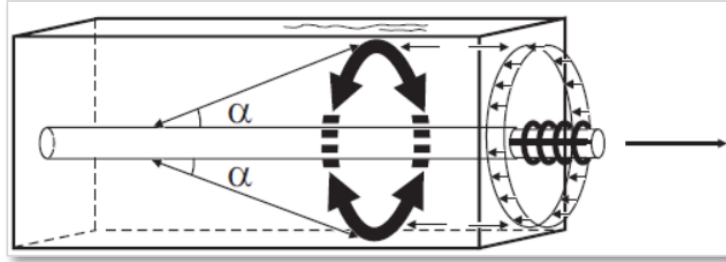


Figure 5:17: Internal bond forces. Tepfers and De Lorenzis, (2003)

Regarding MP2, the provided confinement was effective in preventing concrete splitting and therefore the specimen was able to reach its maximum capacity and fail through GFRP rupture as intended. Intuitively, there is an anticipation that this confinement in the form of external transverse pressure will enhance the bond performance of MP2, since by limiting the development and progression of splitting cracks, the confinement is effectively creating a more intimate contact between the GFRP and the concrete. The existence of a more intimate contact results in an increased efficiency in the transfer of forces from the bar to the concrete. Although it is not appropriate for this experimental program to compare the bond-stress distributions between MP1 and MP2, the data gathered from MP2 does serve the purpose of providing useful information regarding changes in the bond stress distribution up to the point of GFRP rupture. In addition, in real beams, as well as in the current test beams, stirrups provide confinement, so the results of MP2 are useful in assessing the effect of confinement on bond enhancement.

5.5 Bond Stress Distribution and Determination of Required Embedment Length

5.5.1 General

In this section, unless otherwise stated, all stress values as well as elastic moduli are in units of MPa , areas in mm^2 and dimensions in mm . As stated in ACI 440.1, (2006), the concept of bond stress distribution must begin with establishing a simple equilibrium relationship for a reinforcement embedded in another material, in this case a GFRP bar embedded in concrete as shown in Figure 5:18. Up to a certain limit, the intimate contact at the reinforcement-concrete interface resists any attempt to the pulling of the reinforcement from its embedment and this resistance, referred to as the bond stress, along with its distribution, is a primary focus of this study. As described in Sections 1.2 and 1.5 several factors influence the quality of the contact, or the bond, between the reinforcement and the concrete and as the pulling force increases, there is some degradation of this bond. If the quality of bond is very low but there exists sufficient concrete cover or some form of confinement to prevent concrete splitting failure, then there is a high probability that the incremental degradation of the bond with increasing load will progress along the reinforcement through the entire length of the specimen, regardless of the embedment length. This will result in a pullout failure, which is abrupt and undesirable. If instead, the quality of the bond, the cover or confinement and the length of the embedment is adequate, the progression of the bond degradation will be limited and the bar will eventually reach its ultimate strength.

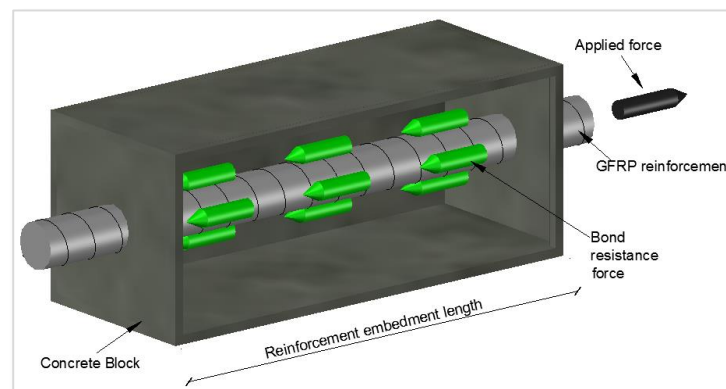


Figure 5:18: Bond resistance of an embedded reinforcement

5.5.2 Current Practice

As established by numerous authors, Perry and Thompson, (1966), Benmokrane et al., (1996), the bond stress distribution along a reinforcement is in fact non-linear and the reason most current guidelines continue to assume uniform distribution is for simplicity. In the presence of good bond quality, the development length is a term referring to the embedment required for the reinforcement to reach a desired stress level and since this is a concept that has a physical meaning and can be quantified easily, current guidelines provide development length equations based on the following procedure.

Imagine an infinitesimal length dx of a reinforcing bar embedded in concrete as shown in Figure 5:19.

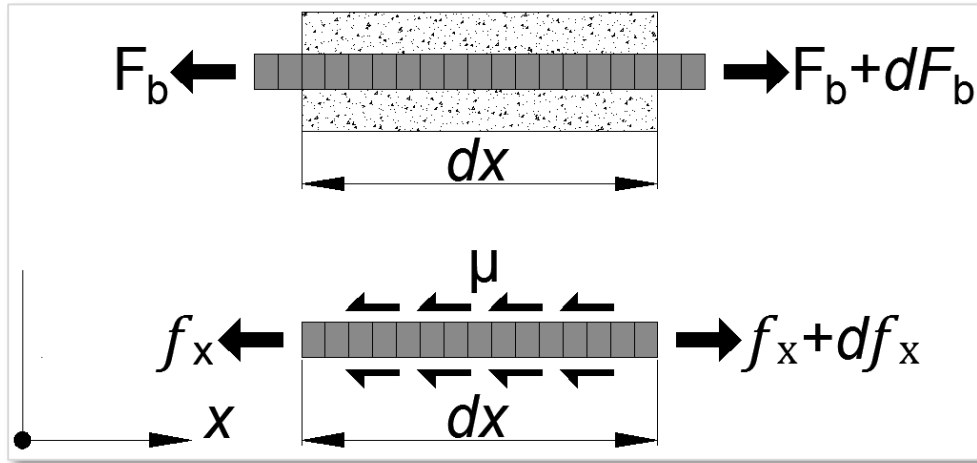


Figure 5:19: State of stress in an infinitesimal length of a reinforcing bar embedded in concrete

Let the bar have diameter d_b and be subjected to increasing axial stress f_x along its length. Let the bond stress be μ and constant over the length dx . From equilibrium of axial forces acting on the bar,

$$A_b(f_x + df_x) - f_x A_b - \mu \pi d_b dx = 0 \quad \text{Equation 5.17}$$

Knowing that $A_F = \frac{\pi d_b^2}{4}$, Equation 5.17 can be recast as,

$$\frac{df_x}{dx} = \frac{4\mu}{d_b} \quad \text{Equation 5.18}$$

For a constant μ and $f_x = 0|_{x=0}$, Equation 5.18 gives,

$$f_x = \frac{4\mu}{d_b}x \quad \text{Equation 5.19}$$

For steel rebar, if $f_x = f_y$, then,

$$f_y = \frac{4\mu}{d_b}l_d \quad \text{Equation 5.20}$$

where l_d is defined as the development length of the bar. For FRP bars, f_y may be replaced either by its ultimate stress, f_{Fu} , or by its design stress at ultimate. Note that in some cases, Equation 5.20 is expressed in a slightly different form as,

$$l_d = \frac{f_y A_b}{\mu \pi d_b} \quad \text{Equation 5.21}$$

The assumption of a uniform bond stress μ is reasonable if the actual bond stress is linearly distributed over the development length, in which case μ represents the average bond stress, but for any other distribution the specification of an average value, without considering the actual form of the distribution is not appropriate. In many cases the crack spacing is much smaller than the development length and the bond stress distribution between two cracks may deviate strongly from linearity. In the latter case knowledge of actual bond stress distribution is necessary, both for evaluating tension-stiffening and for predicting deflection and bond loss, which is crucial to the correct evaluation of the ultimate strength and mode of failure of a beam.

It is widely known and accepted that the bond stress distribution along a bar embedded in concrete is a function of the bond-slip relationship. The amount of slip also depends on the level of stress in the bar. Hence, the bond stress amplitude and shape depend on the amount of slip experienced by the bar. The bond-slip relationship can be derived from basic mechanics as described here:

Consider a reinforcing bar embedded in concrete as in Figure 5:20.

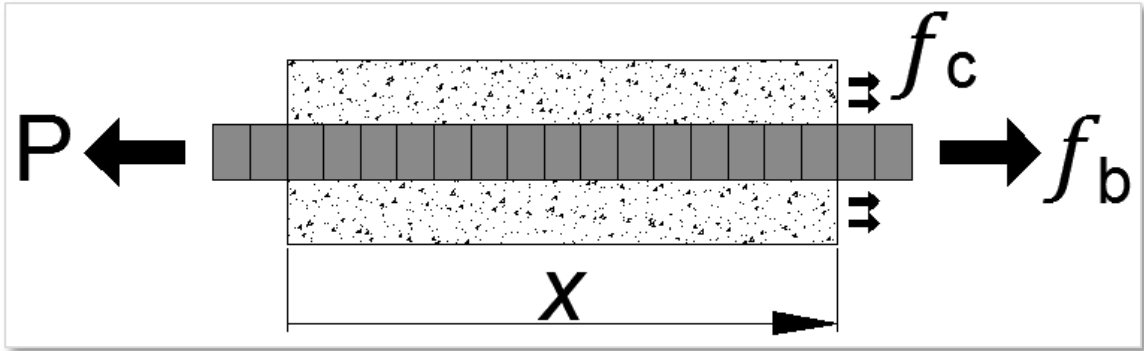


Figure 5:20: Equilibrium of an embedded stressed bar in concrete

From equilibrium of forces,

$$P = F_c + F_b \quad \text{Equation 5.22}$$

where P is the applied force acting on the bar at its loaded-end and F_c and F_b are the forces in concrete and reinforcing bar at a certain distance x , from the loaded-end. Forces F_c and F_b can be expressed in terms of concrete and bar stresses as,

$$P = A_c E_c \varepsilon_c + A_b E_b \varepsilon_b = A_c E_c (\varepsilon_c + n_b \rho \varepsilon_b) \quad \text{Equation 5.23}$$

where n_b and ρ are the modular and reinforcement ratios, respectively. It should be pointed out that in pullout tests; the concrete stress at the loaded-end is actually compressive rather than tensile.

On the other hand, slip, s , is defined as the relative deformation of concrete and the bar at their interface, i.e.,

$$s = \Delta_b - \Delta_c \quad \text{Equation 5.24}$$

or

$$\frac{ds}{dx} = \frac{d\Delta_b}{dx} - \frac{d\Delta_c}{dx} = \varepsilon_b - \varepsilon_c \quad \text{Equation 5.25}$$

where Δ_b and Δ_c are the deformations of the bar and the concrete at their interface at location x along the bar.

If we take the derivative of P with respect to x in Equation 5.23 and knowing that $\frac{dP}{dx} = 0$, then,

$$A_c E_c \left(\frac{d\varepsilon_c}{dx} + n_b \rho \frac{d\varepsilon_b}{dx} \right) = 0 \quad \text{Equation 5.26}$$

which gives,

$$\frac{d\varepsilon_c}{dx} = -n_b \rho \frac{d\varepsilon_b}{dx} \quad \text{Equation 5.27}$$

In view of Equation 5.25 and Equation 5.27,

$$\frac{d^2 s}{dx^2} = (1 + n_b \rho) \frac{d\varepsilon_b}{dx} \quad \text{Equation 5.28}$$

since $\frac{df_b}{dx} = \frac{4\mu}{d_b}$,

$$\frac{d\varepsilon_b}{dx} = \frac{4\mu}{E_b d_b} \quad \text{Equation 5.29}$$

Substituting the latter in Equation 5.28,

$$\frac{d^2 s}{dx^2} = \frac{4(1 + n_b \rho)}{E_b d_b} \mu \quad \text{Equation 5.30}$$

or

$$\frac{d^2 s}{dx^2} = c\mu \quad \text{Equation 5.31}$$

Equation 5.36 is the basic bond stress-slip relationship. Clearly, when μ is not a constant, the solution of this equation depends on the variation of the bond stress, μ . If the bond stress becomes a nonlinear function of slip, which is known to be the case, then Equation 5.36 is a nonlinear differential equation. Previous researchers including Somayaji and Shah, (1981), Yang and Chen, (1988) and Focacci et al., (2000) have proposed

numerous solutions. The assumption that $\frac{dP}{dx} = 0$ does not apply to beams. In beams under flexure, $P = 0$ and $F_b = -F_c$. On the other hand, $F_b = \frac{M}{jd}$, where M is the bending moment and jd is the internal moment arm at section of interest. Proceeding in this manner is not particularly useful as bond-slip is a local phenomenon, rather than an entire cross-sectional phenomenon. Furthermore, concrete stresses at any section vary in a complex manner over the height of the beam, especially after cracking and the advent of nonlinearity. In this study, although some attempt will be made to relate measured slips to theoretically expected values, it is not the purpose of this study to develop a bond-slip model for FRP reinforced beams. Instead, the focus will be on the bond stress distribution, which can be quantified experimentally.

5.5.3 Bar Strain Distribution along Embedment Length

As stated earlier, the LVDTs attached to the unloaded-ends of the beam-bond and the Modified pullout specimens did not show any slippage for the duration of the tests, indicating that the bond and the development length were sufficient in these samples. This statement can also be confirmed by observing the strain distribution along the GFRP bar, particularly within the embedment length. Since MP2 as well as the beam-bond tests failed through GFRP rupture at slightly different stress values in the bar, to make a comparison between these samples, it is necessary to normalize the data by dividing the load from each sample by the respective maximum load obtained during the testing, shown in Table 5:7. Note that for MP1, which experienced concrete splitting, this normalization will occur by using the average ultimate load obtained from the tensile testing results presented in Table 3:1.

Table 5:7: Maximum GFRP load used for normalization

Specimen Designation	P_{max} (kN)
BR1	206.0
BR2	194.0
BN1	213.9
BN2	221.3
MP1	183.4
MP2	178.8

Figure 5:21 to Figure 5:23 show the strain distributions for the specimens in this experimental program at increments of 10% of P_{max} and note that the distributions for MP1 are limited to 70% of P_{max} due to the premature splitting of concrete in this specimen at 76% of its P_{max} . In addition, as stated earlier, since MP1-SG3 malfunctioned during the

test, with reference to Figure 5:23, there is no data available for the bar strain in MP1, at distance of 400 *mm* from the loaded-end.

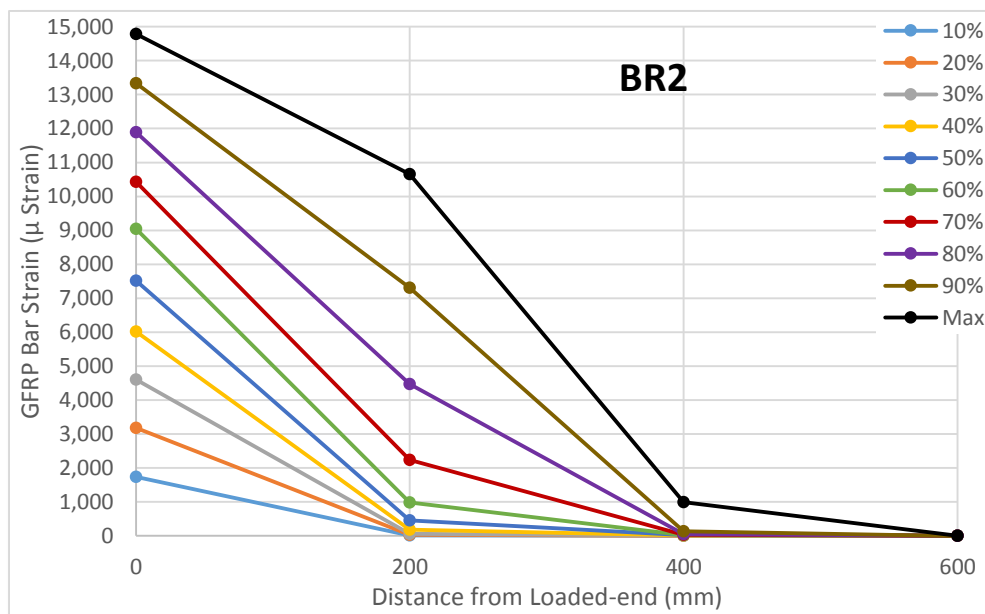
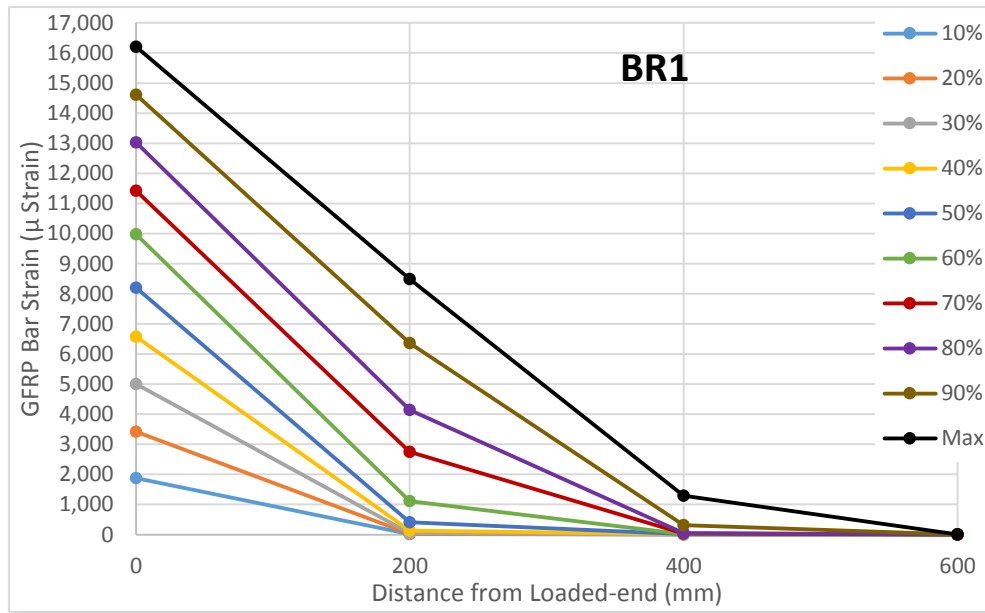
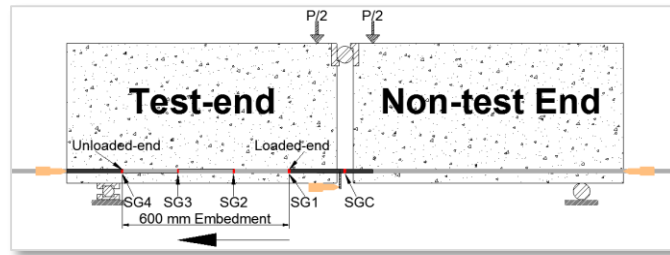


Figure 5:21: Strain distribution along the bar embedment length of the RILEM beams at different percentages of their respective maximum load, P

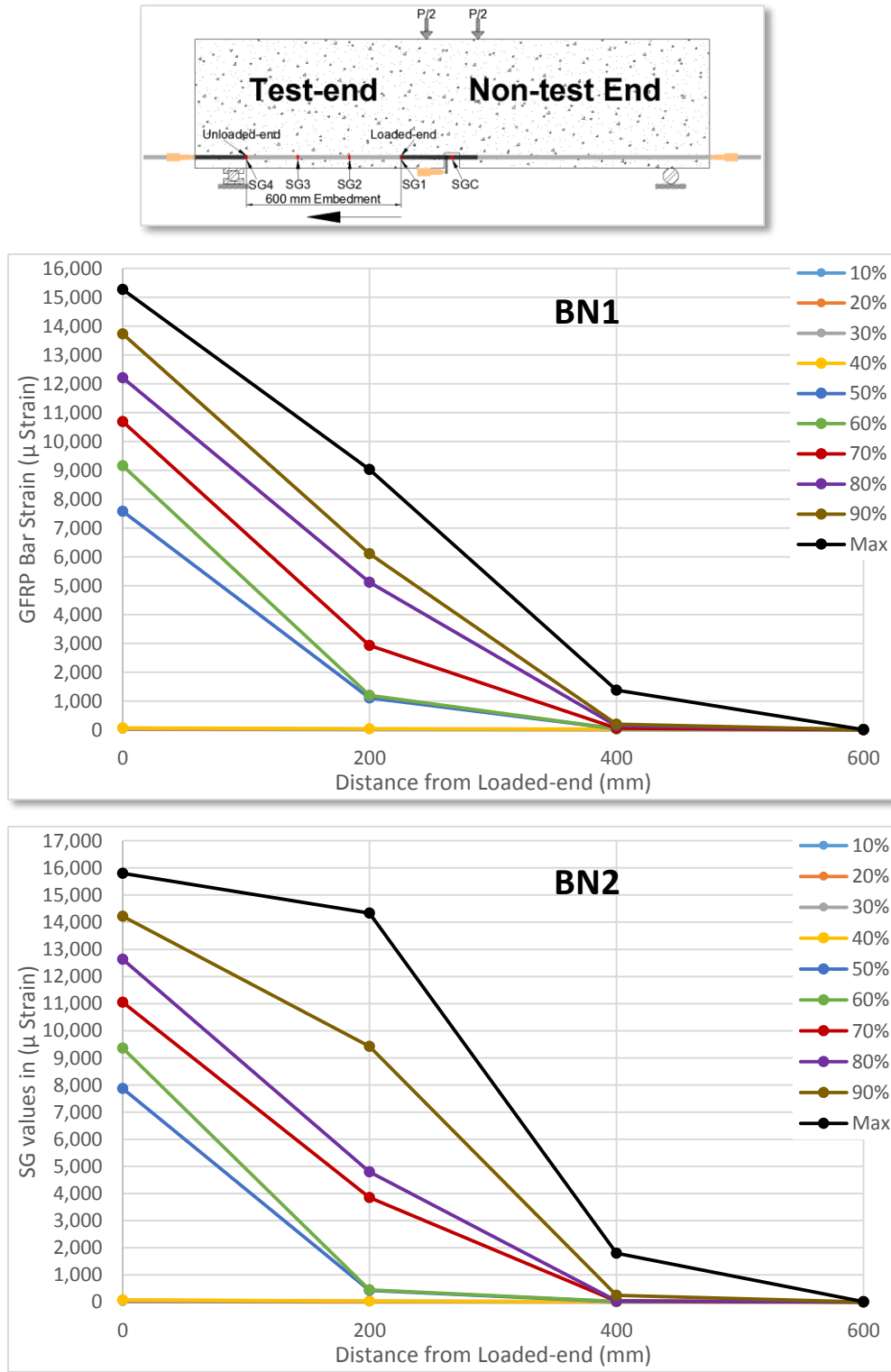


Figure 5:22: Strain distribution along the bar embedment length of the Notched beams at different percentages of their respective maximum load, P

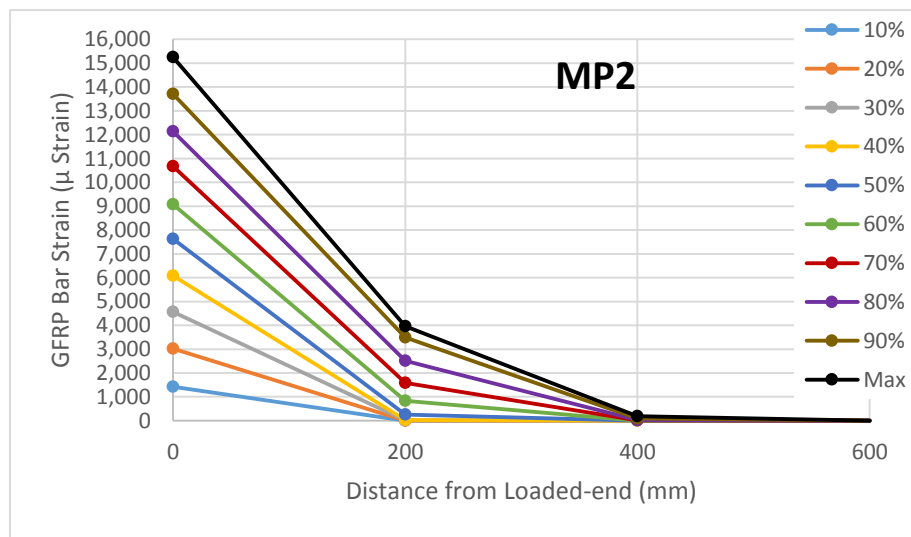
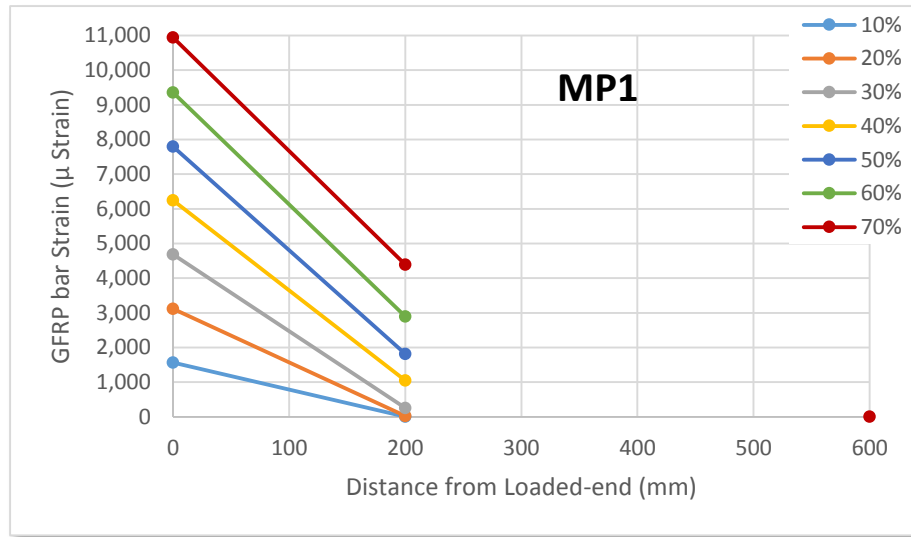
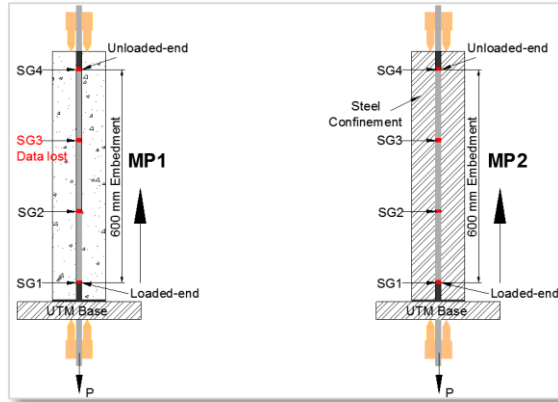


Figure 5:23: Strain distribution along the bar embedment length of the Modified pullout specimens at different percentages of their respective maximum load, P

From the presented strain distribution figures, it is possible to arrive at some conclusions, the first being the non-linearity of the strain distributions particularly at higher bar stress levels. Second, as the bar stress increases, more of the embedment length is mobilized, however, since the bond quality is adequate, there exists a dormant region close the bar unloaded-end, where the strain readings are either non-existent or relatively insignificant. The CEB-FIP, (2000) also notes the existence of a dormant region for what it calls long members. Note that for MP2, this region is slightly larger compared to the other specimens in this study. For the beam-bond specimens, particularly at the maximum load, the region located from 400 mm from the bar loaded-end to the bar unloaded-end is mobilized, however, for MP2, this region remains dormant throughout the test. The cause of a larger dormant region along the embedment length of MP2 may be the transverse pressure around this specimen, which enhanced intimate contact between the GFRP and the concrete, allowing a more efficient and stronger transfer of stresses between the two materials.

For BN2 and to a lesser degree for BR2, in the region within 200 mm from the loaded-end, which is between the location of SG1 and SG2, there is noticeable bond degradation at P_{max} since the difference in strain values between these two limits is decreasing. This does not imply that only BN2 and BR2 experienced bond degradation because all bond specimens undergo a certain degree of bond deterioration, depending on the GFRP bar stress level, but for BN2 and BR2 the severity of this phenomenon at P_{max} is such that it is observable through their strain distribution plots. For the Notched beams, the extent of the concrete contribution to tensile resistance is evident through the fact that up to approximately 50% of P_{max} , the strain values along the GFRP bar embedment length are negligible and this is in contrast to the RILEM beams and the Modified pullout specimens, which do not benefit from this contribution.

5.5.4 Alternative Method

One of main purposes of this study is to suggest a different method that could be used to determine the required development length, specifically, one that does not assume uniform bond stress distribution. At first glance of Figure 5:21 to Figure 5:23, one may conclude that the strain distribution along the GFRP bar embedment length, particularly at lower load levels, is likely exponential, however, this is not the case and the observed pattern is a result of the lack of information with regards to the strain distribution and extent of bond degradation between the positions of the strain gauges. This is the dilemma faced in these types of studies because increasing the number of surface strain gauges will improve the knowledge regarding the variation in the strain along the bar but it will also have negative consequence because it will result in increased debonding of the bar from

the concrete along the embedment length. On the other hand if the number of these gauges are limited as in this study, there is likelihood of full bond between the reinforcement and the concrete, however, knowledge of the complete strain distribution along the bar embedment length may not be attainable. Figure 5:24 provides an illustration of the impact of a lack of data between the positions of strain gauges.

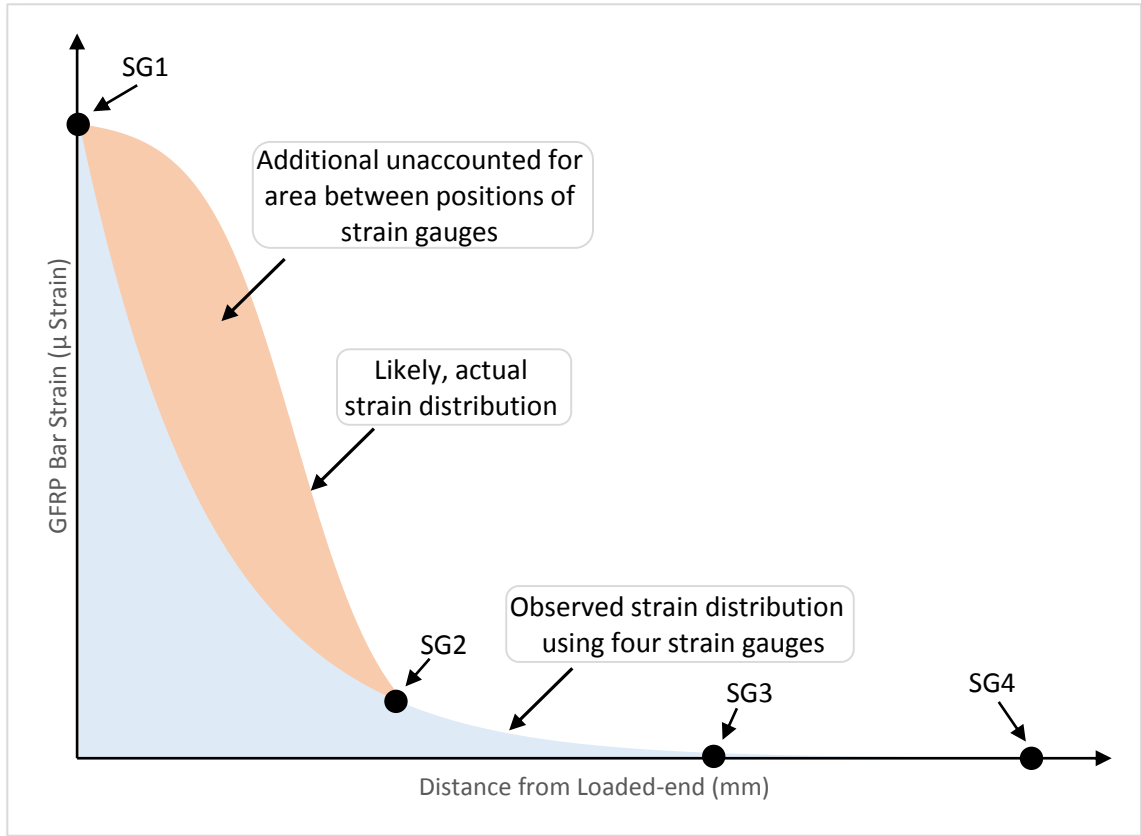


Figure 5:24: Effect of the lack of information on the strain distribution between the positions of strain gauges

From Figure 5:24, it is evident that depending on the spacing of strain gauges along the bar, a lack of knowledge regarding the strain values between these gauges can strongly influence the derived pattern of the strain distribution. Note in this figure, that SG2 will display similar strain values to SG1 only when the GFRP stress level is high enough to cause the bond degradation to extend to the position of SG2 while prior to this occurrence, there is a false notion that the strain distribution is exponential. With reference to Figure 5:21 and Figure 5:22, for BR2 and BN2 at their respective P_{max} , the bond degradation has nearly extended to the position of SG2, which lies 200 mm from the loaded-end and note the strain distribution pattern has no resemblance to an exponential function.

One method of increasing the number of strain gauges along the FRP bar, without decreasing bond, may be to follow the work of Nanni et al., (1995), who in their pullout specimens with a maximum bar embedment length of 127 *mm*, placed internal gauges by boring smooth FRP bars and inserting an aluminum tube with adhered, axially measuring strain gages inside followed by epoxy fillings. The FRP boring method for the Modified pullout specimens of this experimental program would not be practical since the boring distance, including the 600 *mm* embedment length, the 50 *mm* unbonded length to the top of the specimen and the excess GFRP bar needed for LVDT attachments at the unloaded-end of the specimens would be in excess of 650 *mm*. In addition, the boring technique for the beam-bond specimens with total length of 2,000 *mm* would be impractical. Furthermore, the placement of an aluminum tube inside the GFRP bar would significantly reduce the number of glass fibres and not allow this experimental program to achieve specimen failure through bar rupture. Nanni et al., (1995) observed that direct placement of surface strain gauges onto deformed FRP bars produced inconsistent results, but the strain gauge placement technique in this experimental program, which made use of a thin layer of epoxy to ensure a smooth contact surface for the gauges, resulted in quite consistent output from the gauges. Feldman and Bartlett, (2007), following a procedure proposed by Nilson, (1971), used hollow steel bars in their pullout specimens and were therefore able to split the bar in half, place numerous strain gauges inside and rejoin the two halves by welding prior to testing, a technique not possible for GFRP reinforcement which depend on longitudinal fibres for their strength.

Perhaps the best method to ensure a precise and continuous monitoring of strain along a GFRP reinforcement would be to follow the work of Zhou et al., (2003), who incorporated Optical Fibre Brag Grating, (OFBG), directly into the pultrusion manufacturing process of the GFRP bars. This technique is advantageous because it monitors strain at small increments without the debonding, damage and possible inconsistencies associated with the usage of the traditional surface strain gauges. The introduction of these optical fibres was not detrimental to the mechanical properties of the GFRP and CFRP bars and in addition, by placing strain gauges onto the concrete, Zhou et al., (2003) were able to calculate the slip of the bar relative to the concrete by simply taking the difference between the strain from the FRP and the concrete. Overall, the OFBG technique seems to be a good alternative for strain measurements along FRP bars, however, few researchers have used optical sensors in their bond experiments and furthermore as Zhou et al., (2003) illustrated, the OFBGs are limited in terms of the maximum tensile strain that they can record.

If it were possible to obtain the strain distributions at small increments along the reinforcement and to fit an expression that would define this distribution, then as Equation 5.32 indicates, the derivate of this expression, would provide the bond stress function.

$$\mu(x) = \left(\frac{d\varepsilon_b}{dx}\right) \left(\frac{E_b A_b}{\pi d_b}\right) \tag{Equation 5.32}$$

In Equation 5.32 as well as subsequent equations, x is the distance from the onset of the embedment length at the loaded-end towards the unloaded-end. With reference to Figure 5:24 as well as the observation of the strain patterns, particularly for BR2 and BN2 at P_{max} , it is the recommendation here that in the presence of sufficient strain data along the GFRP reinforcement, one could attempt the curve fitting of reinforcement strain along the bar embedment length by a modified form of the logistic growth function. This expression, shown in Equation 5.33 and illustrated graphically in Figure 5:25 for BR2 at P_{max} , includes the impact and extent of bond degradation from the loaded-end and it is able to capture the rapid decrease in strain along the GFRP reinforcement beyond the point of significant bond degradation. Note that Equation 5.33 contains three constants, a , b and c and as it will be illustrated, for a unique solution, it is critical to express two of these constants in terms of the third by using convenient constraints and then optimizing only one constant to fit a curve corresponding to the given data points.

$$\varepsilon_F(x) = \frac{1}{a + be^{cx}} \tag{Equation 5.33}$$

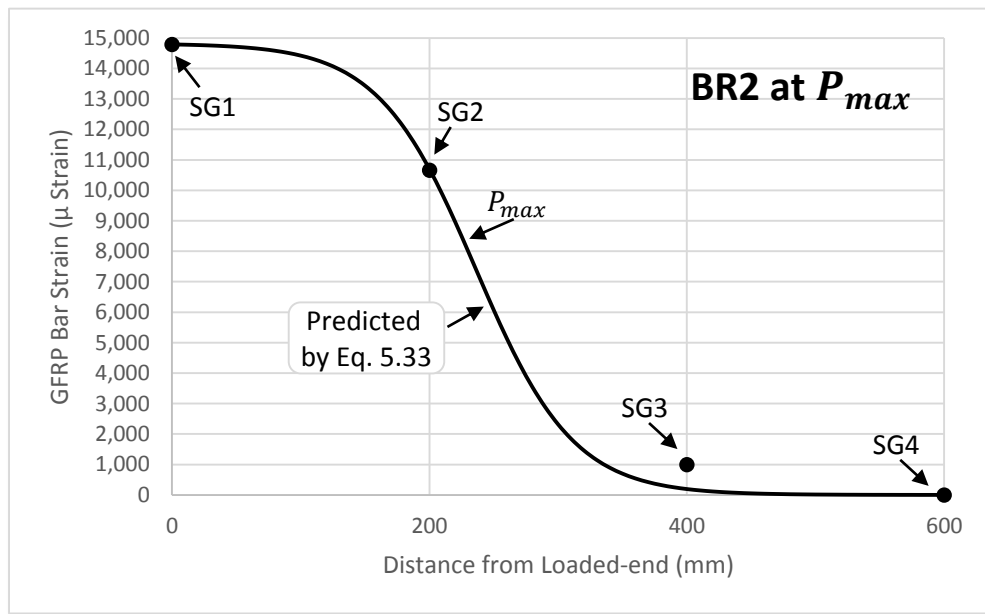


Figure 5:25: Proposed expression for defining strain as a function of bar embedment length

To determine the value of the constants, a , b and c in Equation 5.33, two constraints may be the strain at the onset and end of the embedment length. For example, applying Equation 5.33 to beam BR2 at P_{max} , in order to arrive at the curve shown in Figure 5:25, one would proceed as follows:

$$\varepsilon_F(0) = 14.79 \times 10^{-3}$$

$$\varepsilon_F(l_e) = 0.10 \times 10^{-5} \text{ [If this strain is zero, it must be set at a very small value because due to the nature of this function, a value of zero is not acceptable.]}$$

Substituting $\varepsilon_F(0)$ and $\varepsilon_F(l_e)$ in Equation 5.33 results in,

$$a = \frac{1}{\varepsilon_F(0)} - b \tag{Equation 5.34}$$

$$c = \frac{\ln \left[\frac{1/\varepsilon_F(l_e) - 1/\varepsilon_F(0) + b}{b} \right]}{l_e} \tag{Equation 5.35}$$

Now substituting Equation 5.34 and Equation 5.35 into Equation 5.33 and using curve fit of the strain data points to optimize the value of b produces,

$$b = 0.133$$

which in turn results in,

$$a = 67.480$$

$$c = 0.026$$

Substituting these constants back into Equation 5.33 gives,

$$\varepsilon_F(x) = \frac{1}{67.408 + 0.133e^{0.026x}} \tag{Equation 5.36}$$

By increasing the value of x from zero at the loaded-end to 600 mm at the end of the embedment length, Equation 5.36 was used to generate the curve presented in Figure 5:25 which compares favorably with the measured values given by SG2 and SG3. For the beam-bond specimens and the Modified pullout sample, MP2, at load increments of 30% P_{max} , 60% P_{max} and P_{max} , Figure 5:26 to Figure 5:28 show the experimental data points obtained from the strain gauges along the 600 mm embedment length of the GFRP bar versus the curves generated from Equation 5.33 using the described method. Note that Figure 5:27 only includes analysis of 60% P_{max} and P_{max} since the strain data points at 30% P_{max} , were negligible in the Notched beams.

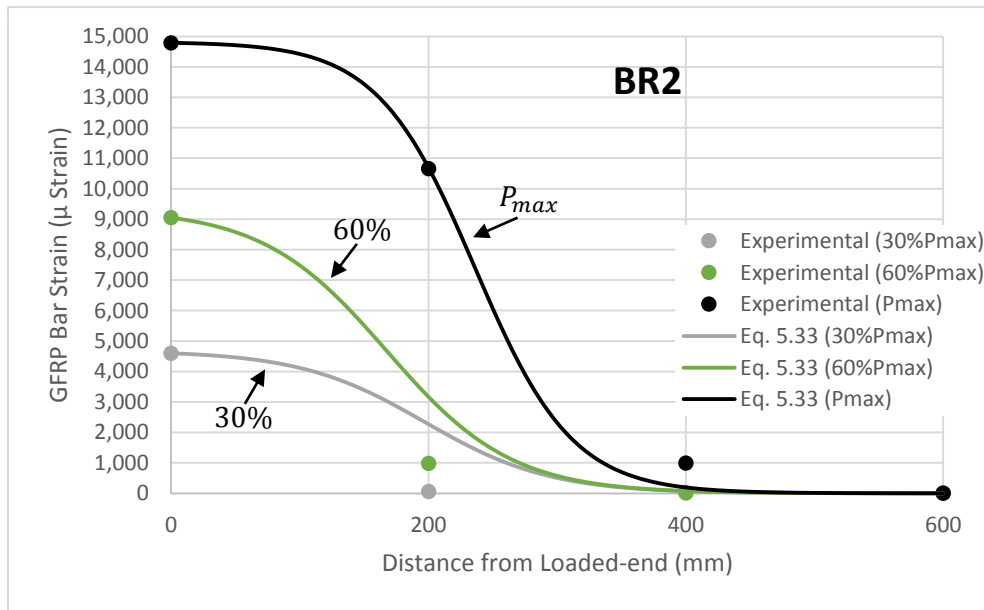
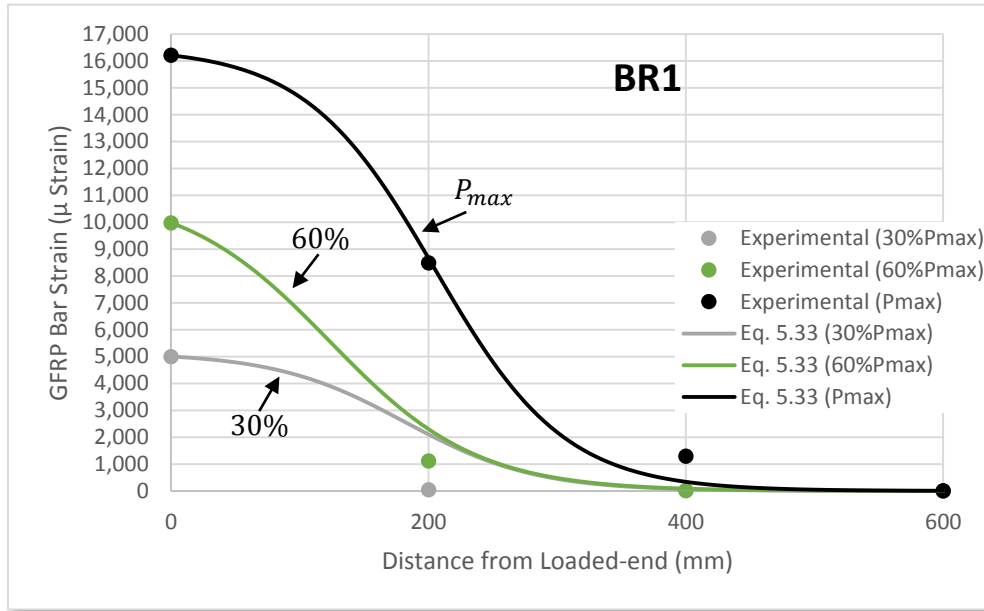
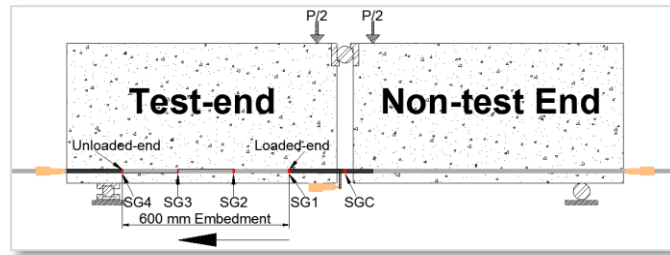


Figure 5:26: Experimental data points versus predicted strain distribution by Equation 5.33 for RILEM beams

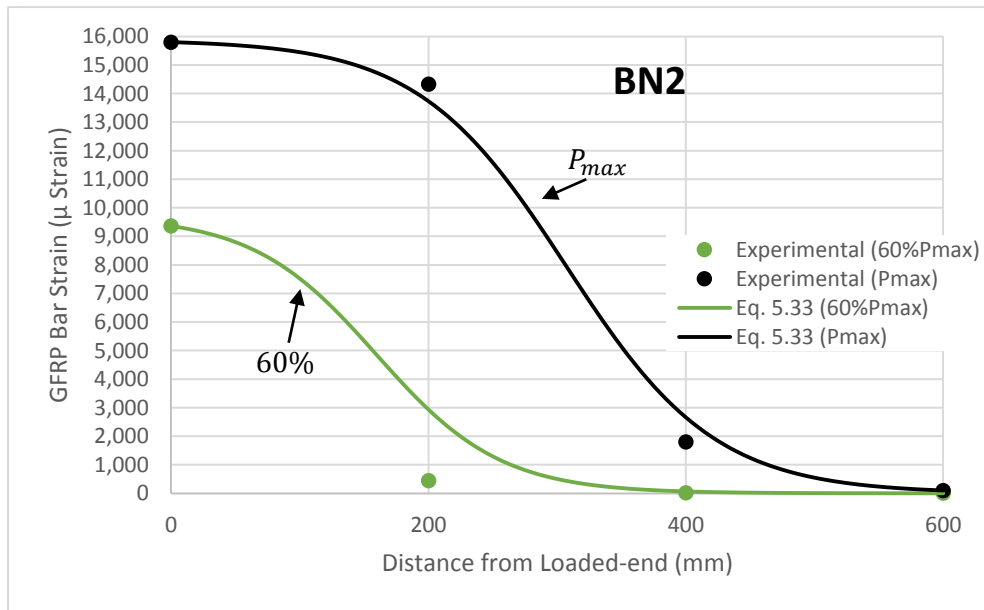
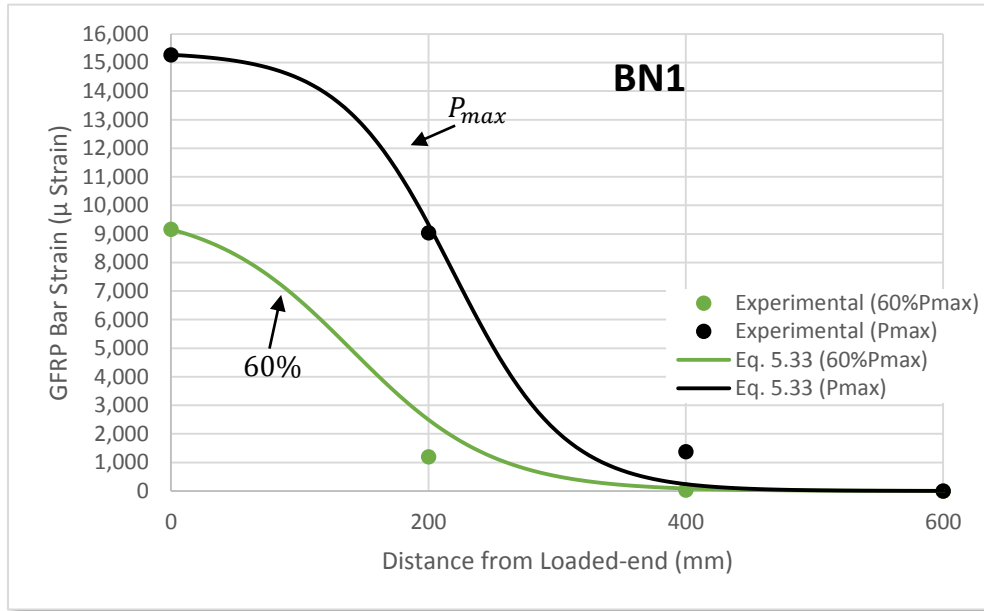
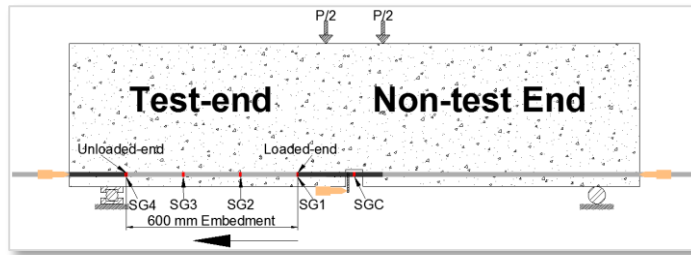


Figure 5:27: Experimental data points versus predicted strain distribution by Equation 5.33 for Notched beams

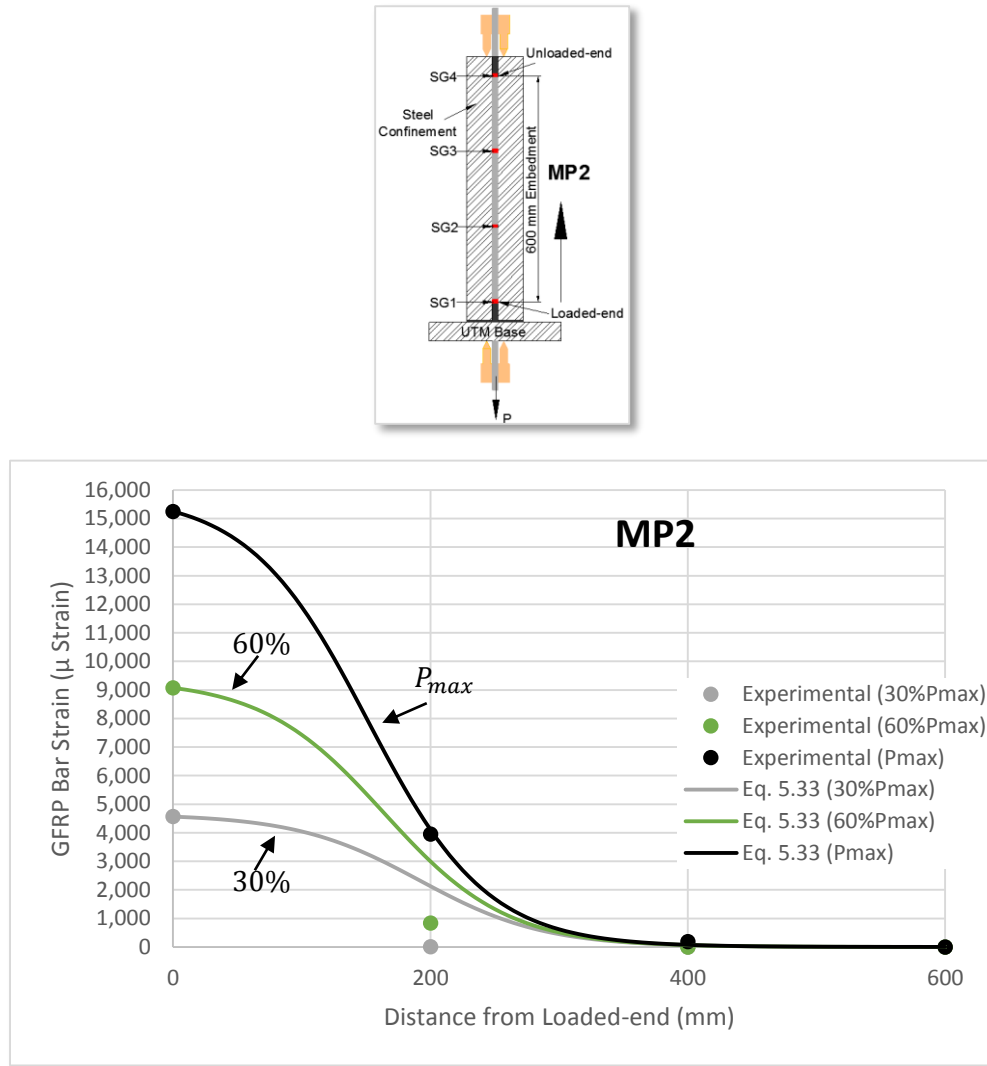


Figure 5:28: Experimental data points versus predicted strain distribution by Equation 5.33 for Modified pullout specimen, MP2

The shape of the curves in Figure 5:26 to Figure 5:28 is consistent with the strain distributions in this experimental program, particularly at higher load levels as well as those obtained by others, Abrams, (1913), Perry and Thompson, (1966), Benmokrane et al., (1996) and Feldman and Bartlett, (2007), who plotted bar stress/strain along the reinforcement embedment length at different load levels. To reiterate, knowledge of the strain distribution at smaller increments than those used in this study would certainly aid in the accuracy of the fitted function. Table 5:8 presents the values of the constants a , b and c in Equation 5.33, used to achieve the fitted curves shown in Figure 5:26 to Figure 5:28.

Table 5:8: Values of the constant, b in Equation 5.33 used to produce fitted curves

Constant in Equation 5.33	BR1	BR2	BN1	BN2	MP2
30% of P_{max}					
a	194.593	213.697	N/A		215.060
b	5.362	3.746			4.070
c	0.020	0.021			0.021
R^2	0.7959	0.7078			0.7125
60% of P_{max}					
a	89.861	107.151	101.291	103.055	106.804
b	10.340	3.370	7.880	3.764	3.414
c	0.018	0.021	0.018	0.021	0.021
R^2	0.9767	0.9285	0.9750	0.9056	0.9198
P_{max}					
a	60.662	67.480	65.049	62.986	63.145
b	1.040	0.133	0.428	0.310	2.416
c	0.020	0.026	0.023	0.017	0.022
R^2	0.9944	0.9960	0.9910	0.9945	0.9998

The writer did not find any past research programs that have attempted to define, clearly, an expression for bar strain and indirectly bond stress, as a function of the embedment length, which highlights the uniqueness of the proposed modified logistic growth function. Note that this function is independent of the bar slip, can be constrained using conventional beam theory and in addition, given strain gauge data along the reinforcement embedment length, can modify its shape based on the extent of the bond degradation. Equation 5.37 is the derivative of Equation 5.33 and inserting this derivative into Equation 5.32 and inputting the parameters of a GFRP bar, results in an expression, Equation 5.38, for the bond stress as a function of distance from the loaded-end.

$$\left| \frac{d\varepsilon_F}{dx} \right| = \frac{bce^{cx}}{(a + be^{cx})^2} \tag{Equation 5.37}$$

$$\mu(x) = \frac{bce^{cx}}{(a + be^{cx})^2} \left(\frac{E_F A_F}{\pi d_{bF}} \right) \tag{Equation 5.38}$$

Figure 5:29 to Figure 5:31 plot the bond stress distribution as a function of embedment length using Equation 5.38, as well as the actual distribution obtained from the experimental data using the method that will be described in Section 5.6 Note that the

proposed strain expression is able to resemble the shape of the actual bond stress distribution.

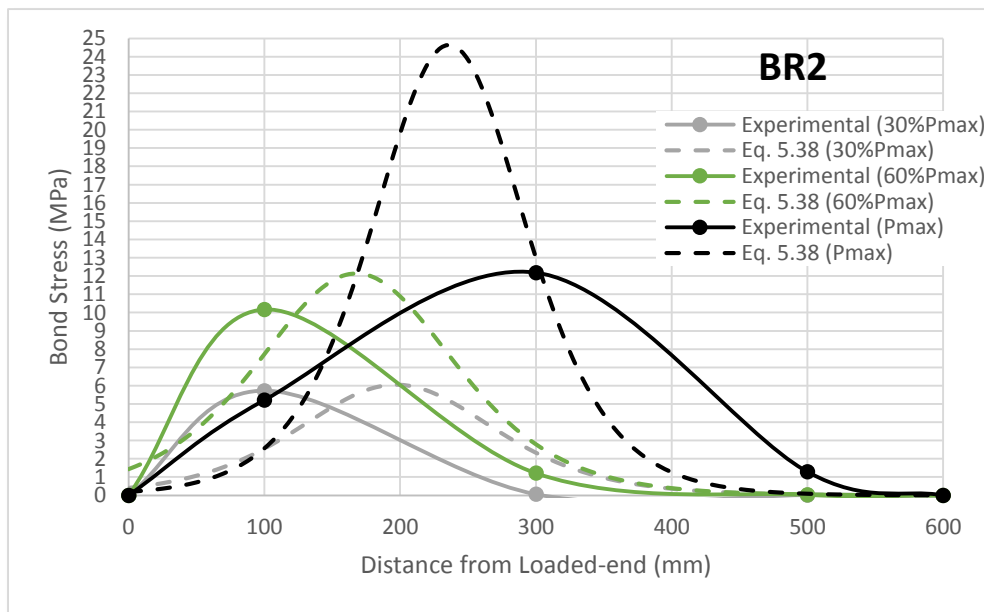
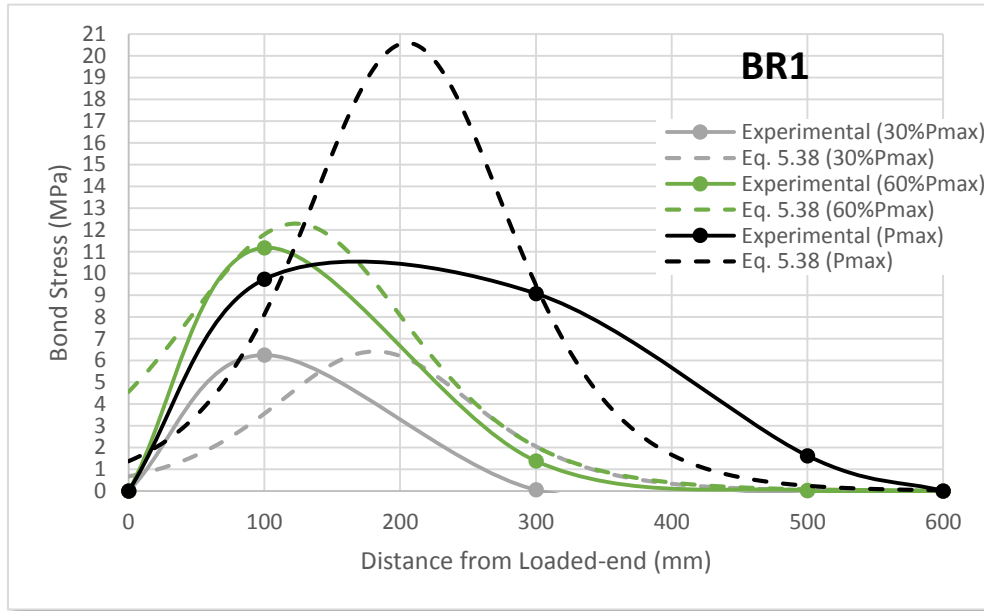
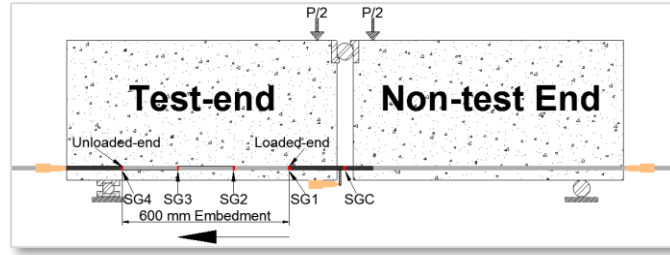


Figure 5:29: Experimental data points versus predicted bond stress distribution by Equation 5.38 for RILEM beams

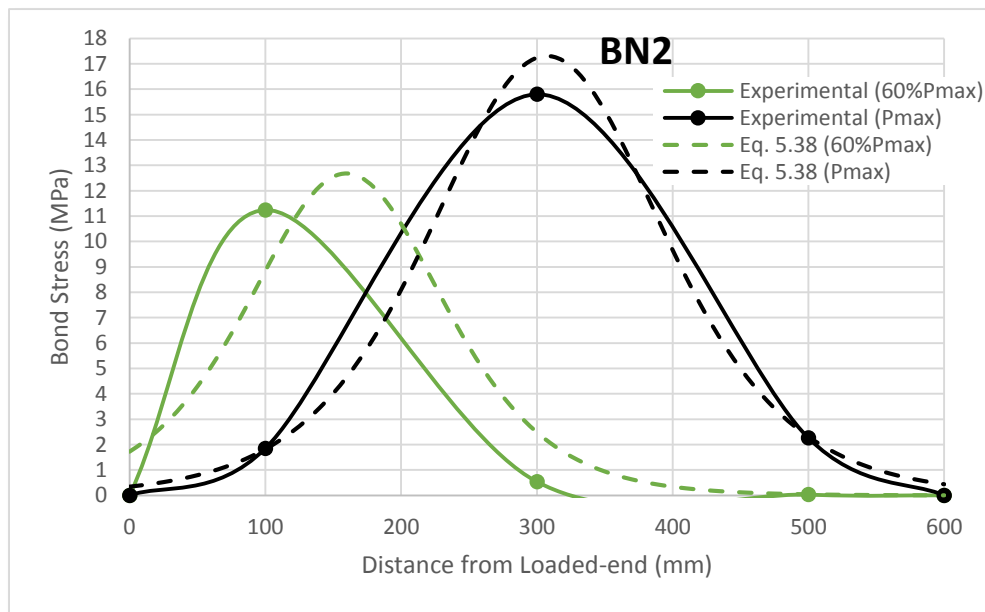
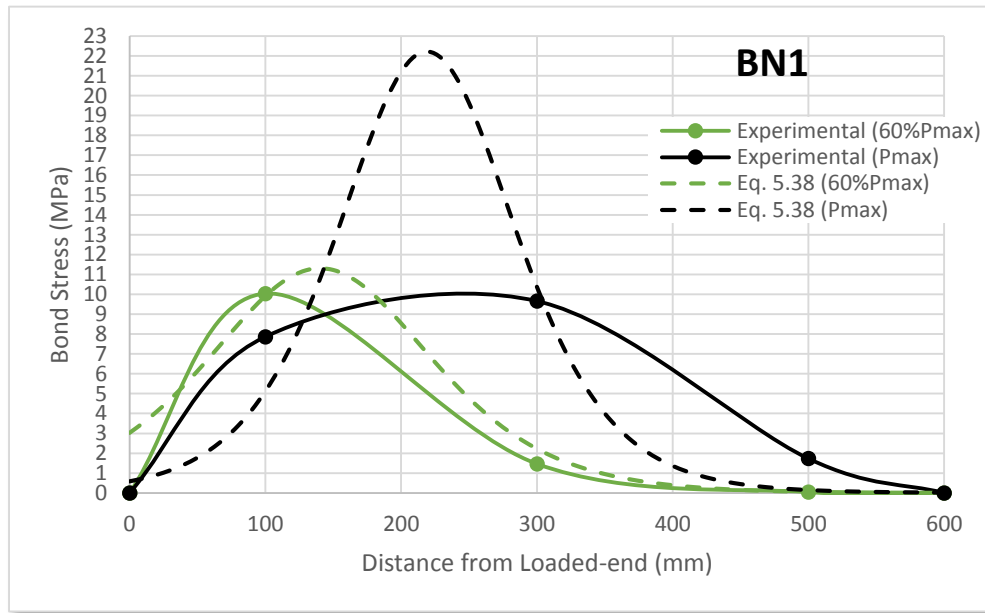
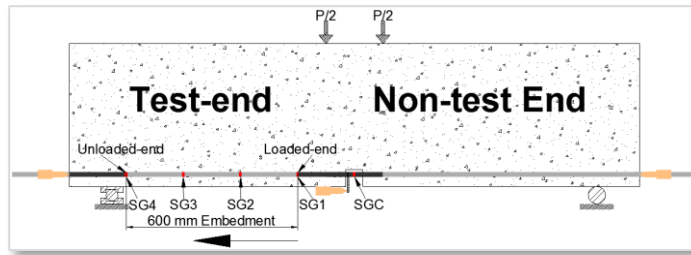


Figure 5:30: Experimental data points versus predicted bond stress distribution by Equation 5.38 for Notched beams

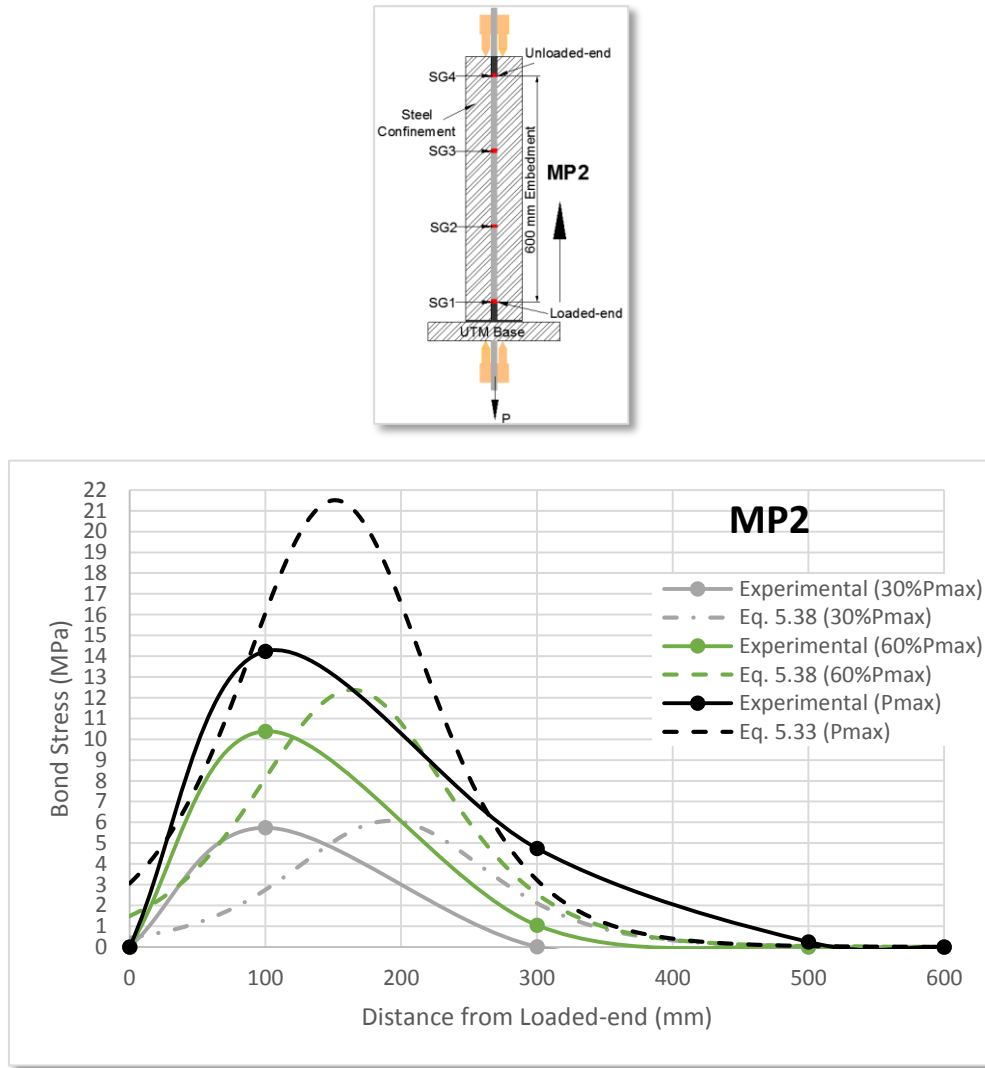


Figure 5.31: Experimental data points versus predicted bond stress distribution by Equation 5.38 for Modified pullouts specimen, MP2

The curves obtained using Equation 5.38 resemble the shape of the actual bond stress distribution and the overall pattern of the theoretical and experimental bond stress distribution is consistent with those reported by other researchers. However, the peak bond stress obtained using Equation 5.38, particularly at P_{max} , is significantly higher for the RILEM beams as well as BN1 and MP2. This is attributed to the high sensitivity of the strain expression to the value of $\epsilon_F(l_e)$, which for all of the specimens in this experimental program was negligible and showed some natural variability at all GFRP stress levels. Therefore, knowledge of the strain distribution along the GFRP bar at small increments with a high degree of accuracy is critical for bar strain distribution analysis and it may be worthwhile to explore other avenues besides bar surface strain gauges, as discussed earlier.

Note that in addition, the method of calculating the actual bond stress from experimental data is also an approximation as it uses the difference between two successive strain gauges. Hence, the accuracy in calculating the actual bond stress distribution increases as distance between strain gauge placement decreases.

It is acknowledged that once the proposed function incorporates a number of other parameters including concrete strength, bar diameter and bar location factors, the resulting expression as well as its derivative may become more complex. Therefore, it is understandable that most current standards have chosen to assume uniform bond stress distribution and furthermore avoid directly referring to the bond stress but rather express their equations in terms of the development length, a concept that is simple to grasp in design applications.

With reference to Equation 5.28, another method of validating the proposed strain expression, Equation 5.33, is to analyze the bar slip along the embedment length. Although as stated earlier, the application of Equation 5.28 to flexural members is dubious, nevertheless, an attempt is made to examine this issue. Inserting Equation 5.37 into Equation 5.28, and using the parameters of a GFRP bar results in,

$$\frac{d^2s}{dx^2} = (1 + n_F\rho) \left[\frac{bce^{cx}}{(a + be^{cx})^2} \right] \quad \text{Equation 5.39}$$

Integrating twice with respect to x ,

$$|s(x)| = (1 + n_F\rho) \left[\frac{\ln(a + be^{cx}) - cx}{ac} \right] \quad \text{Equation 5.40}$$

Observe that for GFRP reinforced members the modular ratio is in the range of 1.5 to 2.5 for concrete strengths of 30 to 40 MPa while ρ for the current beams is roughly 0.001, which render $n_F\rho < 0.003$, much smaller than 1.0. So for the beam-bond specimens, one can ignore $n_F\rho$ in Equation 5.40. For the beam-bond specimens and the Modified pullout specimen, MP2, Figure 5:32 to Figure 5:34 show the results of using Equation 5.40 to generate the predicted slip along the GFRP bar embedment length at load increments of 30% P_{max} , 60% P_{max} and P_{max} with the exception of the Notched beams which do not include 30% P_{max} due to their negligible strain distribution along the bar at this loading stage. This equation can benefit from knowledge of the fact that for the beam-bond and the Modified pullout specimens in this study, the unloaded-end LVDTs, did not show any slip

of the GFRP bar. Thus, the curves in these figures have been shifted vertically such that the bar slip at the end of the 600 *mm* embedment length, the unloaded-end, is zero.

To reiterate, the derivation of Equation 5.28, as stated earlier, assumes that $\frac{dP}{dx} = 0$, which for beam-bond specimens, is not the case. Furthermore, with reference to Equation 5.40, for the beam-bond specimens, the reinforcement ratio, ρ , was taken as $\frac{A_F}{bd}$, which is incorrect since the beam-bond specimen must first be converted into an equivalent pullout specimen. Thus, the curves for the beam-bond specimens, shown in Figure 5:32 and Figure 5:33, only serve as illustration purposes, reinforcing the ability of the proposed strain expression to produce the correct shape of slip along the bar embedment length. Overall, the shape of the curves in Figure 5:32 to Figure 5:34 is consistent with the results produced by other researchers, including Focacci et al., (2000) and Yang and Chen, (1988) who have plotted the slip along the embedment length of a reinforcing bar.

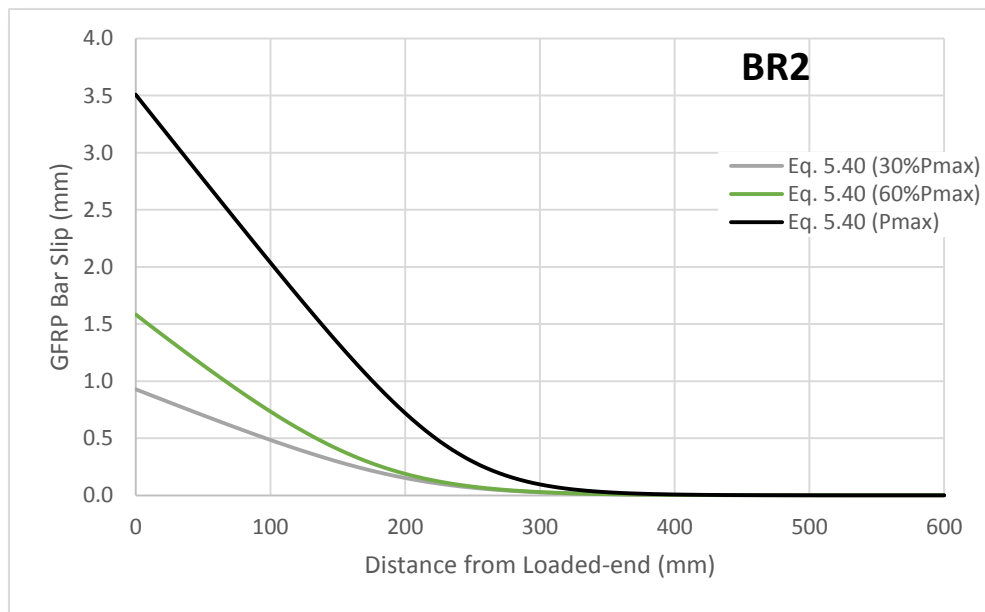
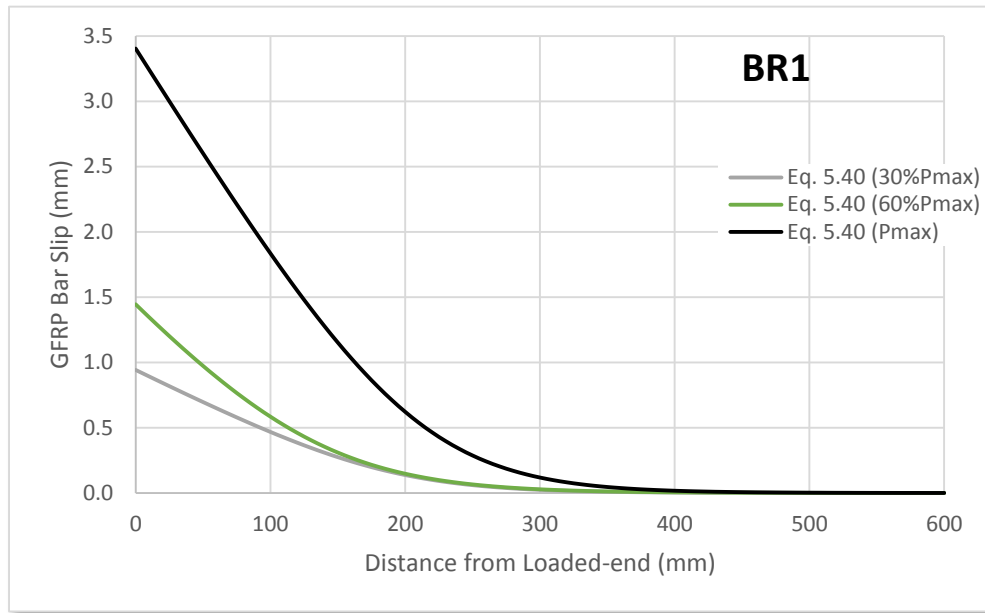
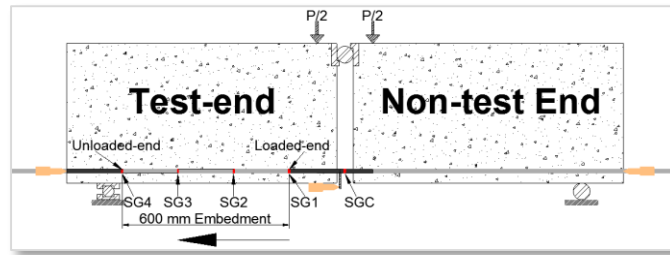


Figure 5.32: GFRP bar slip along embedment length predicted by Equation 5.40 for RILEM beams

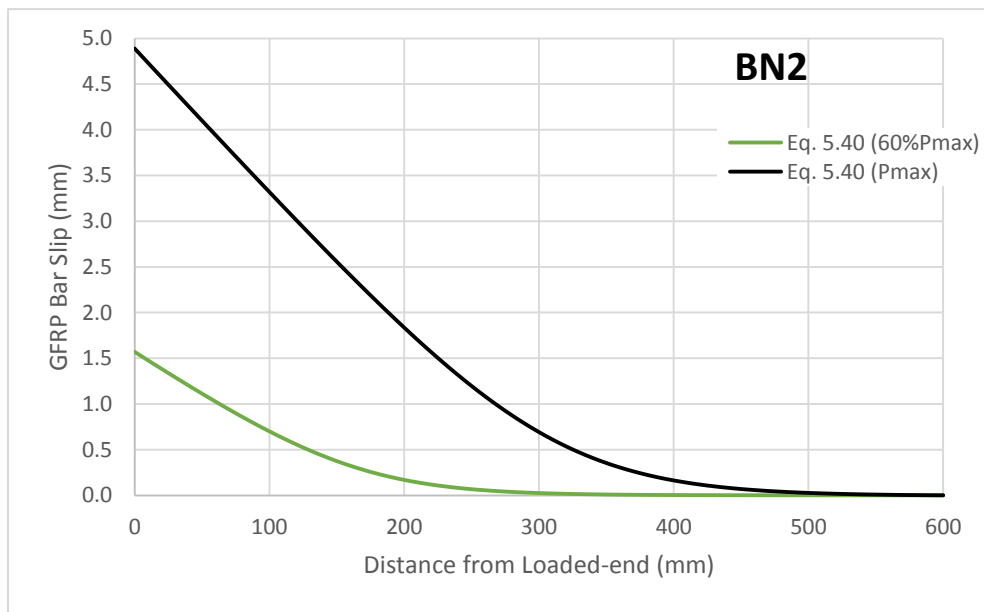
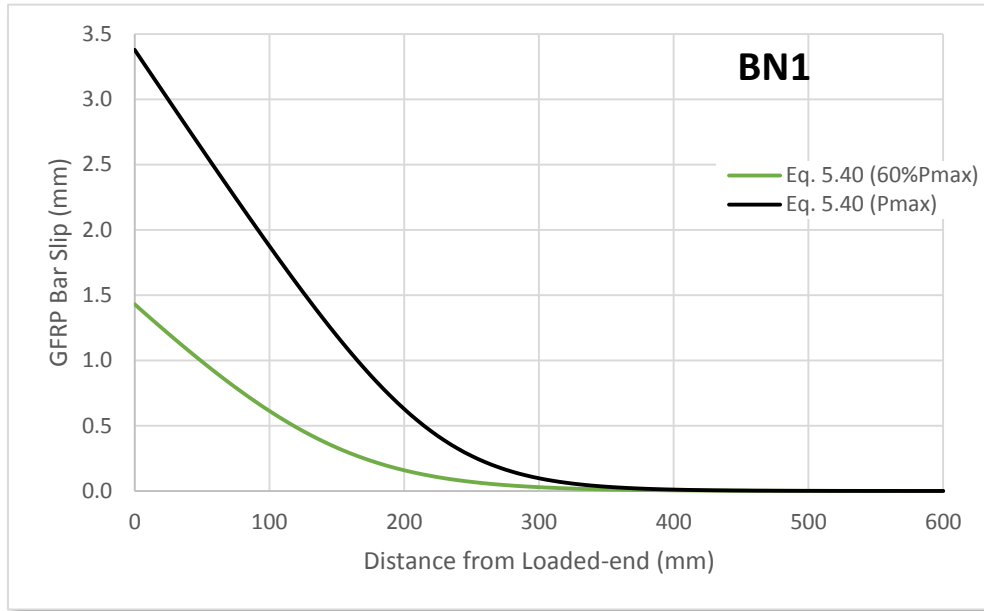
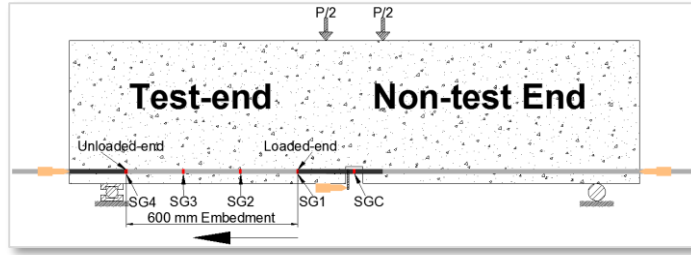


Figure 5.33: GFRP bar slip along embedment length predicted by Equation 5.40 for Notched beams

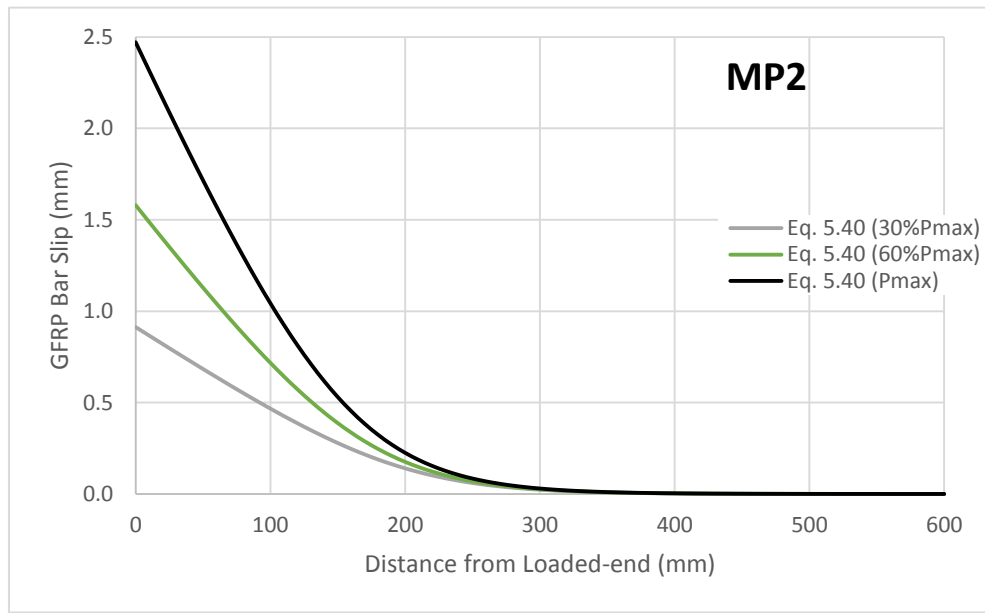
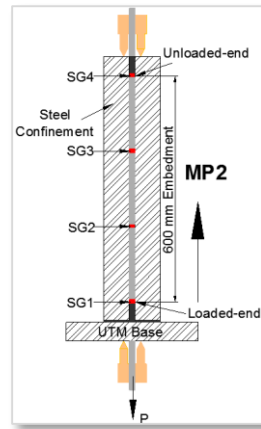


Figure 5:34: GFRP bar slip along embedment length predicted by Equation 5.40 for Modified pullout specimen, MP2

5.6 Actual versus Uniform Bond Stress Distribution

The bond stress distribution calculations for this experimental program make use of Equation 5.41, which, also used by Perry and Thompson, (1966) and Feldman and Bartlett, (2007), calculates a bond stress value between two successive strain gauges by taking the difference between the strain readings and Figure 5:35 provides further illustration. Thus, for the beam-bond and the Modified pullout samples in this experimental program, it becomes possible to calculate three bond stress points along the embedment length of the GFRP at distance of 100, 300 and 500 mm from the loaded-end. Note that the failure of MP1-SG3 prevents the calculation of μ_2 and μ_3 which significantly limits the bond stress distribution analysis for this specimen.

$$\mu_j = \left(\frac{|\varepsilon_{SGi} - \varepsilon_{SGi+1}|}{\Delta l} \right) \left(\frac{E_F A_F}{\pi d_{bF}} \right) \quad \text{Equation 5.41}$$

In Equation 5.41,

i = Index from 1 to 3

j = Index from 1 to 3

Δl = Spacing between strain gauges = 200 mm

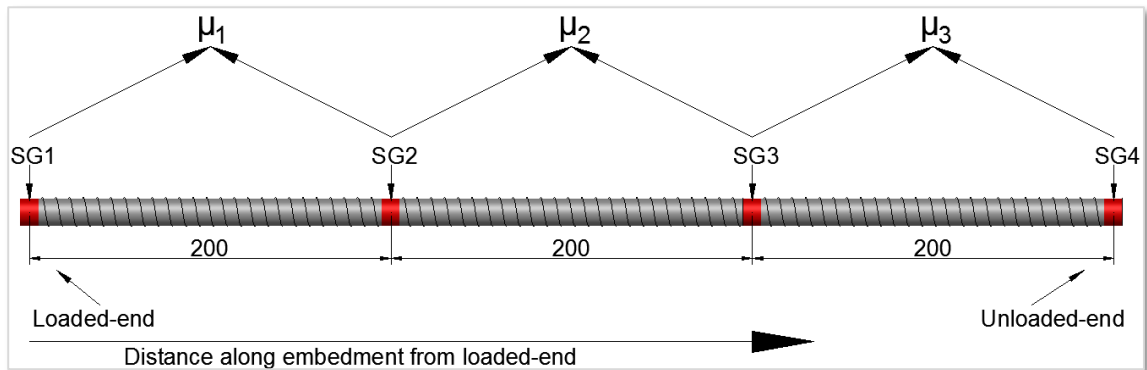


Figure 5:35: Method of calculating bond stress distribution

If one were to assume uniform bond stress distribution then at a desired GFRP stress level, the bond stress would be calculated using Equation 5.42, where l_e , the embedment length, would be 600 mm for the beam-bond and Modified pullout specimens.

$$\mu_{\% pmax} = \left(\frac{(\varepsilon_{SG1}^{\% pmax}) E_F A_F}{\pi d_{bF} l_e} \right) \quad \text{Equation 5.42}$$

At 20% increments of P_{max} , Figure 5:36, Figure 5:37 and Figure 5:38 for the RILEM beams, Notched beams and Modified pullout samples, respectively, show a comparison between actual bond stress distributions along the embedment length, which is nonlinear, versus the assumed uniform distribution. For MP1 in Figure 5:38, note that the value of the actual bond stress at 100 mm from the loaded-end at 60 and 76% of P_{max} , are 8.15 and 8.10 MPa, respectively and therefore they overlap in this figure.

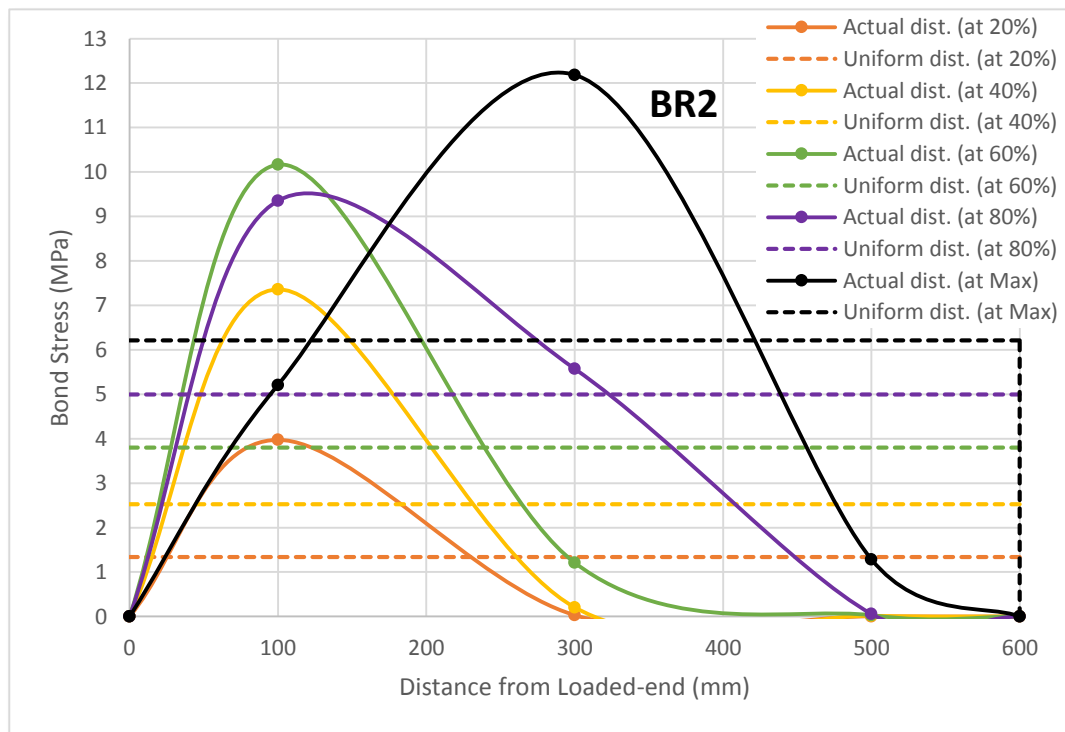
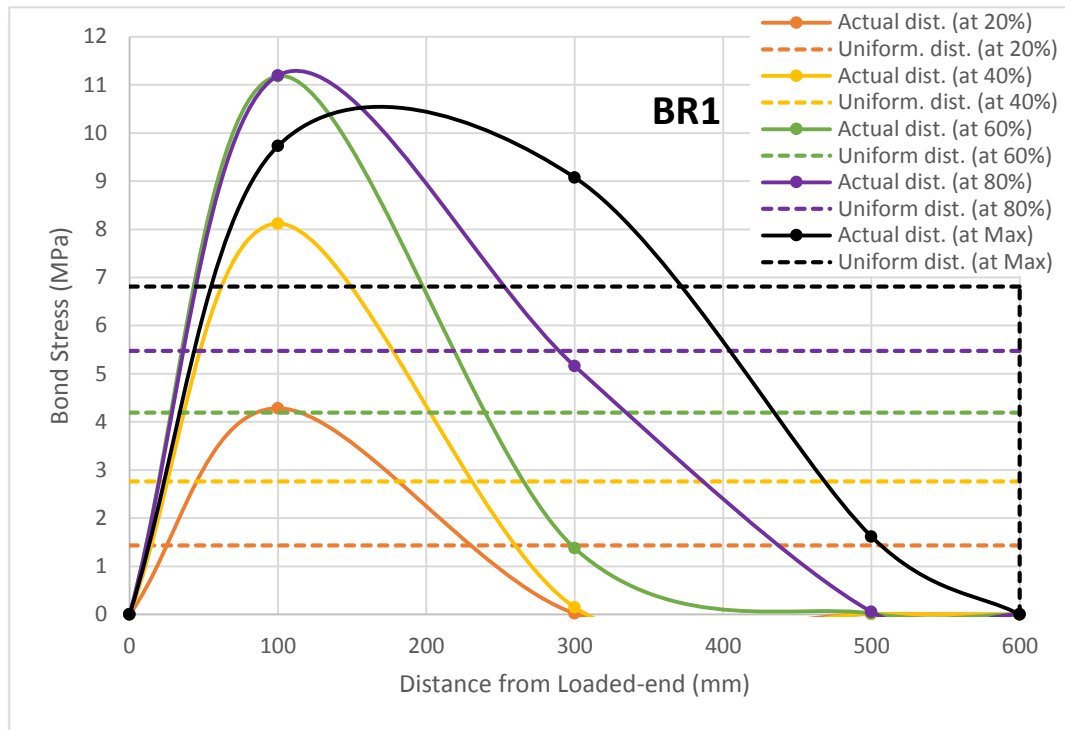


Figure 5:36: Actual versus uniform assumption of bond stress distribution in the RILEM beams at different percentages of their respective maximum load, P

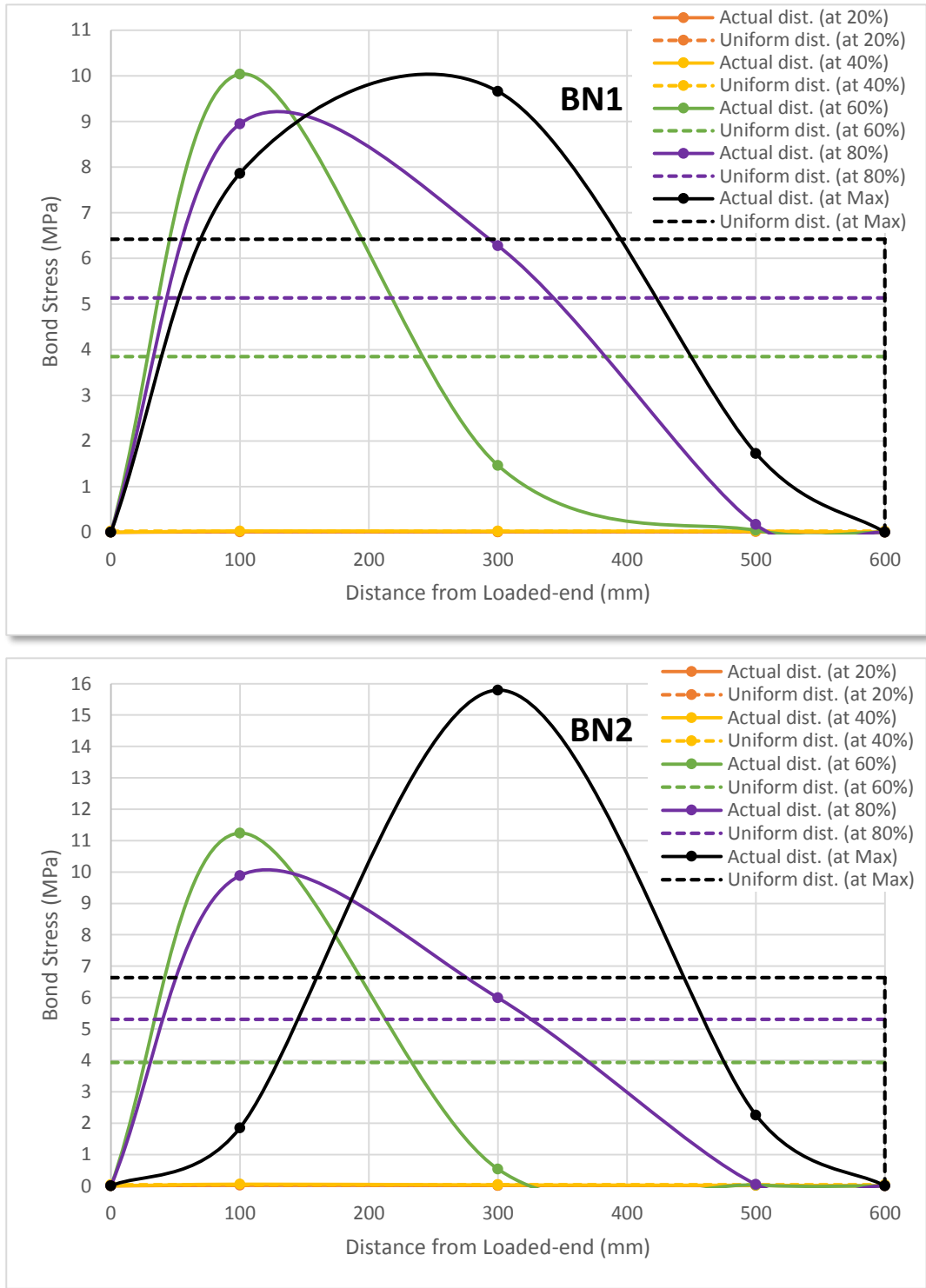


Figure 5:37: Actual versus uniform assumption of bond stress distribution in the Notched beams at different percentages of their respective maximum load, P

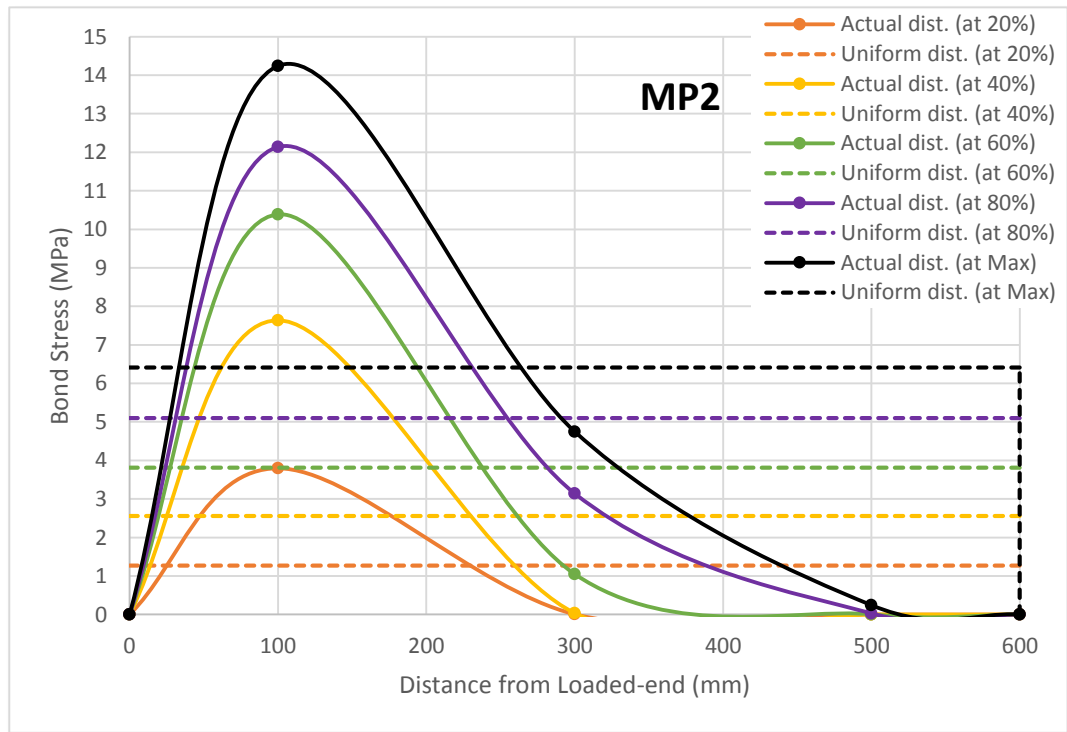
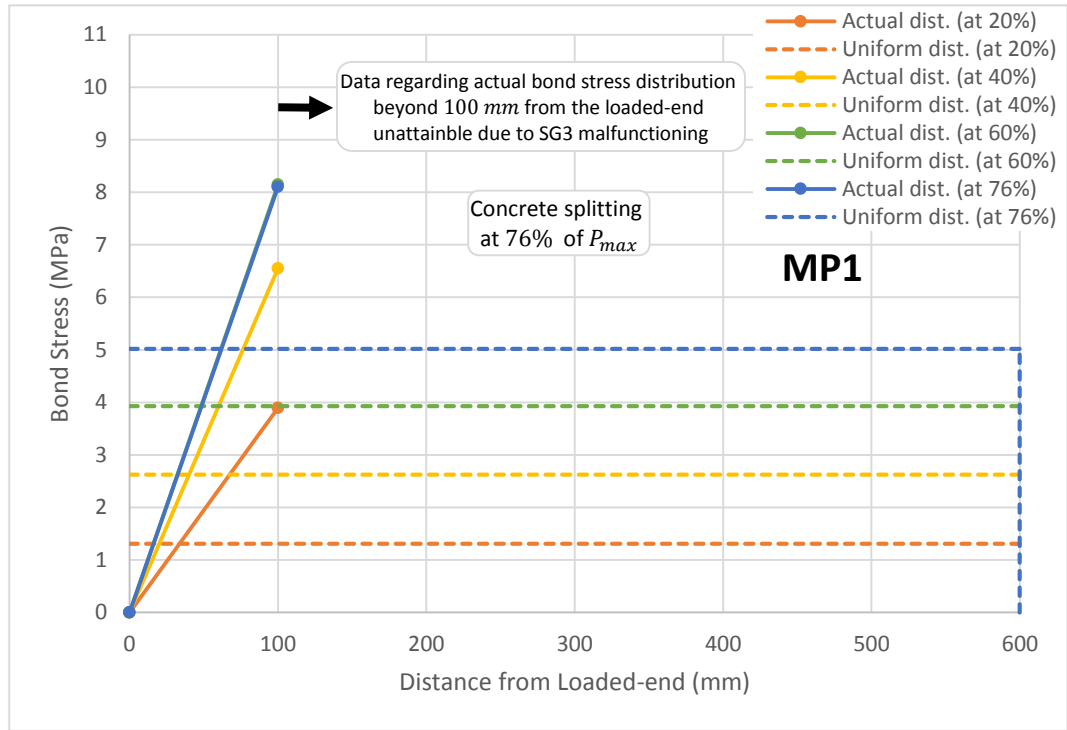


Figure 5:38: Actual versus uniform assumption of bond stress distribution in the Modified pullout specimens at different percentages of their respective maximum load, P

Table 5:9 shows the peak actual bond stress, μ_{peak} obtained for each sample using Equation 5.41, including the location of its occurrence along the embedment length. From the observation of this table as well as Figure 5:36 to Figure 5:38, first, note that the pattern of the actual bond stress distributions in the beam-bond samples and the Modified pullout specimen, MP2, bear a close resemblance to the shape generated using the proposed modified logistic growth function, Equation 5.38. For MP1 in Figure 5:38, data regarding the actual bond stress distribution beyond 100 mm from the loaded-end could not be obtained due to the malfunctioning of SG3, therefore, this prevents the determination of a μ_{peak} for this specimen.

Past researchers including Perry and Thompson, (1966) and Benmokrane et al., (1996) produced bond stress versus the distance from the loaded-end curves that have a similar pattern to the results obtained in this experimental program. As Figure 5:22 illustrated, for the Notched beams, the GFRP strain values along the bar below approximately 50% of P_{max} , which corresponded to the point of midspan flexural cracking, were negligible and this manifests itself through the insignificant bond stress distributions shown in Figure 5:37 within this range.

For the beam-bond specimens, note that as the GFRP stress level continues to increase, the bond between the concrete and the GFRP experiences a significant degradation. As Figure 5:36 and Figure 5:37 illustrate, this deterioration of the bond manifests itself through a shift in the bond stress distribution towards the unloaded-end of the specimens, an observation also made by Perry and Thompson, (1966), Benmokrane et al., (1996) and Feldman and Bartlett, (2007).

Table 5:9: Peak experimental bond stress obtained using Equation 5.41

Specimen Designation	μ_{peak} (MPa)	Distance from loaded-end (mm)
BR1	11.2	100
BR2	12.2	300
RILEM beam avg.	11.7	--
BN1	10.0	100
BN2	15.8	300
Notched beam avg.	12.9	--
MP2	14.2	100

Table 5:10 shows the average bond stress obtained assuming uniform distribution, μ_{avg}^u , using Equation 5.42 and setting $\epsilon_{SG1}^{% pmax}$ equal to the strain obtained from SG1 at P_{max} and the embedment length, l_e equal to the 600 mm used in this study. In addition, this table includes the average uniform bond stress assumed by ACI 440.1, (2006), CSA

S806, (2012) and CSA S6, (2006), $\mu_{avg.}^{u_{code}}$, at P_{max} obtained via substitution of the development length equations from these codes/guidelines for l_e , in Equation 5.42. The development length expressions for the 14.8 mm GFRP bar, considering the present test parameters, simplify to Equation 5.47, Equation 5.48 and Equation 5.49 for ACI 440.1, (2006), CSA S806, (2012) and CSA S6, (2006), respectively, as shown in Section 5.7

From the observation of Table 5:10, it is evident that current codes/guidelines underestimate the bond stress development within a given embedment length and as a results, are conservative. Among the three standards, ACI 440.1, (2006) is the most conservative followed by CSA S806, (2012) and CSA S6, (2006) and this conclusion is reached in Section 5.7 as well where the recommended development lengths by these standards at different stress levels in the GFRP bar are presented.

Table 5:10: Experimental versus theoretical average bond stress assuming a uniform distribution using Equation 5.42, at maximum load, P

Specimen Designation	$\mu_{avg.}^u$ (MPa)	$\mu_{avg.}^{u_{code}}$ (MPa)			$\mu_{avg.}^u / \mu_{avg.}^{u_{code}}$		
		ACI 440.1, (2006)	CSA S806, (2012)	CSA S6, (2006)	ACI 440.1, (2006)	CSA S806, (2012)	CSA S6, (2006)
BR1	6.8	2.4	4.1	5.3	2.8	1.7	1.3
BR2	6.2	2.5			2.5	1.5	1.2
BN1	6.4	2.5			2.6	1.6	1.2
BN2	6.6	2.4			2.8	1.6	1.2
MP1 (at 76% of P_{max})	5.0	2.6			1.9	1.2	0.9
MP2	6.4	2.5	2.6	1.6	1.2		

Note, with reference to Table 5:10, Equation 5.42 and Equation 5.47 to Equation 5.49, that CSA S806, (2012) and CSA S6, (2006) set a minimum value criteria for the embedment length and then assume a single value for the uniform bond stress distribution irrespective of the level of stress in the GFRP bar. However, for ACI 440.1, (2006), the uniform bond stress assumed is dependent on the GFRP stress level and will change accordingly. To better illustrate this point, for BR1 and BR2, at different percentages of their respective, P_{max} , Figure 5:39 plots the average uniform bond stress obtained by inserting Equation 5.47 to Equation 5.49 for l_e , in Equation 5.42. In addition, this figure plots $\mu_{avg.}^u$, which is the uniform bond stress obtained by using Equation 5.42 at different percentages of P_{max} with the embedment length set equal to the 600 mm used in this study.

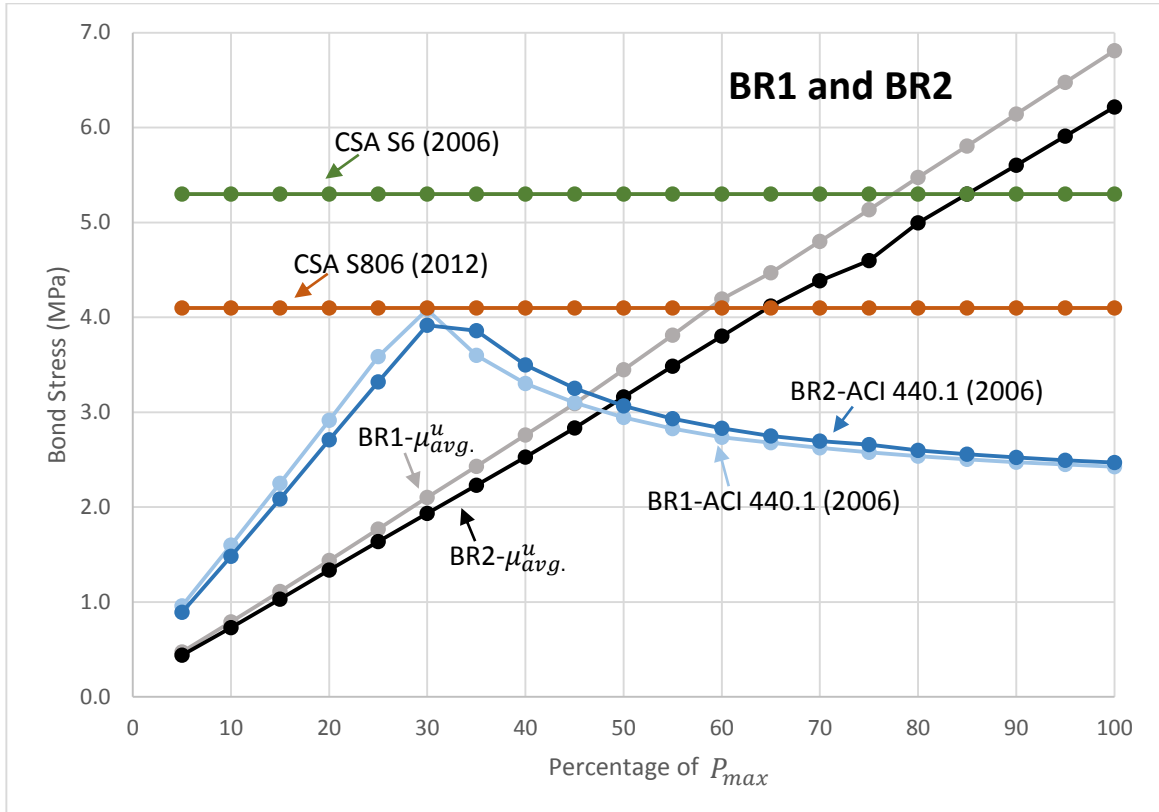


Figure 5:39: Experimental versus theoretical bond stress for the RILEM beams assuming a uniform bond stress distribution

5.7 Experimental versus Recommended Development Length

In this experimental program, since the 600 mm embedment length was sufficient in causing GFRP bar rupture and furthermore, because SG4 readings in all of the samples were negligible throughout the testing, it is certain that the development length for the full capacity of this bar is less than 600 mm. With the assumption that a strain reading of less than 15 μ strain, or equivalently a GFRP stress less than 1 MPa, is indicative that the development length does not extend beyond that particular strain gauge, one can provide a range for the development length of the test specimens at each GFRP stress level.

In order to make a comparison between the experimental and the recommended development length, the ACI 440.1, (2006), CSA S806, (2012) and CSA S6, (2006) expressions for development length are presented first. ACI 440.1, (2006) uses the works

of Wambeke and Shield, (2006), who based on the analysis of a database consisting of 269 beam-bond specimens tested by several investigators, proposed Equation 5.43, which relates the bond stress to the embedment length with the incorporation of the effects of concrete strength, concrete cover, distance between reinforcement in the same layer and lastly, bar diameter. Note that in this database, which included the works by a number of investigators, including that of Daniali, (1992) and Tighiouart et al., (1999), uniform bond stress was assumed.

$$\mu = \left(0.083 \sqrt{f'_c}\right) \left(4.0 + 0.3 \frac{C}{d_{bF}} + 100 \frac{d_{bF}}{l_e}\right) \quad \text{Equation 5.43}$$

where,

C = Smaller of: Concrete cover of the bar or $\frac{1}{2}$ the distance between the reinforcement in the same layer being developed

By using Equation 5.43 and Equation 5.21 with the substitution of f_F for f_y , the bond stress is eliminated and by subsequent addition of a safety factor and other adjustments, Equation 5.44 is arrived at for design applications. In a similar manner, the Canadian Standards CSA S806, (2012) and CSA S6, (2006) do not refer to the bond stress but instead, use the concept of development length to avoid bond failure in design. Equation 5.45 and Equation 5.46 are the development length expressions used by CSA S806, (2012) and CSA S6, (2006), respectively. Note that these equations make use of the same underlying assumptions and methodology as the ACI 440.1, (2006).

$$l_d = \frac{\left(\alpha \frac{f_F}{0.083 \sqrt{f'_c}} - 340\right)}{\left(13.6 + \frac{C}{d_{bF}}\right)} d_{bF} \quad l_d \geq 20d_{bF} \quad \text{Equation 5.44}$$

where,

α = Bar location factor

$C/d_{bF} \leq 3.5$

$$l_d = 1.15 \frac{k_1 k_2 k_3 k_4 k_5}{d_{cs}} \frac{f_F}{\sqrt{f'_c}} A_F \quad l_d \geq 300 \quad \text{Equation 5.45}$$

where,

k_1 = Bar location factor

k_2 = Concrete density factor

k_3 = Bar size factor

k_4 = Bar fibre factor

k_5 = Bar surface profile

d_{cs} = Smaller of: Concrete cover to centre of the bar or 2/3 the distance between reinforcement in the same layer that are to be developed

$$d_{cs} \leq 2.5d_{bF}$$

$$\sqrt{f'_c} \leq 5$$

$$l_d = \frac{0.45k_1k_4}{\left(d_{cs} + k_{tr} \frac{E_F}{E_S}\right)} \frac{f_F}{f_{cr}} A_F \quad l_d \geq 250 \quad \text{Equation 5.46}$$

where,

k_1 = Bar location factor

k_4 = Bar surface factor

d_{cs} = Smaller of: Concrete cover to centre of the bar or 2/3 the distance between reinforcement in the same layer that are to be developed

$$k_{tr} = \frac{0.45A_{tr}f_y}{10.5sn}$$

A_{tr} = Area of reinforcement within l_d that crosses the potential bond-splitting crack

f_y = Specified yield strength of reinforcing bar

s = Maximum centre-to-centre spacing of transverse reinforcement within a distance l_d

n = Number of bars being developed along the potential plane of bond splitting

$$\left[d_{cs} + k_{tr} \frac{E_F}{E_S} \right] \leq 2.5d_{bF}$$

$f_{cr} = 0.4\sqrt{f'_c}$ Cracking strength of concrete

All three guidelines include a minimum embedment length to avoid bar pullout behaviour and they incorporate various factors in order to take into account the effect of some key parameters on the bond strength. Table 5:11 provides the values for these parameters given the materials used in this study along with the relevant construction detail of the beam-bond specimens.

Table 5:11: Determination of recommended development length for the GFRP bar in this experimental program

Relevant information unique to this experimental program		
Single longitudinal GFRP tensile reinforcement	Concrete	Transverse double legged stirrups (Beams)
$d_{bF} = 14.8$ $A_F = 172.0$ $E_F = 68,157$ $f_{Fu} = 1,066$ Surface: Ribbed	Normal density Cover to centre of GFRP: Beams = 42.5 Modified Pullouts = 75 $f'_c = 36.5$	$d_{bs} = 10.5$ $A_s = 86.6$ $s = 50$ $n = 1$ $f_y = 564$ $E_s = 215,593$ Surface: Deformed
Resulting parameter value in development length equation		
ACI 440.1, (2006)	CSA S806, (2012)	CSA S6, (2006)
$\alpha = 1.0$ $C/d_{bF} = 2.9$ $\sqrt{f'_c} = 6.0$	$k_1 = 1.0$ $k_2 = 1.0$ $k_3 = 0.8$ $k_4 = 1.0$ $k_5 = 1.05$ $d_{cs} = 37$ (Limit) $\sqrt{f'_c} = 5.0$ (Limit)	$k_1 = 1.0$ $k_4 = 0.8$ $\left[d_{cs} + k_{tr} \frac{E_F}{E_s} \right] = 37$ (Limit) $f_{cr} = 2.4$

Equation 5.47, Equation 5.48 and Equation 5.49 are the development length expressions for ACI 440.1, (2006), CSA S806, (2012) and CSA S6, (2006), respectively, once the appropriate parameters, shown in Table 5:11 have been included.

$$l_d = (1.8012)f_F - 304.98 \qquad l_d \geq 20d_{bF} \quad \text{Equation 5.47}$$

$$l_d = (0.8981)f_F \qquad l_d \geq 300 \quad \text{Equation 5.48}$$

$$l_d = (0.6973)f_F \qquad l_d \geq 250 \quad \text{Equation 5.49}$$

With reference to these equations, Table 5:12 and Table 5:13 for the RILEM and Notched beams, respectively and Table 5:14 for the Modified pullout samples present the experimental development lengths versus the recommendations by ACI 440.1, (2006), CSA S806, (2012) and CSA S6, (2006). In Table 5:14, for MP1, due to the failure of MP1-SG3, unfortunately, one cannot provide a definitive range for the development length of the bar in this specimen beyond 10% of P_{max} .

Table 5:12: Experimental ranges versus guideline predictions of development length for the RILEM beams

RILEM beams								
Development length l_d (mm)								
	Experimental		ACI 440.1, (2006)		CSA S806, (2012)		CSA S6, (2006)	
% of P_{max}	BR1	BR2	BR1	BR2	BR1	BR2	BR1	BR2
10	< 200	< 200	296	296	300	300	250	250
20	200 to 400	200 to 400	296	296	300	300	250	250
30	200 to 400	200 to 400	309	296	306	300	250	250
40	200 to 400	200 to 400	502	434	402	368	312	286
50	200 to 400	400 to 600	702	618	502	460	390	357
60	400 to 600	400 to 600	920	806	611	554	474	430
70	400 to 600	400 to 600	1,097	976	699	639	543	496
80	400 to 600	400 to 600	1,294	1,154	797	728	619	565
90	400 to 600	400 to 600	1,489	1,332	895	816	695	634
100	400 to 600	400 to 600	1,685	1,511	992	905	770	703

Table 5:13: Experimental ranges versus guideline predictions of development length for the Notched beams

Notched beams								
Development length l_d (mm)								
% of P_{max}	Experimental		ACI 440.1, (2006)		CSA S806, (2012)		CSA S6, (2006)	
	BN1	BN2	BN1	BN2	BN1	BN2	BN1	BN2
10	< 200	< 200	296	296	300	300	250	250
20	200 to 400	200 to 400	296	296	300	300	250	250
30	400 to 600	200 to 400	296	296	300	300	250	250
40	400 to 600	200 to 400	296	296	300	300	250	250
50	400 to 600	400 to 600	626	661	464	482	360	374
60	400 to 600	400 to 600	820	844	561	573	435	445
70	400 to 600	400 to 600	1,007	1,052	654	677	508	525
80	400 to 600	400 to 600	1,194	1,246	748	774	580	601
90	400 to 600	400 to 600	1,381	1,440	841	870	653	676
100	400 to 600	400 to 600	1,570	1,635	935	967	726	751

Table 5:14: Experimental ranges versus guideline predictions of development length for the Modified pullout specimens

Modified pullout specimens								
Development length l_d (mm)								
% of P_{max}	Experimental		ACI 440.1, (2006)		CSA S806, (2012)		CSA S6, (2006)	
	MP1	MP2	MP1	MP2	MP1	MP2	MP1	MP2
10	< 200	< 200	296	296	300	300	250	250
20	MP1-SG3 data lost	< 200	296	296	300	300	250	250
30		< 200	296	296	300	300	250	250
40		200 to 400	462	442	382	372	297	289
50		200 to 400	652	631	477	467	370	362
60		200 to 400	843	809	573	555	445	431
70	200 to 400	1,039	1,006	670	654	520	507	
80	Sample failure by concrete splitting	400 to 600	N/A	1,185	N/A	743	N/A	577
90		400 to 600		1,378		839		652
100		400 to 600		1,568		934		725

From the review of these tables, as well as observation of Figure 5:40 to Figure 5:42, which provide a visual representation of the same results, note that in all cases, with increasing GFRP stress levels, the guidelines recommend a development length that is either comparable or is more conservative than the experimental results, but the ACI 440.1,

(2006) expression is highly conservative compared to that of CSA S806, (2012) and CSA S6, (2006). It is important to investigate how these standards have arrived at such vastly different specifications. At least in the case of the present test results, the CSA S6, (2006) expressions seems much more reasonable.

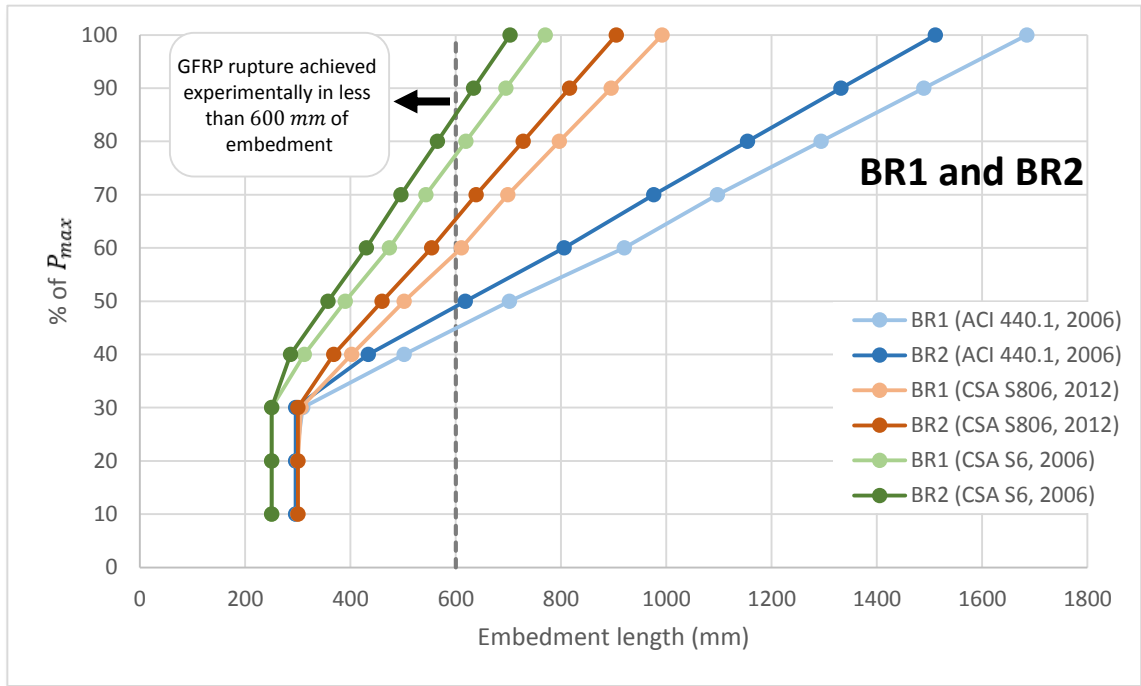


Figure 5:40: Guideline predictions of development lengths with increasing GFRP bar stress in the RILEM beams

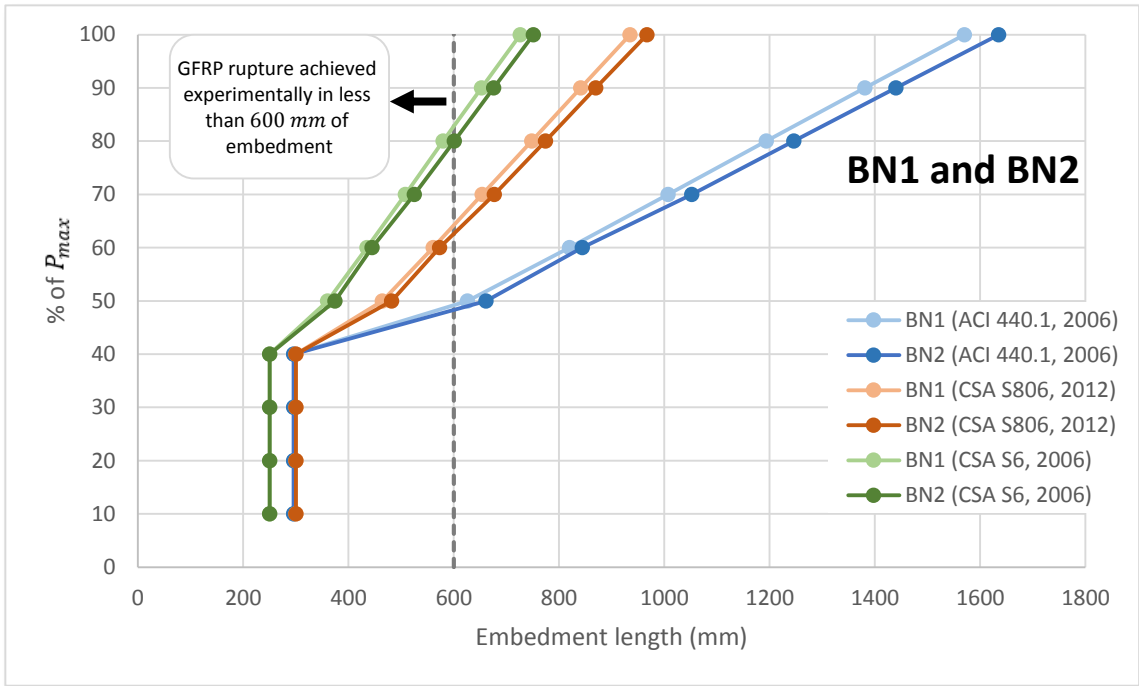


Figure 5:41: Guideline predictions of development lengths with increasing GFRP bar stress in the Notched beams

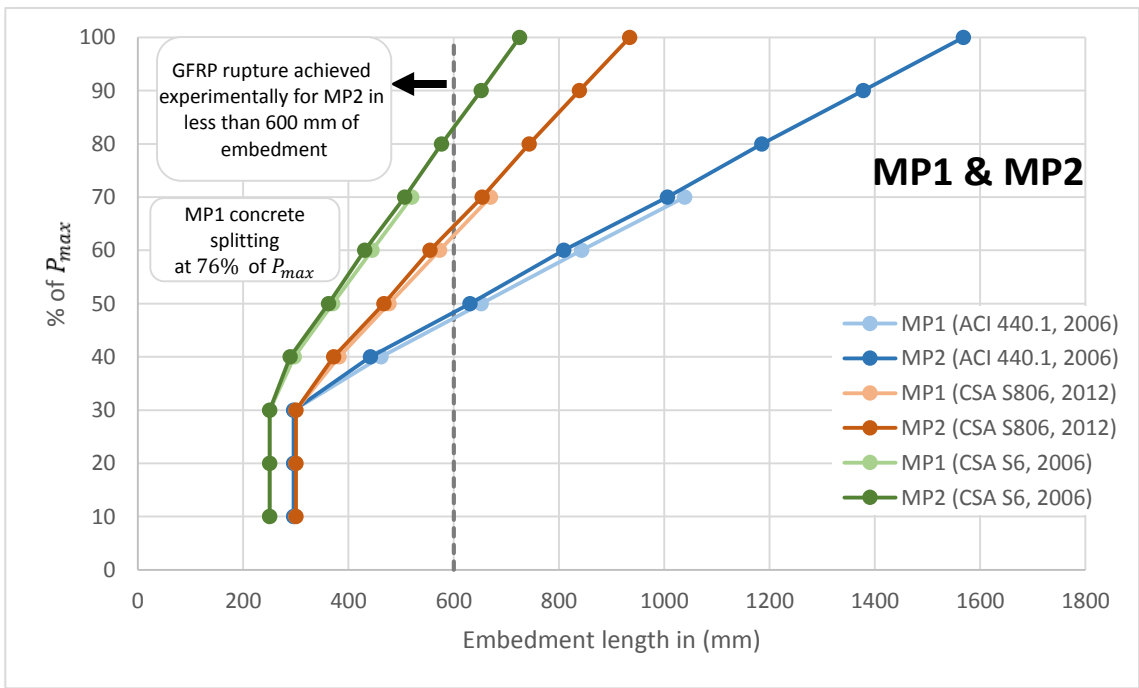


Figure 5:42: Guideline predictions of development lengths with increasing GFRP bar stress in the Modified pullout specimens

5.8 Effect of Test Method on Bond Behaviour and Bond Stress Distribution

One of the purposes of this experimental program is to determine if the bond behaviour in the beam-bond tests where the state of the concrete around the bar is in tension is significantly different from the traditional pullout tests where the concrete is in compression. As Abrams, (1913) mentioned, comparison between different test methods should occur at the same slip values and this is important because it eliminates the bar slip as a variable in the analysis.

For the beam-bond and the Modified pullout specimens, the unloaded-end LVDTs in all of the test-specimens did not show any bar slip for the duration of the tests indicating that the 600 mm embedment length was sufficient in causing the GFRP bar used in this investigation to rupture. Therefore, to obtain the true slip of the bar, one must subtract from the loaded-end LVDT readings any elastic elongation of the bar that occurs from the point of the LVDT attachment to the onset of the embedment length. In terms of the LVDTs, as previously mentioned, L1 for the beam-bond and L3 and L4 for the Modified pullout specimens measured the bar's loaded-end slip and Figure 5:43 and Figure 5:44 provide further clarifications including the distance between the point of the loaded-end LVDT attachment and the onset of the bar embedment.

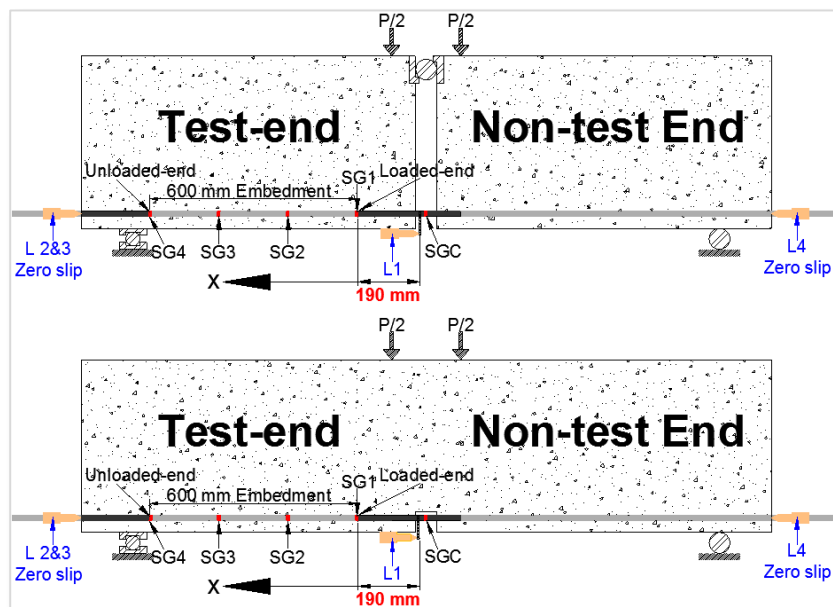


Figure 5:43: Distance from the point of loaded-end LVDT attachment and the onset of the bar embedment for the beam-bond specimens

strain for this specimen along its embedment length is not possible. In Table 5:16, at 10% of P_{max} , the BN1-L1 reading had a negative value and this is attributed to the natural variability of these LVDT readings under relatively small load levels.

Table 5:15: Corrected loaded-end slip for the RILEM beams at different percentages of their respective maximum load, P

RILEM beams								
	L1		$(190) \frac{(\epsilon_{SGC} + \epsilon_{SG1})}{2}$		s_c^l		$\int_0^{600} \epsilon_F(x) dx$	
% of P_{max}	BR1	BR2	BR1	BR2	BR1	BR2	BR1	BR2
10	0.482	0.696	0.380	0.380	0.102	0.316	0.191	0.177
20	0.924	1.242	0.688	0.683	0.236	0.559	0.348	0.324
30	1.395	1.885	0.990	0.963	0.405	0.922	0.512	0.474
40	2.014	2.528	1.256	1.205	0.758	1.323	0.686	0.640
50	2.733	3.195	1.545	1.460	1.188	1.735	0.906	0.847
60	3.674	3.919	1.838	1.723	1.836	2.196	1.224	1.107
70	4.911	4.773	2.140	1.959	2.771	2.814	1.700	1.497
80	6.017	5.790	2.436	2.269	3.581	3.521	2.143	2.092
90	7.710	6.934	2.730	2.539	4.980	4.395	2.796	2.820
100	9.555	8.715	3.024	2.812	6.531	5.903	3.577	3.806

Table 5:16: Corrected loaded-end slip for the Notched beams at different percentages of their respective maximum load, P

Notched beams								
	L1		$(190) \frac{(\epsilon_{SGC} + \epsilon_{SG1})}{2}$		s_c^l		$\int_0^{600} \epsilon_F(x) dx$	
% of P_{max}	BN1	BN2	BN1	BN2	BN1	BN2	BN1	BN2
10	-0.013	0.014	0.002	0.003	-0.015	0.011	0.004	0.004
20	0.018	0.019	0.005	0.007	0.013	0.012	0.008	0.008
30	0.041	0.057	0.009	0.015	0.032	0.042	0.013	0.016
40	0.060	0.068	0.014	0.019	0.046	0.049	0.019	0.019
50	3.040	3.150	1.441	1.495	1.599	1.655	0.986	0.876
60	3.908	3.672	1.741	1.779	2.167	1.893	1.163	1.030
70	4.818	5.291	2.030	2.100	2.788	3.191	1.664	1.884
80	5.838	5.970	2.320	2.401	3.518	3.569	2.272	2.232
90	7.060	7.386	2.610	2.701	4.450	4.685	2.633	3.356
100	8.891	10.463	2.902	3.002	5.989	7.461	3.609	4.808

Table 5:17: Corrected loaded-end slip for the Modified pullout specimen, MP2 at different percentages of its maximum load, P

Modified pullout specimens								
	$\frac{(L3 + L4)}{2}$		$(220.8) \frac{P}{A_F E_F}$		s_c^l		$\int_0^{600} \epsilon_F(x) dx$	
% of P_{max}	MP1	MP2	MP1	MP2	MP1	MP2	MP1	MP2
10	2.453	1.518	0.345	0.313	2.108	1.205	MP1-SG3 data lost	0.142
20	4.389	3.034	0.687	0.666	3.702	2.368		0.302
30	6.149	4.155	1.035	1.008	5.114	3.147		0.458
40	7.526	5.305	1.379	1.343	6.147	3.962		0.614
50	8.680	6.368	1.721	1.683	6.959	4.685		0.813
60	10.014	7.570	2.065	2.003	7.949	5.567		1.074
70	11.337	8.808	2.417	2.357	8.920	6.451		1.386
80	Sample failure by concrete splitting	10.074	Sample failure by concrete splitting	2.681	Sample failure by concrete splitting	7.393		1.721
90		11.215		3.028		8.187		2.088
100		11.722		3.368		8.354		2.355

Theoretically, neglecting the concrete strain, the corrected loaded-end bar slip should be approximately equal to the integration of the bar strain along its embedment length. Feldman and Bartlett, (2007) who conducted pullout testing on smooth bars, took into account the contraction of the concrete, Equation 5.52, assuming strain compatibility and concrete stress uniformity.

$$s_c^l(x) = \left(1 + \frac{E_F A_F}{E_c A_c}\right) \int_0^{600} \epsilon_F(x) dx \quad \text{Equation 5.52}$$

Equation 5.52 results in a relatively small, 2% increase in the integration values presented in Table 5:17, which is negligible. The difference between the corrected loaded-end bar slip and the integration of the bar strains along the 600 mm embedment length shown in Table 5:15 to Table 5:17 and illustrated graphically in Figure 5:45 to Figure 5:47 may be attributed to the sliding of the grip used to attach the loaded-end LVDTs to the GFRP bar. For the beam-bond specimens, this difference is relatively small at first but increases with an increase in the load level, however, for MP2, the difference is noticeable immediately. Overall, it is important for future experimental programs to perform this check in order to assess the reliability of the data gathered from the LVDTs placed at the loaded-end and the unloaded-end. Typical bond-behaviour investigations that do not focus on bond stress

distribution and therefore do not have any strain gauges along the bar embedment length simply report the corrected loaded-end slip.

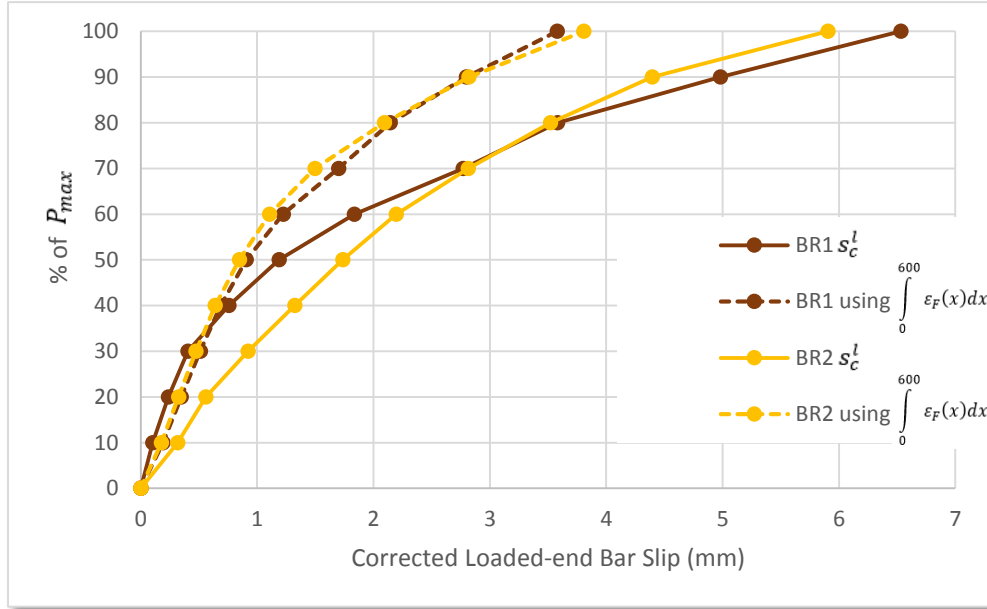


Figure 5:45: Corrected loaded-end bar slip versus integration of bar strains along its embedment length for the RILEM beams

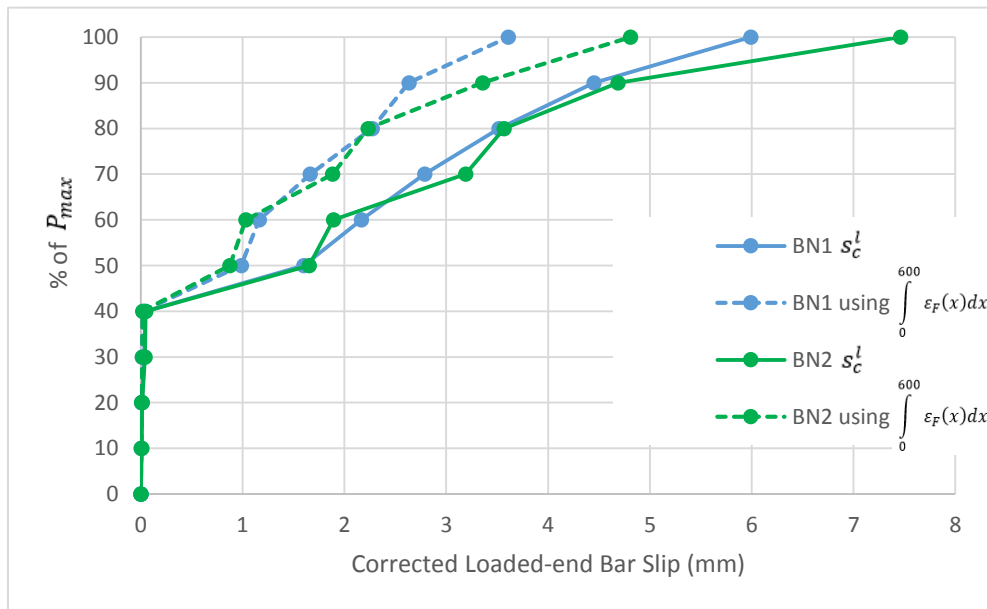


Figure 5:46: Corrected loaded-end bar slip versus integration of bar strains along its embedment length for the Notched beams

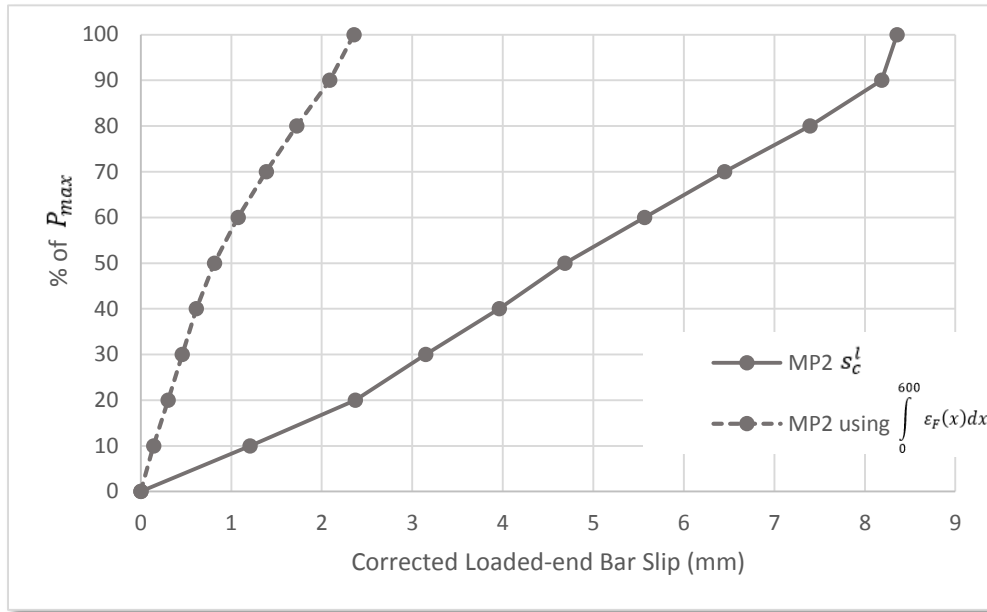


Figure 5:47: Corrected loaded-end bar slip versus integration of bar strains along its embedment length for the Modified pullout specimen, MP2

With the determination of the corrected loaded-end bar slip, one can continue with the goal of this section, which is to highlight the effect different test methods have on the bond behaviour and bond stress distribution of the GFRP bar used in this investigation. The majority of research works that conduct bond behaviour analysis develop bond-slip curves assuming uniform bond stress distribution. Therefore, as a means of comparison, for the beam-bond specimens and the Modified pullout samples, Figure 5:48 is a plot of the average bond stress obtained using Equation 5.42 at 10% increments of the respective P_{max} values versus the corrected loaded-end bar slip. The plot for MP1 includes 76% of P_{max} , the point at which it experienced concrete splitting failure.

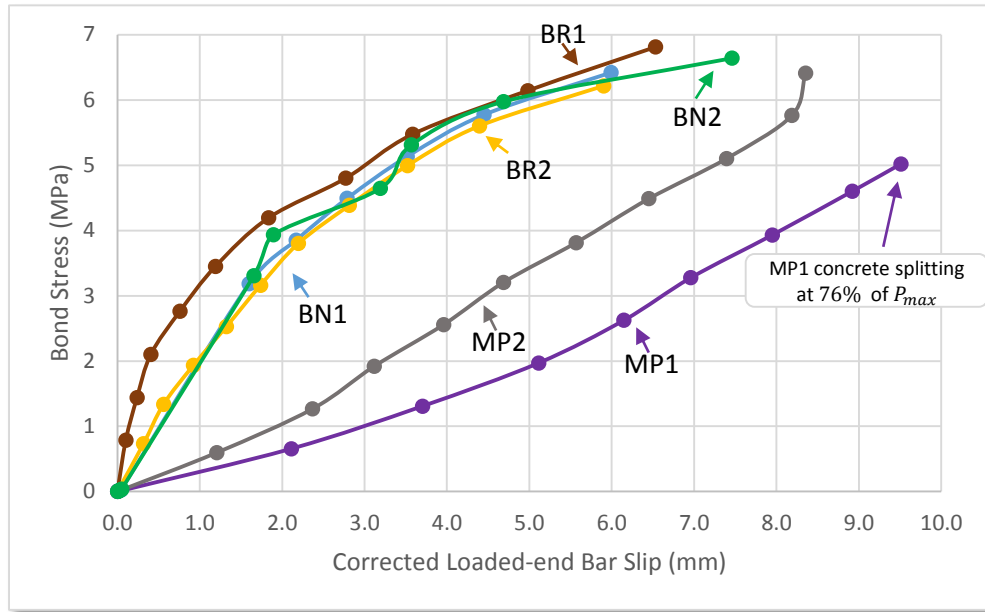


Figure 5:48: Average bond stress versus the corrected loaded-end bar slip assuming uniform bond stress distribution

Table 5:18 provides the corresponding peak average bond stresses, which are identical to Table 5:10 as well as the associated corrected loaded-end bar slip.

Table 5:18: Average bond stress assuming a uniform bond stress distribution versus the corresponding corrected loaded-end bar slip, at the maximum load, P

Specimen Designation	$\mu_{avg.}^u$ (MPa)	s_c^l (mm)
BR1	6.8	6.5
BR2	6.2	5.9
RILEM beam avg.	6.5	6.2
BN1	6.4	6.0
BN2	6.6	7.5
Notched beam avg.	6.5	6.8
MP1 at 76% of P_{max}	5.0	9.5
MP2	6.4	8.4

From the observation of Figure 5:48 and Table 5:18, it is evident that the beam-bond specimens as well as MP2, exhibit similar peak average bond stress values at the point of GFRP bar rupture, however, the corrected loaded-end bar slip for MP2, as also illustrated in Table 5:15 to Table 5:17, is higher. The general shape of the curves in Figure 5:48 for the beam-bond specimens differ slightly from the Modified pullout specimens and this is directly a consequence of the loading mechanism of the universal testing machine used in the pullout testing. The curves also resemble typical bond stress versus bar slip plots

produced by other investigators except for the fact that in this study, due to the rupturing of the GFRP bar at P_{max} , the curves have no descending component.

In conformity with the recommendation of Abrams, (1913), for the beam-bond and the Modified pullout specimen, MP2, Figure 5:49 to Figure 5:53 plot the corresponding bond stress distribution along the bar embedment length at an approximate corrected loaded-end bar slip of 0.1, 0.5, 1, 1.5 and 2 mm using linear interpolation in cases where the corrected loaded-end bar slip did not coincide perfectly with these values. Table 5:19 provides the corresponding actual peak bond stress value.

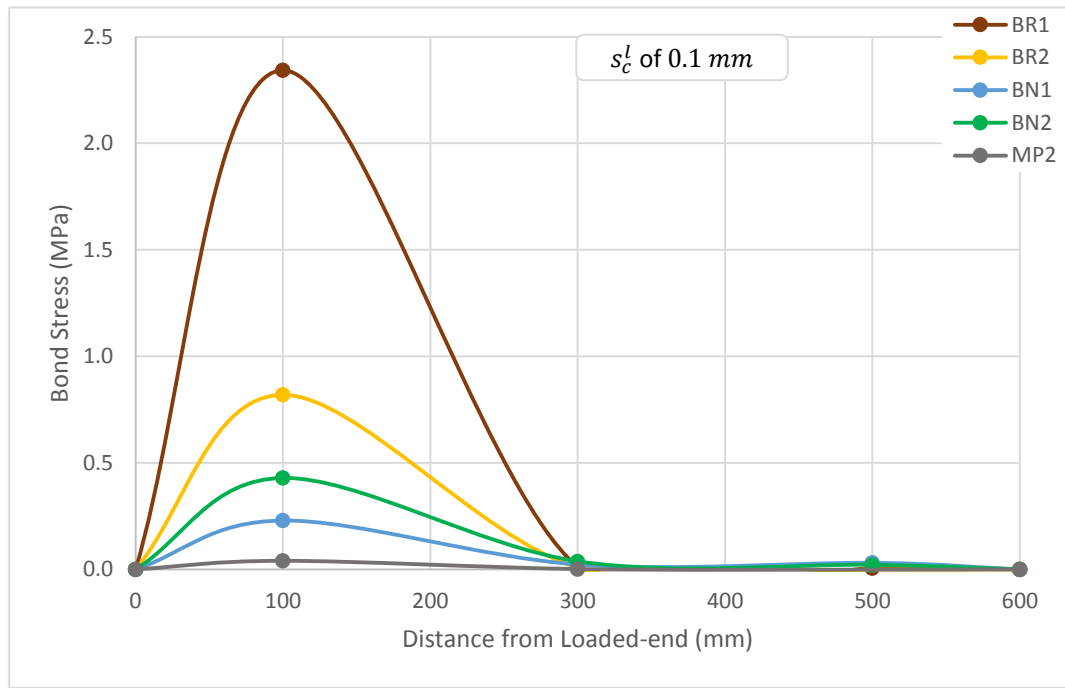


Figure 5:49: Bond stress distribution along the embedment length at a corrected loaded-end bar slip of 0.1 mm

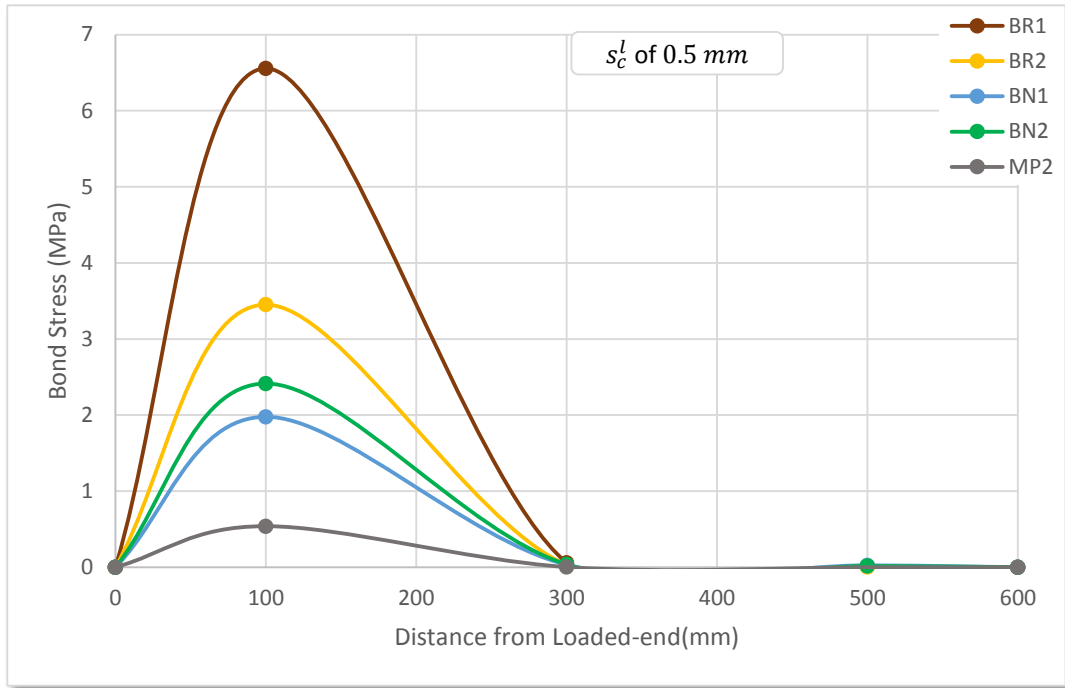


Figure 5:50: Bond stress distribution along the embedment length at a corrected loaded-end bar slip of 0.5 mm

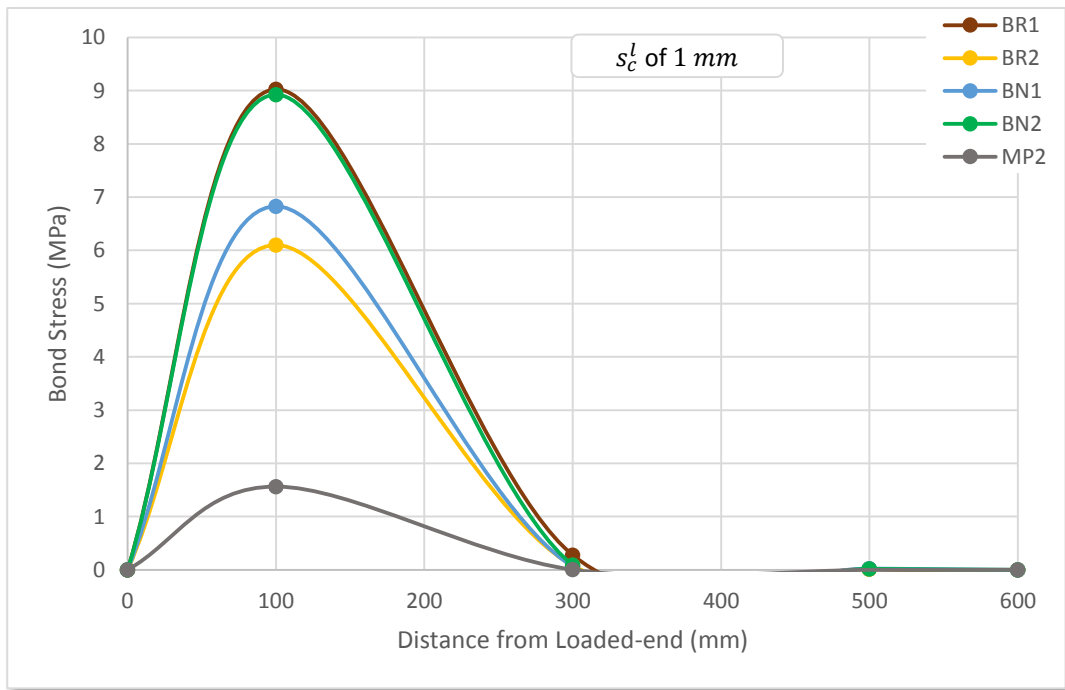


Figure 5:51: Bond stress distribution along the embedment length at a corrected loaded-end bar slip of 1 mm

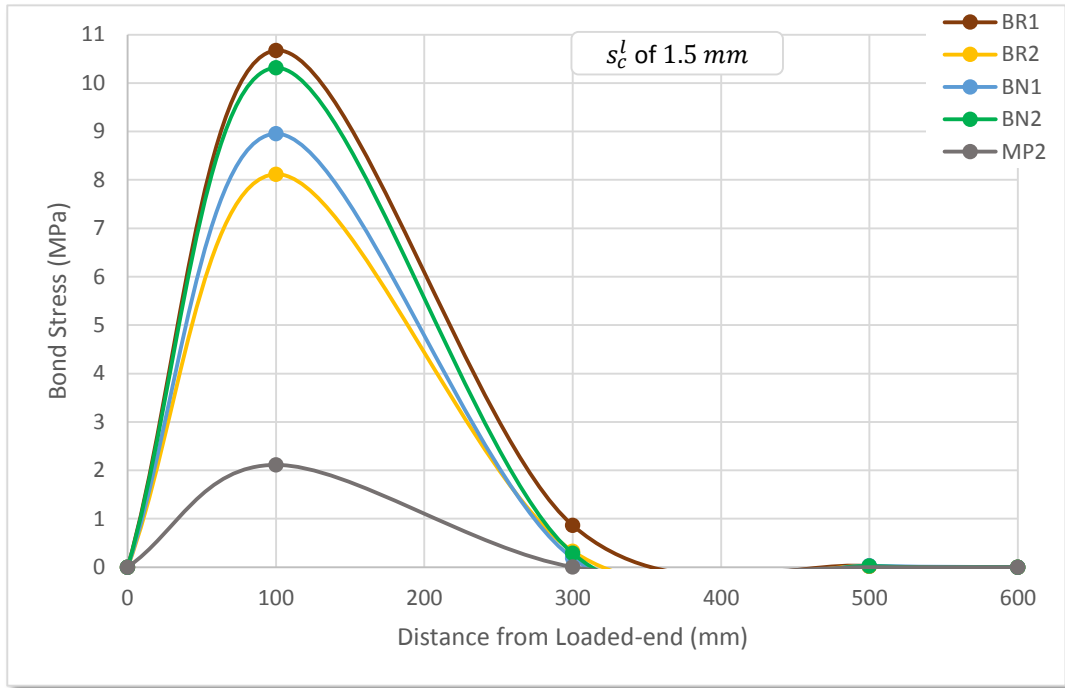


Figure 5:52: Bond stress distribution along the embedment length at a corrected loaded-end bar slip of 1.5 mm

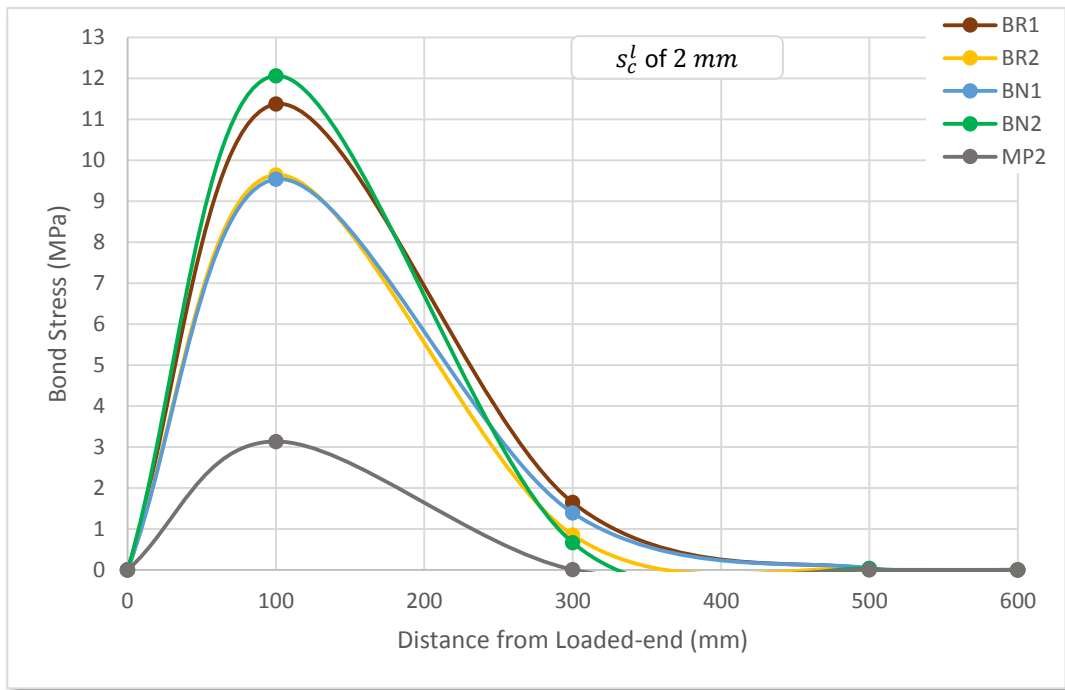


Figure 5:53: Bond stress distribution along the embedment length at a corrected loaded-end bar slip of 2 mm

Table 5:19: Peak bond stress obtained at specified corrected loaded-end bar slip values using the actual bond stress distribution

Specimen Designation	μ_{peak} (MPa) at s_c^l (mm) of,				
	0.1	0.5	1	1.5	2
BR1	2.3	6.6	9.0	10.7	11.4
BR2	0.8	3.5	6.1	8.1	9.6
RILEM beam avg.	1.6	5.1	7.6	9.4	10.5
BN1	0.2	2.0	6.8	9.0	9.5
BN2	0.4	2.4	8.9	10.3	12.1
Notched beam avg.	0.3	2.2	7.9	9.7	10.8
MP2	0.04	0.5	1.6	2.1	3.1

Observation of Figure 5:49 to Figure 5:53 as well as Table 5:19 show that as the corrected loaded-end bar slip increases, the beam-bond specimens show comparable bond stress distributions and peak bond stresses, however, MP2, consistently demonstrates lower results. This is in contrast to the conclusions drawn from Table 5:18, where, assuming uniform bond stress distribution, the beam-bond specimens and MP2 exhibited similar peak average bond stresses. Therefore, this study finds that knowledge of the strain distribution along the embedment length is critical and conclusions drawn from researchers in the past based on uniform bond stress distribution may not be accurate. In addition, the inclusion of beam-bond testing is important in the analysis of bond behaviour and experimenters should not simply rely on data from pullout tests.

Concerning the two beam types, note, with reference to Figure 5:49 to Figure 5:53, that at a corrected loaded-end bar slip value of 1 mm and beyond, the Notched beams are cracked and therefore their bond stress distributions progressively become comparable to the RILEM beams. Thus, one can conclude that after the midspan flexural cracking of the Notched beams, there is no substantial difference between the overall bond behaviour of the two beam types. As stated earlier, the Notched beams are more realistic and they simulate the behaviour of real beams because they include the tension stiffening effects of concrete and in addition, they are easier to construct than the RILEM beams. On the other hand, since the RILEM beams do not undergo midspan flexural cracking, there is a higher probability that strain gauges placed on the longitudinal tensile reinforcement will survive for a longer period and there is a stability associated with the bar strain data from these beams. Since the survivability and stability of the strain data is critical to an analysis of bond stress distribution, this study recommends RILEM beams for future experiments as the benefits associated with the performance of these beams by far surpasses the mentioned advantages gained from using Notched beams. In addition, in most design applications, engineers ignore the tensile contribution from concrete and furthermore, this study finds

that the inclusion of concrete instead of a steel hinge at midspan, especially for bond stress analysis, is not valuable since it produces bar strain data that are negligible prior to the occurrence of midspan flexural cracking.

5.9 Bond Stress Analysis of Standard Pullout Specimens

As CEB-FIP, (2000) mentions, the purpose of the Standard pullout specimens, also referred to as short specimens, is to capture the local bond-slip behaviour between the reinforcement and the concrete and this necessitates the usage of relatively small embedment lengths in order to ensure a fairly uniform bond stress distribution. To define a relationship between the bond and the slip of an FRP bar at the local level, CEB-FIP Model Code, (2010), adopts the double branch model proposed by Cosenza et al., (1995), which is a modified form of Eligehausen et al., (1982)'s B.P.E. model that addressed the bond behaviour of steel reinforcement. In Cosenza et al., (1995)'s model, the first branch of the bond-slip curve, the ascending branch, is identical to Eligehausen et al., (1982)'s expression, which is:

$$\frac{\mu}{\mu_{max}} = \left(\frac{s}{s_{\mu max}} \right)^{\alpha} \quad 0 \leq s \leq s_{\mu max} \quad \text{Equation 5.53}$$

In Equation 5.53, the parameter α is obtained using:

$$A_{exp.}^{asc.} = \frac{(\mu_{max})(s_{\mu max})}{(1+\alpha)} \quad \text{Equation 5.54}$$

where,

$A_{exp.}^{asc.}$ = Area under the ascending portion of the bond-slip curve obtained from experimental data

Note that in their experimental program, Eligehausen et al., (1982), measured the unloaded-end bar slip, however, since the general shape of the bond-slip curves is the same regardless of whether the unloaded-end or loaded-end bar slip is used, this study will evaluate the effectiveness of Equation 5.53 using both unloaded-end and loaded-end bar slip data. For the descending branch of the bond-slip curve, Cosenza et al., (1995) proposed

that the bond stress would decrease linearly with a slope of magnitude $p \frac{\mu_{max}}{s_{\mu max}}$ which results in the following relationship at ultimate conditions:

$$p \frac{(\mu_{max})}{s_{\mu max}} = \frac{(\mu_{max} - \mu_{ult.})}{(s_{ult.} - s_{\mu max})} \quad s_{\mu max} \leq s \leq s_{ult.} \quad \text{Equation 5.55}$$

Rearranging Equation 5.55 results in:

$$(s_{ult.} - s_{\mu max}) = \frac{(\mu_{max} - \mu_{ult.})(s_{\mu max})}{p(\mu_{max})} \quad \text{Equation 5.56}$$

Equation 5.56 is then substituted into Equation 5.57, which leaves the parameter p , as the only unknown.

$$A_{exp.}^{des.} = \frac{(s_{ult.} - s_{\mu max})(\mu_{ult.} + \mu_{max})}{2} \quad \text{Equation 5.57}$$

where,

$A_{exp.}^{asc.}$ = Area under the descending portion of the bond-slip curve obtained from experimental data

Once the value of p is known, a substitution of μ instead of $\mu_{ult.}$ and s instead of $s_{ult.}$ in Equation 5.55 and a subsequent rearrangement results in the general linear expression as shown in Equation 5.58 and in CEB-FIP Model Code, (2010), which is applicable beyond the point of maximum bond stress.

$$\mu = \mu_{max} \left[1 - p \frac{(s - s_{\mu max})}{s_{\mu max}} \right] \quad s_{\mu max} \leq s \leq s_{ult.} \quad \text{Equation 5.58}$$

Equation 5.53 and Equation 5.58 can provide a unique set of parameters for the GFRP reinforcement in this experimental program and for further clarification, Figure 5:54 is a graphical representation of the modified B.P.E. model by Cosenza et al., (1995).

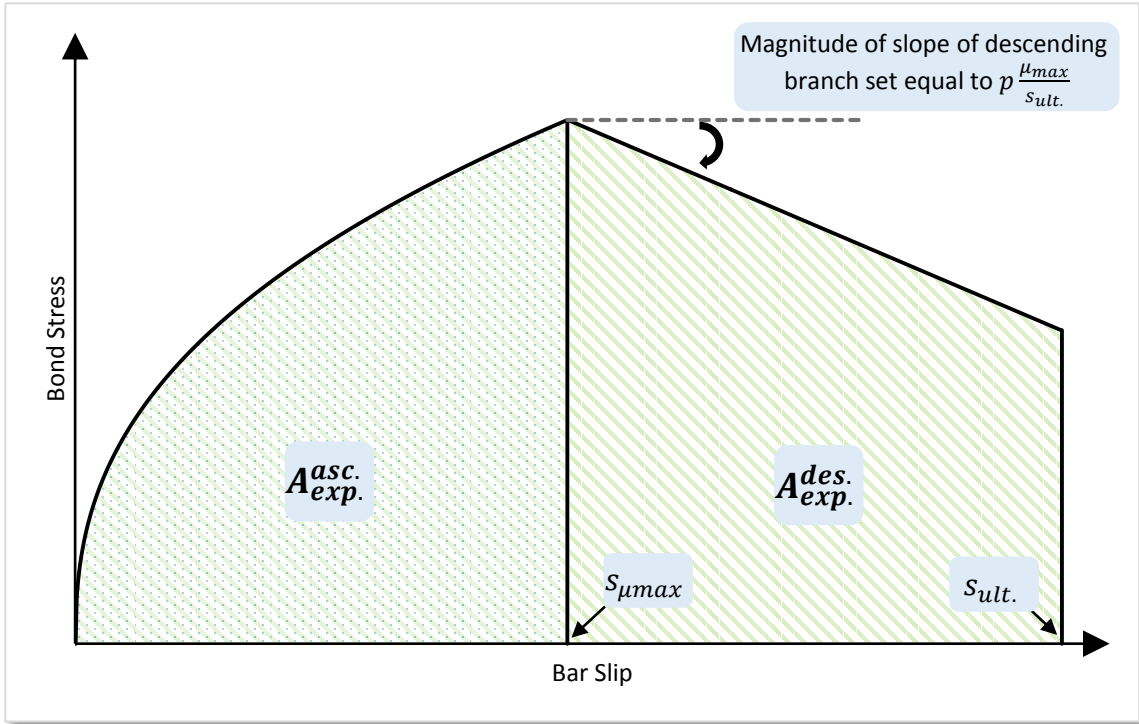


Figure 5:54: Model proposed by Cosenza et al., (1995)

Before the Cosenza et al., (1995) model can be applied to the experimental data, it is first necessary to calculate the $A_{exp}^{asc.}$ and $A_{exp}^{des.}$ which in turn, will allow for the determination of the α and p parameters. Note that the value of $A_{exp}^{asc.}$ and $A_{exp}^{des.}$ depends on whether bond stress versus unloaded-end bar slip data or bond stress versus the corrected loaded-end bar slip data is used and thus for each Standard pullout specimen, two sets of α and p parameters are obtained. With reference to Figure 5:55, the unloaded-end bar slip is the average of L1, L2 and L3 while for the corrected loaded-end bar slip is the average of L4, L5 and L6, taking into account the 255 mm elastic elongation the GFRP bar experienced over the debonded region between the point of loaded-end LVDT attachment and the onset of bar embedment. Assuming uniform bond stress distribution, the calculation of the bond stress for the Standard pullout specimens make use of Equation 5.59.

$$\mu = \left(\frac{P}{\pi d_{bF}(60)} \right) \quad \text{Equation 5.59}$$

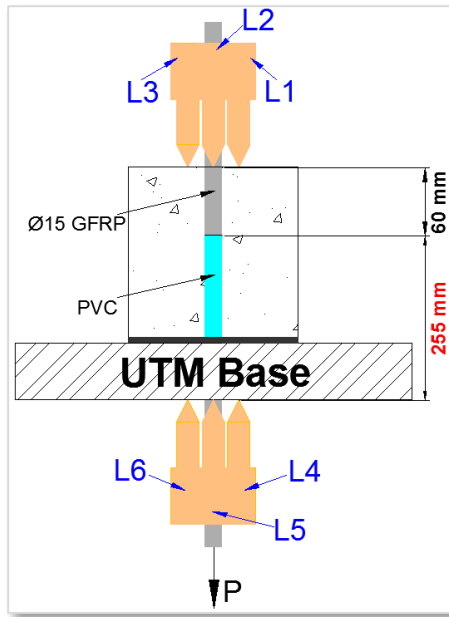


Figure 5:55: Standard pullout specimen detail

Table 5:20 for bond stress versus unloaded-end bar slip data and Table 5:21 for bond stress versus the corrected loaded-end bar slip data, present the values of the A_{exp}^{asc} and A_{exp}^{des} and the resulting α and p parameters. Figure 5:56 to Figure 5:60 present the bond stress versus slip curves for both the unloaded-end and the corrected loaded-end bar slip values and in addition, illustrate the ability of the Cosenza et al., (1995) model to predict the overall bond-slip behaviour of the Standard pullout specimens.

Table 5:20: α and p parameters for Standard pullout specimens obtained using unloaded-end bar slip data

Specimen Designation	$A_{exp}^{asc.}$ (MPa · mm)	Resulting parameter α	$A_{exp}^{des.}$ (MPa · mm)	Resulting parameter p
P1	42.93	0.17	59.19	0.32
P2	25.20	0.24	48.37	0.25
P3	25.64	0.16	33.32	0.32
P4	16.04	0.15	30.56	0.18
P5	31.71	0.13	72.19	0.21
P6	34.97	0.16	59.32	0.26
P7	38.00	0.13	66.10	0.27
P8	27.46	0.12	66.30	0.19
P9	27.36	0.18	62.82	0.21
P10	26.31	0.18	21.00	0.10
Avg.	29.56	0.16	51.92	0.23
S.D.	7.61	0.03	17.69	0.07
COV (%)	25.73	21.28	34.07	29.04

Table 5:21: α and p parameters for Standard pullout specimens obtained using corrected loaded-end bar slip data

Specimen Designation	$A_{exp}^{asc.}$ (MPa · mm)	Resulting parameter α	$A_{exp}^{des.}$ (MPa · mm)	Resulting parameter p
P1	54.55	0.38	54.19	0.52
P2	37.21	0.61	40.72	0.56
P3	36.07	0.53	28.89	0.69
P4	23.97	0.61	28.94	0.40
P5	49.18	0.44	60.80	0.50
P6	51.57	0.60	50.34	0.63
P7	50.82	0.48	57.22	0.54
P8	38.98	0.46	60.26	0.40
P9	40.62	0.56	58.07	0.45
P10	41.39	0.80	20.71	0.24
Avg.	42.44	0.55	46.01	0.49
S.D.	9.26	0.12	15.02	0.13
COV (%)	21.81	21.85	32.65	26.27

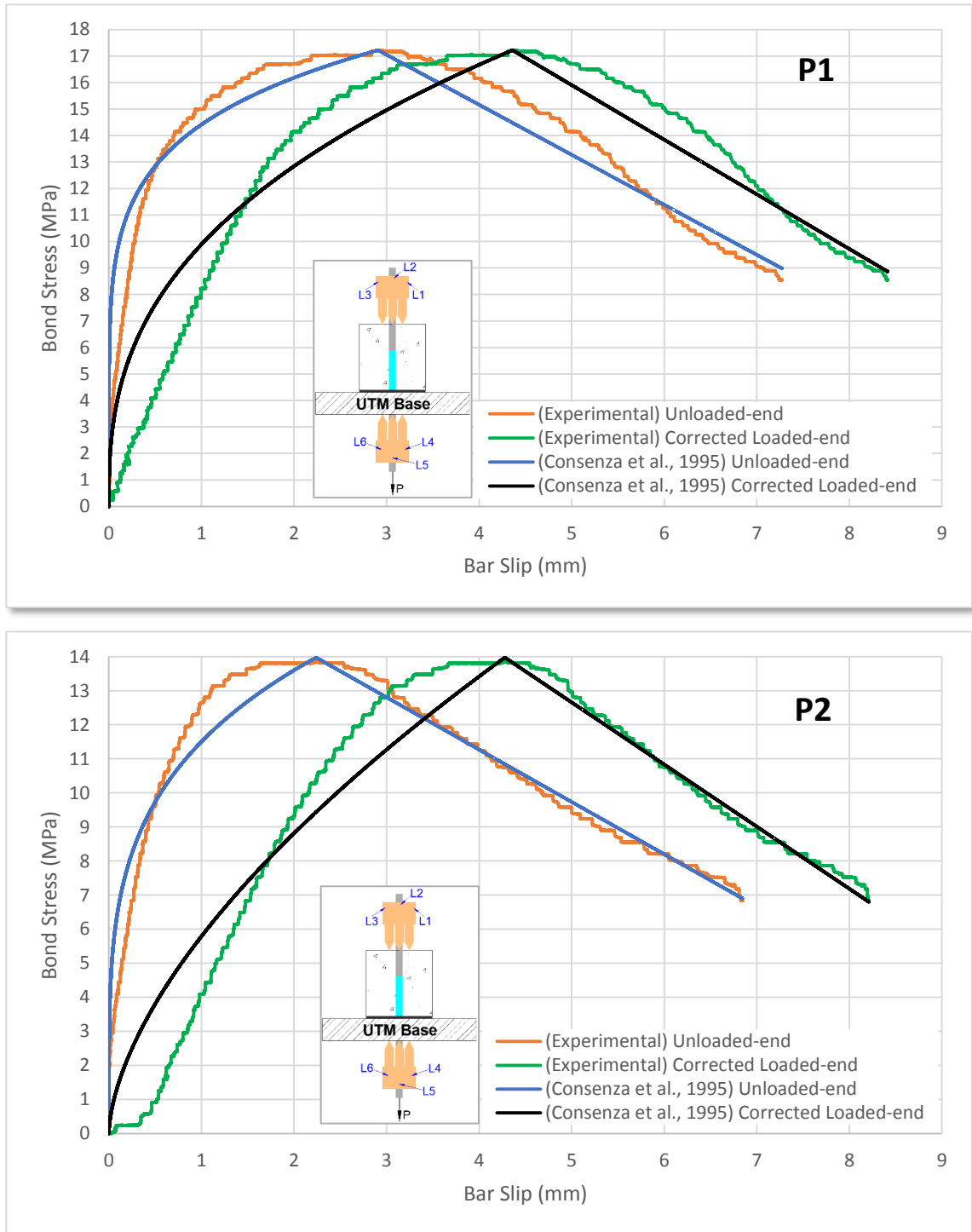


Figure 5:56: Bond stress-GFRP bar slip in P1 and P2

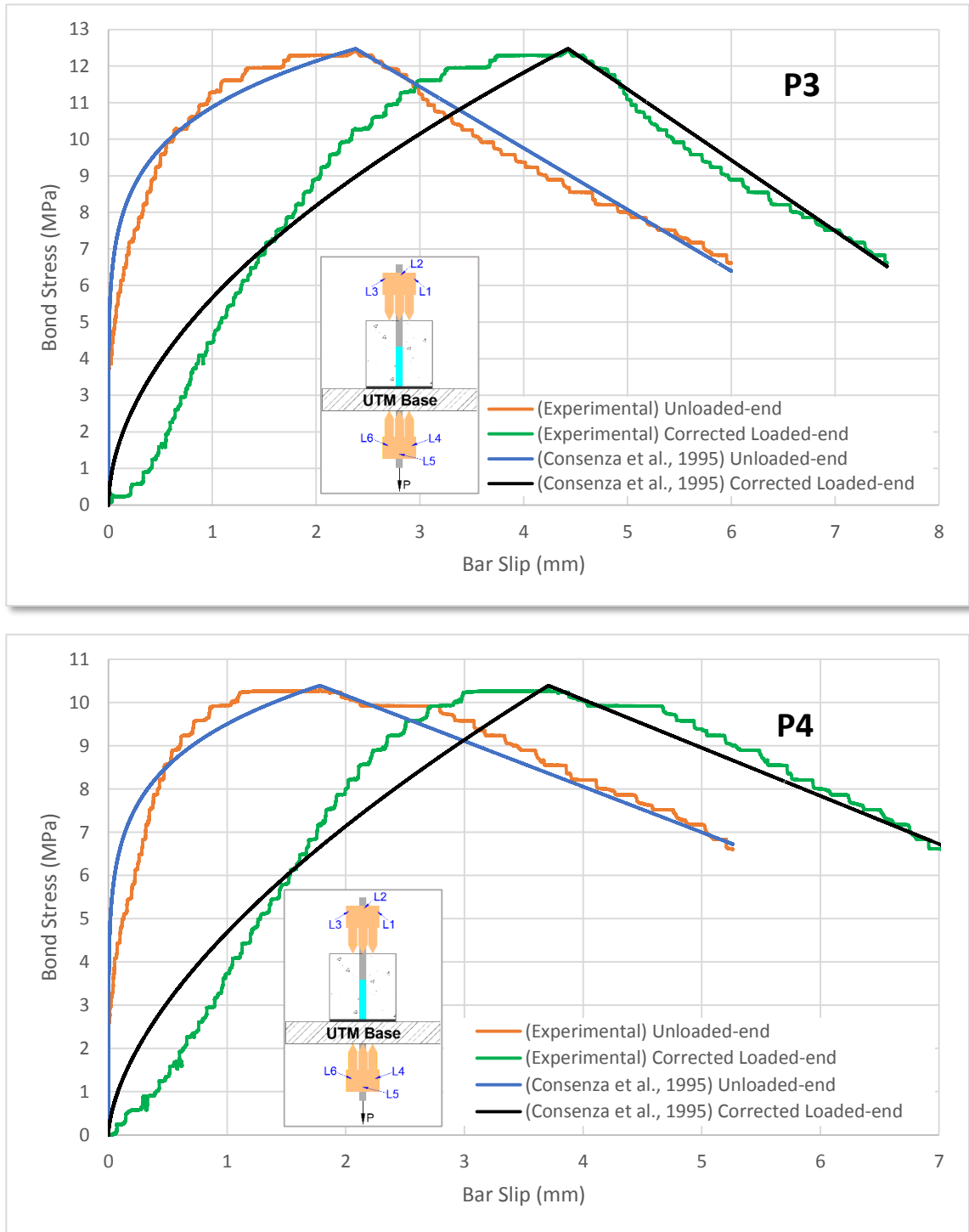


Figure 5:57: Bond stress-GFRP bar slip in P3 and P4

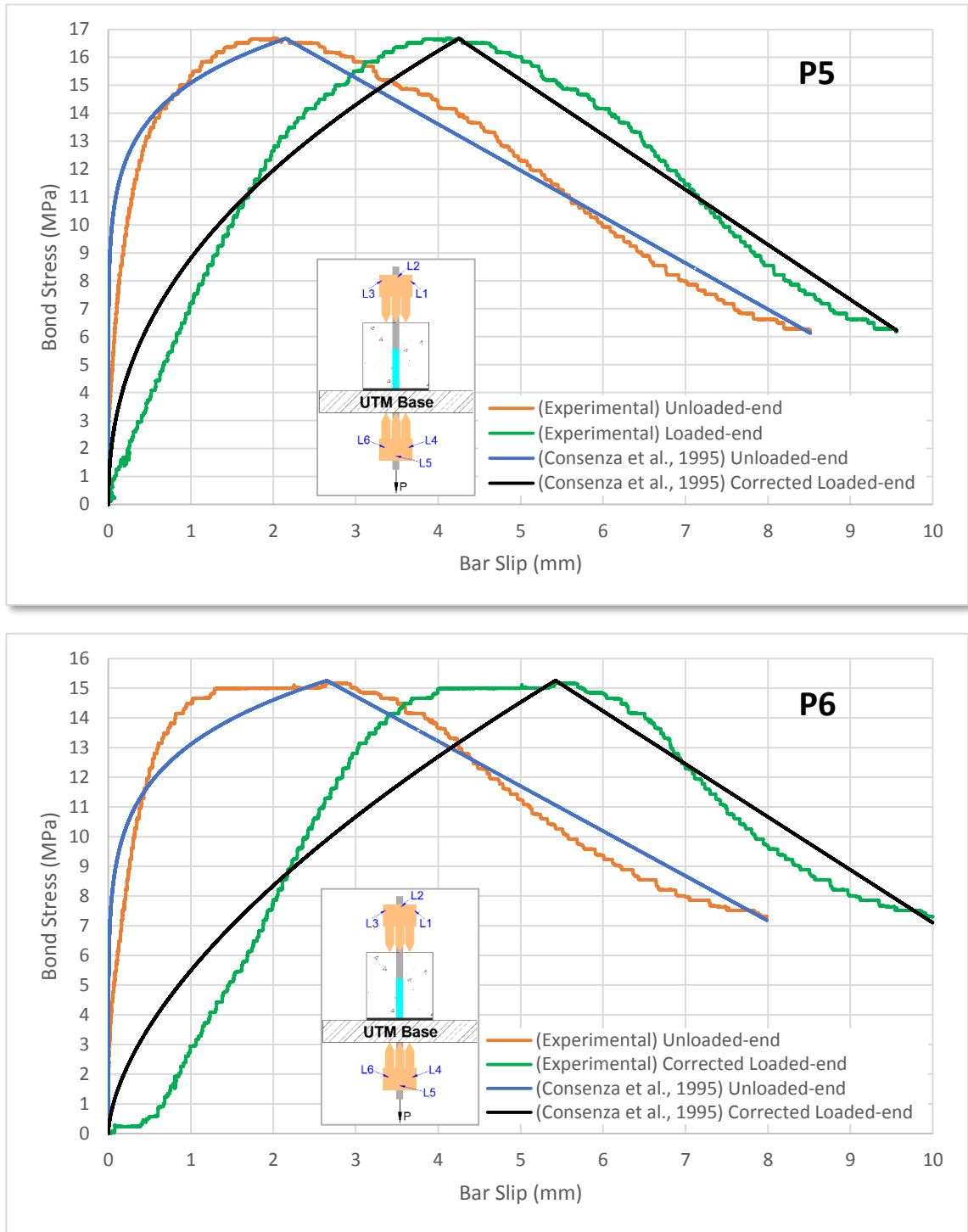


Figure 5:58: Bond stress-GFRP bar slip in P5 and P6

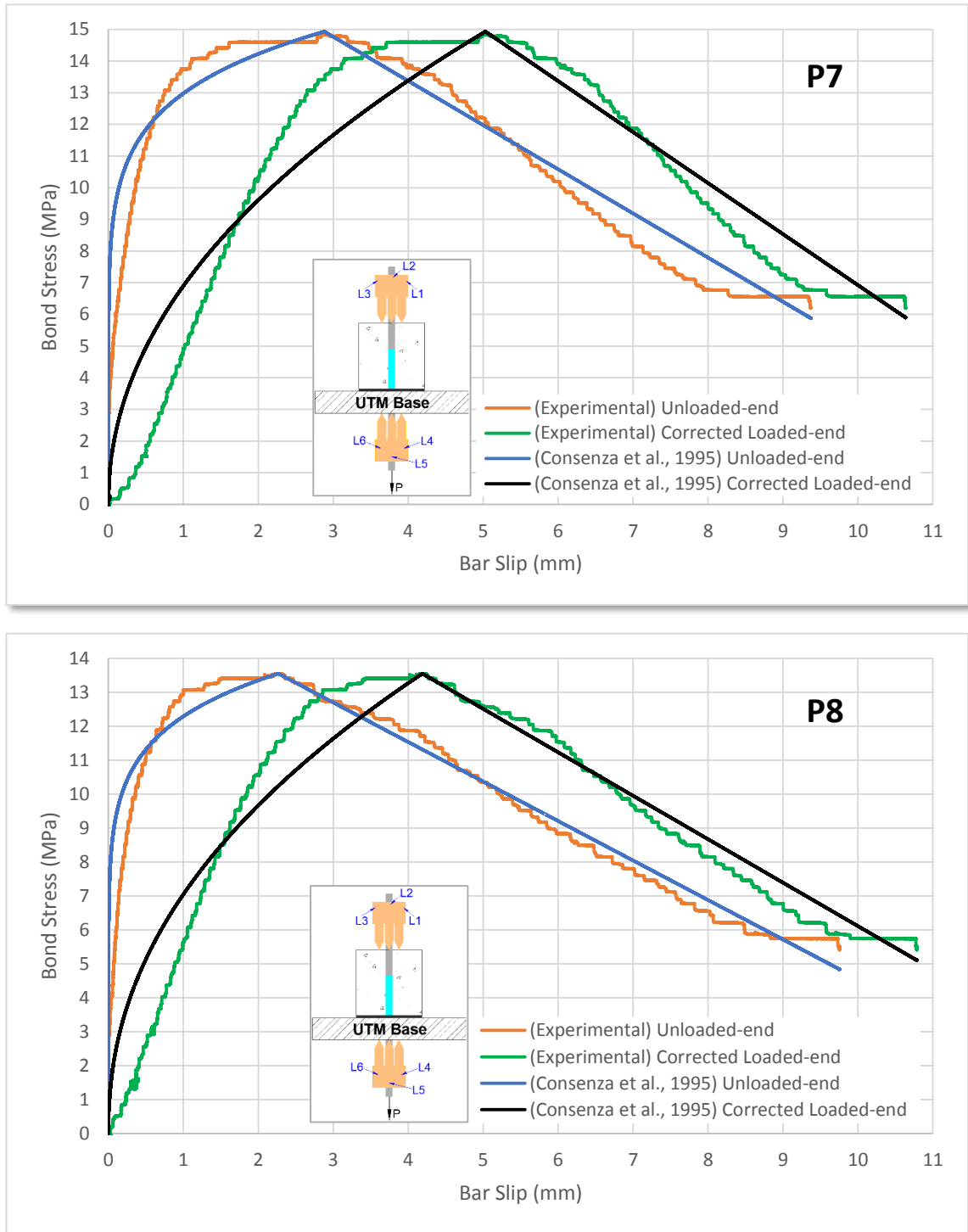


Figure 5:59: Bond stress-GFRP bar slip in P7 and P8

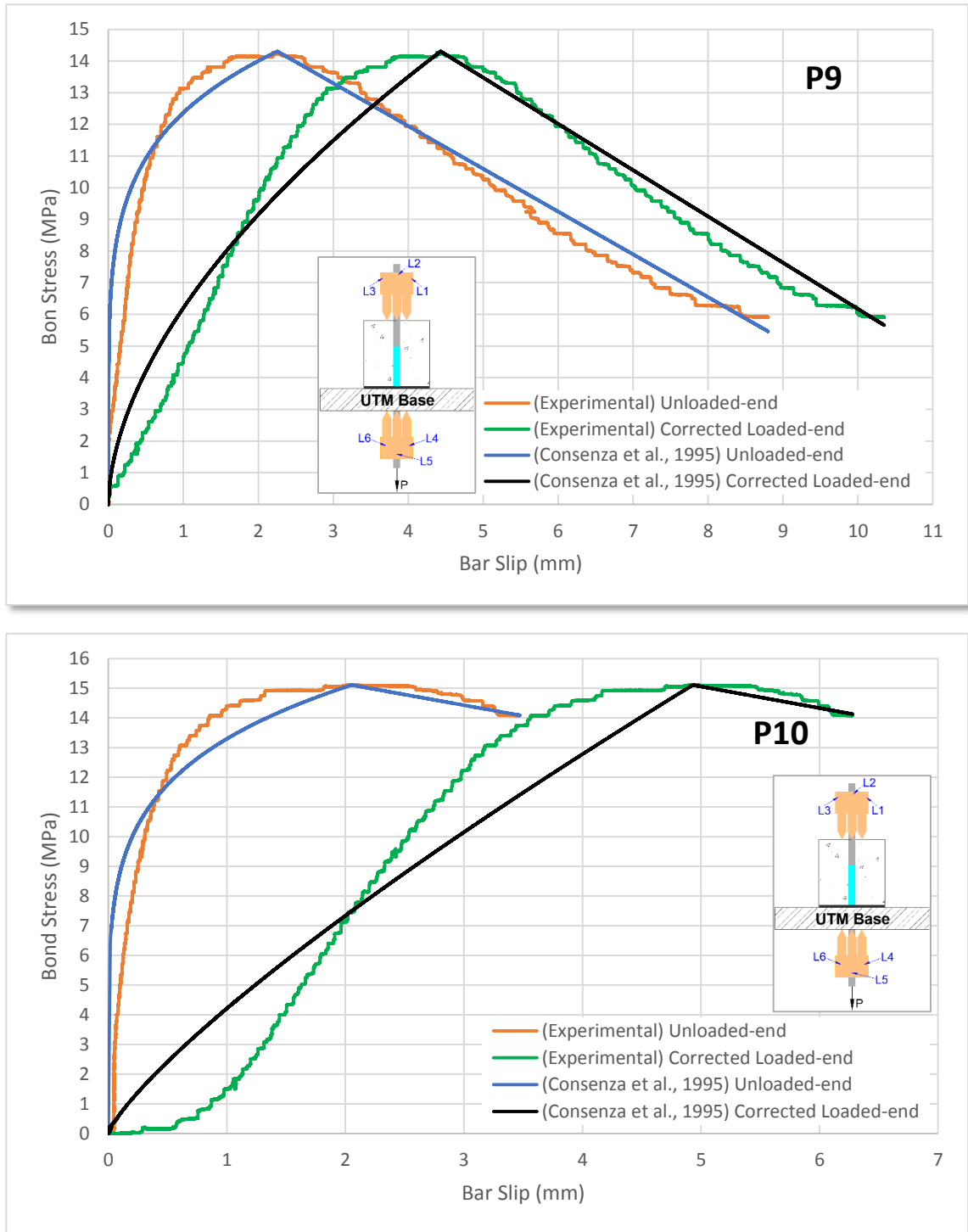


Figure 5:60: Bond stress-GFRP bar slip in P9 and P10

From the observation of the presented figures, one can make a generalized statement that the proposed model by Cosenza et al., (1995) is able to predict, reasonably accurately, the overall pattern of the ascending and descending branches of the bond stress-slip curves for FRP reinforcement. A review of Table 5:20 and Table 5:21 however, shows that the α and p parameters have a high degree of variability between the samples and this does not allow the writer to state that the average values for α and p are unique to the GFRP bar in this study and will reasonably predict the bond stress versus slip behaviour of successive samples. However, if one were to conduct a substantial number of pullout testing, then it is possible that a regression analysis would produce an accurate approximation of α and p parameters that would be applicable to a specific bar.

With reference to Figure 5:54 note, Cosenza et al., (1995) assume that at the onset of loading, there is an immediate slip of the GFRP bar and this essentially ignores the existence of the chemical adhesion component of the bond between the GFRP bar and the concrete. As Table 5:22 illustrates, the onset of the slip at the loaded-end of the specimens occur at a non-zero load however, this load is negligible to the point that the assumption by Cosenza et al., (1995) becomes accurate. Thus, one can conclude that the chemical adhesion component of the bond between GFRP reinforcement used in this study and the concrete is insignificant and cannot be relied upon, which puts a greater emphasis on the contribution from the mechanical bearing and the frictional components of bond.

Table 5:22: Load value corresponding to onset of corrected loaded-end bar slip

Specimen Designation	Load value, P (kN) corresponding to the initiation of s_c^l
P1	0.654
P2	0.023
P3	0.243
P4	0.003
P5	0.260
P6	0.023
P7	0.234
P8	0.009
P9	0.659
P10	0.003
Avg.	0.211

With reference to Table 5:23, the average maximum bond stress and corrected loaded-end bar slip for the Standard pullout specimens was 14.4 MPa and 4.5 mm, respectively. Due to the difference in bar embedment length between the Standard pullout specimens and the beam-bond and Modified pullout samples, it would be incorrect to compare the

values between Table 5:23 and Table 5:18. However, one can conclude that, in terms of bond behaviour, the Standard pullout testing method has no resemblance to actual structural elements with significantly higher embedment lengths nor can it provide any useful information in terms of bond stress distribution and required bar development length.

Table 5:23: Maximum bond stress and corresponding corrected loaded-end bar slip

Specimen Designation	μ_{max} (MPa)	$s_{c\mu max}^l$ (mm)
P1	17.2	4.4
P2	14.0	4.3
P3	12.5	4.4
P4	10.4	3.7
P5	16.7	4.3
P6	15.3	5.4
P7	14.9	5.0
P8	13.6	4.2
P9	14.3	4.4
P10	15.1	4.9
Avg.	14.4	4.5
S.D.	2.0	0.5
COV (%)	13.8	10.9

Chapter 6 Summary, Conclusions and Recommendations for Future Research

6.1 Summary

In an effort to study the bond behaviour of GFRP bars in concrete, four beam-bond and two Modified pullout specimens were tested and the strain distribution along the embedment length of the GFRP bar as well as the bar slip were measured. In addition, ten Standard pullout specimens with short embedment length were tested for bond. The design of two of the beam-bond specimens was in accordance with RILEM TC-RC5, (1994) recommendations and consisted of the characteristic half-beams joined at the top by a steel hinge and at the bottom by the continuous longitudinal tensile reinforcement. The other two beams were a modified form of the ACI 208, (1958) beam design method and possessed a notch at midspan at the bottom of the beam and had better resemblance to typical beams used in construction. Besides the mentioned difference between the RILEM and Notched beams, all other aspects, including the cross section, reinforcement detailing and spacing as well as the embedment length, diameter and type of GFRP bar selected for bond investigation were identical in the four beam-bond specimens. The beams, which had an overall length of 2,000 *mm*, had one-half designated as the “Test-end” with 600 *mm* GFRP bar embedment and the other half as the “Non-test End” with 900 *mm* embedment. Thus, if the beams were to experience a pullout failure, it was expected to occur first in the “Test-end” of the beams with the smaller embedment length. The two Modified pullout specimens, although in accordance with CSA S806, (2012) in terms of cross section, had an overall length of 700 *mm* with the GFRP having an embedment length of 600 *mm*, identical to the beam-bond specimens, hence allowing a direct comparison between the two test methods. Lastly, the Standard pullout specimens, in accordance with CSA S806, (2012), had embedment length of 60 *mm*, or four times the nominal GFRP bar diameter.

All beam-bond specimens, subjected to four-point bending, experienced a flexural tension failure through GFRP bar rupture and as anticipated, the 600 *mm* embedment length was sufficient to prevent any bar slip from the unloaded-end of the embedment. In addition, the moment capacity obtained experimentally agreed well with the theoretical predictions in accordance with CSA S806, (2012). The first Modified pullout specimen experienced a concrete splitting failure at a load value of approximately 76% of the anticipated GFRP rupture load and because of this, the second Modified pullout specimen

was confined and as a result, experienced a failure through GFRP rupture. Certain strain gauges in both the beam-bond and the modified pullout specimens failed at load values of approximately 45 to 93% of the anticipated GFRP rupture load, attributed mainly to a combination of the strain gauges debonding from the bar surface and gradual detachment of external GFRP bar fibres with increasing stress levels. For the Notched beams, strain gauge failures in the midspan region was also attributed to the inability of these gauges to withstand the reloading phase after the shock and energy release associated with the occurrence of midspan flexural cracking and the subsequent reloading phase. All ten Standard pullout specimens experienced pullout failure.

6.2 Conclusions

The focus of this experimental program was on analyzing the bond stress distribution along the embedment length of the GFRP bar and to that extent, the following conclusions are reached:

1. The strain distribution along the embedment length of the GFRP bar is nonlinear and at any stage of loading can be described using a modified form of the logistic growth function that is independent of the bar slip. The advantage of this expression is that if it is validated by extensive experimental data, then conventional beam theory can be used to constrain this expression while strain gauges on the embedded reinforcement can modify its general shape based on the progression of bond degradation. The derivative of this function allows for the precise determination of the bond stress as a function of the distance from the loaded-end and produces a characteristic shape similar to a parabolic distribution.
2. The actual bond stress distribution has practically a parabolic form and the average uniform bond stress assumption by current standards underestimate the bond stress development within a given embedment length. Experimentally, for the RILEM and Notched beam-bond specimens, an average peak bond stress of 11.7 MPa and 12.9 MPa was achieved, respectively. For the Modified pullout specimen, MP2, at the point of GFRP bar rupture, the peak bond stress was 14.2 MPa .
3. In conformity with previous studies, due to increase in bar stress and subsequent bond degradation, the location of the peak bond stress progressively moves from the loaded-end towards the unloaded-end of the embedded bar.

-
4. Experimentally, the 600 *mm* embedment length was sufficient to allow the 15 *mm* nominal diameter GFRP bar to reach rupture, however, the empirical development length required for this bar size by ACI 440.1 and to a lesser degree by CSA S806 and CSA S6, are much longer than 600 *mm*. On average, for GFRP bar rupture, ACI 440.1 recommended a development length of 1,594 *mm* while CSA S806 and CSA S6 suggested 947 and 735 *mm*, respectively. This indicates that the current development length recommendations need to be revisited by the appropriate committees responsible for their specifications.
 5. As Abrams mentioned over 100 years ago, comparison of bond performance of different test methods must occur at the same bar slip value. To that extent, in this experimental program it is evident that given the same corrected loaded-end bar slip of 0.1, 0.5, 1, 1.5 and 2 *mm* and using the actual bond stress distribution, the Modified pullout specimen, MP2, consistently developed a lower bond strength than the beam-bond specimens. This may be attributed to the confinement provided by the transverse reinforcement in the beam-bond specimens. Therefore, one cannot make a general statement that either test method will always provide higher or lower bond strength than the others because factors such as transverse confinement or even concrete strength may influence the results.
 6. The corrected loaded-end bar slip for all of the beam-bond specimens was found to be lower than that of the Modified pullout specimen, MP2.
 7. In comparing the two beam-bond test methods, although the Notched beams resemble actual beam elements in practice and can be more easily constructed, given the same loaded-end bar slip value, after midspan flexural cracking, they produce bond stresses that are comparable to the RILEM beams.
 8. The shock and release of energy upon midspan flexural cracking of the Notched beams increases the chances of strain gauge failure in this region and therefore, comparatively, the RILEM beams are able to provide a more reliable and consistent set of bond related data since they do not experience any midspan cracking. Thus, for the purposes of bond-behaviour investigation, particularly strain distribution along embedment length; it seems that the steel hinge design by RILEM TC-RC5 is superior to the beam-bond test recommended by ACI 208.
 9. Standard pullout testing on cubic concrete specimens is currently common practice, however, one must note that such testing merely serves as quality assurance rather than providing accurate data regarding the bond strength and stress distribution along the embedded length of a GFRP rebar in beams. The average bond strength for ten Standard pullout specimens as well as the associated average corrected loaded-end bar slip was found to be 14.4 *MPa* and 4.5 *mm*, respectively.

6.3 Recommendations for Future Research

In order to achieve further understanding concerning the bond behaviour and bond stress distribution of GFRP bars in particular, the following are recommendations for future studies:

1. Due to the different types of surface finishes, profiles and FRP bar sizes and strengths, a systematic study must be undertaken, using preferably the RILEM beam-bond test, to investigate the effect of all key parameters on the peak bond stress and bond stress distribution along various embedment lengths.
2. If possible, clear guidelines need to be developed that can be used to calibrate the pullout test results against the beam-bond test results.
3. The effect of transverse or confining FRP reinforcement on the bond strength and embedment length need to be investigated. Most current studies have used steel as transverse reinforcement rather than FRP.
4. Since failure of FRP reinforced structures is normally required to be initiated by failure of concrete rather than FRP rupture, the bond stress evaluation with increased bar stress need to be properly established. This will allow one to determine the required development length as function of the bar maximum stress.
5. Investigating the generality of a modified form of the logistic growth function in predicting the bond stress distribution as a function of the embedment length including the continual effect of bond degradation.
6. Develop an expression describing the GFRP bond stress as a function of the embedment length and evaluate the ability of this expression to sufficiently accommodate the effects of flexural and shear cracks, concrete cover, transverse reinforcement and bar material type and surface finish.
7. Establish the rate of bond degradation between the reinforcement and the concrete as a function of the loading type, such as bending and axial load and the loading rate.
8. Investigating the bond stress distribution along the reinforcement embedment length using beam-bond specimens with preplaced flexural cracks in order to simulate the behavior of real structural elements.

List of References

- Abrams, D. A. (1913). *Tests of bond between concrete and steel*. Urbana, (Illinois): University of Illinois.
- ACI 208. (1958). *Test procedure to determine relative bond value of reinforcing bars*. (No. 55-1). Redford Station (Detroit): American Concrete Institute.
- ACI 315. (1999). *Details and detailing of concrete reinforcement*. (No. ACI 315-99). Farmington Hills (Michigan): American Concrete Institute.
- ACI 408. (2003). *Bond and development of straight reinforcing bars in tension*. (No. ACI 408R-03). Farmington Hills (Michigan): American Concrete Institute.
- ACI 440. (2007). *Report on fiber-reinforced polymer (FRP) reinforcement of concrete structures*. (No. ACI 440R-07). Farmington Hills (Michigan): American Concrete Institute. Retrieved from www.concrete.org
- ACI 440.1. (2006). *Guide for the design and construction of structural concrete reinforced with FRP bars*. (No. 440.1R-06). Farmington Hills (Michigan): American Concrete Institute.
- ACI 440.3. (2004). *Guide for the test methods for fiber-reinforced polymers (FRPs) for reinforcing or strengthening concrete structures: B.3-Test Method for bond strength of FRP bars by pullout testing*. (No. 440.3R-04). Farmington Hills (Michigan): American Concrete Institute.
- ASTM A370. (2014). *Standard test methods and definitions for mechanical testing of steel products*. West Conshohocken, (Pennsylvania): ASTM International.
doi:10.1520/A0370-14
- ASTM C192/C192M. (2014). *Standard practice for making and curing concrete test specimens in the laboratory*. West Conshohocken, (Pennsylvania): ASTM International. doi:10.1520/C0192_C0192M-14
- ASTM C39/C39M. (2014). *Standard test method for compressive strength of cylindrical concrete specimens*. West Conshohocken, (Pennsylvania): ASTM International.
doi:10.1520/C0039_C0039M-14A

-
- ASTM C469/C469M. (2014). *Standard test method for static modulus of elasticity and poisson's ratio of concrete in compression*. West Conshohocken, (Pennsylvania): ASTM International. doi:10.1520/C0469_C0469M
- ASTM C617/C617M. (2012). *Standard practice for capping cylindrical concrete specimens*. West Conshohocken, (Pennsylvania): ASTM International. doi:10.1520/C0617_C0617M-12
- ASTM D7205/D7205M. (2011). *Standard test method for tensile properties of fiber reinforced polymer matrix composite bars*. West Conshohocken, (Pennsylvania): ASTM International. doi:10.1520/D7205_D7205M-06R11
- Benmokrane, B., Tighiouart, B., & Chaallal, O. (1996). Bond strength and load distribution of composite GFRP reinforcing bars in concrete. *ACI Materials Journal*, 93(3), 246-253.
- Bentz, E., & Collins, M. P. (2001). *Response 2000*. Toronto (Ontario):
- BSI 12269-1. (2000). *Determination of the bond behaviour between reinforcing steel and autoclaved aerated concrete by the "beam test"-part 1: Short term test (BS EN 12269-1:2000 ed.)*. London (England): British Standards Institute.
- CEB-FIP. (2000). *Bond of reinforcement in concrete (state-of-art report) bulletin 10*. Lausanne, (Switzerland): International Federation for Structural Concrete (fib).
- CEB-FIP Model Code. (2010). *Fib model code for concrete structures*. Lausanne (Switzerland): International Federation for Structural Concrete (fib).
- Chen, X., Zhou, J., & Chen, S. (2012). Effect of different environments on bond strength of glass fiber-reinforced polymer and steel reinforcing bars. *I6(6)*, 994-1002, ISSN 1226-7988. doi:10.1007/s12205-012-1462-3
- Collins, M. P., & Mitchell, D. (1991). *Prestressed concrete structures*. Englewood Cliffs (New Jersey): Prentice Hall.
- Cosenza, E., Manfredi, G., & Realfonzo, R. (1995). Analytical modelling of bond between FRP reinforcing bars and concrete. *Non-Metallic (FRP) Reinforcement for Concrete Structures - Proceedings of the Second International RILEM Symposium (FRPRCS-2)*, 164-171.

-
- CSA A23.3. (2004). *Design of concrete structures* (Third ed.). Mississauga (Ontario): Canadian Standards Association.
- CSA S6. (2006). *Canadian highway bridge design code* (Tenth ed.). Mississauga (Ontario): Canadian Standards Association.
- CSA S806. (2002). *Design and construction of building components with fibre-reinforced polymers*. Mississauga (Ontario): Canadian Standards Association.
- CSA S806. (2012). *Design and construction of building structures with fiber-reinforced polymers*. Mississauga (Ontario): Canadian Standards Association.
- CSA S807. (2010). *Specification for fiber-reinforced polymers*. Mississauga (Ontario): Canadian Standards Association.
- Daniali, S. (1992). Development length for fibre reinforced plastic bars. *Advanced Composite Materials in Bridges and Structures 1st International Conference*, Sherbrook (Quebec). 179-188.
- Davalos, J. F., Chen, Y., & Ray, I. (2008). Effect of FRP bar degradation on interface bond with high strength concrete. *Cement and Concrete Composites*, 30(8), 722-730. doi:10.1016/j.cemconcomp.2008.05.006
- Desnerck, P., Schutter, G., & Taerwe, L. (2010). Bond behaviour of reinforcing bars in self-compacting concrete: Experimental determination by using beam tests. *Materials and Structures*, 43, 53-62. doi:10.1617/s11527-010-9596-6
- Eligehausen, R., Popov, E. P., & Bertero, V. V. (1982). Local bond stress-slip relationships of deformed bars under generalized excitations. *Proceedings of the 7th European Conference on Earthquake Engineering*, 69-80.
- Esfandeh, M., Sabet, A. R., Rezaoust, A. M., & Alavi, M. B. (2009). Bond performance of FRP rebars with various surface deformations in reinforced concrete. *Polymer Composites*, 30(5), 576-582. doi:10.1002/pc.20589
- Feldman, L. R., & Bartlett, F. M. (2005). Bond strength variability in pullout specimens with plain reinforcement. *ACI Structural Journal*, 102(6), 860-867. doi:10.14359/14794

-
- Feldman, L. R., & Bartlett, F. M. (2007). Bond stresses along plain steel reinforcing bars in pullout specimens. *ACI Structural Journal*, 104, No. 6, 685-692.
- Focacci, F., Nanni, A., & Bakis, C. (2000). Local bond-slip relationship for FRP reinforcement in concrete. *Journal of Composites for Construction*, 4(1), 24-31. doi:10.1061/(ASCE)1090-0268(2000)4:1(24)
- Ghali, A., & Favre, R. (1986). *Concrete structures: Stresses and deformations*. London (England): Chapman and Hall Ltd.
- Hao, Q., Wang, Y., He, Z., & Ou, J. (2009). Bond strength of glass fiber reinforced polymer ribbed rebars in normal strength concrete. *Construction and Building Materials*, 23(2), 865-871. doi:10.1016/j.conbuildmat.2008.04.011
- Hognestad, E., Hanson, N. W., & McHenry, D. (1955). Concrete stress distribution in ultimate strength design. *ACI Journal*, 52, 457-479.
- Intelligent sensing for innovative structures (Module 2). (2006). *An introduction to FRP composites for construction*. Winnipeg (Manitoba): Intelligent sensing for innovative structures.
- Intelligent sensing for innovative structures (Module 3). (2006). *An introduction to FRP-reinforced concrete*. Winnipeg (Manitoba): Intelligent sensing for innovative structures.
- Intelligent sensing for innovative structures (Module 6). (2006). *Application and handling of FRP reinforcement for concrete*. Winnipeg (Manitoba): Intelligent sensing for innovative structures.
- Intelligent sensing for innovative structures (Module 8). (2006). *Durability of FRP composites for construction*. Winnipeg (Manitoba): Intelligent sensing for innovative structures.
- Katz, A., Berman, N., & Bank, L. C. (1999). Effect of high temperature on bond strength of FRP rebars. *Journal of Composites for Construction*, 3(2), 73-81.

-
- Lee, J. -, Kim, T. -, Kim, T. -, Yi, C. -, Park, J. -, You, Y. -, & Park, Y. -. (2008). Interfacial bond strength of glass fiber reinforced polymer bars in high-strength concrete. *Composites Part B: Engineering*, 39(2), 258-270. doi:10.1016/j.compositesb.2007.03.008
- MacGregor, J. G., & Wight, J. K. (2005). *Reinforced concrete mechanics and design* (Fourth ed.). Upper Saddle River, (New Jersey): Pearson Prentice Hall.
- Mallick, P. K. (1988). *Fibre reinforced composites: Materials, manufacturing and design*. New York: Marcel Dekker, Inc.
- Mazaheripour, H., Barros, J. A. O., Sena-Cruz, J. M., Pepe, M., & Martinelli, E. (2013). Experimental study on bond performance of GFRP bars in self-compacting steel fiber reinforced concrete. *Composite Structures*, 95, 202-212. doi:10.1016/j.compstruct.2012.07.009
- Menezes, F., Debs, M. K., & Debs, A. L. H. C. (2008). Bond-slip behavior of self-compacting concrete and vibrated concrete using pullout and beam tests. *Materials and Structures*, 41(6), 1073-1089. doi:10.1617/s11527-007-9307-0
- Moreno, C., & Bastos, A. S. (2006). Experimental and numerical evaluation of bond properties between reinforcement and concrete. *5th International Conference on Mechanics and Materials in Design*, Porto. 1-17.
- Nanni, A., Al-Zaharani, M., Al-Dulaijan, S., Bakis, C., & Boothby, T. (1995). Bond of FRP reinforcement to concrete - experimental results. *Non-Metallic (FRP) Reinforcement for Concrete Structures - Proceedings of the Second International RILEM Symposium (FRPRCS-2)*, 135-145.
- Nilson, A. H. (1971). *Bond stress-slip relations in reinforced concrete*. (No. 345). Ithaca (New York): Department of Structural Engineering Cornell University.
- Oh, H., Sim, J., Kang, T., & Kwon, H. (2010). *An experimental study on the flexural bonding characteristics of a concrete beam reinforced with a GFRP bar* - Korean Society of Civil Engineers. doi:- 10.1007/s12205-011-1018-y
- Park, R., & Paulay, T. (1975). *Reinforced concrete structures*. New York-London-Sydney-Toronto: Wiley Interscience.

-
- Pauw, A. (1960). Static modulus of elasticity of concrete as affected by density. *Journal Proceedings*, 57(12) doi:10.14359/8040
- Perry, E. S., & Thompson, J. N. (1966). Bond stress distribution on reinforcing steel in beams and pullout specimens. *ACI Journal*, 63(No. 8), 865-875.
- Popovics, S. (1970). A review of stress-strain relationships for concrete. *Journal Proceedings*, 67(3) doi:10.14359/7266
- RILEM TC-RC5. (1994). In RILEM (Ed.), *RILEM recommendations for the testing and use of constructions materials* (RC5-Bond test for reinforcement steel. 1. Beam test, 1982-TC9-RC ed.). Bagnaux (France): E & FN SPON.
- RILEM TC-RC6. (1994). In RILEM (Ed.), *RILEM recommendations for the testing and use of constructions materials* (RC6-Bond test for reinforcement steel. 2. Pull-out test, 1983-TC9-RC ed.). Bagnaux (France): E & FN SPON.
- Somayaji, S., & Shah, S. P. (1981). Bond stress versus slip relationship and cracking response of tension members. *Journal Proceedings*, 78(3) doi:10.14359/6920
- Soong, W. H., Raghavan, J., & Rizkalla, S. H. (2011). Fundamental mechanisms of bonding of glass fiber reinforced polymer reinforcement to concrete. *Construction and Building Materials*, 25(6), 2813-2821. doi:10.1016/j.conbuildmat.2010.12.054
- Soretz, S. (1972). A comparison of beam tests and pull out tests. *Materials and Structures*, 5(28), 261-264.
- Tepfers, R. (1973). *A theory of bond applied to overlapped tensile reinforcement splices for deformed bars* (73:2 ed.). Gothenburg, (Sweden): Chalmers University of Technology.
- Tepfers, R., & De Lorenzis, L. (2003). Bond of FRP reinforcement in concrete a challenge. *Mechanics of Composite Materials*, 39(4), 315-328. doi:10.1023/A:1025642411103
- Thorenfeldt, E., Tomaszewicz, A., & Jenson J.J. (1987). Mechanical properties of high-strength concrete and application in design. *Proceedings of the Symposium on Utilization of High-Strength Concrete*, Stavanger, (Norway). 149-159.

-
- Tighiouart, B., Benmokrane, B., & Gao, D. (1998). Investigation of bond in concrete member with fibre reinforced polymer (FRP) bars. *Construction and Building Materials*, 12(8), 453-462. doi:10.1016/S0950-0618(98)00027-0
- Tighiouart, B., Benmokrane, B., & Mukhopadhyaya, P. (1999). Bond strength of glass FRP rebar splices in beams under static loading. *Construction and Building Materials*, 13(7), 383-392. doi:10.1016/S0950-0618(99)00037-9
- Wambeke, B. W., & Shield, C. K. (2006). Development length of glass fiber-reinforced polymer bars in concrete. *ACI Structural Journal*, 103, 11-17.
- Wu, W.P. (1990). *Thermomechanical properties of fibre reinforced plastic (FRP) bars*. West Virginia University. , 292.
- Xu, G., Ai, T., Wang, Q., & Huang, J. (2011). Beam test research on bond behavior between steel bar and concrete in salt-frost environment. *Advanced Materials Research*, 261-263, 50-55. doi:10.4028
- Yang, S., & Chen, J. (1988). Bond-slip and crack width calculations of tension members. *Structural Journal*, 85(4) doi:10.14359/2693
- Zhou, Z., Ou, J. P., & Wang, B. (2003). Smart FRP-OFGB bars and their application in reinforced concrete beams. *Proceedings of the 1st International Conference on Structural Health Monitoring and Intelligent Infrastructure*, Tokyo, (Japan). , 2 861-866.

Appendix A

A.1 General

The design of the RILEM and Notched beam-bond specimens were in accordance with CSA S806, (2012) and unless stated otherwise, all mentioned clauses henceforth refer to this standard however; the flexural capacity calculations will not use any material reduction factors because we are interested in the nominal strength. For the shear design calculations, the material reduction factors are included in order to ensure that this type of failure does not occur since the purpose of the beam-bond specimens were to simulate the behaviour of typical beams which are often designed to fail in flexure. Table A:1 shows the materials properties of the GFRP longitudinal tensile reinforcement, the steel bar used for compression reinforcement in the Notched beams and transverse reinforcement in all of the beams as well as the concrete. Since this section is intended to be a refined version of the preliminary design calculations, note that the GFRP, steel and concrete material properties in Table A:1 are reproduced from the experimental test results presented in Section 3.2 with the exception of the elastic modulus of the GFRP bar and the concrete. Due to the consistency of the test data obtained from the two RILEM beams, an elastic modulus of 68.2 GPa , in accordance with Table 5:2 will be used in these calculations. In addition, the compressive strength of concrete at a time corresponding to testing of the beam and pullout specimens will be used to calculate the concrete elastic modulus.

Table A.1: GFRP, steel and concrete properties

	Parameter	Value
GFRP	A_F	172 mm ²
	d_{bF}	14.8 mm
	E_F	68.2 GPa
	f_{Fu}	1,066 MPa
Steel	A_s	87.0 mm ²
	d_{bs}	10.5 mm
	E_s	215.6 GPa
	f_{su}	735 MPa
	f_y	564 MPa
	ϵ_y	0.0026
Concrete	E_c	27.2 GPa
	f'_c	36.5 MPa
	w_c	2,370 kg/m ³

A.2 Flexural Calculations

Although GFRP reinforced beams are often designed to experience a compression failure through concrete crushing in accordance with CSA S806, (2012), for the purposes of this experimental program, it was necessary to ensure tension failure through GFRP bar rupture. As mentioned previously, the main assumptions of CSA S806, (2012) in the theoretical ultimate flexural calculations are that plane sections remain plane before and after bending, there exists a perfect bond between the reinforcement and the concrete and lastly, the concrete does not provide any resistance to tension and hence, there is no tension stiffening effect.

For the Notched beams, the first step in the design process is to calculate the balanced reinforcement ratio as follows,

- Determine the ultimate concrete and GFRP strain

$$\epsilon_{cu} = 0.0035 \qquad \text{Cl. 8.4.1.2} \qquad \text{Equation A.1}$$

$$\epsilon_{Fu} = \frac{f_{Fu}}{E_F} = 0.016 \qquad \text{Equation A.2}$$

- Calculate the equivalent stress block parameters at ultimate state

$$\begin{aligned} \alpha_1 &= 0.85 - 0.0015f'_c \geq 0.67 && \text{Cl. 8.4.1.5} \quad \text{Equation A.3} \\ &= 0.795 \\ \beta_1 &= 0.97 - 0.0025f'_c \geq 0.67 \\ &= 0.879 \end{aligned}$$

- With reference to Figure A:1 and Figure A:2, the use of strain compatibility, the equivalent stress block as well as the requirement of force equilibrium allows for the calculation of the balanced reinforcement ratio.

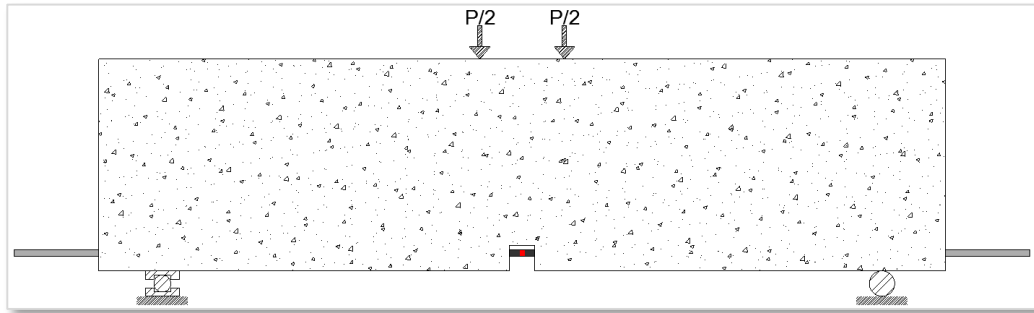


Figure A:1: Notched beam detail

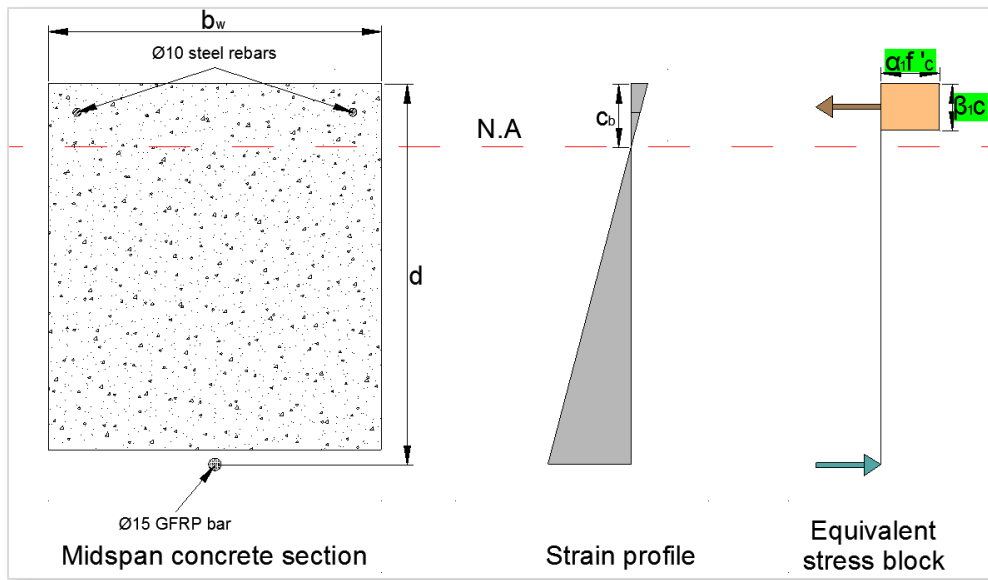


Figure A:2: Strain compatibility and equivalent stress block assumption

$$\begin{aligned}
 \frac{c_b}{d} &= \frac{\varepsilon_{cu}}{\varepsilon_{cu} + \varepsilon_{Fu}} && \text{Equation A.4} \\
 c_b &= d \left(\frac{\varepsilon_{cu}}{\varepsilon_{cu} + \varepsilon_{Fu}} \right) \\
 C_c &= T_F \\
 \alpha_1 f'_c \beta_1 c_b b_w &= f_{Fu} A_F \\
 \alpha_1 f'_c \beta_1 d \left(\frac{\varepsilon_{cu}}{\varepsilon_{cu} + \varepsilon_{Fu}} \right) b_w &= f_{Fu} A_F \\
 \rho_b &= \frac{A_F}{b_w d} = 0.0043
 \end{aligned}$$

In order to guarantee tension failure through GFRP rupture, there is a need for a reinforcement ratio lower than the balanced value and therefore a decision was made to choose a beam with width 400 mm, height 500 mm and length of 2,000 mm. In addition, there was 35 mm of clear cover provided for the GFRP longitudinal reinforcement and 15 mm clear cover for the steel stirrups. Table A:2 presents the overall beam detail while Equation A.5 shows the resulting provided reinforcement ratio.

Table A:2: Overall beam detail

Parameter	Value (mm)
b_w	400
h	500
d	457.6
d'	35
d_{cIF}	35
d_{cIS}	15
jd_{BR1}	432.6
jd_{BR2}	428.6
L	2,000
s	50
Beam shear span	750

$$\rho = \frac{A_F}{b_w d} = \frac{172.0}{(400)(500-35-d_{bF}/2)} = 9.4 \times 10^{-4} \ll \rho_b \quad \text{Equation A.5}$$

With knowledge of the reinforcement ratio and the cross section detail, the second step in the design process is to use an iterative procedure based on strain compatibility in order to establish force equilibrium at ultimate conditions. Note that the value of α_1 and β_1 cannot be determined using Equation A.3 since the concrete is not at its ultimate strain at the time

of the beam's flexural failure and therefore it is necessary to use the expressions outlined in detail in Section 5.3.3 .

As the first iteration, the choice of a neutral axis depth of $c = 36 \text{ mm}$, which, given the chosen cross section, is less than $c_b = 82 \text{ mm}$ and the assumption of the compression steel reinforcement not yielding at the beam failure state, leads to the following force equilibrium equation,

$$\begin{aligned} C_c + f_s(2A_s) &= T_F && \text{Equation A.6} \\ (\alpha_1 f_c \beta_1 c b_w) + f_s(2A_s) &= f_{Fu} A_F \end{aligned}$$

From strain compatibility,

$$\begin{aligned} \frac{\varepsilon_c}{c} &= \frac{\varepsilon_{Fu}}{d - c} && \text{Equation A.7} \\ \varepsilon_c &= 1.3 \times 10^{-3} \\ \frac{\varepsilon_c}{c} &= \frac{\varepsilon_s}{c - d'} \\ \varepsilon_s &= 3.7 \times 10^{-5} \\ f_s &= \varepsilon_s E_s = 8.0 \text{ MPa} \leq f_y \end{aligned}$$

From the expressions provided in Section 5.3.3 ,

$$\begin{aligned} \frac{f_c}{f'_c} &= \frac{n(\varepsilon_c/\varepsilon'_c)}{n - 1 + (\varepsilon_c/\varepsilon'_c)^{nk}} && \text{Equation A.8} \\ f_c &= 34.8 \text{ MPa} \\ \alpha_1 \beta_1 &= \frac{\varepsilon_c}{\varepsilon'_c} - \frac{1}{3} \left(\frac{\varepsilon_c}{\varepsilon'_c} \right)^2 = 0.55 \\ \beta_1 &= \frac{4 - \varepsilon_c/\varepsilon'_c}{6 - 2 \varepsilon_c/\varepsilon'_c} = 0.72 \end{aligned}$$

Thus,

$$\begin{aligned} (\alpha_1 f_c \beta_1 c b_w) + f_s(2A_s) &= f_{Fu} A_F && \text{Equation A.9} \\ 276,786 \text{ N} &\neq 183,352 \text{ N} \end{aligned}$$

Successive iterations converge on a neutral axis value of $c = 30.8693 \text{ mm}$ and note that this results in the steel bars at the top of the section contributing to tensile resistance, though the amount of this contribution as it will be demonstrated is, negligible. The assumption that the steel does not yield given $c = 30.8693 \text{ mm}$ is correct since its strain was 1.5×10^{-4} which is much lower than its yield strain of 2.6×10^{-3} .

$$\begin{aligned} C_c &= T_F + f_s(2A_s) && \text{Equation A.10} \\ 189,032 &\cong 183,352 + 5,680 \\ 189,032 &\cong 189,032 \end{aligned}$$

Based on a neutral axis depth of $c = 30.8693 \text{ mm}$, the resulting parameters are,

$$\begin{aligned} \varepsilon_c &= 1.1 \times 10^{-3} && \text{Equation A.11} \\ \varepsilon_s &= 1.5 \times 10^{-4} \\ f_s &= \varepsilon_s E_s = 32.6 \text{ MPa} \leq f_y \\ f_c &= 31.3 \\ \alpha_1 \beta_1 &= 0.49 \\ \beta_1 &= 0.71 \end{aligned}$$

With reference to Figure A:3, the ultimate moment capacity for the Notched beams becomes,

$$\begin{aligned} M_{max} &= T_F \left(d - \frac{\beta_1 c}{2} \right) + T_s \left(d' - \frac{\beta_1 c}{2} \right) && \text{Equation A.12} \\ &= (f_{Fu} A_F) \left(d - \frac{\beta_1 c}{2} \right) + [\varepsilon_s E_s (2A_s)] \left(d' - \frac{\beta_1 c}{2} \right) \\ &= 81.9 + 0.1 = \mathbf{82.0 \text{ kN} \cdot \text{m}} \end{aligned}$$

Thus, it is evident that the contribution of the steel bars at the top portion of the cross section to the ultimate moment capacity of the Notched beams is negligible.

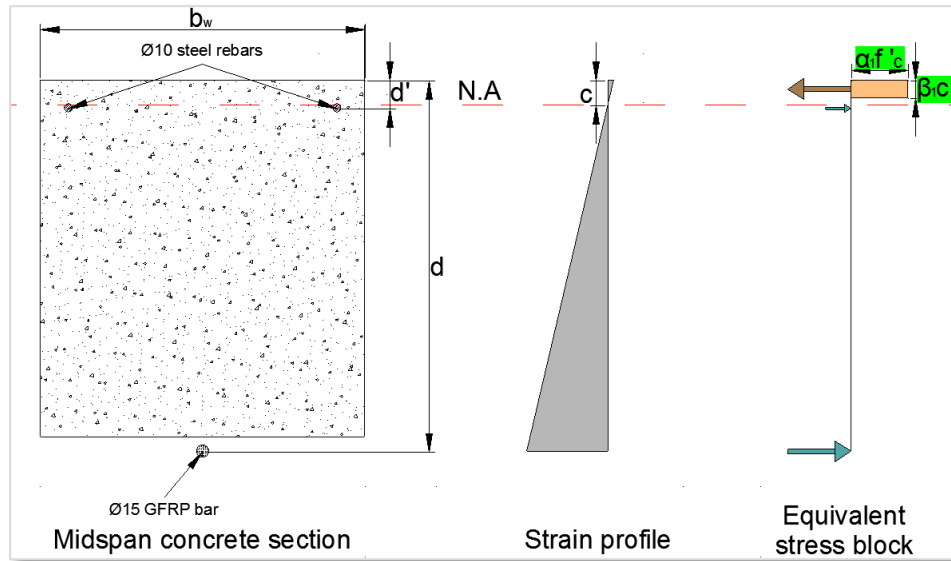


Figure A:3: Ultimate moment capacity calculation

With reference to Figure A:4, one can estimate the cracking moment for the Notched beams through the following steps,

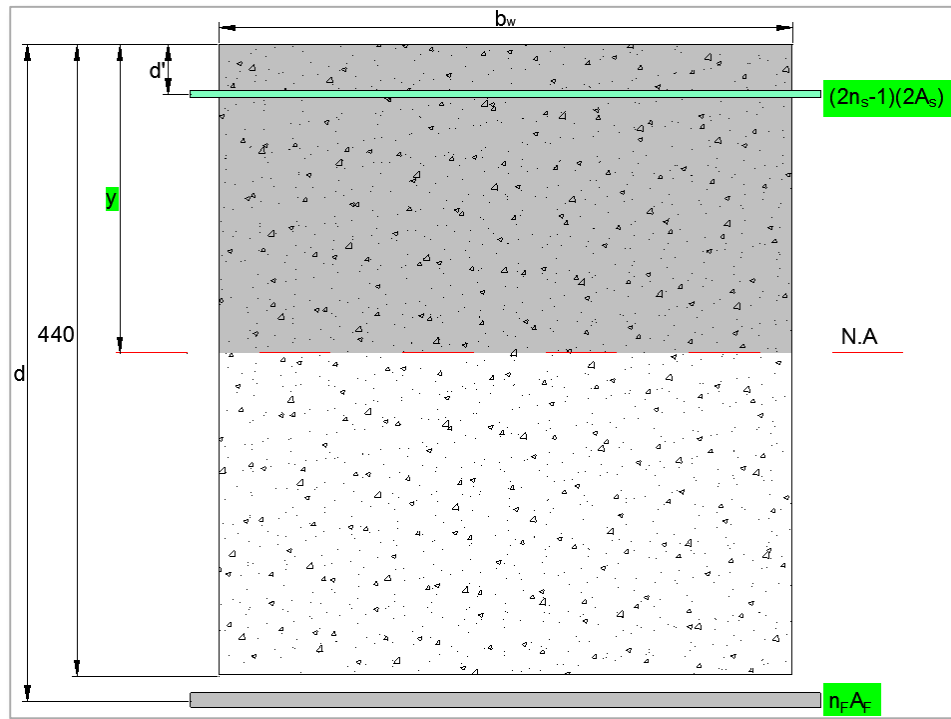


Figure A:4: Midspan cracking moment calculation for the Notched beams (All dimensions are in mm)

- Depth of neutral axis

$$y = \frac{(440/2)(b_w)(440) + d'(2n_s - 1)(2A_s) + d(n_F A_F)}{b_w(440) + (2n_s - 1)(2A_s) + n_F A_F} \quad \text{Equation A.13}$$

$$n_s = \frac{E_s}{E_c}$$

$$n_F = \frac{E_F}{E_c}$$

$$y = 217.9 \text{ mm}$$

- Gross moment of inertia

$$I_g = \frac{b_w y^3}{3} + \frac{b_w (440 - y)^3}{3} + (2n_s - 1)(2A_s)(y - d')^2 + n_F A_F (d - y)^2 \quad \text{Equation A.14}$$

$$= 2,951,517,385 \text{ mm}^4$$

- Modulus of rupture of concrete

$$f_r = 0.6\lambda\sqrt{f'_c} = 3.6 \text{ MPa} \quad \text{Cl. 8.3.2.8} \quad \text{Equation A.15}$$

where,

$$\lambda = 1.0 \text{ for Normal density concrete} \quad \text{Equation A.16}$$

- Cracking moment of beam

$$M_{cr}^{mid.} = f_r \times \frac{I_g}{(440 - y)} \quad \text{Cl. 8.3.2.6} \quad \text{Equation A.17}$$

$$= 48.2 \text{ kN} \cdot \text{m}$$

Note that for the Notched beams, M_{max} is approximately $1.7 M_{cr}^{mid.}$ and this satisfies the requirements of Cl. 8.4.2.1

For the purposes of this study, it is also necessary to calculate the cracking moment of inertia, which, with reference to Figure A:5, becomes,

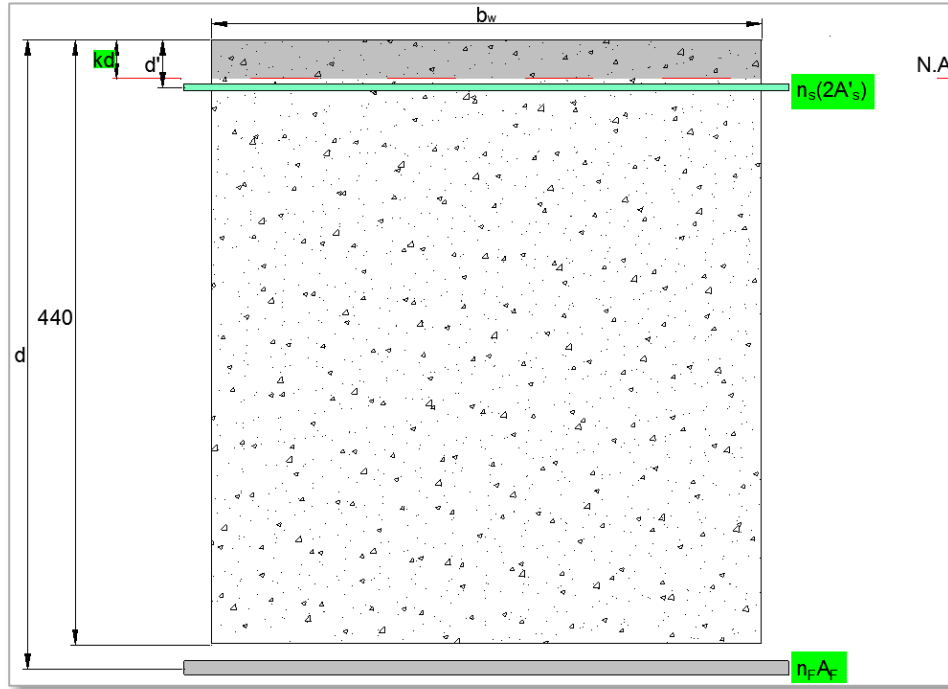


Figure A:5: Midspan cracked moment of inertia for the Notched beams (All dimensions are in mm)

- Depth of neutral axis

$$b_w(kd)(kd/2) = n_F A_F(d - kd) + n_S(2A_S)(kd - d')$$

$$kd = 30.8 \text{ mm}$$

Equation A.18

- Cracked moment of inertia

$$I_{cr} = \frac{b_w(kd)^3}{3} + n_F A_F(d - kd)^2 + n_S(2A_S)(d' - kd)^2$$

$$= 82,466,941 \text{ mm}^4$$

Equation A.19

As stated earlier, experimentally, it was observed that the vertical extent of the midspan flexural crack was substantial such that 50 and 40 mm of uncracked concrete remained intact for BN1 and BN2, respectively and this is comparable to the theoretical cracked neutral axis depth, kd of 30.8 mm. In addition, note that the kd value is approximately

equal to the neutral axis depth, c of 30.9 mm , at the ultimate beam capacity and this validates the experimental observation that after its occurrence, the midspan flexural crack had minimal further progression.

Concerning the RILEM beams, with reference to Figure A:6 and Section 4.2.1 , since the moment arm prior to testing is known and as previously discussed, does not change significantly throughout the testing process, an estimation of the ultimate flexural capacity of BR1 and BR2 becomes,

$$M_{max}(BR1) = f_{Fu}A_F(jd_{BR1}) = 79.3\text{ kN} \cdot \text{m} \quad \text{Equation A.20}$$

$$M_{max}(BR2) = f_{Fu}A_F(jd_{BR2}) = 78.6\text{ kN} \cdot \text{m} \quad \text{Equation A.21}$$

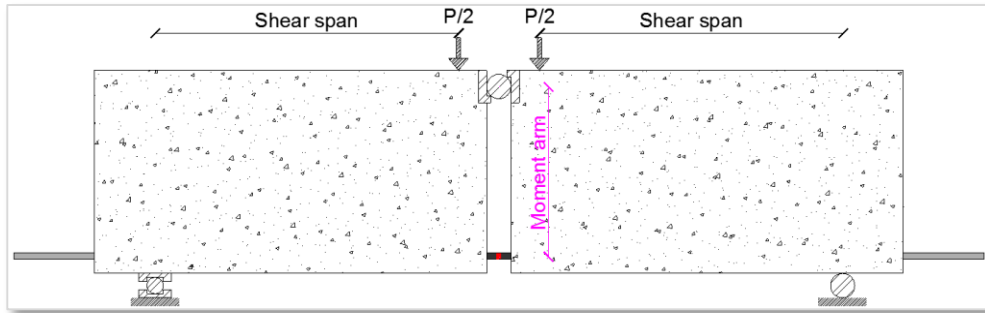


Figure A:6: RILEM beam detail

Thus, theoretical calculations predict that the Notched beams will have a moment capacity of $82.0\text{ kN} \cdot \text{m}$ while the RILEM beams BR1 and BR2 will have a moment capacity of 79.3 and $78.6\text{ kN} \cdot \text{m}$, respectively. The average, theoretical ultimate moment for the beam-bond tests is therefore $80.0\text{ kN} \cdot \text{m}$ which, under four-point bending results in the bending moment and shear diagram shown in Figure A:7.

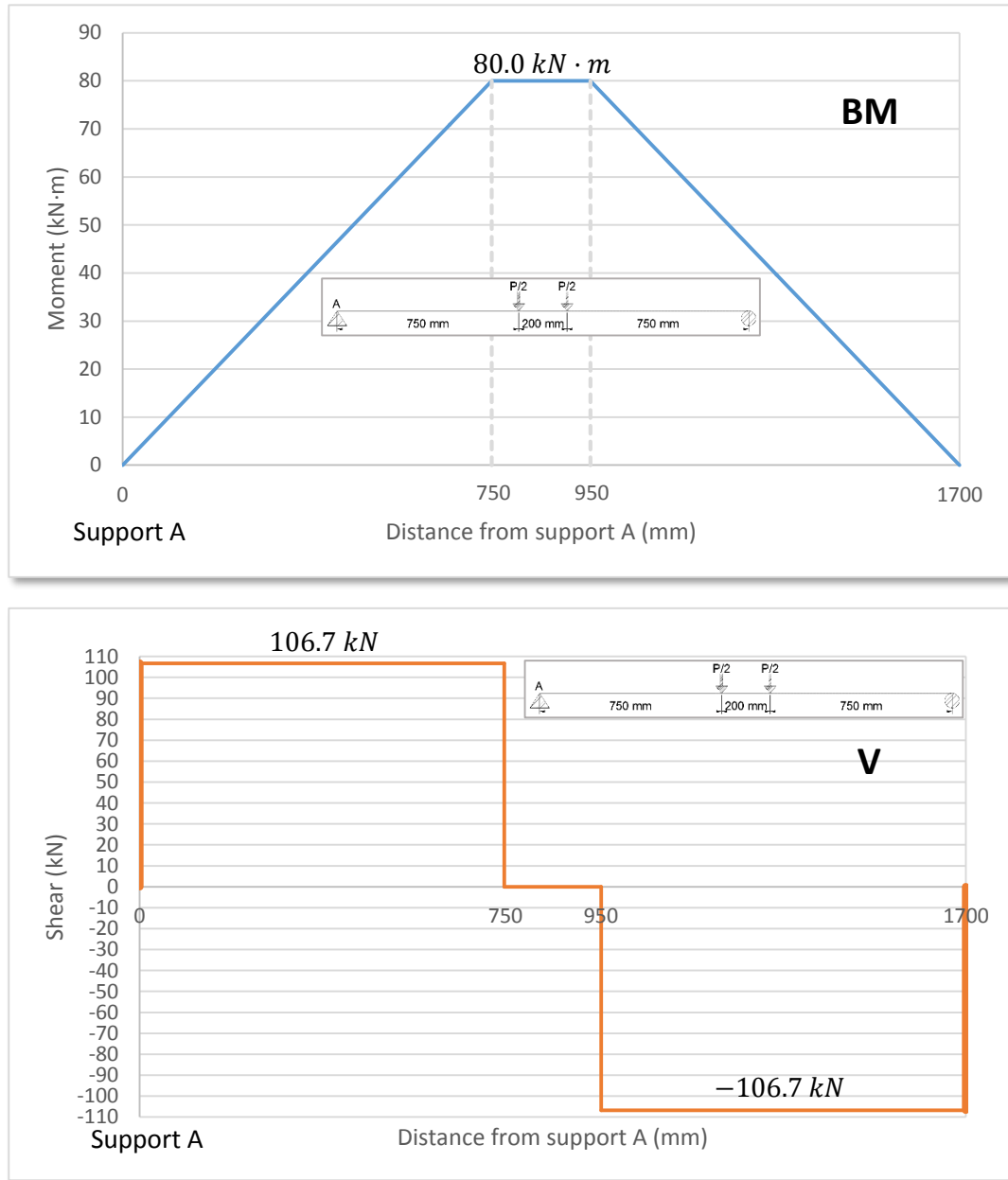


Figure A:7: Average bending moment and shear diagrams for beam-bond specimens

A.3 Shear Calculations

With reference to Figure A:7, with an average moment demand, M_f of $80.0 \text{ kN} \cdot \text{m}$, the shear resistance provided must be greater than the shear demand, V_f of approximately 106.7 kN . For the transverse reinforcement of the beam-bond specimens, the choice of No. 10 steel stirrups, their 50 mm spacing, as well as their 15 mm clear cover was in accordance with the RILEM TC-RC5, (1994) recommendation. The shear resistance for the beam-bond specimens is calculated through,

$$V_r = V_c + V_{ss} < 0.22\phi_c f'_c b_w d_v \quad \text{Cl. 8.4.4.4} \quad \text{Equation A.22}$$

$$V_c = 0.05\lambda\phi_c k_m k_r (f'_c)^{1/3} b_w d_v \quad \text{Cl. 8.4.4.5} \quad \text{Equation A.23}$$

$$0.11\phi_c \left(\sqrt{f'_c} \right) b_w d_v < V_c < 0.22\phi_c \left(\sqrt{f'_c} \right) b_w d_v$$

$$k_m = \sqrt{\frac{V_f d}{M_f}} = 0.78 \leq 1.0$$

$$k_r = 1 + (E_F \rho)^{1/3} = 5.05$$

The effective shear depth d_v is 411.8 mm and to remain conservative in the prediction of shear resistance, the calculations include the modification factor due to member size k_s , in accordance with Cl. 8.4.4.7, but neglect the arch effect factor k_a mentioned in Cl. 8.4.4.6.

$$\phi_c = 0.65 \quad \text{Cl. 6.5.3.2} \quad \text{Equation A.24}$$

$$k_s = \frac{750}{450 + d} = 0.83 \leq 1.0 \quad \text{Cl. 8.4.4.7} \quad \text{Equation A.25}$$

$$71.2 \text{ kN} < V_c = 58.1 \text{ kN} < 142.3 \text{ kN} \quad \text{Equation A.26}$$

$$\text{Thus, } V_c = 71.2 \text{ kN}$$

$$V_{ss} = \frac{\phi_s(2A_s)f_y d_v}{s} \cot\theta \quad \text{Cl. 8.4.4.9} \quad \text{Equation A.27}$$

$$30^\circ < \theta = 30^\circ + 7000\varepsilon_l < 60^\circ$$

$$\varepsilon_l = \frac{\frac{M_f}{d_v} + V_f}{2(E_F A_F)} = 0.013$$

$$30^\circ < \theta = 120^\circ < 60^\circ$$

$$\text{Thus, } \theta = 60^\circ$$

Note that the 50 mm spacing of the transverse reinforcement satisfies Cl. 8.4.6.1.

$$\phi_s = 0.85 \quad \text{Cl. 6.5.4} \quad \text{Equation A.28}$$

$$\text{Thus, } V_{ss} = 396.6 \text{ kN} \quad \text{Equation A.29}$$

$$V_r = V_c + V_{ss} = 467.8 \text{ kN} < 859.8 \text{ kN} \quad \text{Equation A.30}$$

$$\text{Thus, } V_r = 467.8 \text{ kN}$$

In summary, using the most conservative estimation of the shear resistance in the beam-bond specimens leads to,

$$V_r = 467.8 \text{ kN} > V_f = 106.7 \text{ kN} \quad \text{Equation A.31}$$

As stated previously, for the purposes of this experimental program, it was critical for the beam-bond specimens not to experience shear failure but rather fail by flexure through the rupture of the GFRP longitudinal tensile reinforcement.